DYNAMICS OF HIGH- AND LOW-PRESSURE PLASMA REMEDIATION

BY

XUDONG XU

B.S., Hefei University of Technology, 1985
M.S., Anhui Institute of Optics & Fine Mechanics, Chinese Academy of Sciences, 1988
M.S., University of Illinois at Urbana-Champaign, 1995

THESIS

Submitted in partial fulfillment of the requirements
for the degree of Doctor of Philosophy in Electrical Engineering
in the Graduate College of the
University of Illinois at Urbana-Champaign, 2000

Urbana, Illinois

DYNAMICS OF HIGH- AND LOW-PRESSURE PLASMA REMEDIATION

Xudong “Peter” Xu
Department of Electrical and Computer Engineering
University of Illinois at Urbana-Champaign, 1999
Mark J. Kushner, Advisor

Plasma remediation is an efficient and promising technology to destroy toxic and greenhouse gases. In this work we computationally study the dynamics of high-pressure dielectric barrier discharges (DBDs) and low-pressure plasma processing reactors. The high-pressure systems are examined in the context of volatile organic compound (VOC) and NO_x remediation. The low-pressure systems are studied in the context of the consumption and generation of perfluorocompounds (PFCs) in an inductively coupled plasma (ICP) etching reactor and abatement of PFCs in a plasma burn box. The plasma kinetic processes are discussed with the goal of providing insight for optimizing efficiencies.

In electropositive gas mixtures, the expanding microdischarges in DBDs maintain a fairly uniform electron density as a function of radius. In electronegative gas mixtures, the electron density has a maximum value near the streamer edge due to dielectric charging and attachment at smaller radii at lower E/N (electric field/number density). The expansion and ultimate stalling of the microdischarge is largely determined by charging of the dielectric at larger radii than the core of the microdischarge.

The dynamics of adjacent microdischarges are similar to a single microdischarge, with the exception that the electron density peaks at the interface. The residual charge on the dielectric in DBDs from a preceding microdischarge can significantly change the dynamics of microdischarges produced by the next voltage pulse.

Remediation of carbon tetrachloride (CCl_4) in DBDs progresses by chain chemistry. Though dissociative electron attachment is primarily responsible for initial dissociation of CCl_4, dissociative excitation and charge transfers from Ar^*, Ar^{**}, Ar^+, and O_2^+ to CCl_4 play a significant role. Choosing the proper O_2 to CCl_4 ratio and preventing the presence of water vapor in gas mixtures can considerably increase the remediation efficiency of CCl_4.

C_2F_6 (or CF_4) consumption in the plasma etching reactor increases with increasing ICP power deposition, and decreasing C_2F_6 (or CF_4) mole fraction or total gas flow rate, but the efficiency of removal of C_2F_6 (eV/molecule) is only strongly dependent on the C_2F_6 mole fraction and total gas flow rate. All PFCs in the effluent can generally be remediated in the burn-box at high power deposition with a sufficiently large flow of additive gases (O_2, H_2, or H_2O). In general, CF_4 generation occurs during abatement of C_2F_6 using O_2 as an additive, especially for high power with low O_2 input. CF_4 is not, however, substantially produced when H_2 or H_2O is used as additives.

The use of DBDs as excimer ultraviolet (UV) lighting sources was also studied. The mixture $Xe/Cl_2 \approx 99/1$ was found to be an optimum gas mixture for the generation of the $XeCl^*$. Higher applied voltage improves both the intensity and efficiency of UV photon generations. The strong attachment at high Cl_2 concentration (e.g., $\geq 5\%$) leads to electron shell propagation to smaller radii after the voltage pulse.

ACKNOWLEDGMENTS

I would like to express my gratitude and deep appreciation to my advisor, Professor Mark J. Kushner, for his guidance, encouragement, inspiration, and support that made this work possible. He has helped me greatly and constantly in both my professional and personal development with his wisdom, experience, and intuition.

My sincerely thanks go to the professors of my final dissertation committee, Herman Krier, Kenneth Beard, Ilesanmi Adesida, and J. Gary Eden for their thoughtful comments.

I am also grateful to all my fellow members in the Computational Optical and Discharge Physics Group, Ron Kinder, Da Zhang, Junqing Lu, Dan Cronin, Kelly Voyles, Dr. Trudy van der Straaten, Dr. Shahid Rauf, Dr. Robert Hoekstra, Dr. Eric Keiter, Dr. Michael Grapperhaus, Dr. Helen Hwang, Dr. Fred Huang, and Dr. Wenli Collison. Special thanks go to Rajesh Dorai and Brian Lay at some crucial moments.

Finally, I am most indebted to my wife, my son, my parents, and my sister for their everlasting love, encouragement, patience, and support throughout the course of my education. They have always been a great source of inspiration to me.

TABLE OF CONTENTS

Page

1. INTRODUCTION 1
    1.1 References 10

2. DESCRIPTION OF THE MODELS 16
    2.1. Introduction 16
    2.2. One-Dimensional Plasma Chemistry and Hydrodynamic Model 16
    2.3. One-Dimensional Plasma Chemistry and Hydrodynamic Model 19
    2.4. Two-Dimensional Hybrid Plasma Equipment Model (HPEM) 21
        2.4.1. The Electromagnetic Module (EMM) 22
        2.4.2. The Electron Energy Transport Module (EETM) 23
        2.4.3. The Fluid-Kinetics Simulation (FKS) 24
    2.5. References 28

3. SINGLE MICRODISCHARGE DYNAMICS IN DIELECTRIC BARRIER DISCHARGES 30
    3.1. Introduction 30
    3.2. Dynamics of Microdischarges in Pure Nitrogen Gas 30
    3.3. Dynamics of Microdischarges in N_2/O_2 and $N_2/O_2/H_2O$ 35
    3.4. Dynamics of Microdischarges in Ar, Ar/O_2 and $Ar/O_2/CCl_4$ 38
    3.5. Concluding Remarks 39
    3.6. References 55

4. MULTIPLE MICRODISCHARGE DYNAMICS IN DIELECTRIC BARRIER DISCHARGES 56
    4.1. Introduction 56
    4.2. Multiple Microdischarges Dynamics in N_2 56
    4.3. Multi-microdischarges Dynamics in N_2/O_2 60
    4.4. Consequences of Remnant Surface Charges on Microdischarge Spreading . 62
    4.5. Concluding Remarks 64

5. REMEDIATION OF CARBONTETRACHLORIDE IN DIELECTRIC BARRIER DISCHARGES 76
    5.1. Introduction 76
    5.2. Reaction Mechanisms in Remediation of CCl_4 77
    5.3. Spatial Dependencies in Remediation of CCl_4 80
    5.4. Optimization of Remediation Conditions 83
    5.5. Effects of H_2O on CCl_4 Remediation 86
    5.6. Concluding Remarks 88
    5.7. References 102

6. MODELING EXCIMER EMISSION IN DIELECTRIC BARRIER DISCHARGES 104
6.1. Introduction 104
6.2. Formation of Excimers 105
6.3. Spatial Dependencies in Excimer Generation 108
6.4. Optimization of Discharge Conditions for Excimer and Photon Generation . 110
6.5. Concluding Remarks 113
6.6. References 131

7. PLASMA REMEDIATION OF PERFLUOROCOMPOUNDS IN INDUCTIVELY COUPLED PLASMA REACTORS 133

7.1. Introduction 133
7.2. Plasma Characteristics, Consumption and Generation of PFCs in an ICP Etching Reactor 134
7.3. Plasma Abatement of PFCs in a Burn-box 138
  7.3.1. Validation 138
  7.3.2. O_2 as an additive for PFC abatement 141
  7.3.3. H_2 as an additive for PFC abatement 146
  7.3.4. H_2O as an additive for PFC abatement 148
7.4. Concluding Remarks 150
7.5. References 177

8. CONCLUDING REMARKS 178

APPENDIX A. LIST OF SPECIES FOR $N_2/O_2/H_2O$, $A/O_2/H_2O/CCl_4$, Xe/Cl_2 AND/$CF_4/C_2F_6/H_2/O_2/H_2O$ PLASMAS 181

APPENDIX B. LIST OF REACTIONS FOR $N_2/O_2/H_2O$, $A/O_2/H_2O/CCl_4$, Xe/Cl_2 AND/$CF_4/C_2F_6/H_2/O_2/H_2O$ PLASMAS 182
B.1. References 205

VITA. 212

1. INTRODUCTION

Plasma processing provides innovative and promising new approaches to selectively remediating toxic and greenhouse gases [1-2]. These techniques are potentially lower in cost and more efficient than conventional thermal incineration. In these plasmas, the majority of electrical energy is expanded in heating electrons, rather than heating gas. The plasmas are nonequilibrium with the electrons, ions, and neutrals having different temperatures. Usually the electrons are hot (typical temperature in the range of a few to 10s eV), whereas the ions and neutrals are near ambient temperature.

Various types of atmospheric-pressure nonthermal plasma devices have been developed and studied for environmental applications. The most extensively investigated applications of this type are used to treat dilute concentrations of toxic molecules in airstreams. Potential advantages of the high-pressure, nonthermal plasma approach include the highly energy efficient selectivity provided by the plasma chemistry and its capability for minimizing secondary-waste production. Atmospheric pressure operation is preferred for high-throughput waste processing. Electrical-beam irradiation and electrical discharge methods, such as pulsed corona and dielectric barrier discharges, can produce these plasmas at atmospheric pressure.

In an electron beam system, electrons are created and then accelerated by high voltage under vacuum before being injected into the gas stream through a thin foil window. The high-energy electrons ionize the background gas in a reaction chamber, generating a plasma. The process creates up to several thousand secondary electrons for every high-energy electron produced by the beam. Pilot-scale systems to investigate

NO_x, SO_2 and volatile organic compounds (VOCs) removal have been operated [3-12]. The principal issue with the electron beam approach is the design of an appropriate e-beam window. The window should be thin enough to allow high-energy electrons to penetrate into the reaction chamber, and also be strong enough to sustain a vacuum seal and endure the physical stresses generated by heat resulting from the beam. For metal-foil windows, several hundred KeV of acceleration is required. For processing the high gas-flow rates from fossil-fuel plants, these facilities usually utilize MeV range electron beams. Electrons having these energies can lead to the formation of X-rays, which require heavy external shielding.

Corona is a discharge-based device that exists in several forms, depending on the polarity of the field and the electrode geometrical configuration [13-29]. In a point-plane electrode configuration, a positive corona can be generated when a sufficiently high positive voltage is applied to the point. The first positive corona phenomenon observed is the onset from the point, followed rapidly by glow corona and spark discharge. In the same geometry, a negative corona can be produced when the point is connected to a high negative voltage. The negative corona initially forms a Trichel pulse corona, followed by pulseless corona and spark discharge. For a wire-cylinder or wire-plate electrode arrangement, a discharge with a positive wire electrode may have a tight sheath around the electrode or be a streamer moving away from electrode. A discharge with a negative electrode may display a quickly moving glow or may be concentrated in small active spots [30].

Dielectric barrier discharges (DBDs), also known as *silent electrical discharges*, occur in discharge configurations with at least one dielectric barrier between the electrodes. This discharge arrangement was originally used by Werner Siemens in 1857. DBDs have long been used for ozone syntheses [31-35] and are now being investigated for use in plasma remediation of toxic gases [36-50] and as excimer (*exci*ted di*mers*, or tri*mers*) ultraviolet (UV) radiation sources [51-54]. By applying an alternating (sine or square wave) potential of several kV with a frequency of a few hundreds to several thousand hertz to the electrodes, at least one of which is covered by a dielectric, filamentary microdischarges are created that have area densities of 10s to 100s cm^{-2} (see Fig. 1.1). (All figures/tables appear at end of chapter.) The discharge plasma channels are terminated when charge accumulation on the dielectric surface (or surfaces) reduces the voltage across the gap at the position of the microdischarge to a value below the self-sustaining level. Typical microdischarge current pulses have a duration of a few to 100 ns and diameters of 10s to 100 μm.

Though electron beams and corona discharges can also create nonthermal plasmas, DBDs may be a more promising technology for some toxic gas streams. Some examples are these streams from mobile emitting sources (for example, NO_x emission from diesel truck engines), remote or sporadically emitting sources (for example, diesel emergency generators) or small installations (for example, volatile organic solvents, VOCs, released from dry cleaners). These systems require inexpensive, low-voltage, compact, and reliable systems that efficiently and selectively convert the toxic gases to benign or more treatable products. Dielectric barrier discharges are attractive candidates for these systems.

Although the DBDs have been known and used for a long time, quantitative understanding of the dynamics of DBDs is limited due to their inhomogeneous discharge structures with complex reaction mechanics. Several investigations [33, 55-57] have computationally addressed microdischarge dynamics in DBDs. One-dimensional simulations in the direction perpendicular to the electrodes have shown that early during the discharge pulse the electric field is large in the gap; however, formation of a cathode fall reduces the bulk electric field, which in turn reduces excitation rates [55-57]. Eliasson and Kogelschatz [33] developed a two-dimensional simulation [$(r,\ z)$ in the plane perpendicular to the electrodes] to investigate the expansion of microdischarges and charging of the dielectric in xenon and oxygen plasmas. They found that for a 1-mm gap in 1 atm of oxygen, the microdischarge expanded to a radius of 10s to 100s μm in ≈50 ns. Similar computational results were obtained by Braun et al. [57].

In typical applications of DBDs, the gas pressure is sufficiently large ($pd > 75$ - 100 Torr-cm) and current pulses sufficiently short (<10s ns) that diffusion is not a dominant process in the ion kinetics. Volumetric processes (ionization, attachment, and dissociative recombination), which are generally exponentially dependent on the magnitude of the local electric field, dominantly determine the ion density and mole fractions. Typically, there is a unique value of E/N (electric field/gas number density) for a given gas mixture where self-sustaining or steady state ion kinetics can be achieved and where volumetric ion sources balance volumetric ion sinks. (This is strictly true only for discharges dominated by attachment and in which multistep processes are not important.) At a given radial location, as the microdischarge charges the dielectric and removes voltage from the gap, the electric field in the bulk plasma necessarily transitions from being above self-sustaining (required to avalanche the gas) to being below self-sustaining (required to extinguish the discharge). The dependence of rate coefficients on E/N for such things as ionization, attachment, recombination, and ion-ion neutralization can be markedly different. As a result, the ion kinetics, and therefore ion composition, of the microdischarge can be expected to be very different as a function of time as the dielectric charges and *E/N* changes. This situation is further complicated by the fact that the microdischarge radially expands during the current pulse from 10s to 100s μm. As the microdischarge expands, the sequence of avalanche, dielectric charging, and quenching occurs in a wavelike fashion propagating to larger radii. Ion composition may therefore depend not only on time but also radius. Since ion chemistry can greatly affect the efficiency of, for example, plasma remediation processes, the radial dynamics of microdischarge expansion and their effect on ion chemistry, warrants further study.

To investigate the dynamics and kinetics of plasma remediation in DBDs, one-dimensional (1-D) and a two-dimensional (2-D) plasma chemistry and hydrodynamics models have been developed. The 1-D model is radially dependent and is applied to the study of a single DBD dynamic. The 2-D model is a Cartesian-coordinate simulation which can be used to investigate dynamics of multiple, radially asymmetric, microdischarges in close vicinity. The details of the two models are discussed in Chapter 2.

In this work, computer models are used to investigate the dynamics and kinetics of plasma remediation. In Chapter 3, the 1-D model is applied to the study of ion kinetics in an expanding microdischarge in a DBD. The context of this study is the use of DBDs for toxic gas remediation, and therefore, three representative gas systems are investigated: Ar and N_2 (nonattaching); Ar/O_2, N_2/O_2, and N_2/O_2/H_2O (moderately attaching); and Ar/O_2/CCl_4 (highly attaching). It was found that as the *E/N* in the bulk plasma transitions from avalanche to below self-sustaining, the ion kinetics in these three representative systems differ markedly.

In Chapter 4, results from the 2-D model for the expansion of multiple, closely spaced microdischarges in DBDs are discussed. Because the final applications of interest are plasma remediation of toxins from air, N_2 and dry air (N_2/O_2) discharges were investigated as examples of nonattaching and attaching discharges. Parametric studies for microdischarge development for one to four adjacent microdischarges are discussed.

Carbon tetrachloride (CCl_4) is an important industrial solvent, which is widely used as degreasing and cleaning agent in the dry-cleaning and textile industries. CCl_4 is a toxin and needs to be carefully disposed of. Several recent experimental studies to destroy CCl_4 have been conducted by using electron-beam irradiation, corona discharges and dielectric barrier discharges [12, 43, 46, 49]. In Chapter 5, we present an in-depth study of CCl_4 remediation in Ar/O_2 and $Ar/O_2/H_2O$ mixtures in DBDs. The reaction mechanisms and the optimal conditions are determined.

Another important application of DBDs is to produce narrow-band excimer ultraviolet radiation. UV photon sources have a number of applications such as biological sterilization, photochemical degradation of organic compounds in flue gases, photo-induced surface modification and material deposition, and lithography. During the last few years DBD UV sources have been investigated using many different excited species, including rare gas excimers (such as Ar_2^*, Kr_2^*, and Xe_2^*), molecular rare gas-halide excimers (such as $ArCl^*$, $KrCl^*$, $XeCl^*$, $XeBr^*$, and XeI^*), and halogen dimers (such as F_2^*, Cl_2^*, Br_2^* and I_2^*), where a wide range of (V)UV spectrum can be covered

[51-54, 58, 59]. In Chapter 6, the kinetics and optimization of the $XeCl^*$ (308) excimer system is discussed.

In Chapter 7, the 2-D Hybrid Plasma Equipment Model (HPEM) was used to investigate plasma remediation of perfluorocompounds (PFCs) for low-pressure discharges. (An overview of the HPEM is given in Chapter 2.) PFCs are important to the semiconductor industry because they are widely used as process gases in microelectronics fabrication for etching and chamber cleaning [60-67]. However, these PFCs are absorbers of infrared radiation, having long atmospheric lifetimes, and thus have high global warming potentials (see Fig. 1.2) [68]. The Environmental Protection Agency (EPA) and individual semiconductor companies signed a memoranda of understanding in March 1996 in an effort to reduce PFC emissions. There are four generally accepted approaches to reducing PFC emission: process optimization, substitution, recycling and recovery, and abatement [69]. There have been significant efforts to optimize etching and cleaning processes to increase PFC utilization and decrease emissions. However, it has been difficult for process optimization to achieve the desired reductions in PFC emissions without detrimentally affecting product throughput, especially in plasma etching. Though some alternative chemicals (C_3F_8 and NF_3) [69-72] show promise as substitutes, they also have high global warming potentials and may result in PFC by-product generation. Recycling and recovery of the unreacted PFCs from the effluent may be desirable from a PFC utilization standpoint; however, current recovery technologies are not economical for existing fabrication facilities. Plasma remediation of gas emissions from plasma and thermal reactors is therefore an attractive alternative abatement strategy.

Plasmas have experimentally demonstrated to efficiently destroy C_2F_6, a found in reactor effluent at low pressures. For example, Mohindra et al. [72] used a microwave tubular reactor to destroy the PFCs. Hartz and coworkers [73] demonstrated the advantage of utilizing low-pressure surface wave plasmas to destroy C_2F_6. A commercial point-of-use RF abatement system developed by Litmas was investigated by Tonnis et al. [74]. The expansion of the semiconductor industry has resulted in a potential corresponding increase in PFC emissions, so a need for new methods of PFC remediation is necessary. It is therefore important to computationally investigate the kinetic processes of plasma remediation of PFCs in order to optimize the process. In Chapter 7, the dissociation of PFCs in an inductively coupled plasma (ICP) etching reactor and their subsequent remediation in a downstream plasma burn-box are discussed.

Finally, conclusions are made in Chapter 8.

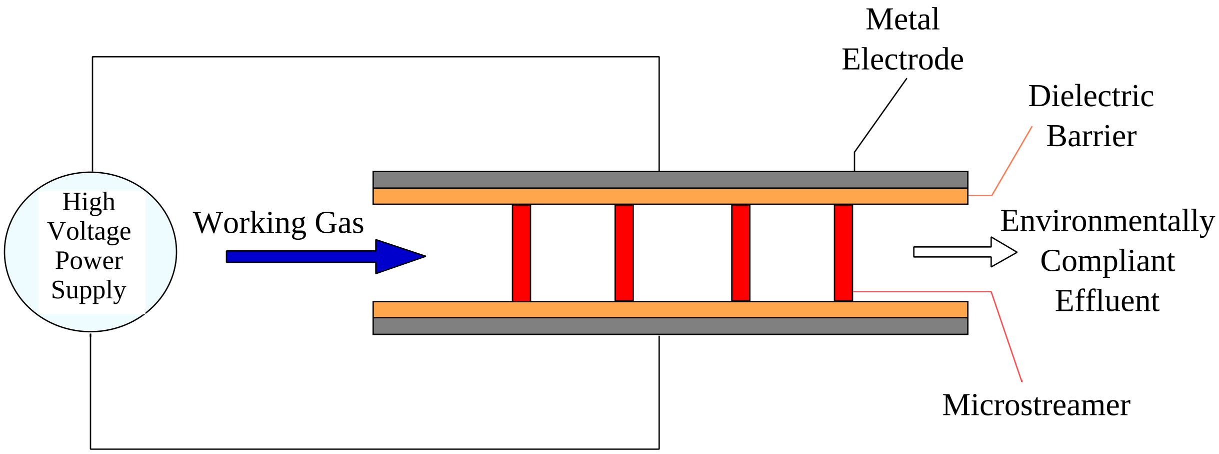

Fig. 1.1. Schematic of a dielectric barrier discharge (DBD) plasma reactor for gaseous-based hazardous waste.

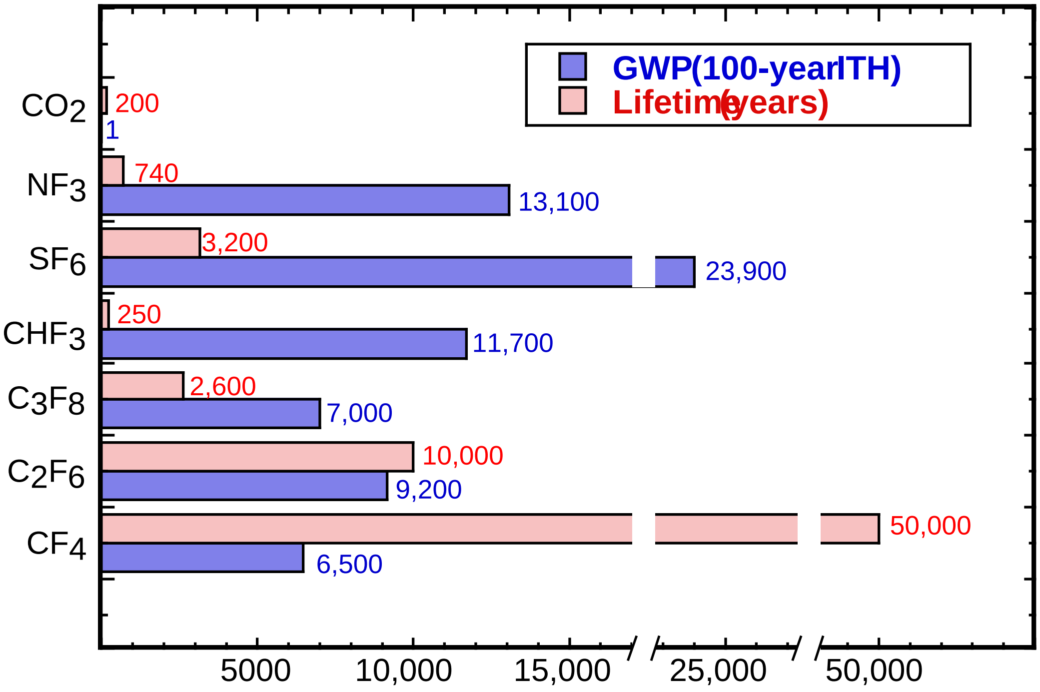

Fig. 1.2. Atmospheric lifetimes and global warming potentials of PFCs and CO_2 [68].

1.1 References

[1] *Nonthermal Plasma Techniques for Pollution Control*, edited by B. N. Penetrante and S. E. Schultheis (Springer, Berlin, 1993), Parts A and B.

[2] *Plasma Science and the Environment*, edited by W. Manheimer, L. E. Sugiyama, T. H. Stix (American Institute of Physics, Woodbury, NY, 1997).

[3] D. J. Helftitch and P. L. Feldman, Radiat. Phys. Chem. **24**, 129 (1984).

[4] J. C. Person and D. O. Ham, Radiat. Phys. Chem. **31**, 1 (1988)

[5] P. Fuchs, B. Roth, U. Schwing, H. Angele, and J. Gottstein, Radiat. Phys. Chem. **31**, 45 (1988).

[6] B. M. Penetrante, M. C. Hsiao, B. T. Merritt, and G. E. Vogtlin, Appl. Phys. Lett., **66**, 3096 (1995).

[7] A. G. Chmielewski, E. Iller, Z. Zemek, M. Romanowski, and K. Koperski, J. Phys. Chem. **46**, 1063 (1995).

[8] L. Prager, H. Langguth, S. Rummel, and R. Mehnert, Radiat. Phys. Chem. **46**, 1137 (1995).

[9] S. A. Vitale, K. Hadidi, D. R. Cohn, and L. Bromberg, Radiat. Phys. Chem. **49**, 421 (1997).

[10] S. A. Vitale, K. Hadidi, D. R. Cohn, and P. Falkos, Plasma Chem. Plasma Process, **16**, 651 (1996).

[11] N. W. Frank, Radiat. Phys. Chem. **45**, 989 (1995).

[12] L. Bromberg, D. R. Cohn, R. M. Patrick, and P. Thomas, Phys. Lett. A **173**, 293 (1993).

[13] R. Morrow, Phys. Rev. A**32**, 1799 (1985).

[14] J.-S. Chang, J. Aerosol Sci. **20**, 87 (1988).

[15] I. Gallimberti, Pure Appl. Chem. **60**, 663 (1988).

[16] S. R. Stearns, J. Appl. Phys. **66**, 2899 (1989).

[17] R. J. van Brunt and S. V. Kulkarni, Phys. Rev. A**42**, 4908 (1990).

[18] P. Pignolet, S. Hadj-Ziane, B. Held, R. Peyrous, J. M. Benas, and C. Coste, J. Phys. D: Appl. Phys. **14**, 1069 (1990).

[19] T. Ohkubo, S. Hamasaki, Y. Nomoto, J. Chang, and T. Adachi, IEEE Trans. Ind. Appl. **26**, 542 (1990).

[20] F. A. van Goor, J. Phys. D: Appl. Phys. **26**, 404 (1993).

[21] F. Grange, N. Soulem, J. F. Loiseau, and N. Spyrou, J. Phys. D: Appl. Phys. **28**, 1619 (1995).

[22] N. Bonifac, A. Denat, and V. Atrazhez, J. Appl. Phys. **81**, 2717 (1997).

[23] A. A. Kulikovsky, IEEE Trans. Plasma Sci. **25** 439 (1997).

[24] A. A. Kulikovsky, J. Phys. D: Appl. Phys. **30**, 441 (1997).

[25] R. Morrow, J. Phys. D: Appl. Phys. **30**, 3099 (1997).

[26] Y. S. Mok, S. W. Ham, and I. S. Nam, IEEE Trans. Plasma Sci. **26**, 1566 (1998).

[27] M. Cemak, T. Hosokawa, S. Kobayashi, and T. Kaneda, J. Appl. Phys. **83**, 5678 (1998).

[28] M. Simek, V. Babicky, M. Clupek, S. DeBenedictis, G. Dilecce, and P. Sunka, J. Phys. D: Appl. Phys. **31**, 2591 (1998).

[29] S. Kanazawa, J.-S. Chang, G. F. Round, G. Sheng, T. Ohkubo, Y. Nomoto, and T. Adachi, Combust. Sci. Tech. **133**, 93 (1998).

[30] J.-S. Chang in *Nonthermal Plasma Techniques for Pollution Control*, edited by B. N. Penetrante and S. E. Schultheis (Springer, Berlin, 1993), Part A, pp. 2-32.

[31] B. Eliasson, M. Hirth, and U. Kogelschatz, J. Phys. D.: Appl. Phys., **20**, 1421 (1987).

[32] W. Elgi and B. Eliasson, Helvetica Physica Acta **62**, 302 (1989).

[33] B. Eliasson and U. Kogelschatz, IEEE Trans. Plasma Sci., **19**, 309 (1991).

[34] V. I. Gibalov, J. Drimal, M. Wronski, and V. G. Samoilovich, Contrib. Plasma Phys. **31**, 89 (1991).

[35] J. Kitayama and M Kuzumoto, J. Phys. D.: Appl. Phys., **30**, 2453 (1997).

[36] M. B. Chang, J. H. Balbach, M. J. Rood, and M. J. Kushner, J. Appl. Phys., **69**, 4409 (1991).

[37] H. Esron and U. Kogelschatz, Appl. Surf. Sci., **54**, 440 (1992).

[38] D. Evans, L. A. Rosocha, G. K. Anderson, J. J. Coogan, and M. J. Kushner, J. Appl. Phys., **74**, 5378 (1993).

[39] A. C. Gentile and M. J. Kushner, J. Appl. Phys., **78**, 2074 (1995).

[40] A. C. Gentile and M. J. Kushner, J. Appl. Phys., **78**, 2977 (1995).

[41] M. C. Hsiao, B. T. Merritt, B. M. Penetrante, and G. E. Voglin, J. Appl. Phys., **78**, 3451 (1995).

[42] B. M. Penetrante, M. C. Hsiao, B. T. Merritt, G. E. Vogtlin, Appl. Phys. Lett., **66**, 3096 (1995).

[43] B. M. Penetrante, M. C. Hsiao, J. N. Bardsley, B. T. Merritt, G. E. Vogtlin, P. H. Wallman, A. Kuthi, C. P. Burkhart, and J. R. Bayless, Phys. Lett., **209**, 69 (1995).

[44] W. Sun, B. Pashaie, S. K. Dhali, and F. I. Honea, J. Appl. Phys., **79**, 3438 (1996).

[45] A. C. Gentile and M. J. Kushner, J. Appl. Phys., **79**, 3877 (1996).

[46] R. G. Tonkyn, S. E. Barlow, and T. M. Orlando, J. Appl. Phys., **79**, 3451 (1996).

[47] Z. Fralkenstein, J. Adv. Oxid. Technol., **1**, 1 (1997).

[48] B. M. Penetrante, M. C. Hsiao, J. N. Bardsley, B. T. Merritt, G. E. Vogtlin, A. Kuthi, C. P. Burkhart, and J. R. Bayless, Plasma Sources. Sci. Technol. **6**, 251 (1997).

[49] W. Niessen, O. Wolf, R. Schruft, and M. Neiger, J. Phys. D.: Appl. Phys., **31**, 542 (1998).

[50] F. Massines, A. Rabehi, P. Decomps, and R. B. Gadri, J. Appl. Phys., **83**, 2950 (1998).

[51] U. Kogelschatz in *Nonthermal Plasma Techniques for Pollution Control*, edited by B. N. Penetrante and S. E. Schultheis (Springer, Berlin, 1993), Part B, pp. 339-354.

[52] J. Zhang and I. W. Boyd, J. Appl. Phys., **80**, 633 (1996).

[53] Z. Falkenstein and J. J. Coogan, J. Phys. D.: Appl. Phys., **30**, 2704 (1997).

[54] J. Zhang and I W. Boyd, J. Appl. Phys. **84**, 1174 (1998).

[55] D. Braun, U. Kuchler, and G. Pietsh, J. Phys. D.: Appl. Phys., **24**, 564 (1991).

[56] Y. Sakai, A. Oda, and H. Akashi, Rep. Inst. Fluid Science, **10**, 29 (1997).

[57] D. Braun, V. Gibalov, and G. Pietsch, Plasma Sources. Sci. Technol. **1**, 166 (1992).

[58] B. Eliasson and U. Kogelschatz, Appl. Phys. B**46**, 299 (1988).

[59] U. Kogelschatz, Appl. Surf. Sci. **54**, 410 (1992).

[60] *Plasma Etching: An Introduction*, edited by D. M. Manos and D. L. Flamm (Academic, San Diego, CA, 1989).

[61] S. Ito, K. Nakamura, and H. Sugai, Jpn. J. Appl. Phys. **33**, L1261 (1994).

[62] P. Verdonck, J. Swart, G. Brasseur, and P. De Geyter, J. Electrochem. Soc. **142**, 1971 (1995).

[63] K. Takahashi, M. Hori, and T. Goto, J. Vac. Sci. Technol. A**14**, 2004 (1996).

[64] A. Tserspi, W. Schwarzenbach, J. Derouard, and N. Sadeghi, J. Vac. Sci. Technol. A**15**, 3120 (1997).

[65] M. A. Sobolewski, J. G. Langan and B. S. Felker, J. Vac. Sci. Technol. B**16**, 173 (1998).

[66] T. E. F. M. Standaert, M. Schaepkens, N. R. Rueger, P. G. M., Sebel, G. S. Oehrlein, and J. M. Cook, J. Vac. Sci. Technol. A**16**, 239 (1998).

[67] B. E. E. Kastenmeier, P. J. Matsui, G. S. Oehrlein, and J. G. Langan, J. Vac. Sci. Technol. A**16**, 2047 (1998).

[68] L. Beu, P. T. Brown, J. Latt, J. U. Papp, T. Gilliland, T. Tamayo, J. Harrison, J. Davison, A. Cheng, J. Jewett, W. Worth, *Current State of Technology: Perfluorocompound (PFC) Emissions Reduction*, SEMATECH Technology Transfer 98053508A-TR, 1998.

[69] E. Meeks, R. S. Larson, S. R. Vosen, and J. W. Shon, J. Electrochem. Soc. **144**, 357 (1997).

[70] M. Schaekens, G. S. Oehrlein, C. Hedlund, L. B. Jonsson, and H. O. Blom, J. Vac. Sci. Technol. A**16**, 3281 (1998).

[71] S. P. Sun, D. Bennett, L. Zazzera, and W. Reagen, Semicond. Int., 85, (1998).

[72] V. Mohindra, H. Chae, H. H. Sawin, and M. T. Mocella, IEEE Trans. Semicond. Manufact., **10**, 399 (1997).

[73] C. L. Hartz, J, W. Bevaan, M. W. Jackson, and B. A. Wofford, Environ. Sci. Technol. **32**, 682 (1998).

[74] E. J. Tonnis, V. Vartanian, L. Beu, T. Lii, R. Jewett, and D. Graves, *Evaluation of a Litmas "Blue" Point-of-Use (POU) Plasma Abatement Device for Perluorocompound (PFC) Destruction*, SEMATECH Technology Transfer 98123605A-TR, 1998.

2. DESCRIPTION OF THE MODELS

2.1 Introduction

In this chapter, detailed descriptions of the 1-D and the 2-D Plasma Chemistry and Hydrodynamics Models (PCHMs) for high-pressure DBD processing of gases and the 2-D Hybrid Plasma Equipment Model (HPEM) for low-pressure plasma abatement are presented. In Section 2.2, we describe the 1-D PCHM used in Chapter 3 to study ion kinetics in an expanding microdischarge for a single microdischarge, in Chapter 5 to investigate CCl_4 remediation processing, and in Chapter 6 to examine excimer photon generation. In Section 2.3, we describe the 2-D PCHM used in Chapter 4 to study the expansion of multiple, closely spaced microdischarges and the effect of surface remaining charges on microdischarges in DBDs. In Section 2.4, we describe the 2-D HPEM used in Chapter 7 to investigate the PFC consumption and generation of PFCs in an ICP-etching reactor and the abatement of PFCs in a plasma burn box.

2.2 One-Dimensional Plasma Chemistry and Hydrodynamic Model

The model used in this study is a modified version of the 1-D microdischarge simulation previously discussed in [1]. The model begins by assuming that the DBD is composed of a uniformly spaced array of identical, radially symmetric microdischarges. The numerical mesh is discretized in the radial direction with varying resolution from submicron near the center to a few microns at the outer radius. The last numerical cell has a square outer boundary and circular inner boundary in order to apply reflective boundary conditions. The spacing of the microdischarges is sufficiently large that they do not significantly interact, and therefore, a single microdischarge employing reflective boundary conditions can be used. Typically 800-900 radial points are used in the simulation.

The model is composed of four components: an external circuit model, a solution of Boltzmann's equation for the electron energy distribution, a heavy plasma chemistry model, and a transport module. A schematic of the modules of PCHM is shown in Fig. 2.1. The external circuit model calculates the voltage across the plasma, which is then used to obtain the time evolution of the electron energy distribution from the solution of Boltzmann's equation. The heavy particle plasma chemistry model produces the concentrations of neutral and charged particles, and also provides the plasma conductivity for the external circuit model. The motion of species between mesh points is addressed in the transport module. Electron impact rate coefficients for use in the plasma chemistry model are obtained using the local field approximation. Solutions of Boltzmann's equation [2] are parameterized over a wide range of *E/N*, and the resulting rate and electron impact rate coefficients are placed in a look-up table for use during execution of the model.

The equations we solve in the transport module are

$$\frac{\partial r}{\partial t} = \nabla \cdot (r\mathbf{v}) \tag{2.1}$$

$$\frac{\partial (r\mathbf{v})}{\partial t} = -\nabla P - \nabla \cdot (r\mathbf{v}_\mathbf{i}\mathbf{v}_\mathbf{i}) - \nabla \cdot t \tag{2.2}$$

$$\frac{\partial (c_p rT)}{\partial t} = \frac{\partial Q}{\partial t} + \nabla \cdot k\nabla T - \nabla \cdot (c_p rT\mathbf{v}) - P(\nabla \cdot \mathbf{v}) \tag{2.3}$$

where r is the mass density, $\mathbf{v}$ is the velocity, T is the temperature, c_p is the heat capacity, P is the thermodynamic pressure (assuming ideal gas behavior), t is the viscosity tensor, Q is the enthalpy, and k is the thermal conductivity. The form of the viscosity tensor used is given by Thompson [3]. The viscosity and thermal conductivity of the gas was obtained using Lennard Jones parameters and applying the mixture rules as described in Hirshfelder et al. [4]. The time rate of change in enthalpy is

$$DQ = \mathbf{J}\cdot\mathbf{E} - \sum_i \left(\frac{dN_i}{dt}\right)\cdot DH_i - \left(\frac{dn_e}{dt}\right)\cdot\frac{3}{2}k\cdot T_e \tag{2.4}$$

where $\mathbf{J} = s\mathbf{E}$, (s is the plasma conductivity) is the current density, $\mathbf{E}$ is the local electric field, H_i is the enthalpy of heavy particle species i, and T_e is the electron temperature. Although the model is 1-D in the radial dimension, we account for axial boundaries by employing no-slip conditions on the top and bottom surfaces, and including the appropriate term in the viscosity tensor.

The densities of individual species are obtained by solving separate continuity equations:

$$\frac{\partial r_i}{\partial t} = -\nabla\cdot\left(r_i\mathbf{v} - rD_i\nabla\left(\frac{r_i}{r}\right)\right) + S_i \tag{2.5}$$

where r_i is the mass density of species i, D_i is its diffusion coefficient, and S_i is the source function due to electron impact and heavy particle collisions. Ambipolar enhanced diffusion coefficients are used for ions. The transport equations were explicitly integrated in time using a fourth-order Runga-Kutta-Gill technique. Spatial derivatives are formulated using conservative finite difference donor cell techniques on a staggered mesh (r and T are obtained at cell vertices whereas $r\mathbf{v}$ is obtained at cell boundaries). In addition, a finite surface conductivity for the dielectric was used in order to simulate the spreading of charge on the dielectric surface.

2.3 Two-Dimensional Plasma Chemistry and Hydrodynamic Model

The 2-D model of DBDs used in this study is analog to the 1-D model described above. We resolve the two dimensions parallel to the electrodes and therefore do not address the cathode fall dynamics. This model addresses the positive column characteristics of the microdischarge. To begin, we select a gas mixture, gap spacing, dielectric properties, and voltage pulse shape. A small initial electron density (10^8-10^9 cm^{-3}), having a radial extent of a few microns, is specified as an initial condition. The voltage pulse is applied, and the compressible Navier-Stokes equations are solved for continuity, momentum conservation, and energy density of the gas mixture. Continuity equations are solved for all heavy particle species (neutrals and ions) and electrons. We invoke the local field approximation for electron transport. In doing so, the electron transport coefficients are obtained from the spatially dependent value of E/N and a two-term spherical harmonic solution of Boltzmann's equation.

The transport equations were explicitly integrated in time using a fourth-order Runga-Kutta-Gill technique. Spatial derivatives are formulated using conservative finite difference donor cell techniques on a staggered mesh (r[mass density] and T

[temperature] are solved for at cell vertices, whereas $r\mathbf{v}$[momentum] is obtained at cell boundaries). The 2-D mesh was rectilinear with (usually) equal spacing in each direction. In the cases where we have bulk gas flow through the device (e.g., a “right to left” flow field), we simply superimposed a bulk flow velocity $\mathbf{v}_b$ parallel to the electrodes. To account for no-slip flow and formation of boundary layers in the axial direction, we include an axial sheer term in the viscous drag term of the momentum equation. This term is formulated using $L = d/p$ (d is the gap spacing) as the transport length. The axial electrical field is also provided by solving circuit equations for the pulse power apparatus and dielectric charging. Given the E/N in the plasma, electron impact rate coefficients are obtained using the local field approximation from a two-term spherical harmonic expansion of Boltzmann’s equation for the electron energy distribution. In the plasma chemistry model, the densities for all species, the gas temperature, and the charge density on the dielectric are updated independently at each mesh point while excluding transport. This method allow us to use a different integration time step at each mesh point, which tends to be shorter ($<10^{-11}$ s) in the active microdischarge region and longer outside the microdischarge. After the update of the local kinetics, the densities are then updated based on advection and diffusion in the hydrodynamic model where the momentum equations are simultaneously solved. We enforced electrical neutrality, so the electron density at each mesh point is forced to be equal to the charge weighted sum of the ion densities.

Initial conditions are generated by specifying (or randomly distributing) a center point for each microdischarge in the 2-D domain. The microdischarge is assumed to be initially radially symmetric and composed of a seed electron density having a super-Gaussian profile.

2.4 Two-Dimensional Hybrid Plasma Equipment Model (HPEM)

The HPEM which will be used to model the consumption and abatement of PFCs in low-pressure plasma tools is a 2-D plasma equipment model that was developed at the University of Illinois [5-9]. The 2-D HPEM is an (r, z) cylindrically symmetric simulation which consists of three main sections: the Electromagnetic Module (EMM), the Electron Energy Transport Module (EETM), and the Fluid-Kinetics Simulation (FKS). A schematic of the modules in the HPEM is shown in Fig. 2.2. The EMM calculates the electric and magnetic fields in the reactor which are inductively coupled from transformer coils. The fields are used in the EETM to generate the electron temperature and electron impact reaction coefficients. These values are computed in the EETM as a function of position and then passed to the FKS. In the FKS, continuity, momentum, and energy equations are integrated for all neutral and charged densities, and Poisson’s equation is solved for the electric potential. The plasma conductivity produced in FKS is passed to the EMM, and the species densities and time-dependent electrostatic potential are transferred to the EETM. The modules are iterated until the cycle-averaged plasma and neutral densities converge. Acceleration algorithms are used to speed the rate of convergence of the model.

2.4.1 The Electromagnetic Module (EMM)

The electromagnetic fields that generate the plasma in an inductively coupled plasma reactor are described by Maxwell's equation in the EMM. Under the assumption that there is charge neutrality ($\nabla \cdot \mathbf{E} = 0$), the electric field **E** is governed by

$$\nabla^2\mathbf{E} + \frac{w^2}{c}\mathbf{E} = iwm_0\mathbf{J} \tag{2.6}$$

where w is the frequency, c is the speed of light, μ_0 is he vacuum permeability, and **J** is the current density. Time harmonic conditions have been assumed. The current density **J** is the sum of the external antenna current $\mathbf{J}_0$ and the conduction current $\mathbf{J}_c$. In the collisional approximation, the conduction current in the steady state is determined by

$$\mathbf{J}_\mathbf{c} = s\mathbf{E}, \qquad s(\mathbf{r}) = \sum_j \frac{q_j^2 n_j(\mathbf{r})}{m_j [n_j(\mathbf{r}) + iw]} \tag{2.7}$$

where q_j, n_j, m_e, and n_j are the charge magnitude, density, mass and momentum transfer collision frequency of species j. The coil is assumed to be made of nested annuli in the 2-D HPEM so that the electric field is purely azimuthal. The method of successive-over-relaxation is used to iteratively solve for E_q. Once the electric field is determined, the magnetic field is obtained by

$$\mathbf{B} = \frac{i}{w}\nabla \times \mathbf{E} \tag{2.8}$$

2.4.2 The Electron Energy Transport Module (EETM)

There are two methods for determining the electron energy distribution (EED) as a function of position in EETM. The first one is by solving the Boltzmann and electron energy conservation equations in Boltzmann-electron energy equation module (BEM). The second method uses the electron Monte Carlo simulation (EMCS) for spatially varying EED.

In the BEM, Boltzmann's equation is solved using a two-term spherical harmonic expansion for a range of the reduced electric field *E/N* as follows:

$$\frac{\partial f_e}{\partial t} + (\boldsymbol{v} \cdot \nabla) f_e + \frac{q_e}{m_e}(\boldsymbol{E} + \boldsymbol{v} \times \boldsymbol{B}) \cdot \nabla_v f_e = -n f_e \tag{2.9a}$$

$$f_e = f_{e0} + \frac{\boldsymbol{v}}{v} f_{e1} \tag{2.9b}$$

where f_e is the electron distribution function, $\boldsymbol{n}$ is the electron momentum transfer collision frequency, q_e is the electron charge, $\boldsymbol{E}$ is the electric field, and $\boldsymbol{B}$ is the magnetic field. A table of electron transport properties as a function of electron temperature is created. The interpolated data are used in solving electron energy equation as follows;

$$\frac{\partial\left(\frac{3}{2} n_e k_b T_e\right)}{\partial t} = P(T_e) - n_e \sum_i N_i k_i - \nabla \cdot \left(\frac{5}{2} k_b T_e \mathbf{G} - l \nabla T_e\right) \tag{2.10}$$

where T_e is the electron temperature, n_e is the electron density, P is the electron power deposition, k_b is Boltzmann's constant, k_i is the rate coefficient of power loss for collisions of electrons with species i having density N_i, l is the electron thermal conductivity, and $\mathbf{G}$ is the electron flux. This equation is solved in the steady state using successive over relaxation. Finally the electron transport coefficients such as electron impact rate coefficients, source terms for electrons and ions, and transport coefficients are updated using the spatially dependent electron temperature.

The alternative method for determining the electron transport and energy properties is used by EMCS. The electron EMCS is executed using a few thousand pseudoparticles. Electrons are initialized as a Maxwellian velocity distribution and distributed in the reactor weighted by the electron density from the FKS. The particle trajectories are simulated under a Lorentzian force from the local electric and magnetic fields as a function of time. The EMCS is performed for ≈ 20–50 RF cycles for each iteration. The resulting time-averaged electron energy distribution is used to generate electron impact source functions for each process.

2.4.3. The Fluid-Kinetics Simulation (FKS)

The FKS solves the fluid transport equations for all charged and neutral species with chemical and electron impact reactions and Poisson’s equation or an ambipolar field solution for the electrostatic potential. Electron density and flux are obtained by solving the drift-diffusion equations. For all other charged and neutral species, we solve the species continuity, momentum, and energy equations as follows

$$\frac{\partial n_i}{\partial t} = -\nabla \cdot (n_i \mathbf{v_i}) + S_i \tag{2.11}$$

$$\frac{\partial(n_i\mathbf{v}_i)}{\partial t} = -\frac{\nabla(n_i kT_i)}{m_i} - \nabla\cdot(n_i\mathbf{v_i}\mathbf{v_i}) + \frac{q_i n_i(\mathbf{E}+\mathbf{E_s})}{m_i}$$

$$+\sum_j\left(\frac{m_j}{m_i+m_j}\right)n_i n_j n_{ij}(\mathbf{v}_j - \mathbf{v}_i) \tag{2.12}$$

$$\frac{\partial(n_i e_j)}{\partial t} = -\nabla\cdot\mathbf{Q_i} - P_i\nabla\cdot\mathbf{v_i} - \nabla\cdot(n_i\mathbf{v_i}e_{i)}) + \frac{n_i q_i n_i}{m_i(n_i^2+w^2)}E^2$$

$$+\frac{n_i q_i^2}{m_i n_i}E_s^2 + \sum_j 3\frac{m_{ij}}{m_i+m_j}n_i n_j n_{ij}k(T_j - T_i) \tag{2.13}$$

where n_i, $\mathbf{v}_i$, m_i, T_i, q_i, e_i, Q_i, P_i, and n_i, are, respectively, the number density, velocity, mass, temperature, charge, thermal energy, thermal flux, pressure, and momentum transfer collision frequency of species *i*. S_i is the source function for species *i* resulting from heavy particle and electron impact collision. The parameter n_{ij} is the rate constant for the collision between species *i* and *j*, $m_{ij} = m_i m_j/(m_i + m_j)$ is the reduced mass, and *k* is Boltzmann's constant. Equations (2.11) and (2.12) are solved in space and time, while Equation (2.13) is solved only in the steady state because the time scale of the energy equation is several orders of magnitude longer than other plasma time scales. The average gas temperature, which is a density weighed average of neutral species, is computed for chemical reactions which are dependent on temperature.

At sufficiently high pressures, gas atoms achieve thermal equilibrium with surfaces they come in contact with. The gas and surface temperature are, therefore, essentially the same at the interface. However, at low pressures there might not be sufficient numbers of collisions to efficiently couple the gas and adjacent surfaces, resulting in a temperature difference. This condition is known as the *temperature jump* *effect* [10-12]. Because ICPs generally operate at low pressures (<10s mTorr), a temperature jump at reactor walls is accounted for using the method developed by Kennard [10]. Using this method, the difference between the wall temperature T_w and the gas temperature T_g at the wall are given by

$$T_w - T_g = g\frac{\partial T_g}{\partial x}\ . \tag{2.14}$$

The temperature T_g and its derivative are computed at the wall. The factor g is

$$g = \frac{(2-\alpha)(9\gamma - 5)}{2\alpha(\gamma + 1)}\lambda\ , \tag{2.15}$$

where α, γ, and λ are, respectively, the accommodation coefficient, ratio of specific heats, and mean free path. The accommodation coefficient determines how well the gas thermally couples to the surface and its value varies from 0 (no coupling) to 1 (perfect coupling). The actual value depends on the gas and condition of the surface.

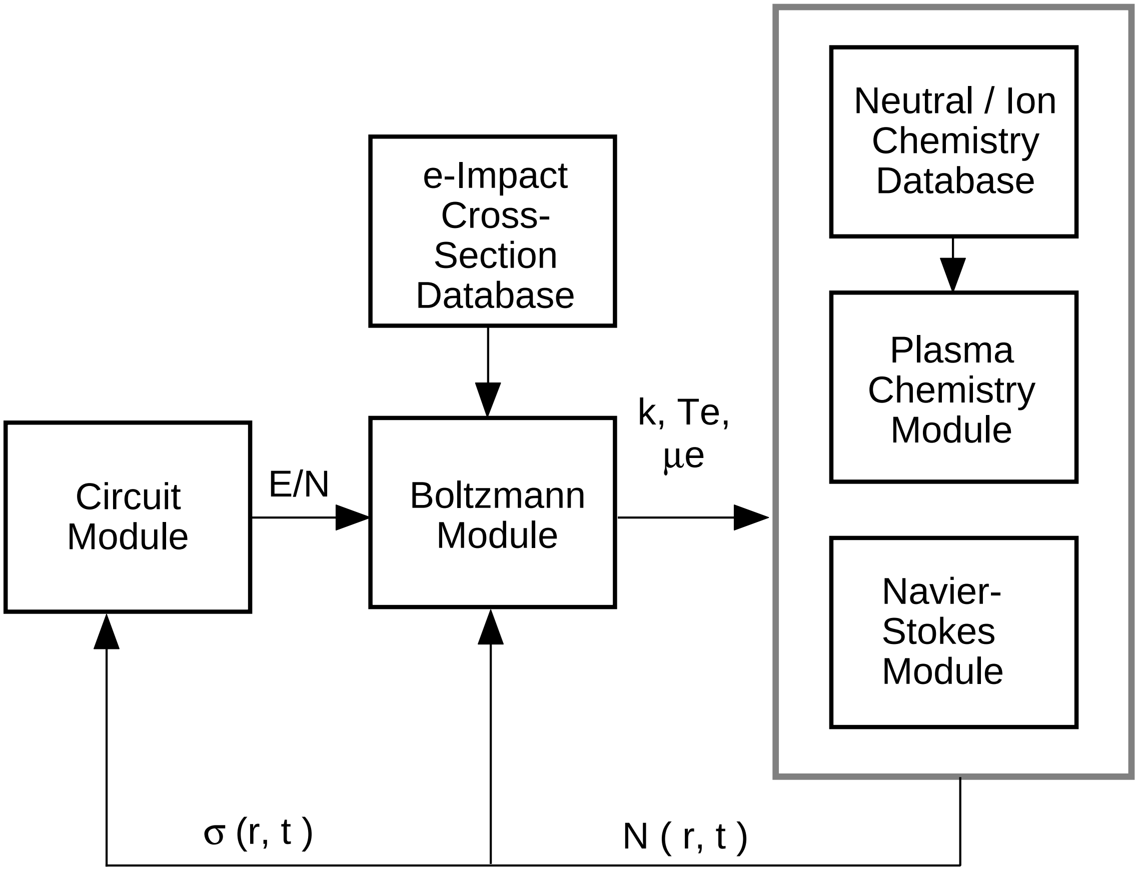

Fig. 2.1. Schematic of the 1-D and 2-D Plasma Chemistry and Hydrodynamics Models (PCHMs).

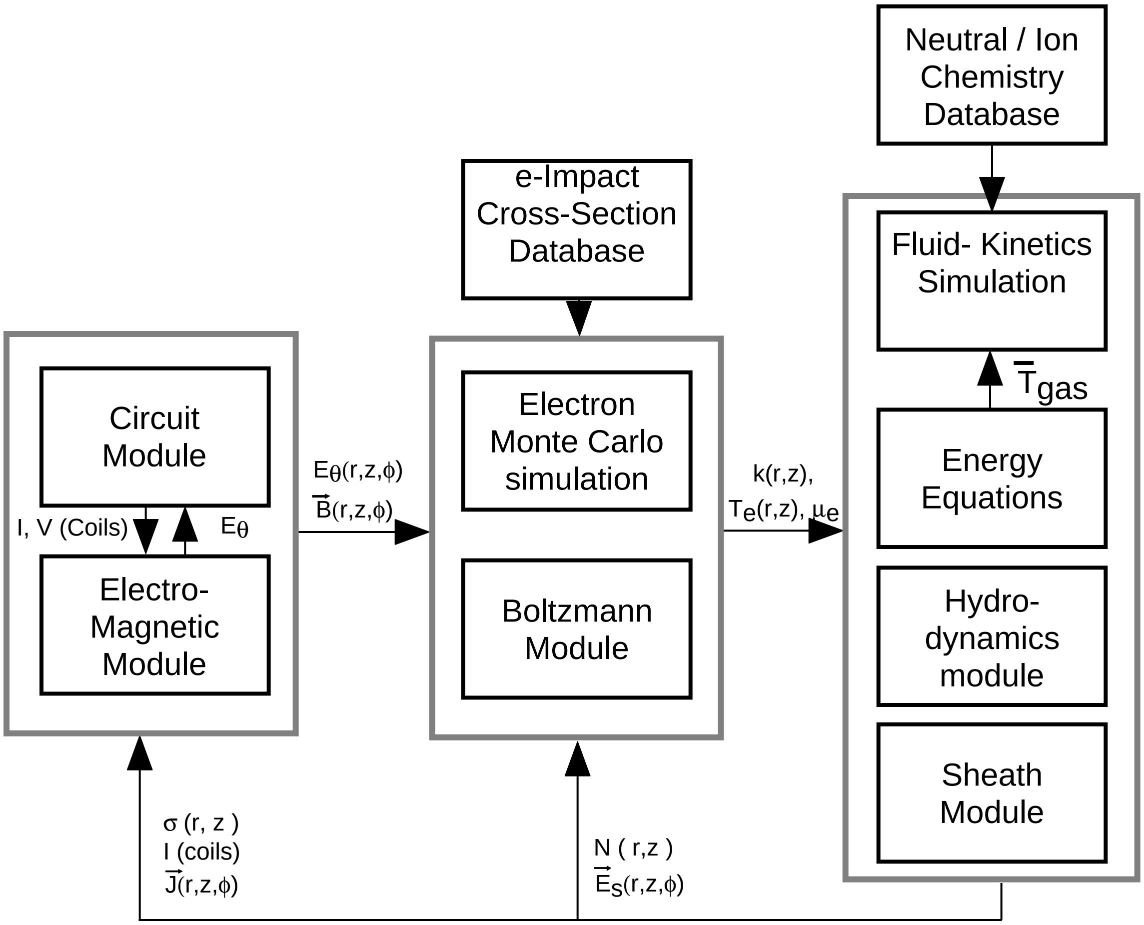

Fig. 2.2. Schematic of the Hybrid Plasma Equipment Model (HPEM).

2.5 References

[1] A. C. Gentile and M. J. Kushner, J. Appl. Phys., **79**, 3877 (1996).

[2] S. D. Rockwood, Phys. Rev. A., **6**, 2348 (1993).

[3] P. A. Thompson, *Compressible Fluid Dynamics* (McGraw-Hill, NY, 1972), p. 9 and Appendix E.

[4] J. O. Hirschfelder, C. F. Curtiss, and R. B. Bird, in *Molecular Theory of Gases and Liquids* (Wiley, New York, 1954), Chap. 8.

[5] P. L. G. Ventzek, R. J. Hoekstra, and M. J. Kushner, J. Vac. Sci. Technol. B. **12**, 461 (1994).

[6] W. Z. Collison and M. J. Kushner, Appl. Phys. Lett. **68**, 903 (1996).

[7] S. Rauf and M. J. Kushner, J. Appl. Phys. 82, 2805 (1997).

[8] M. J. Grapperhaus, Z. Krivokapic, and M. J. Kushner, J. Appl. Phys. 83, 35 (1998).

[9] S. Rauf and M. J. Kushner, J. Appl. Phys. 83, 5087 (1998).

[10] E. H. Kennard, *Kinetic Theory of Gases* (McGraw-Hill, NY, 1938).

[11] Y. Sone, T. Ohwada, and K. Aoki, Phys. Fluids A **1**, 363 (1989).

[12] S. K. Loyalka, Physica A **163**, 813 (1990).

3. SINGLE MICRODISCHARGE DYNAMICS IN DIELECTRIC BARRIER DISCHARGES

3.1 Introduction

In this chapter, we apply a 1-D radially dependent PCHM to the study of ion kinetics in an expanding microdischarge in a DBD. The goal is to quantify the transition of the bulk *E/N* from avalanche to below self-sustaining as the microdischarge expands, and to determine the consequences on charged particle densities and radical generation. The context of this study is the use of DBDs for toxic gas remediation, and so we have investigated for three representative gas systems: Ar and N_2 (nonattaching); Ar/O_2, N_2/O_2, and $N_2/O_2/H_2O$ (humid moderately attaching); and $Ar/O_2/CCl_4$ (highly attaching). The species included in each class of discharge ($N_2/O_2/H_2O$, $Ar/O_2/Cl_4$) are listed in Appendix A. A complete listing of reactions included for each case can be found in Appendix B. In all cases, the dominant source of positive ions is electron impact on ground state species, and feedstock gases in particular.

A detailed study of the microdischarges of pure nitrogen is given in Section 3.2. The micodischarges in N_2/O_2 and $N_2/O_2/H_2O$ mixtures are discussed in Sections 3.3. Section 3.4 presents the results of microdischarges in Ar, Ar/O_2, and $Ar/O_2/CCl_4$ mixtures. Our concluding remarks are given in Section 3.5.

3.2 Dynamics of Microdischarges in Pure Nitrogen Gas

We begin our discussion of microdischarge dynamics in DBDs by examining a single microdischarge in pure N_2. The voltage pulse is 12 kV and 40 ns duration. The pressure is one atmosphere at 400 K with a 0.2-cm gas gap. One electrode is covered by

0.5 mm thickness of a dielectric having permittivity of $5\varepsilon_o$. The initial seed electron density has a distribution 20 μm in radius and 10^9 cm^{-3} peak value. The electron (essentially equal to the N_2^+ density), N atom density and voltage across the gap during and following the voltage pulse are shown in Fig. 3.1. During the 40 ns that the voltage pulse is on, avalanche in the core of the microdischarge ramps the electron density to a maximum of 1.8×10^{13} cm^{-3}. As the axial discharge current charges the dielectric, voltage is removed from the gap. The dielectric charging time is ≈10 ns. After this time, voltage is nearly completely removed from the gap at a given radial location, which then terminates electron avalanche. The microdischarge radius expands by lateral diffusion of electrons to larger radii where the dielectric is uncharged and so the electric field is large. Avalanche occurs, which increases the axial current density and charges the dielectric, thereby removing voltage from the gap. As a result, a low voltage region is produced in the core of the microdischarge which propagates outwards, as shown in Fig. 3.1(b). Because electron-ion recombination is relatively slow (rate coefficient 5×10^{-7} cm^{-3} s^{-1}, yielding a rate of ≈5×10^6 s^{-1}), the electron density decreases by only ≈10–15% in the core of the microdischarge after the avalanche is terminated by charging of the dielectric, as shown in Fig. 3.1(a). The end result is a nearly top-hat shaped ion density expanding laterally with a depression in the center due to electron-ion recombination.

Just prior to the end of the 40-ns voltage pulse the dielectric is nearly fully charged to the line voltage. At the end of the voltage pulse, when the line voltage is pulled to zero, there is an inverse (or negative) bias across the gap, resulting from the previous charging of the dielectric. This inverse voltage extends only to the edge of the just terminated microdischarge. Because the gap is, in a sense, “preionized” by the yet to fully recombine plasma, there is a secondary rapid avalanche that nearly doubles the peak ion density. Because the electron density in the microdischarge is large compared to the initial density prior to the primary avalanche, discharging the dielectric is more rapid (≈2.6 ns) and occurs nearly simultaneously across the entire radius. Any lateral diffusion of electrons, of which there is a small component, does not significantly expand the microdischarge. The "stationary" microdischarge results from the fact that for the secondary avalanche, the gap voltage beyond the boundary of the microdischarge is zero, whereas for the primary avalanche, the gap voltage is always largest outside the microdischarge. After the short secondary avalanche, the electron and ion density continue their slow decrease by dissociative recombination.

The N atom density resembles the ion density as a function of position and time. N atoms, produced by electron impact dissociation of N_2, accumulate during the current pulse since the rate of reassociation to form N_2 (or ionization to form N^+) is slow. The radial profile of the N atom density is even more uniform than for the ions since the volumetric sink terms and rate of radial diffusion are both smaller.

It was found that the energy deposition and peak electron density in the microdischarge increased nearly linearly with increasing the dielectric capacitance (either by increasing ε or decreasing thickness) for a given line voltage. The maximum microdischarge radius, however, is a weak function of dielectric properties and energy deposition, provided that the line voltage is constant. We found that the rate of expansion of the microdischarge radius depends most sensitively on the line voltage. In agreement with Eliasson and Kogelschatz [1], we found that the rate of microdischarge expansion is largely a function of the rate of electron avalanche, which for our conditions increases with increasing voltage. This trend is shown in Fig. 3.2(a) where the microdischarge radius is plotted as a function of time for increasing charging voltage during a 40 ns pulse. The microdischarge radius increases nearly linearly with time after the first 5-10 ns. The short induction time is the duration required for electron avalanche to increase the axial current to the magnitude required to fully charge the dielectric, and collapses the gap voltage in the center of the microdischarge. This induction time increases with decreasing line voltage.

In the absence of there being a mechanism to charge the dielectric at larger radii than the expanding microdischarge, a process which removes voltage from the gap, the microdischarge will continue to grow as long as the voltage is on. (Under conditions of high energy deposition, hydrodynamic effects that rarefy the microdischarge core and "snow plow" a high gas density shell will reduce the *E/N* at large radius and eventually terminate expansion [2]. The energy deposition in these cases is insufficient for this to occur.) The experimental observation is that the expansion of the microdischarge stalls after 10-30 ns, which conflicts with these results.

In the two-dimensional modeling results of Eliasson and Kogelschatz, in which the electric potential is obtained from solving Poisson's equation in the (*r*, *z*) plane, charging of the dielectric produced a lateral component of the electric field [1]. This lateral component redirected charge flowing to the dielectric to radii greater than the main body of the microdischarge. The reduced gap voltage at large radii (or lengthened field lines) lowered ionization rates sufficiently to stall expansion. In our one-dimensional model, we can capture this behavior by allowing a finite surface conductivity (or less than infinite surface resistance) for the dielectric. The finite surface resistance allows the charge on the dielectric to spread laterally to larger radii than the microdischarge region. As a result, the gap voltage at large radii is eventually reduced to values lower than that required for avalanche and stalls the expansion of the microdischarge during the voltage pulse. For example, the microdischarge radius is shown in Fig. 3.2(b) as a function of time for a 12-kV pulse with and without surface conductivity. The expansion of the microdischarges is similar in the initial stage (< 4-5 ns). Lateral charging of the dielectric when there is a nonzero surface conductivity, however, essentially halts the expansion after ≈5 ns. Further expansion is slow, although there is some small amount of additional microdischarge growth during the secondary avalanche. In the case of there being no surface conductivity, the microdischarge expands as long as there is voltage across the gap.

The peak gas temperature in the microdischarge depends on the total energy deposition, manner of dissipation of the deposited energy and change in enthalpy due to chemical reactions and radiative decay of excited states. For our default conditions ($e/e_0 = 5$, dielectric capacitance of 88.5 pF/cm^2, 2-mm gas gap, and 40-ns 12-kV pulse) the rise in bulk temperature is ≈4 K. The rise is ≈27 K for a line voltage of 17 kV with dielectric capacitance 442.5 pF/cm^2. As excited states of N_2 are quenched and dissipate their energy into translational modes, there is an additional temperature rise of ≈23 K in the first 0.34 μs after the termination of the voltage pulse. We note that when using high permittivity dielectrics (50-200ε_0), there will be sufficient temperature increases to induce hydrodynamic effects such as rarefaction [2]. In the remainder of this chapter, we will discuss microdischarges generated by a 40-ns pulse without surface conductivity for the dielectric. These conditions are most conducive to investigating changes in charged particle composition resulting from dielectric charging.

3.3 Dynamics of Microdischarges in N_2/O_2 and $N_2/O_2/H_2O$

Addition of O_2 to N_2 produces additional electron losses by dissociative and three-body electron attachment to O_2, followed by ion-ion recombination between O^- and O_2^- with all positive ions. Humid air mixtures add dissociative attachment to H_2O as an electron loss mechanism, followed by ion-ion recombination of H^- with all positive ions. The dissociative attachment cross sections for O_2 and H_2O are similar in that they are resonant and have a threshold energy of 5.38 eV an 5.53 eV, respectively.

Negative ion and electron densities for a microdischarge through dry air (N_2/O_2 = 80/20) for the standard conditions are shown in Fig. 3.3 during and after the 40-ns voltage pulse. In comparison to pure nitrogen, the dry air discharge expands faster, a consequence of the larger rate of avalanche for a given (high) *E/N*. The peak electron density during the primary avalanche is $\approx 3 \times 10^{12}$ cm^{-3}, somewhat higher than that for N_2. The primary source of O^- is dissociative attachment to O_2, whose rate coefficient increases with increasing *E/N* over the range of interest. The primary sink for O^- is ion-ion neutralization whose rate coefficient at atmospheric pressure is $\approx 2 \times 10^{-6}$ cm^{-3}s^{-1}. We therefore see a sharp rise in the O^- density at the leading edge of the expanding microdischarge where the rate coefficient for its formation is largest, and a decrease in the O^- density at trailing edge and center of the microdischarge where the *E/N* and dissociative attachment rates are smaller. Additional sinks of O^-, such as $O^- + O \rightarrow O_2 +$

e, also contribute to reducing the O^- density in the center of the microdischarge. The electron density also decreases in the center of the microdischarge, though at a lower rate due to its lower rate of electron-ion recombination and due to the presence of a source of electrons from O^- detachment. The density of O_2^- does not exhibit a peak at the leading edge of the expanding microdischarge because the rate coefficient for 3-body attachment decreases with increasing E/N and will, in fact, increase after the voltage collapses in the gap.

The microdischarge dynamics of $N_2/O_2/H_2O$ mixtures differs markedly from that of dry air. For example, the electron density and gap voltage are shown in Fig. 3.4 for a $N_2/O_2/H_2O$ = 80/5/15 mixture, as might be found in combustion effluent. Ion densities at 36 ns are also shown. Negative ion densities (H^-, O^-, O_2^-) are shown in Fig. 3.5. During the 40 ns voltage pulse, the electron density sharply peaks at the edge of the microdischarge, a much more dramatic effect than in dry air. The peak electron density is lower than either the nitrogen or dry air cases due to the higher rate of momentum transfer and attachment to H_2O. A major consequence of adding H_2O (and decreasing O_2) is that the rate of electron attachment at intermediate E/N (below avalanche) increases and the rate of detachment of O^- decreases. The end result is that as the dielectric charges and voltage collapses in the center of the microdischarge, the attachment rate increases, and the electron density decreases. The lower electron current density in the center of the microdischarge is, in fact, sufficiently small that the dielectric does not totally charge to the line voltage, as shown in Fig. 3.4(b). That is, a residual voltage remains across the gap, and particularly so at large radius compared to the case for nitrogen or dry air. The electron density has a strong maximum near the edge of the microdischarge while the negative ion densities are uniform in comparison. The hollow core of the electron density profile results from rapid losses to attachment, followed by slower rates of loss of the negative ions. The positive ion densities [Figs. 3.4(c) and 3.4(d)], which are largely immune to these dynamics, do not show the sharp peaking at large radius, as does the electron density.

When the 40-ns voltage pulse terminates and the line voltage is driven to zero, the "reverse voltage" resulting from the dielectric charging [time 40.1 ns in Fig. 3.4(b)] produces a secondary avalanche near the center of the microdischarges. The secondary avalanche eventually fully discharges the dielectric. However, at large radii, the reverse voltage is sufficiently low, due to incomplete dielectric charging, that avalanche does not occur. In fact, the low *E/N* at that radius merely serves to increase attachment to O_2 and H_2O, which further reduces the electron density, as shown in Fig. 3.5. The end result is a residual charge on the dielectric that persists to long times. Any surviving residual voltage will then add to the applied voltage on the negative half of the voltage cycle.

The peak of electron density generally decreases with increasing water content. For example, electron densities for $N_2/O_2/H_2O$ = 80/19/1, 80/15/5, and 80/0/20 are shown in Fig. 3.6 as is the gap voltage. Positive ion densities at 36 ns, and negative ion densities for the 80/0/20 case, are shown in Fig. 3.7. As the water content increases, the "hollow shell" appearance of the electron density increases, and dramatically so for the $N_2/O_2/H_2O$ = 80/0/20 mixture. Due to the large fraction of H_2O, the attachment rate is larger at all *E/N*, and the self-sustaining *E/N* is higher. At the leading edge of the voltage pulse, avalanche ramps the electron density to a peak of $\approx 4 \times 10^{12}$ cm^{-3}. As the dielectric charges and removes voltage from the gap in the center of the microdischarge, attachment soon dominates, driving the electron density to low values (≈10^{10} cm^{-3}). The rapid decrease in electron density at small radii leaves an expanding shell of avalanching electrons and an inner core which is essentially a negative ion-positive ion plasma, as shown in Fig. 3.7.

The low electron density in the core for the $N_2/O_2/H_2O$ = 80/0/20 case decreases the current density to sufficiently low values that the dielectric again cannot fully charge, leaving a ≈6.5-kV voltage across the gap. When the pulse is terminated and the line voltage is driven to zero, the residual dielectric charge generates an insufficient voltage to produce a secondary avalanche. As a result, the dielectric charge persists and will be available to add to the negative potential applied on the second half of the voltage cycle.

3.4 Dynamics of Microdischarges in Ar, Ar/O_2, and $Ar/O_2/CCl_4$

Plasma remediation of VOCs is typically performed in closed cycle systems to both contain products and to tailor the gas mixture for optimum efficiency. For example, mixtures of $Ar/O_2/H_2O$/VOC or Ar/O_2/VOC have been investigated for remediation [3]. CCl_4 is a particularly interesting VOC in this regard due to its extremely large rates of dissociative electron attachment at low *E/N*. For example, the rate coefficient for $e + CCl_4 \rightarrow CCl_3 + Cl^-$ is 4×10^{-8} - 2×10^{-7} cm^{-3} s^{-1} for electron temperatures of 0.1 - 1 eV. The spatial distribution of the electron density can be heavily influenced by even small admixtures of CCl_4.

For comparison, the electron and ion densities during microdischarge development in $Ar/O_2/CCl_4$ = 100/0/0, 95/5/0, 94.9/5/0.1, and 94/5/1 gas mixtures are shown in Figs. 3.8 and 3.9. The qualitative behavior of the Ar microdischarge is similar to that of the N_2 discharge. The microdischarge expands radially, fully charging the dielectric leaving behind a positive ion-electron plasma which slowly recombines. A secondary discharge raises the electron and ion density across the entire "preionized" radius when the line voltage is pulled to zero. The addition of 5% O_2 does not appreciably change the electron profiles other than reducing the density in the low *E/N* core due to attachment.

With the addition of 0.1% CCl_4 ($Ar/O_2/CCl_4$ = 94.9/5/0.1) there is a large increase in the attachment rate at low *E/N.* As the dielectric charges, thereby lowering *E/N* in the center of the microdischarge, attachment dominates, leaving behind an expanding avalanching shell of electrons, and a core that is largely composed of negative and positive ions. This effect is heightened by increasing the CCl_4 fraction to 1% ($Ar/O_2/CCl_4$ = 94/5/1). Here the higher attachment rate in the core consumes the electrons within a few ns of the local *E/N* falling below self sustaining, leaving behind a thin electron shell. The charged particle core of the microdischarge is composed almost exclusively of CCl_3^+ and Cl^-. The secondary avalanche generates more uniform electron distribution within the streamer due to “preionization.”

3.5 Concluding Remarks

Microdischarge dynamics in dielectric barrier discharges have been investigated for gas mixtures with varying degrees of electronegativity. We found that in electropositive mixtures, the expanding microdischarge retains a fairly uniform electron density as a function of radius, suffering a small reduction in the core of the microdischarge due to electron-ion recombination. Dielectric charging and the reduction of *E/N* at small radius has little effect on recombination rates. However in electronegative gas mixtures, particularly those whose attachment rate increases with decreasing *E/N*, the core of the microdischarge may quickly evolve to a negative ion-positive ion plasma. The effect is particularly acute in thermal attaching gas mixtures such as those containing CCl_4. Microdischarge expansion will, in the absence of dielectric charging at radii ahead of the core, proceed unimpeded as long as voltage is available. The stalling of the expansion is attributed to transverse components of the electric field on or near the dielectric which charges the dielectric ahead of the body of the microdischarge.

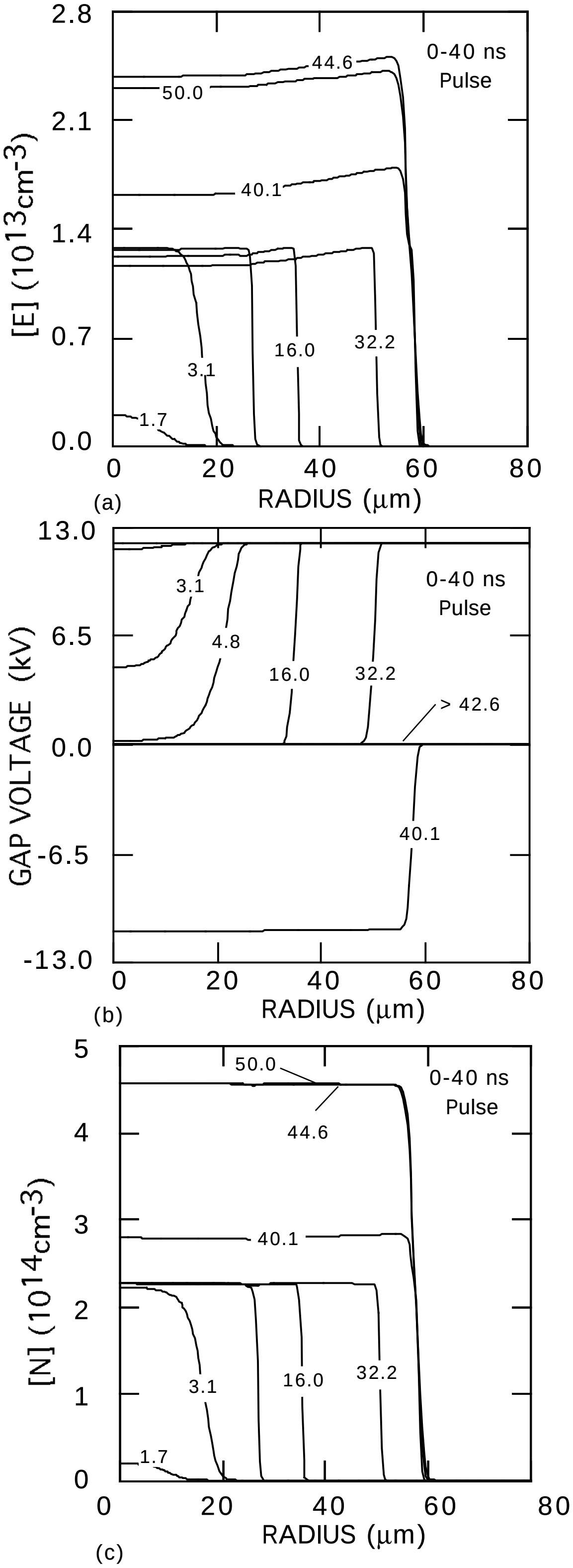

Fig. 3.1. Microdischarge parameters for a pure N_2 plasma: (a) electron density, (b) gap voltage, and (c) N atom density. The plots for particle densities show values for 0-50 ns as a function of radius at various times in the inset, and densities over the longer term in the contour plots. The rate of recombination in the core of the streamer is sufficiently low, and conductivity remains sufficiently high, that the dielectric fully charges during the voltage pulse. As a consequence, a secondary avalanche is produced with the line voltage is pulled to zero.

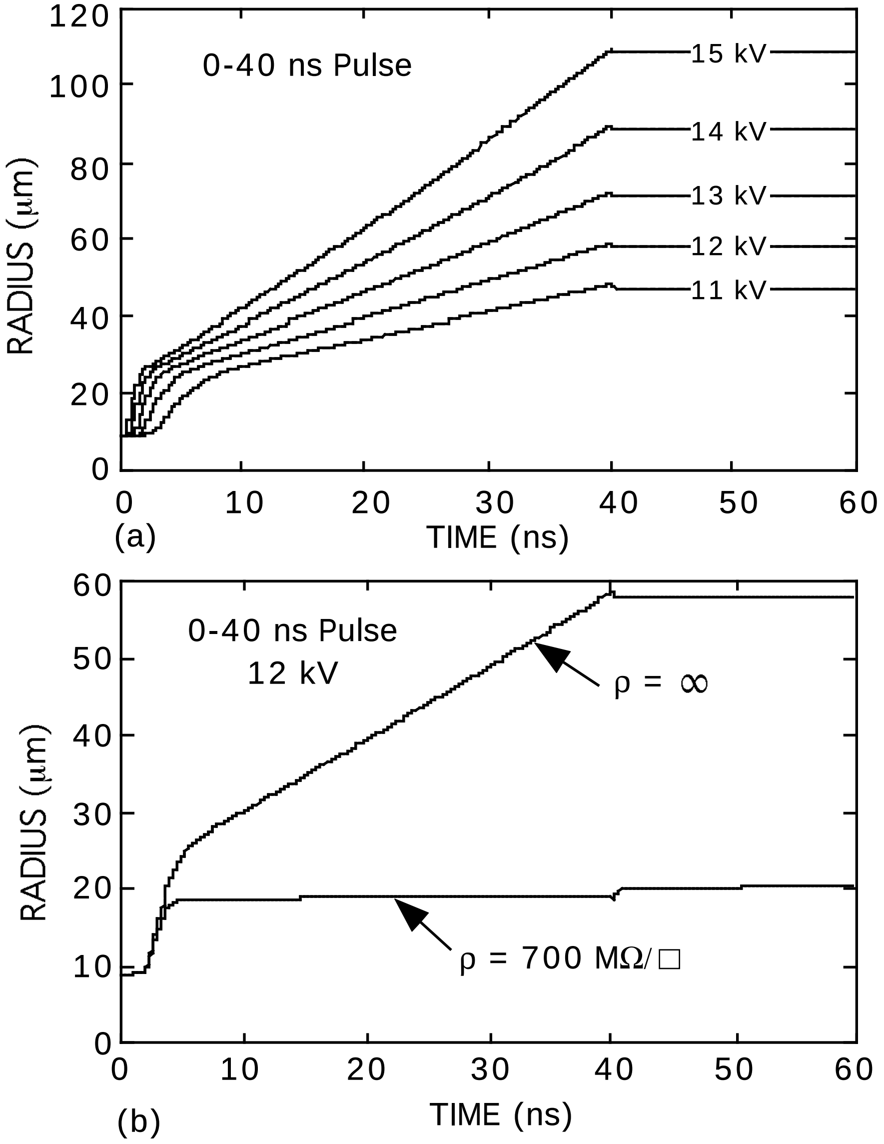

Fig. 3.2. Radius of the microdischarge in N_2 (a) as a function of line voltage and (b) with/without surface conductivity. In the absence of a mechanism to reduce gap voltage ahead of the body of the microdischarge, the microdischarge continues to expand as long as voltage is applied. A small surface conductivity bleeds charge to larger radii, thereby reducing the gap voltage and halting expansion.

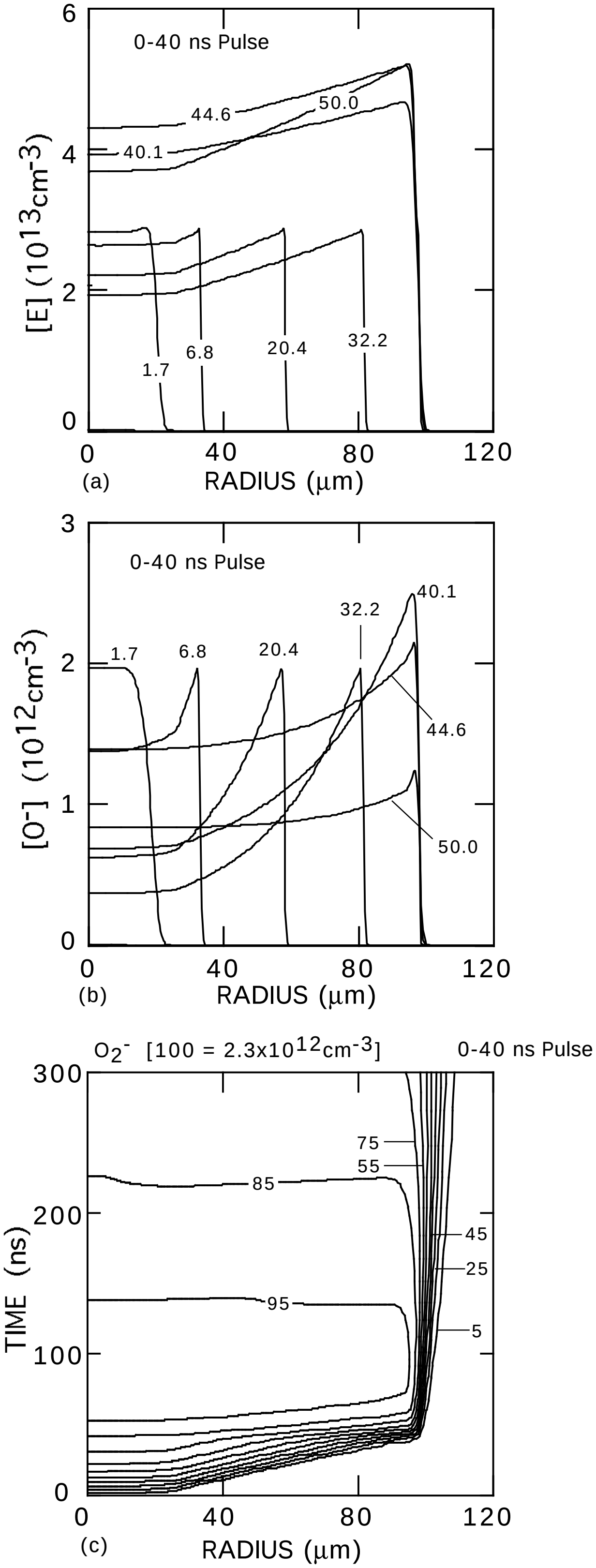

Fig. 3.3. Charged particle densities for a microdischarge in N_2/O_2 = 80/20: (a) electron density, (b) O^- density and, (c) O_2^- density. A moderate amount of attachment at intermediate values of E/N reduces the electron density in the core of the microdischarge.

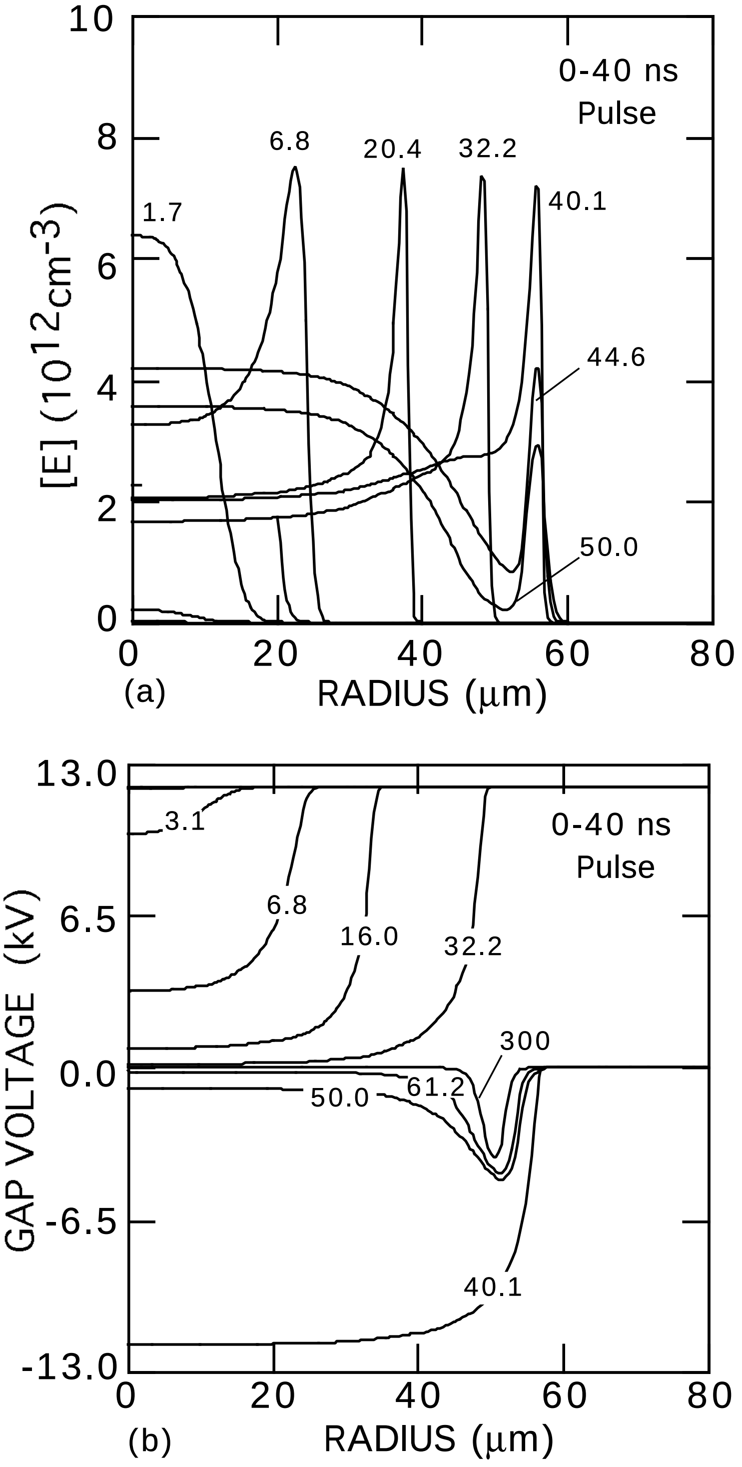

Fig. 3.4. Microdischarge parameters for an $N_2/O_2/H_2O$ = 80/5/15 plasma: (a) electron density, (b) gap voltage, (c) positive ion densities at 36 ns, and (d) negative ion densities at 36 ns. The larger rate of attachment and momentum transfer at intermediate E/N depletes the electron density in the core of the microdischarge as the dielectric charges.

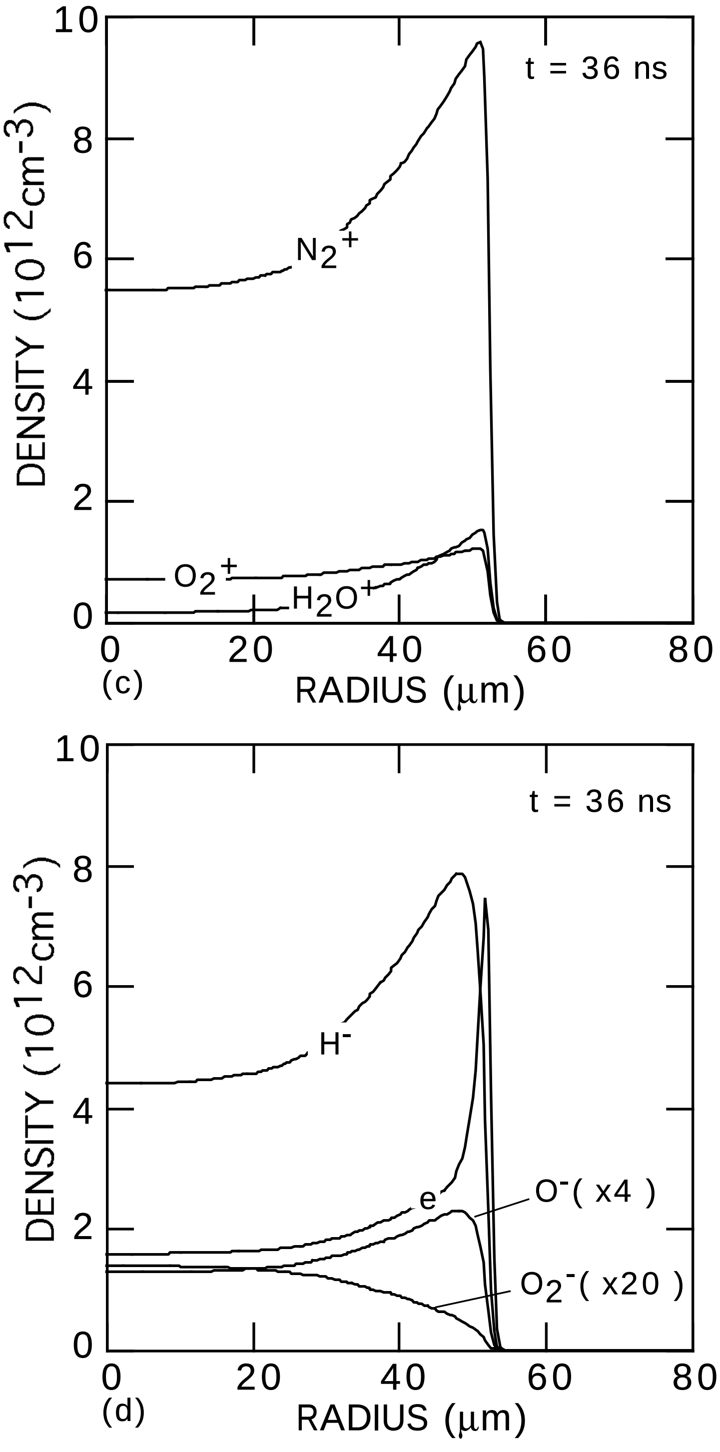

Fig. 3.4. Continued.

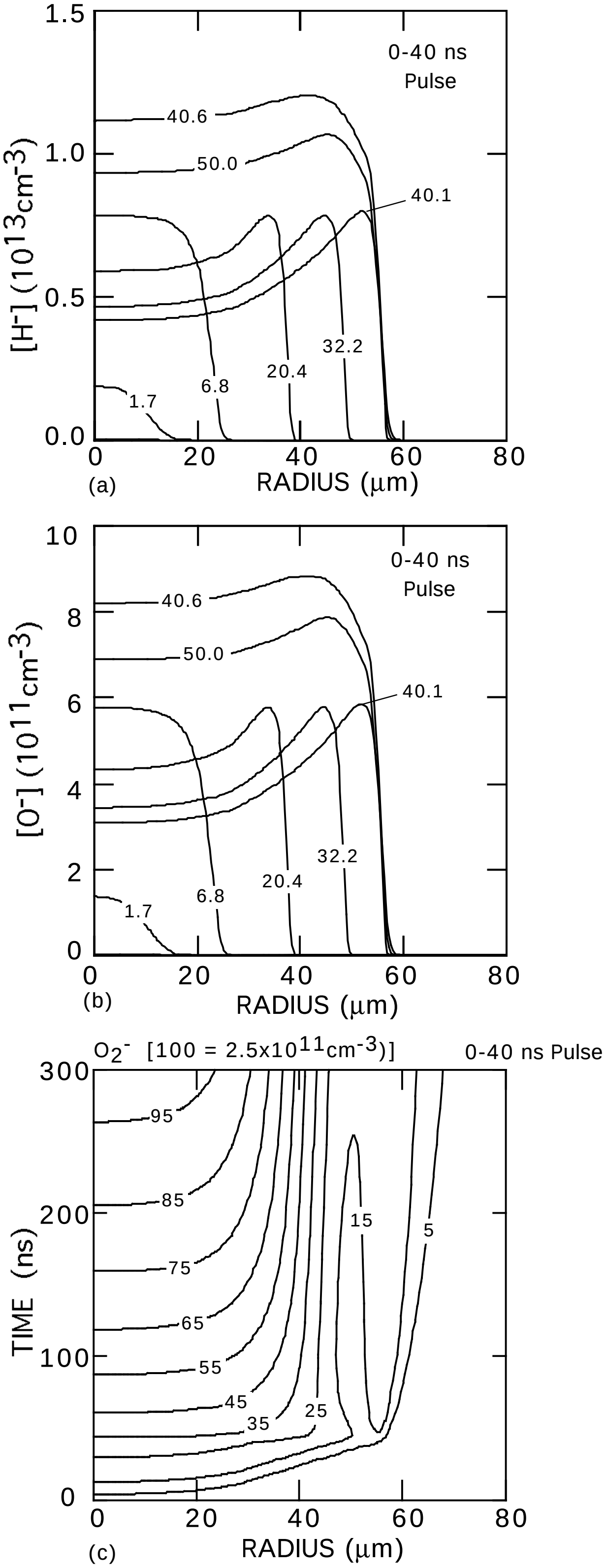

Fig. 3.5. Negative ion densities in a microdischarge sustained in $N_2/O_2/H_2O$ = 80/5/15: (a) H^-, (b) O^-, and (c)O_2^-. The plots for H^- and O^- show values for 0-50 ns as a function of radius at various times in the inset, and densities over the longer term in the contour plots. The negative ion densities persist in the core to long times, particularly near the edge of the microdischarge where the electrons are depleted by attachment.

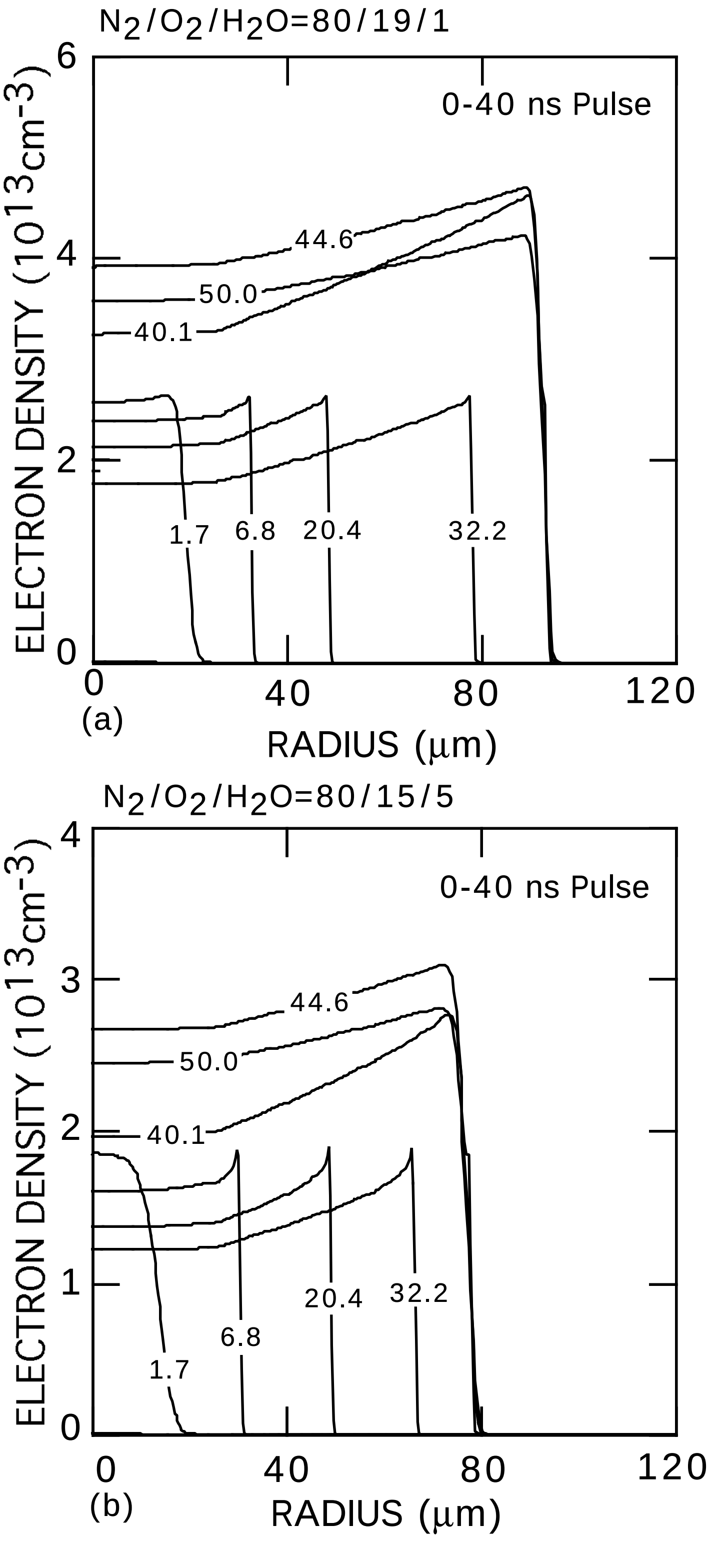

Fig. 3.6. Microdischarge characteristics for $N_2/O_2/H_2O$ mixtures with increasing mole fractions of water. The electron density as a function of radius at increasing times during the microdischarge are shown for $N_2/O_2/H_2O$ = (a) 80/19/1, (b) 80/15/5, and (c) 80/0/20. The gap voltage is shown in (d) for the 80/0/20 mixture. With increasing water mole fraction, the electron density is depleted by attachment more rapidly, leaving a shell of electron density. The electron current density is eventually small enough that the dielectric is not fully charged.

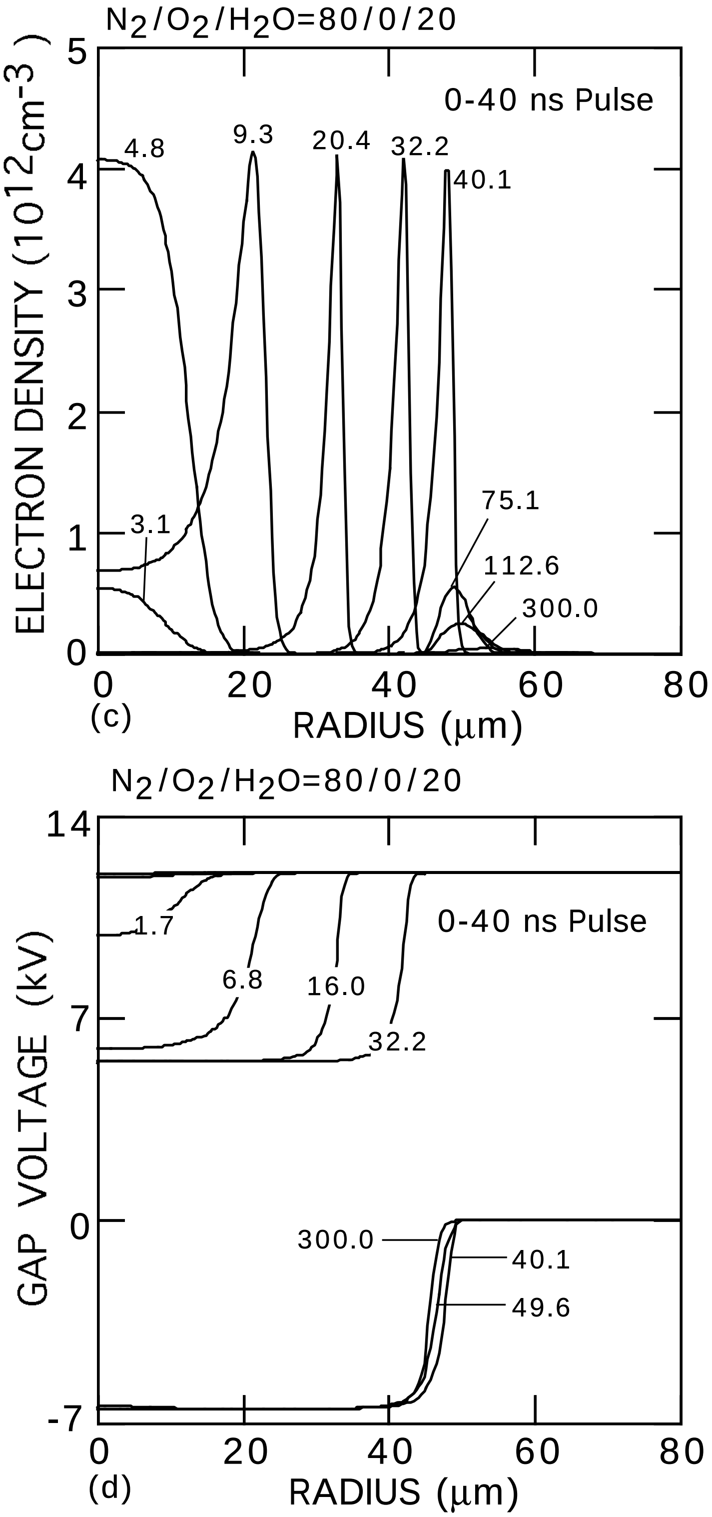

Fig. 3.6. Continued

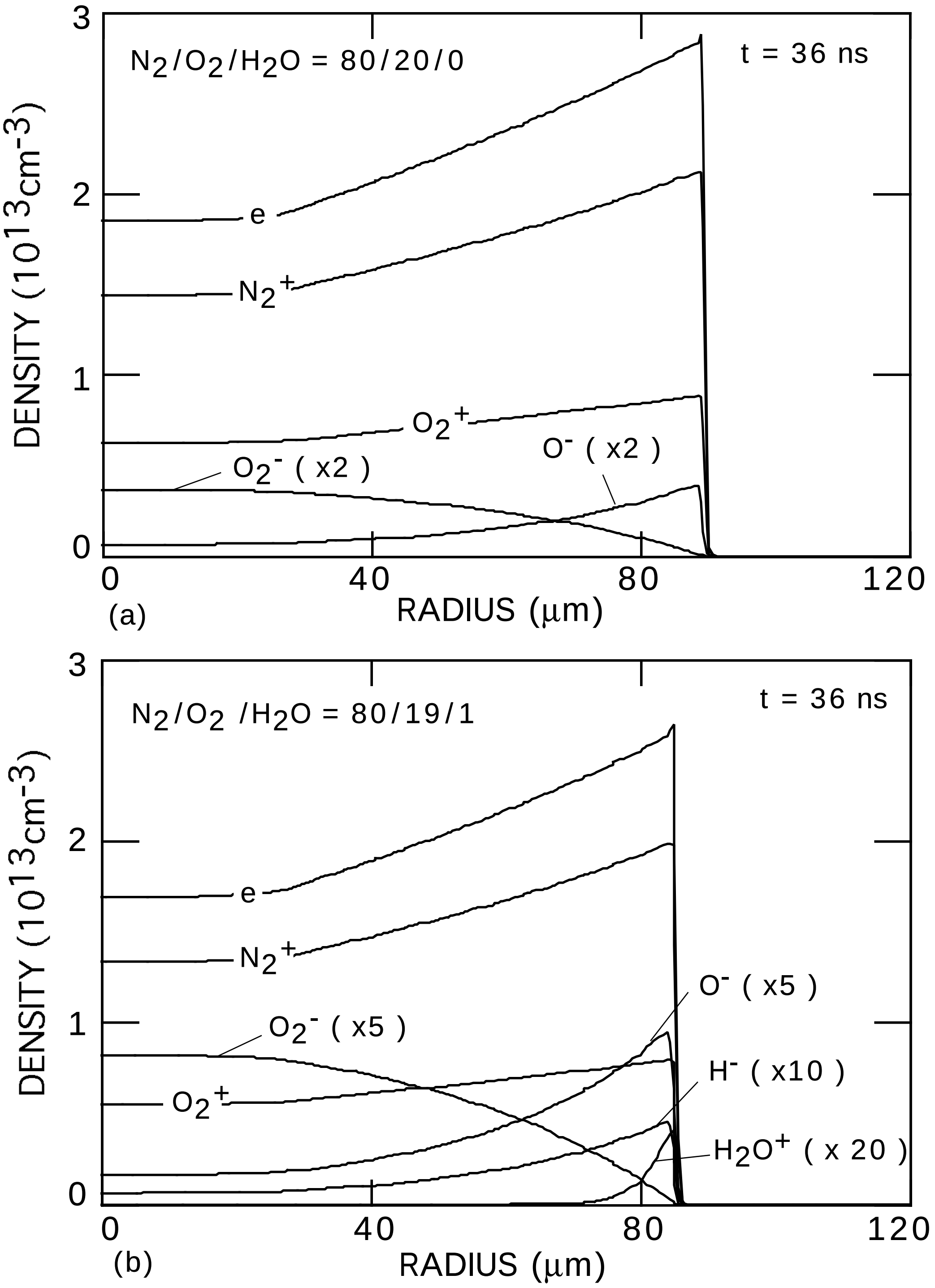

Fig. 3.7. Ion densities at 36 ns for microdischarges in $N_2/O_2/H_2O$ = (a) 80/20/0, (b) 80/19/1, (c) 80/15/5, and (d) 80/0/20. The core of the microdischarge is essentially a negative ion-positive ion plasma with the higher water mole fraction.

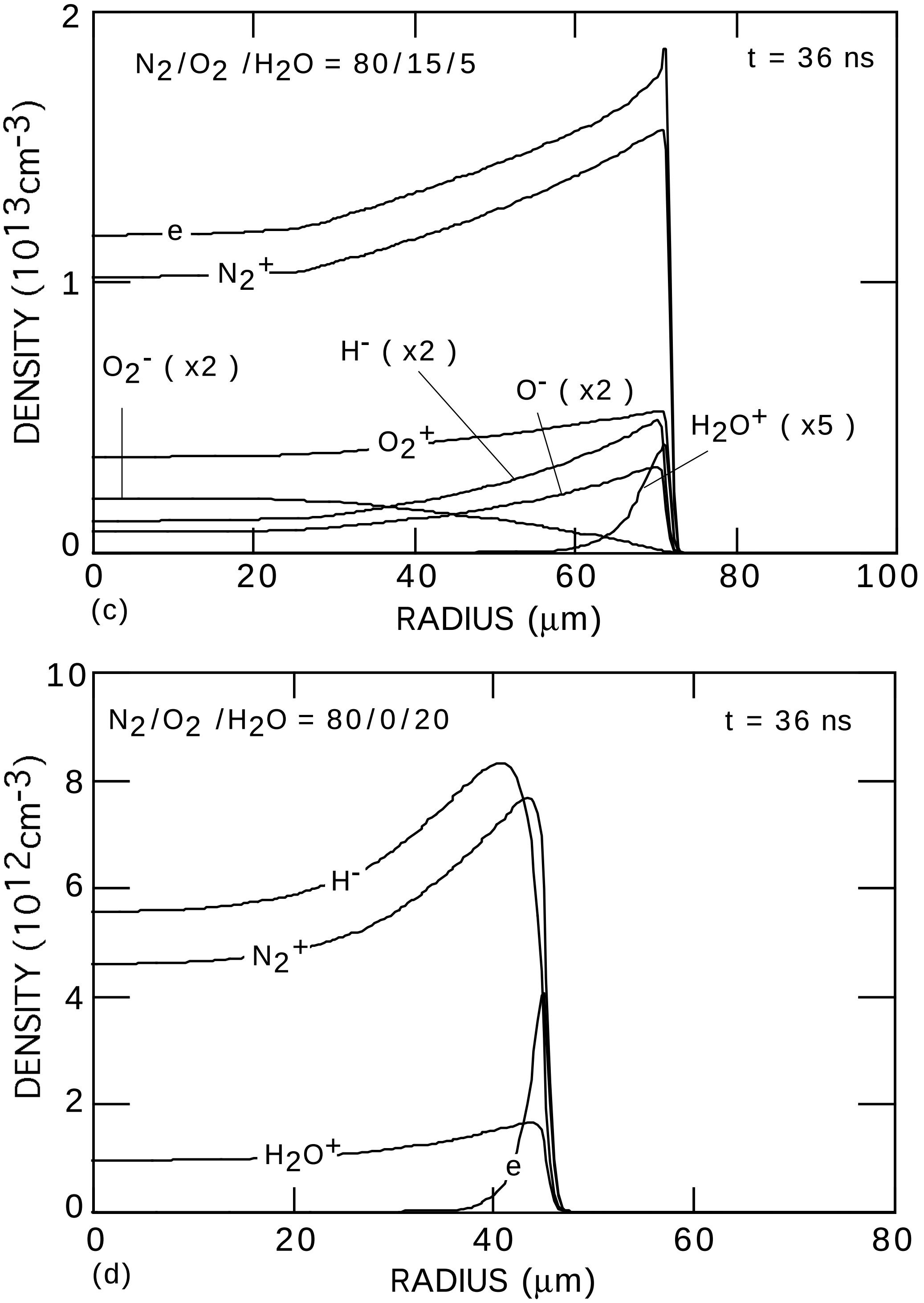

Fig. 3.7. Continued.

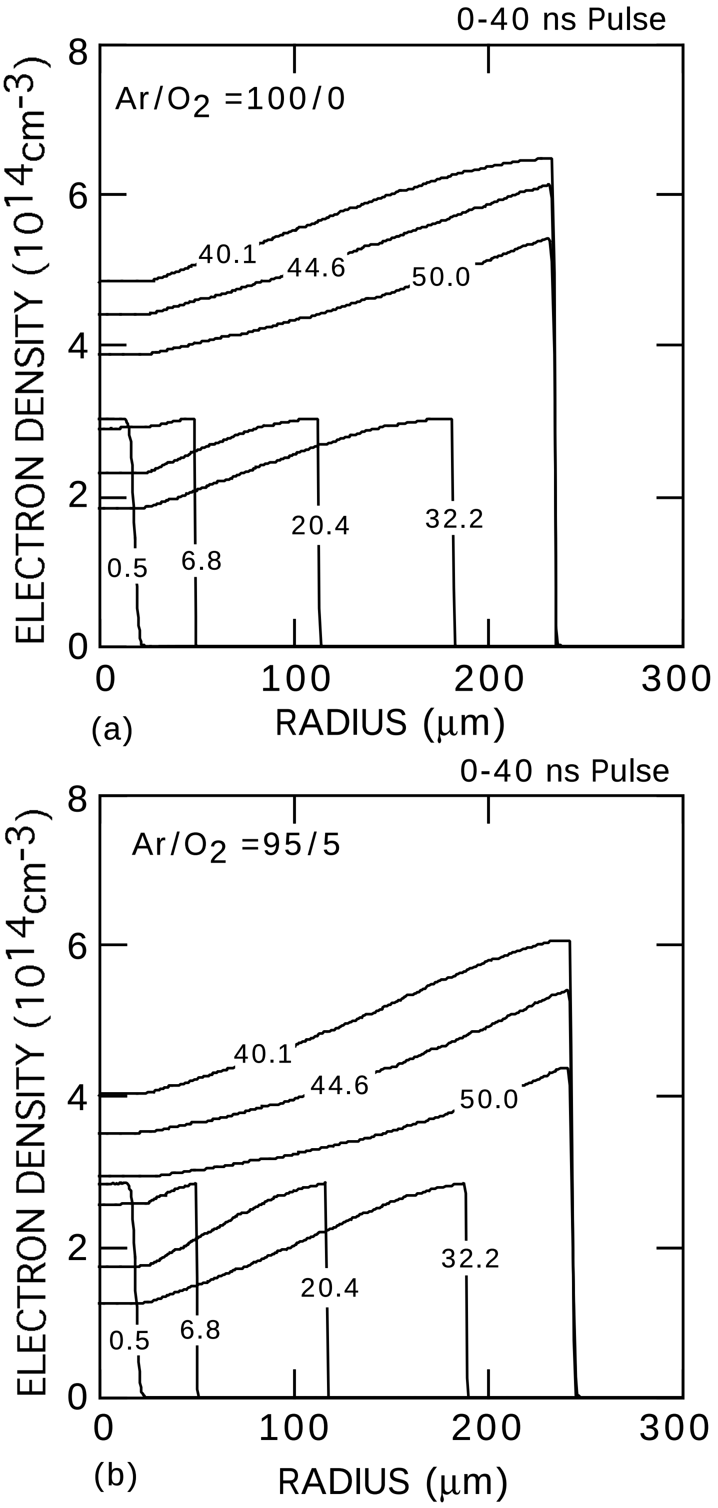

Fig. 3.8. Electron densities as a function of radius at increasing times for microdischarges in Ar/O_2/CCl_4: (a) 100/0/0, (b) 95/5/0, (c) 94.9/5/0.1, and (d) 94/5/1. As the CCl_4 density increases, the “shell” of expanding electron density becomes thinner. The electron density in the core of the microdischarge for the larger CCl_4 density is below 10^3 cm^{-3}.

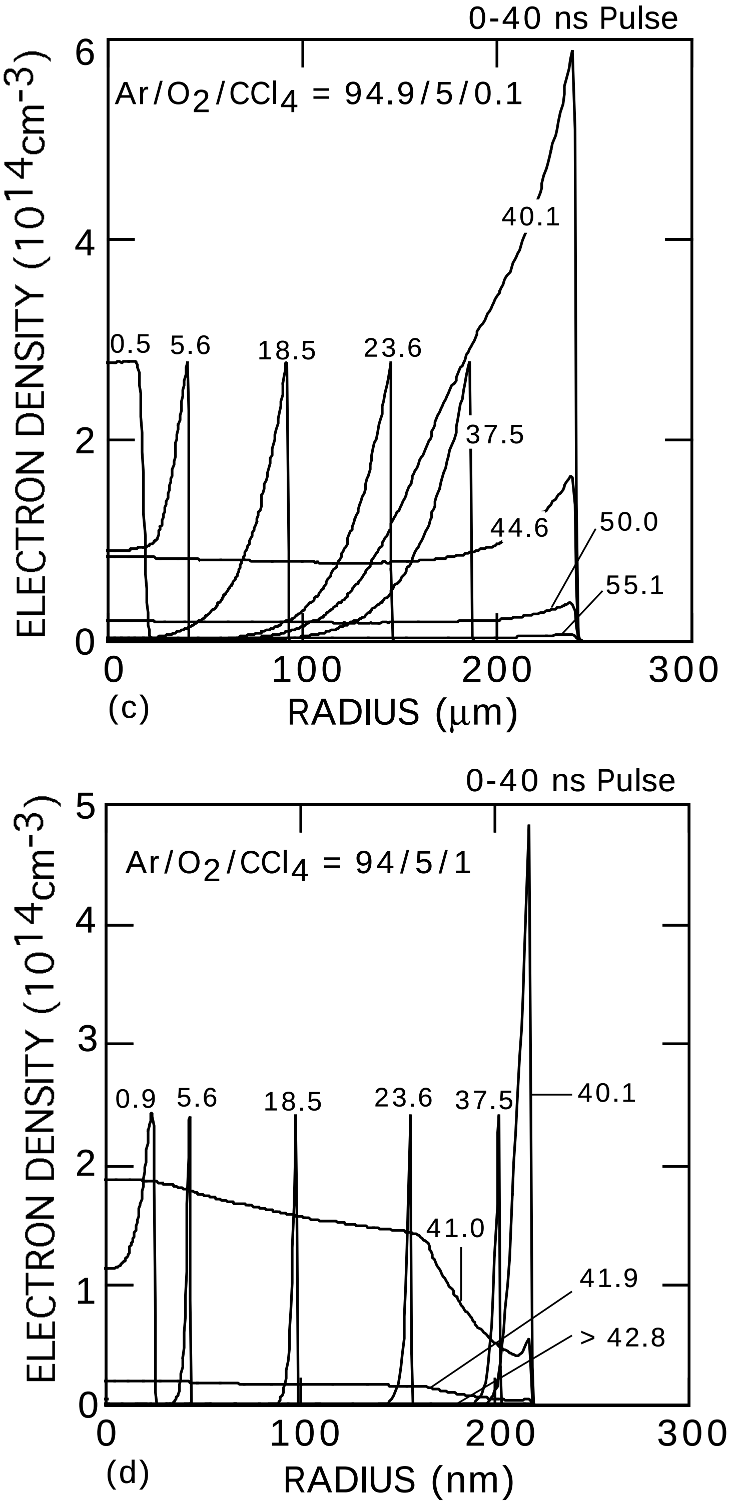

Fig. 3.8. Continued.

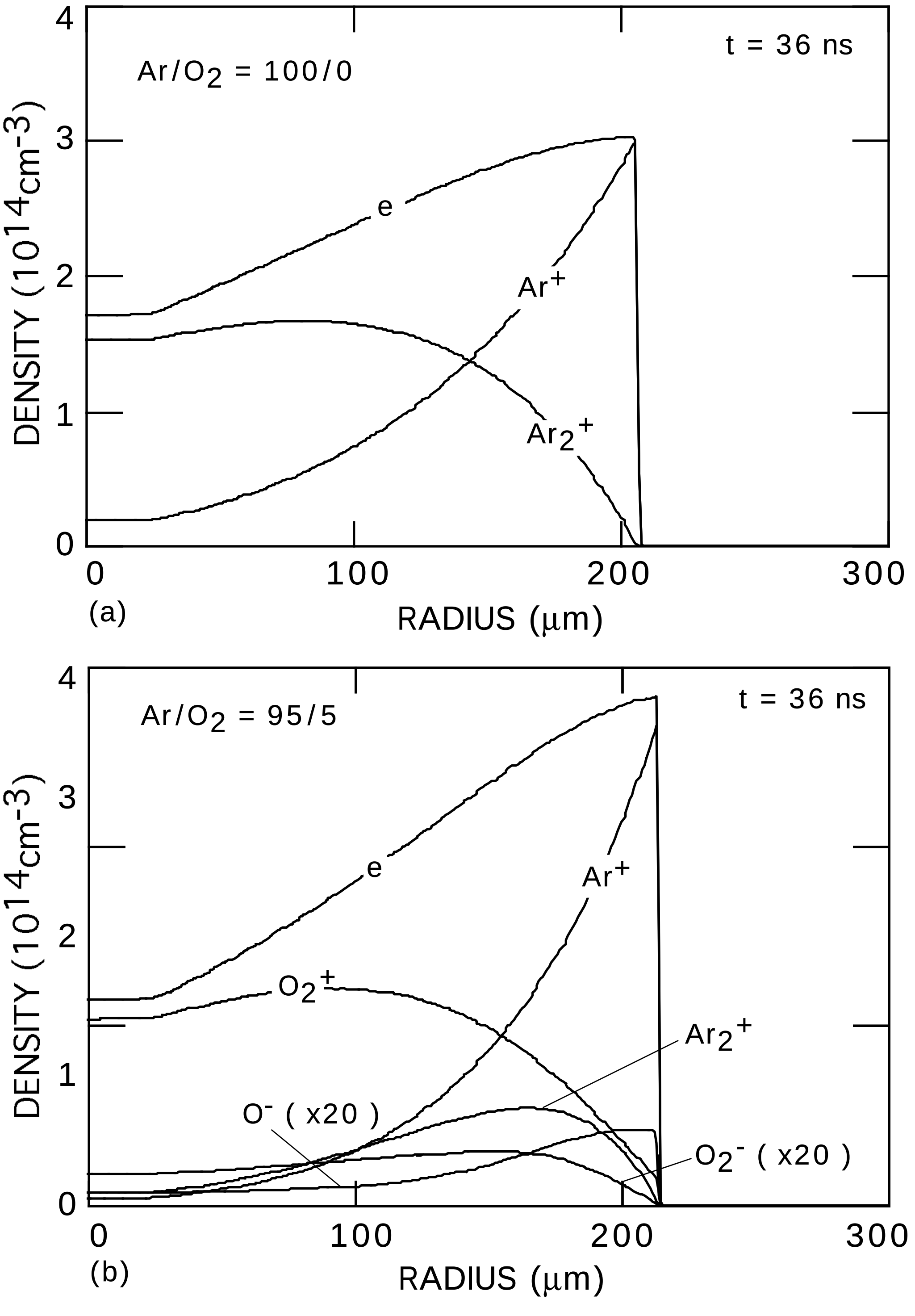

Fig. 3.9. Ion densities as a function of radius at 36 ns for microdischarges in Ar/O$_2$/CCl$_4$: (a) 100/0/0, (b) 95/5/0, (c) 94.9/5/0.1, and (d) 94/5/1.

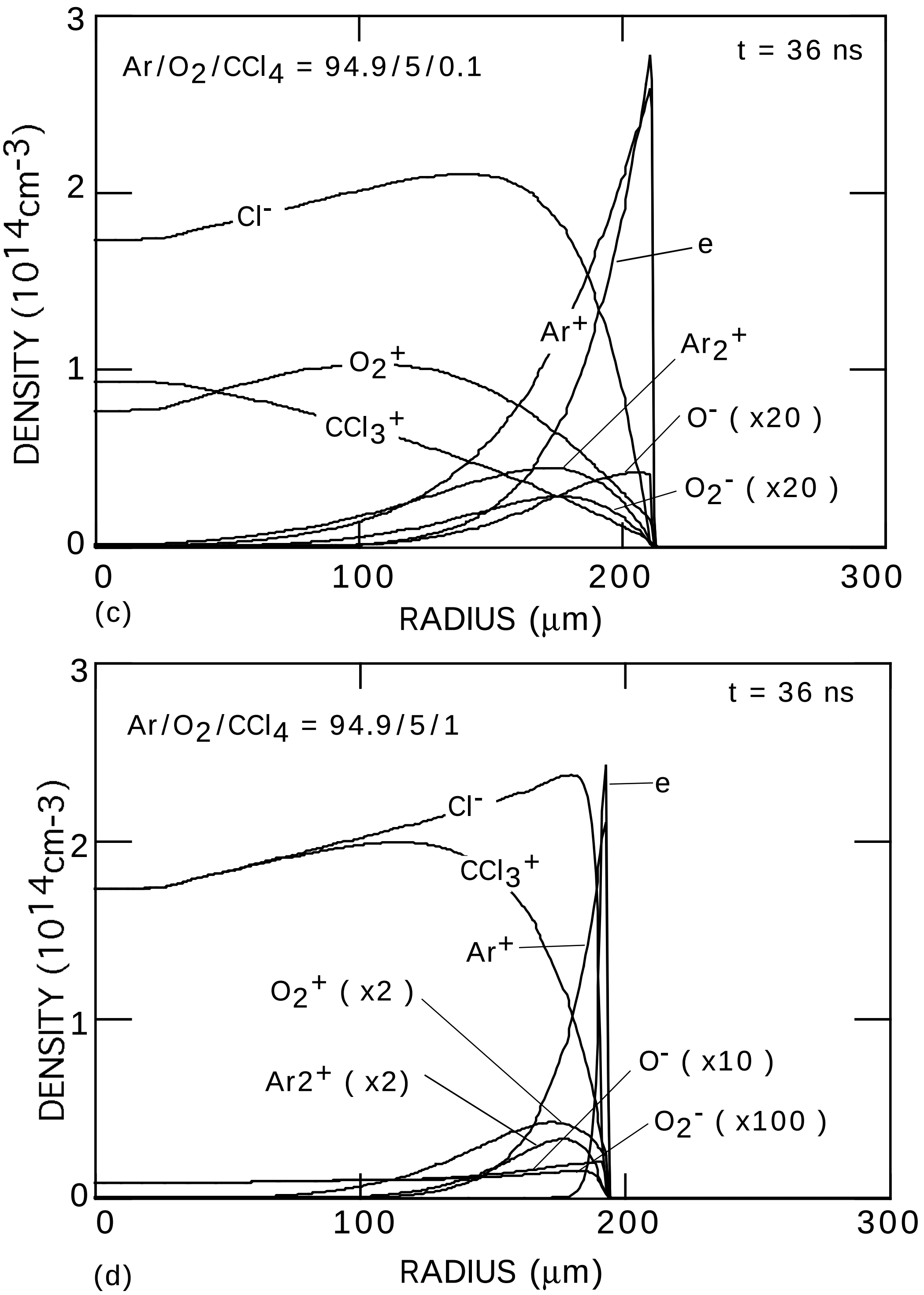

Fig. 3.9. Continued.

3.6 References

[1] B. Eliasson and U. Kogelschatz, IEEE Trans. Plasma Sci. **19**, 309 (1991).

[2] A. C. Gentile and M. J. Kushner, J. Appl. Phys. **79**, 3877 (1996).

[3] L. A. Rosocha, G. K. Anderson, L. A. Bechtold, J. J. Coogan, H. G. Hech, M. Kang, W. H. McCulla, R. A. Tennant, and P. J. Wantuck, in *Nonthermal Plasma Techniques for Pollution Control*, edited by B. N. Penetrante and S. E. Schultheis (Springer, Berlin, 1993), Part B, pp. 281.

4. MULTIPLE MICRODISCHARGE DYNAMICS IN DIELECTRIC BARRIER DISCHARGES

4.1 Introduction

In the last chapter, we addressed the radially symmetric dynamics of a single microdischarge. In this chapter, we report on results from a 2-D PCHM modeling study in which we address the complementary problem of the expansion of multiple, and hence radially asymmetric, microdischarges in close vicinity. We will investigate N_2 and dry air (N_2/O_2) discharges as examples of nonattaching and attaching discharges. The microdischarge development for 1-4 adjacent microdischarges in N_2 is presented in Section 4.2. In Section 4.3, we examine the dynamics of two closely space microdischarges in N_2/O_2. In Section 4.4, we discuss the consequences of remnant surface charges on microdischarge spreading. Our concluding remarks are in Section 4.5.

4.2 Multi-Microdischarges Dynamics in N_2

We begin our discussion of multi-microdischarge dynamics in DBDs by examining two microdischarges in pure N_2. Initial conditions are generated by specifying (or randomly distributing) a center point for each microdischarge in the 2-D domain. The microdischarge is assumed to be initially radially symmetric and composed of a seed electron density having a super-Gaussian profile with peak density of $n_0 = 10^9$ cm^{-3} and radius $r_0 = 15$ μm. Initial electron densities that would be smaller than 10^{-4} n_0 are set equal to zero. The pressure is one atmosphere at 400 K. One electrode is covered by 0.5-mm thickness of a dielectric having permittivity of $25\varepsilon_0$ with 0.25-cm gas gap. The applied voltage is a square pulse of specified duration and magnitude unless stated otherwise.

The electron density is shown in Fig. 4.1 for two microdischarges in N_2 separated by 300 μm for a square wave 40-ns voltage pulse of 12 kV. Results are shown for times of 0.8, 26, 41 and 100 ns. One-dimensional slices of the electron density through the axis of symmetry are shown in Fig. 4.2. Only the upper half of the microdischarges are shown in Fig. 4.1, taking advantage of symmetry across the lower horizontal axis. As in Chapter 3, we have chosen conditions for which the microdischarge will continue to expand for the duration of the voltage pulse in order to reduce the importance of issues related to surface conductivity of the substrate. The expanding microdischarges retain their initial circular profiles until they collide. Note the somewhat hollow appearance of the microdischarges. As in the case of the single microdischarge, charging of the dielectric in the center of the microdischarge produces a collapse of the *E/N* in the bulk plasma, which reduces the rate of electron generating collisions (e.g., ionization) and increases the rate of electron consuming collisions, in this case dissociative recombination. At 40 ns when the voltage is pulled to zero, the electric field resulting from charging the dielectric produces a secondary discharge in a manner similar to that for the single discharge. Further expansion does not occur during the secondary avalanche since the dielectric outside the microdischarge is not charged.

When the microdischarges collide, a peak in the electron density occurs at the interface, having an enhancement of ≈13% over the single microdischarge. This increase can be attributed to two causes. The first, in a sense, is a consequence of the initial conditions. Electrons from the microdischarge diffuse into regions of uncharged dielectric, followed by avalanche that begins charging the dielectric. The peak electron density occurs as the voltage across the gap falls below the self-sustaining value and net electron generation turns negative. The peak electron density therefore weakly depends on the initial electron density since there is some dynamic "overshoot" of the equilibrium conditions. Since we have contributions from expansion by both microdischarges to the effective n_0 at the interface, the initial electron density for avalanche at that location is larger. As a consequence the maximum electron density is larger. The second effect is hydrodynamic in nature. The ions and neutrals can, from a hydrodynamic standpoint, be considered well coupled fluids. The inertia of the expanding plasma column results in the shells of the colliding microdischarges producing a higher gas density. Since the ions are entrained in this flow, the ion density increases commensurably.

The plasma expansion of the microdischarges terminates on the sides where the collision occurs, but continues to expand on the opposite sides. The end result is an elongated appearance to the microdischarges. The microdischarges do not "pass through" each other as would, for example, expanding acoustic waves. Recall that the expansion of the microdischarges is sustained by diffusion of electrons into regions in which the dielectric is uncharged, thereby enabling avalanche and growth of the microdischarge. Since at the interface, electron diffusion occurs into regions in which the dielectric is already charged, further avalanche and expansion does not occur.

The gas temperature in the microdischarge depends on the total energy deposition, manner of dissipation of deposited energy and change in enthalpy due to chemical reactions and radiative decay of excited states. Gradients in temperature also produce a pressure gradient which can lead to advection. For example, 1-D slices of the gas temperature and total gas mass density are shown in Figs. 4.3 and 4.4 for the two microdischarges in N_2. During and just after the voltage pulse the gas temperature increases by only 8 K and has profiles similar to the electron distribution with the exception that there is a short delay in time resulting from collisional de-excitation of excited states. After 74 ns, the gas temperature in the microdischarge continuously increases with time as excited states of N_2 are quenched and dissipate their energy into translation modes. There is an additional temperature rise of ≈7 K from 0.1 μs to 0.37 μs, producing a total temperature rise of about 24 K. The resulting gas density, shown in Fig. 4.4, shows a corresponding rarefaction and compression that resembles a weak "blast wave." The gas densities do not directly correlate to the inverse of the gas temperature due to inertial effects during the short pulse. To first order, the energy deposition appears to occur instantaneously, followed by acceleration by the resulting pressure gradient. The gas density is marginally rarefied in the center of the microdischarge during the current pulse and compressed at the interface and edges. Significant rarefaction and compression only occur after termination of the pulse. As time proceeds, and the advective expansion slowly continues, the minimum and maximum mass densities can be found near the edge of avalanche region.

Given the random location of microdischarges, it is conceivable that a cluster of discharges might occur in proximity of each other. To investigate this possibility, four closely spaced microdischarges were simulated using the standard conditions with the exception that the line voltage is 11 kV. The electron density during and following the 40 ns voltage pulse is shown in Fig. 4.5 at 0.8, 14, 41, and 100 ns. The expanding microdischarges retain their initial circular shapes until they collide. At t = 14 ns the two closest streamers contact one another, thereby stalling their expansion along the interface. The other microdischarges continue to expand until they too collide with their neighbors. Their expansion then stalls and they coalesce. Note that the expanding shell of high electron density is ultimately located at the periphery of the coalesced microdischarges.

4.3 Multi-Microdischarges Dynamics in N_2/O_2

The microdischarge dynamics in dry air (N_2/O_2 = 80/20) differ from those in pure nitrogen. Because O_2 has a larger ionization rate than N_2 for a given *E/N*, a microdischarge in dry air at high *E/N* produces a larger electron density and has a higher rate of expansion. At low *E/N*, however, electron attachment ($O_2 + e \rightarrow O + O^-$ and $O_2 + e + M \rightarrow O_2^- + M$) adds to dissociative recombination to more rapidly decrease the electron density compared to N_2. For example, 1-D slices of electron densities through dry air microdischarges where two the two microdischarges are initially separated by 0.3 mm are shown in Fig. 4.6 for a line voltage of 12 kV. Due to the addition of the attachment processes, the electron density in the interior of the microdischarge decreases more rapidly after the dielectric charges and *E/N* collapsed compared to the N_2 microdischarges. As a result, the spike in electron density where the microdischarges collide is more pronounced, being 50% higher than in pure N_2.

For lower applied voltages, the lower electron density in the core of the microdischarges for N_2/O_2 = 80/20 gas mixtures reduces the current density to a sufficiently low value that the dielectric cannot fully charge. As a consequence, there is residual *E/N* across the core of the microdischarge for the full duration of the voltage pulse. For example, electron densities and voltage across the gap are shown in Fig. 4.7

for dry air microdischarges with a line voltage of 8.5 kV. Since in this gas mixture the attachment rate peaks at a non-zero *E/N* the residual, but subavalanche, electric field in the middle of the microdischarges actually produces more net electron loss by attachment. The end result is a more hollow-looking shell for the microdischarges and a more pronounced peaking of the electron density in the overlap region. Due to the incomplete charging of the dielectric, when the voltage is pulled to zero at the end of the pulse, the electric field produced by the charge is also subavalanche in its strength, and serves only to increase the rate of attachment. As a consequence, the microdischarges are rapidly quenched compared to those for N_2.

The spatial dependence and ion composition of the N_2/O_2 microdischarges when the dielectric is fully charged and not fully charged are shown in Fig. 4.8. Here we plot the ion and electron densities for N_2/O_2 = 80/20 microdischarges at 36 ns for line voltages of 8.5 and 12 kV. The separation between the microdischarges is 0.2 mm in order to insure that they will collide during the 40 ns voltage pulse. For the lower voltage, the current density is low enough that the dielectric is not fully charged, leaving an electric field in the center of the microdischarges which is subavalanche and promotes attachment. The charged particle composition is dominantly negative ions and positive ions in the middle of the microdischarges. At the edges of the microdischarges and in the interface, the current density was large enough that charging of the dielectric was complete, thereby removing nearly all the voltage from the gap which produced a less attaching environment. In those regions, the electron density has about the same density as the negative ions.

With a line voltage of 12 kV, the peak electron density is 10 times larger than at 8.5 kV but, more importantly, the current density is large enough that the dielectric fully charges. This removes voltage from the gap which produces a less attaching environment, and results in a charged particle inventory with is dominantly electrons and positive ions. The final charged particle inventory is a sensitive function of the dependence of attachment on *E/N* in the sub-avalanche regime.

4.4 Consequences of Remnant Surface Charges on Microdischarge Spreading

The residual charge on the dielectric from a previous discharge pulse can have a significant effect on the microdischarge dynamics of a subsequent pulse. To illustrate this dependence, we have set up the following conditions. A pair of microdischarges in dry air with a line voltage of 8.5 kV have previously occurred. Their locations, labeled "pulse 1" are shown in Fig. 4.9. The voltage is sufficiently low that the dielectric is not fully discharged, and there is residual charge left on the dielectric. On a second inverted voltage pulse, a single microdischarge, labeled "pulse 2," occurs adjacent to the first pair. The residual charge left by the first pair of microdischarges then adds to the inverted line voltage on the second pulse. The resulting electron density and voltage across the gap during and after the second 40-ns voltage pulse are shown in Fig. 4.10 at 0.8, 12.1, 18.3, 36.6, 40.7 (just after the voltage pulse), 67.2, and 100.0 ns.

Initially (0.8 ns), the gap voltage is uniformly at 8.5 kV, except where the residual voltage is left on the dielectric. At those locations the voltage is 13.3 kV. The electron density is initially large only in the vicinity of the second microdischarge. As the second microdischarge progresses (12.1 ns), it charges the dielectric beneath it, thereby removing voltage from the gap. The electron density in the center of the microdischarge then decreases due to attachment. At the same time, the expanding microdischarge encroaches on the region of the dielectric which was previously charged. Since this region now has a larger gap voltage, electron avalanche rapidly occurs producing a "daughter" microdischarge (18.3 ns) having an even larger electron density than its "parent." The higher *E/N* for the first daughter microdischarge produces a higher current density, which fully charges the dielectric, thereby removing voltage from the gap. The expansion of the first daughter microdischarge encroaches on the second high *E/N* region produced by the residual charge on the dielectric (36.6 ns). A second daughter microdischarge occurs, repeating the pattern of the first. The higher *E/N* produces a large current density which completely charges the underlying dielectric, thereby removing voltage from the gap. The electron densities in the center of the parent microdischarge are smaller than in the center of the daughter microdischarges due to the higher, but sub-avalanche, residual *E/N* in the center of the parent microdischarge.

At the end of the second pulse when the line voltage is pulled to zero, the second daughter microdischarge has yet to expand to fill the entire high *E/N* region (40.7 ns). A secondary avalanche occurs for both of the daughter microdischarges which fully discharges the dielectric in their domains (67.2 ns). The parent microdischarge, which was produced by the lower voltage that did not fully charge the dielectric, experiences a weak secondary avalanche that leaves residual charge on the dielectric. The end result (100 ns) is that residual charge (and voltage across the gap) is left on the dielectric in the location of the parent microdischarge and in the peripheries of the daughter microdischarges.

4.5 Concluding Remarks

A 2-D model has been developed to investigate microdischarge dynamics in dielectric barrier discharges operating in pure nitrogen and dry air. The electron density in a single microdischarge peaks in an expanding shell where the rate of avalanche is highest. In the interior of the microdischarge, where the dielectric is charged, thereby removing voltage from the gap, the electron density is typically smaller due to the lower ionization rate and higher rates of electron loss processes at the lower *E/N*. The dynamics of adjacent expanding microdischarges that collide with each other are similar, with the exception that the electron density peaks at the interface by at most a percentage of a few tens. The expanding ionization waves of the individual microdischarges do not propagate through each other as would acoustic waves. The ionization waves are sustained by avalanche produced in regions of uncharged dielectric. Since the dielectric is charged by its partner in advance of the expanding microdischarge, the avalanche stalls at the interface. Residual charge on the dielectric from a previous microdischarge can significantly alter the dynamics of following microdischarges. The residual charge typically adds to the voltage for the subsequent microdischarge, thereby leading to more intense avalanche and providing a mechanism for microdischarges to expand beyond their single microdischarge domains.

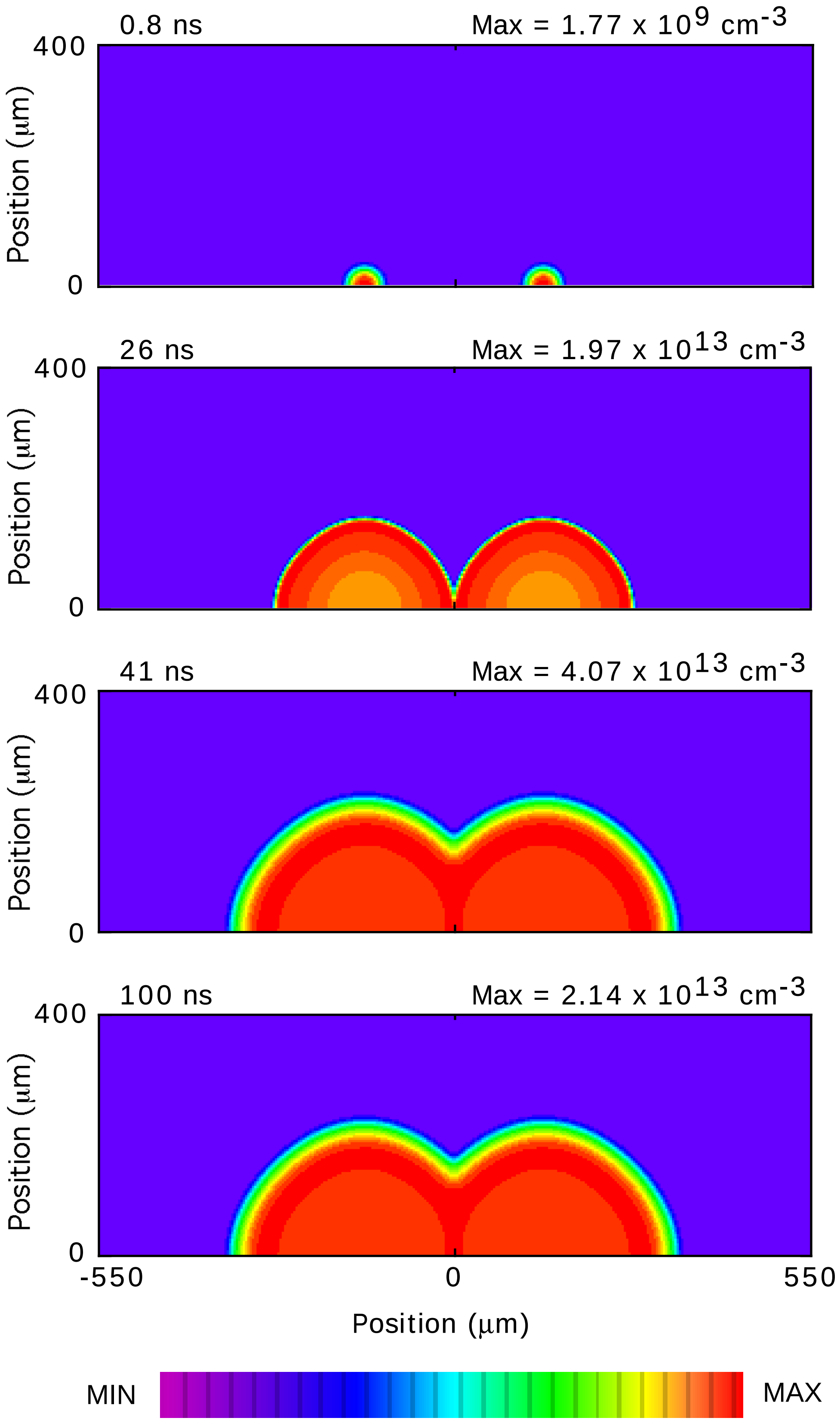

Fig. 4.1. Electron density distribution for two closely spaced microdischarges in N_2 at 0.8, 26, 41 and 100 ns. The separation of the two microdischarges is 300 µm and the applied voltage is a 40-ns square wave pulse at 12 kV. The maximum electron density in each frame is indicated. The color scale is linear with density. The results are symmetric across the bottom axis.

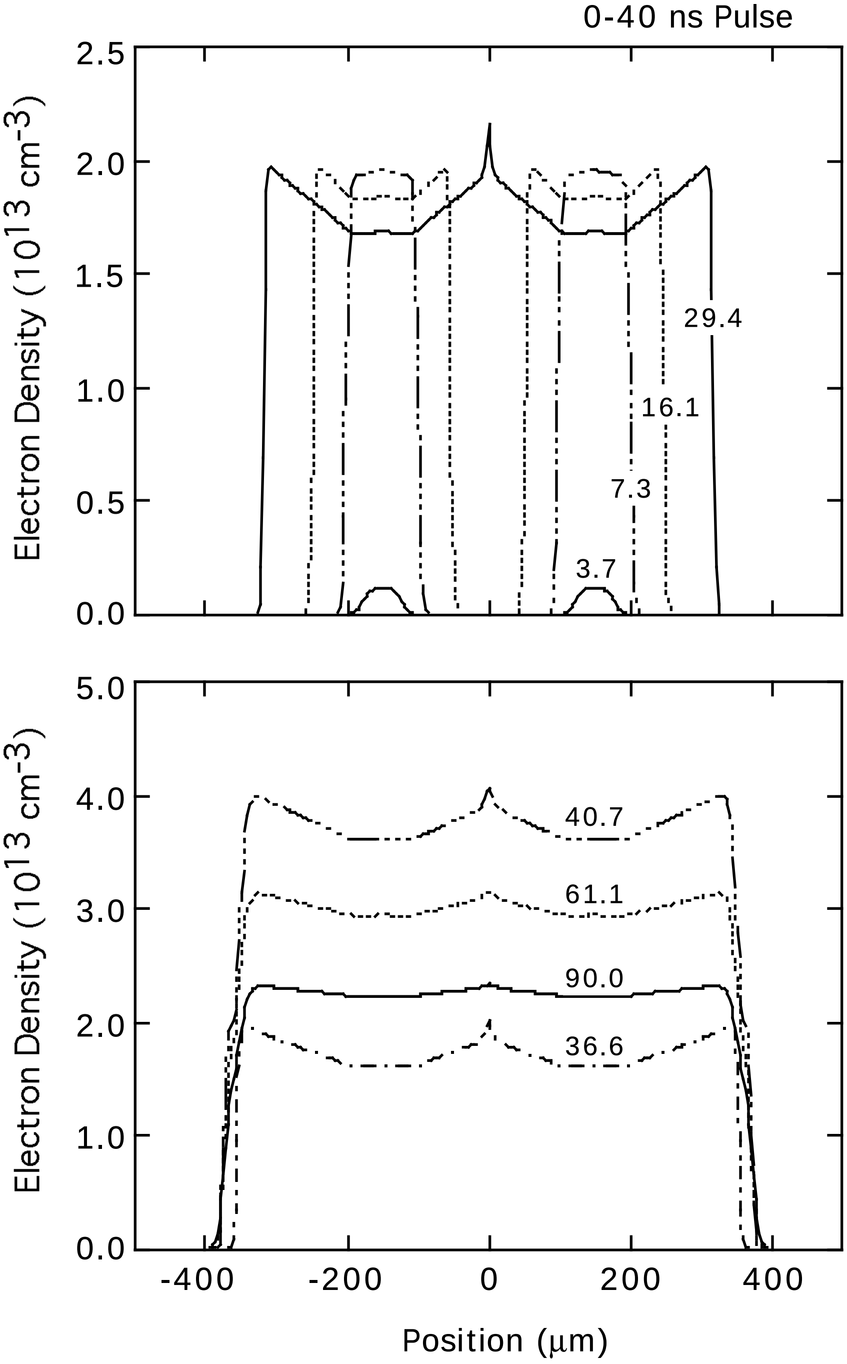

Fig. 4.2. Electron density along the axis of symmetry at various times in an N_2 microdischarge for the conditions of Fig. 4.1. The curves are labeled with their time (ns) after start of the voltage pulse. The peak electron density occurs at the interface of the expanding microdischarges with a 13% increase compared to a single microdischarge.

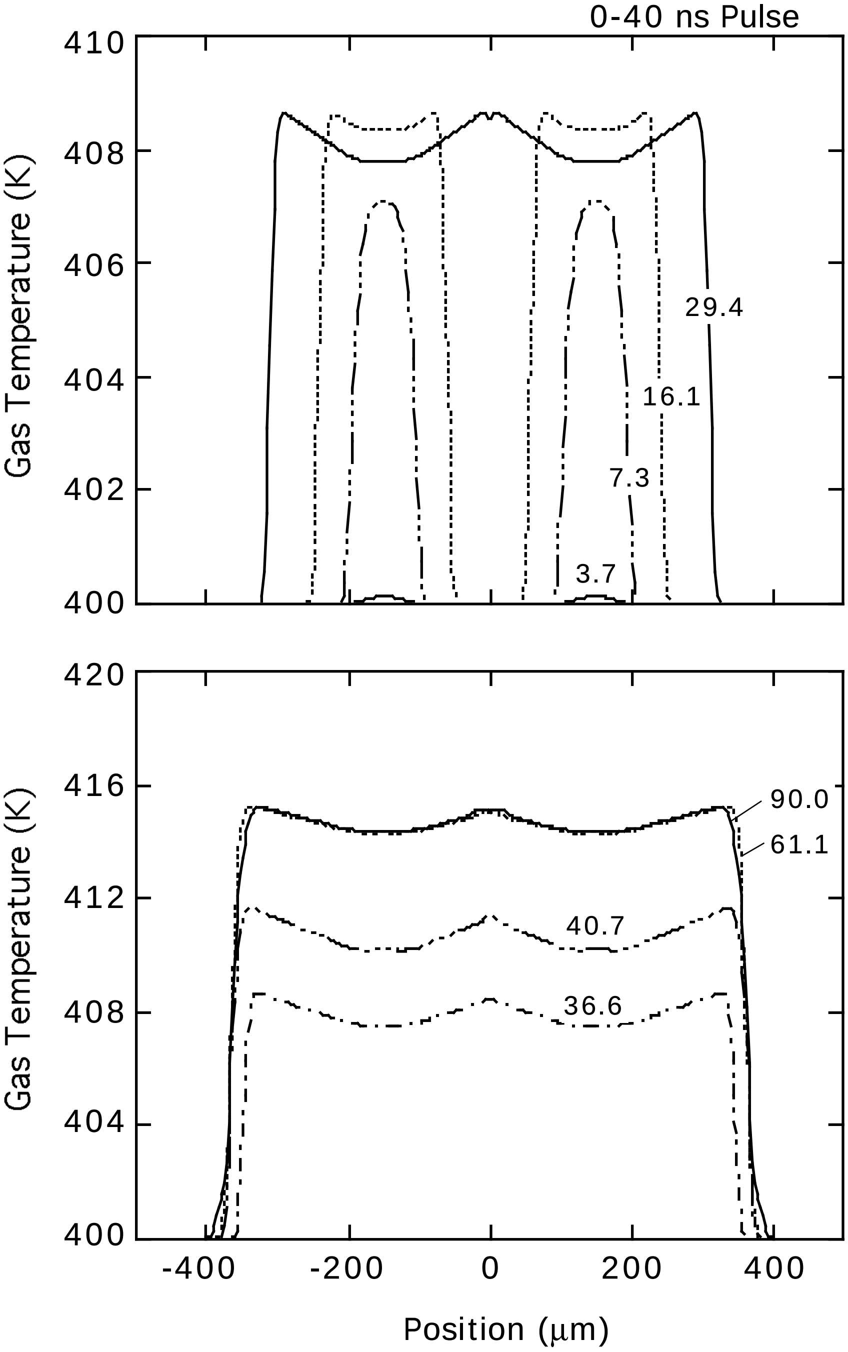

Fig. 4.3. Gas temperature along the axis of symmetry at various times in an N_2 microdischarge for the conditions of Fig. 4.1. The curves are labeled with their time (ns) after start of the voltage pulse. Unlike the electron density, the gas temperature continues to increase after the voltage pulse is terminated due to dissipation of energy from excited states of N_2 into translational modes.

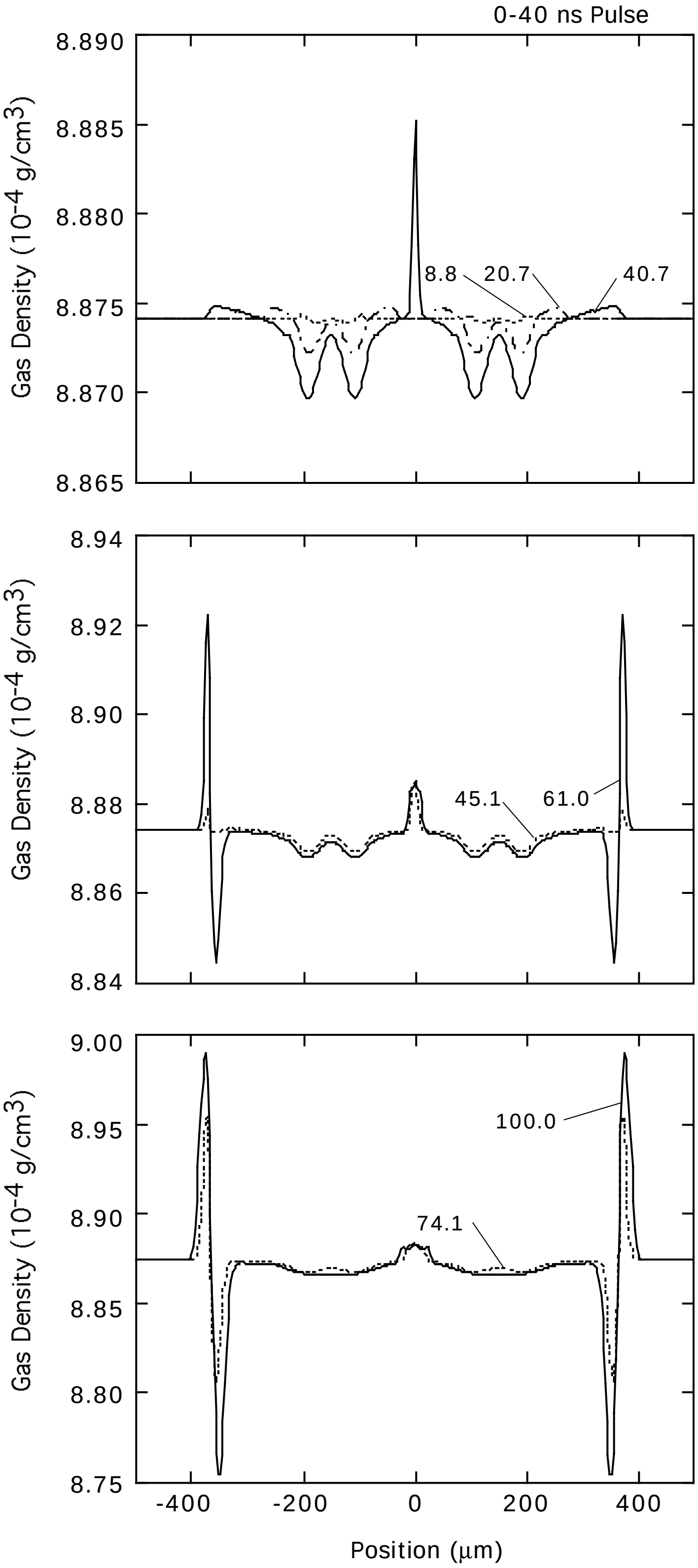

Fig. 4.4. Gas density along the axis of symmetry at various times for the conditions of Fig. 4.1. The curves are labeled with their time (ns) after start of the voltage pulse. At long times, the gas density profiles resemble a weak blast wave.

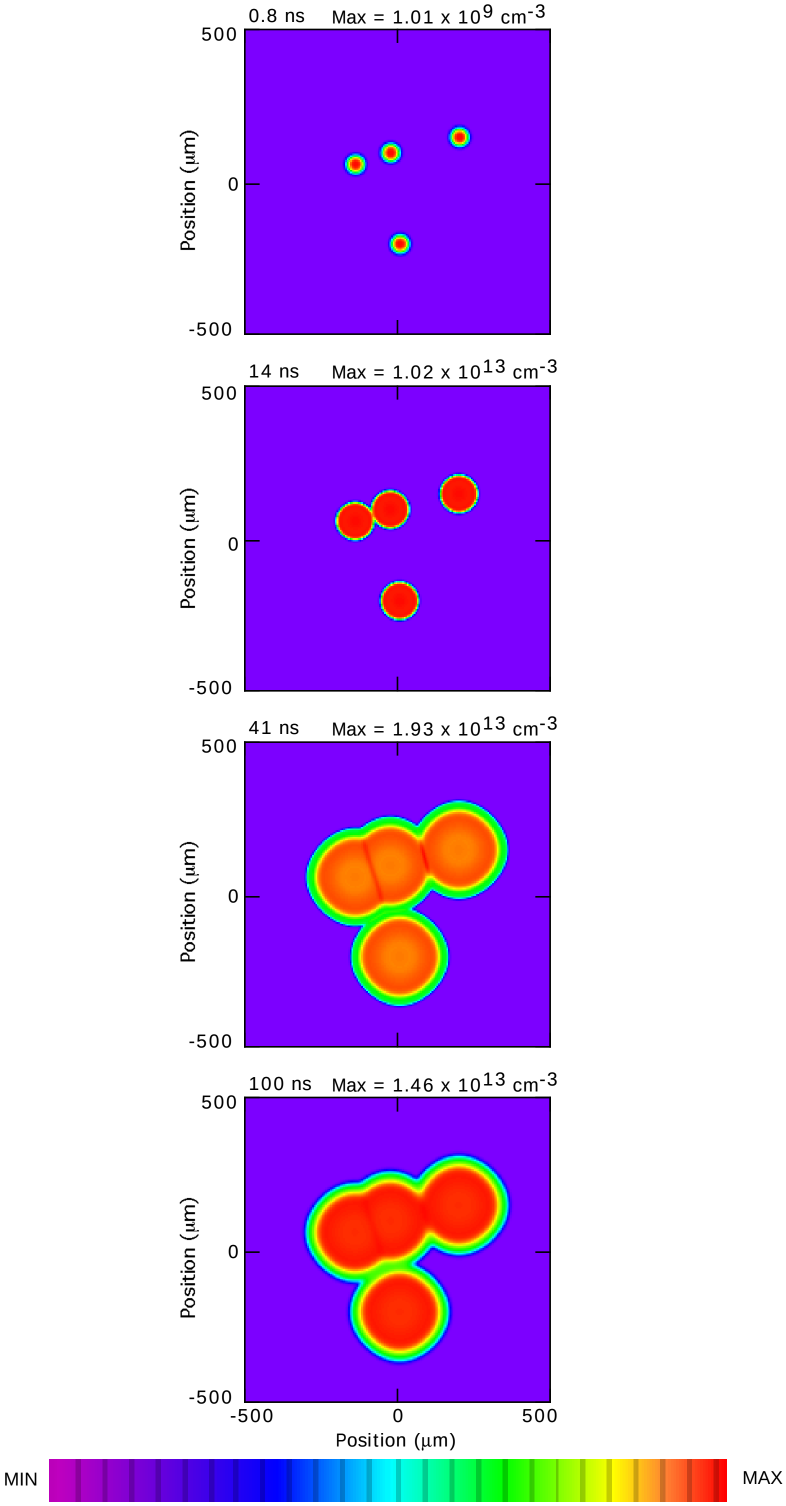

Fig. 4.5. Electron density for four closely spaced microdischarges in N_2 at 0.8, 14, 41, and 100 ns. The applied voltage is a square wave 40 ns pulse at 11 kV. The color scale is linear with density.

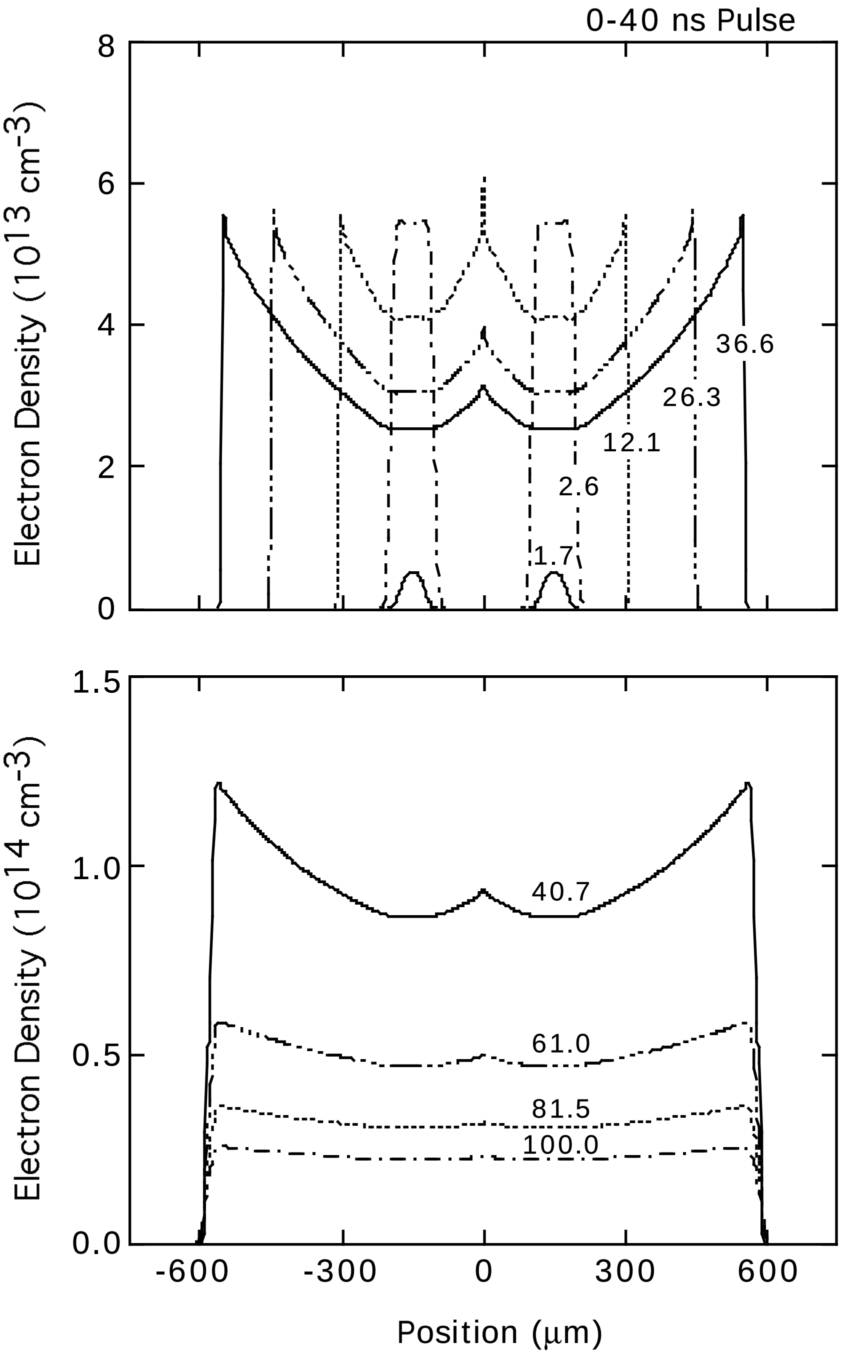

Fig. 4.6. Electron density along the axis of symmetry in an N_2/O_2 = 80/20 microdischarge. The curves are labeled with their time (ns) after start of the voltage pulse. The separation of the two microdischarges is 300 μm and the applied voltage is a square wave 40 ns pulse at 12 kV. The larger rate of electron loss at low E/N in the center of the microdischarge produces a more hollow appearing electron density.

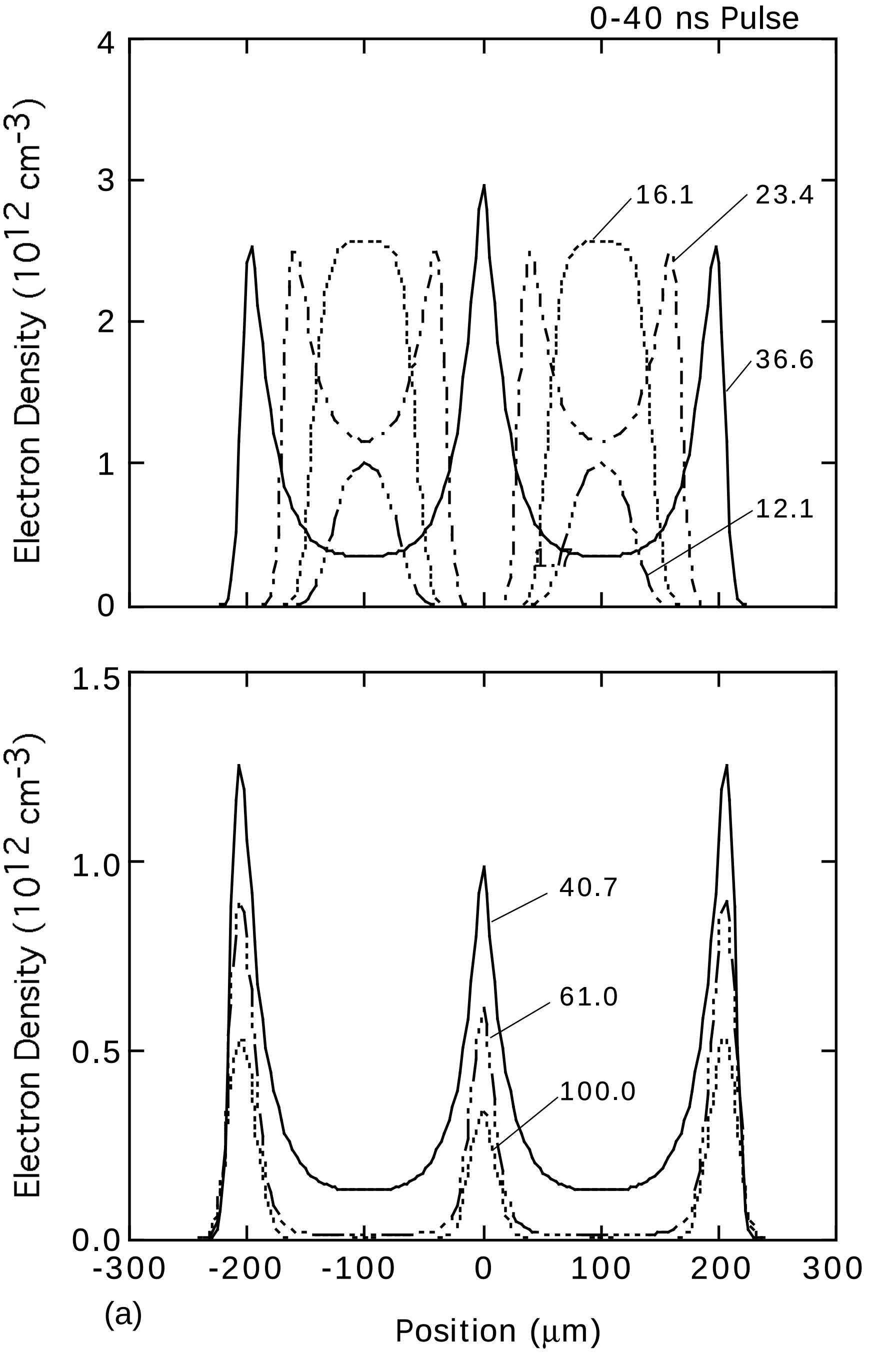

Fig. 4.7. Microdischarge properties along the axis of symmetry for N_2/O_2 = 80/20 microdischarges having a square wave 40 ns voltage pulse at 8.5 kV: (a) electron density and (b) gap voltage. The curves are labeled with their time (ns) after start of the voltage pulse. The separation of two microdischarges is 200 μm. The residual E/N across the gap increases attachment in the post avalanche phase, thereby consuming electrons.

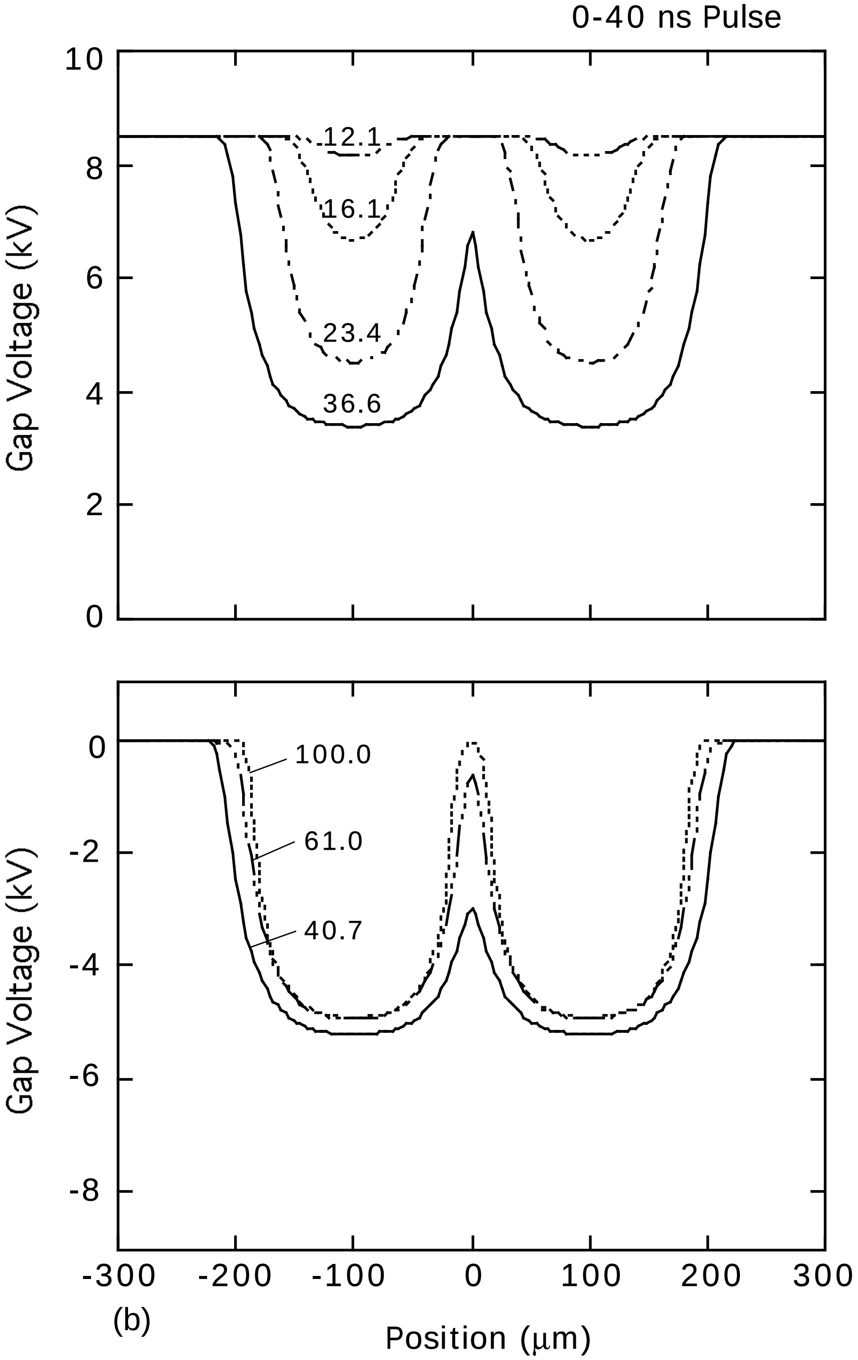

Fig. 4.7. Continued.

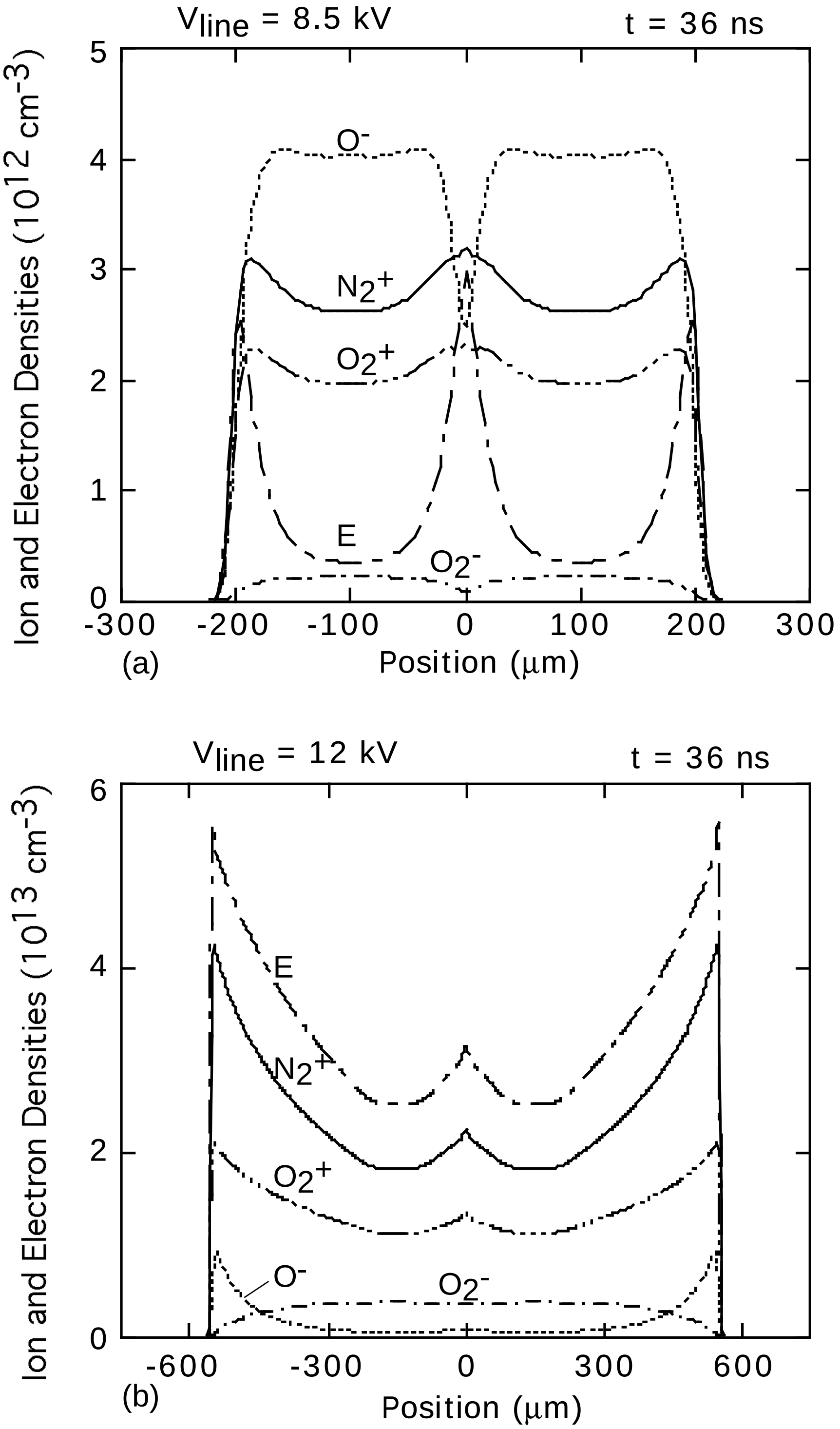

Fig. 4.8. Ion and electron densities for N_2/O_2 = 80/20 microdischarges at 36 ns for the conditions of Figs. 4.6 and 4.7: (a) 8.5-kV line voltage and (b) 12-kV line voltage. O^- is the dominant negative charge carrier in the center of the microdischarge for lower line voltage while electrons are dominant for higher line voltages.

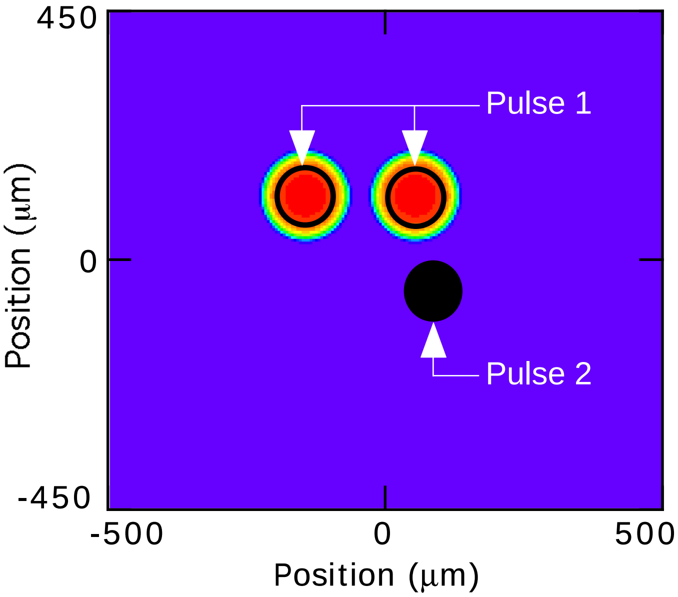

Fig. 4.9. Locations of microdischarges for Pulses 1 and 2, and residual charge on the dielectric resulting from Pulse 1 for a dry air microdischarge for the conditions of Fig. 4.7. The second pulse will have an inverse voltage from the first, and so the residual charge will add voltage to the applied potential.

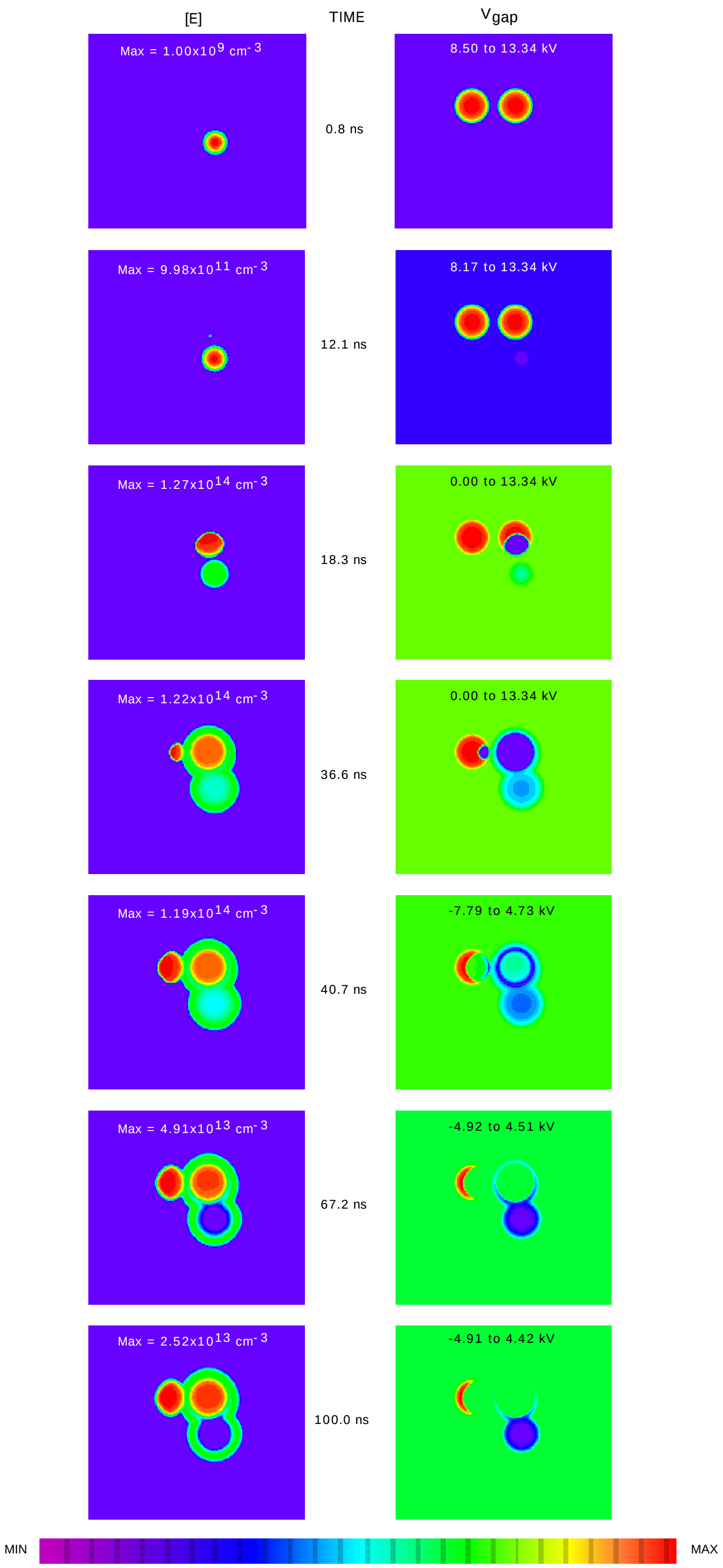

Fig. 4.10. Electron density and gap voltage at 0.8, 12.1, 18.3, 36.6, 40.7, 67.2, and 100.0 ns for the conditions of Fig. 4.9. The daughter microdischarges avalanche to a higher density because of the larger *E*/*N* enabled by residual charge on the dielectric.

5. REMEDIATION OF CARBONTETRACHLORIDE IN DIELECTRIC BARRIER DISCHARGES

5.1 Introduction

Carbon tetrachloride (CCl_4) is primarily used as an industrial solvent. CCl_4 contamination in the environment is a concern due to its long lifetime and the large volumes in use. Under ambient conditions, CCl_4 is not decomposed easily [1, 2]. In the atmosphere, CCl_4 is almost unreactive with the hydroxyl radical (OH) but can be decomposed via direct photolysis in the stratosphere [3, 4]. The persistence of CCl_4 in the environment is of concern because it is a suspected human carcinogen and as a result is an Environmental Protection Agency (EPA) priority pollutant [5, 6].

Several methods have been applied to the remediation of gas-phase CCl_4 such as incineration [7], reduction over metallic iron [8], and decomposition with low temperature plasmas [9-13]. In particular, dielectric barrier discharges are attractive for this purpose due to their ability to operate stably at atmospheric pressure and due to their low-cost maintenance [9].

In Chapter 3 we have shown that the characteristics of microdischarge development in $Ar/O_2/CCl_4$ was appreciably influenced by small amounts of CCl_4. Due to the large rate of dissociative attachment of CCl_4 at low E/N, electron densities showed an expanding shell with a core composed of largely negative ions and positive ions. In this chapter, we examine the kinetics and mechanism of plasma remediation of CCl_4 in Ar/O_2 and $Ar/O_2/H_2O$ gas mixtures in DBDs and determine the optimum strategies for its remediation.

5.2 Reaction Mechanisms in Remediation of CCl_4

A schematic of the dominant reaction pathways for plasma remediation of CCl_4 in an $Ar/O_2/H_2O$ gas is shown in Fig. 5.1. (A complete listing of species and reaction rate coefficients can be found in Appendices A and B.) The initial CCl_4 is highlighted by a diamond. The 12 major end products are boxed. Plasma remediation for operating conditions typical of DBDs progresses through electron, ion, radical, and other species-assisted reactions.

At high concentrations of CCl_4, direct electron impact reactions, such as dissociative ionization, and vibrational and electronic excitations leading to dissociation, will be significant:

$$e + CCl_4 \rightarrow CCl_3^+ + Cl + 2\,e, \qquad k = 5.268\times10^{-9}\ cm^3\ s^{-1}, \tag{5.1}$$

$$e + CCl_4 \rightarrow CCl_2^+ + Cl_2 + 2\,e, \qquad k = 2.527\times10^{-10}\ cm^3\ s^{-1}, \tag{5.2}$$

$$e + CCl_4 \rightarrow CCl^+ + Cl_2 + Cl + 2\,e, \qquad k = 1.013\times10^{-10}\ cm^3\ s^{-1}, \tag{5.3}$$

$$e + CCl_4 \rightarrow CCl_3 + Cl^+ + 2\,e, \qquad k = 9.722\times10^{-12}\ cm^3\ s^{-1}, \tag{5.4}$$

$$e + CCl_4 \rightarrow CCl_2 + Cl_2^+ + 2\,e, \qquad k = 5.8\times10^{-13}\ cm^3\ s^{-1}, \tag{5.5}$$

$$e + CCl_4 \rightarrow CCl_2 + 2\,Cl + e, \qquad k = 5.867\times10^{-8}\ cm^3\ s^{-1}. \tag{5.6}$$

(The rate coefficients listed for electron-impact processes were obtained from our solution of Boltzmann's equation at $E/N = 2 \times 10^{-15}$ V cm^2.) However, the E/N in the interior of microdischarges quickly decreases to small values due to charge accumulation on dielectric surfaces. At low CCl_4 concentrations <0.1%, the fraction of discharge power deposited in CCl_4 and these dissociative pathways do not contribute significantly to the fragmentation of CCl_4.

A more significant process for dilute CCl_4 mixtures is a dissociative electron attachment for a dilute CCl_4 gas mixture, which has high reaction rates ($4\times10^{-8} – 2\times10^{-7}$ $cm^3\ s^{-1}$) at small electron temperatures (0.1 – 1eV).

$$e + CCl_4 \rightarrow CCl_3 + Cl^- \qquad (5.7)$$

Other important reaction mechanisms for the dissociation could be excitation and charge transfers from Ar^*, Ar^{**}, Ar^+ Ar_2^+, O_2^+, O^+, and H_2O^+ to CCl_4.

$$Ar^* \text{ (or } Ar^{**}) + CCl_4 \rightarrow Ar + CCl_2 + Cl_2 \qquad k = 1.0\times10^{-10}\ cm^3\ s^{-1} \qquad (5.8)$$

$$Ar^+ + CCl_4 \rightarrow Ar + CCl_3^+ + Cl, \qquad k = 1.0\times10^{-9}\ cm^3\ s^{-1}, \qquad (5.9)$$

$$Ar_2^+ + CCl_4 \rightarrow 2\ Ar + CCl_3^+ + Cl, \qquad k = 1.0\times10^{-9}\ cm^3\ s^{-1}, \qquad (5.10)$$

$$O_2^+ + CCl_4 \rightarrow O_2 + CCl_3^+ + Cl, \qquad k = 1.0\times10^{-9}\ cm^3\ s^{-1}, \qquad (5.11)$$

$$O^+ + CCl_4 \rightarrow O + CCl_3^+ + Cl, \qquad k = 1.0\times10^{-9}\ cm^3\ s^{-1}, \qquad (5.12)$$

$$H_2O^+ + CCl_4 \rightarrow H_2O + CCl_3^+ + Cl, \qquad k = 1.0\times10^{-9}\ cm^3\ s^{-1}. \qquad (5.13)$$

In addition, the radicals O (the triplet ground state atomic oxygen), $O(^1D)$, and OH can dissociate CCl_4 as follows:

$$O + CCl_4 \rightarrow CCl_3 + ClO, \qquad k = 6.0\times10^{-13} \exp(-2630/T)\ cm^3\ s^{-1}, \qquad (5.14)$$

$$O(^1D) + CCl_4 \rightarrow CCl_3 + ClO, \qquad k = 3.5\times10^{-10}\ cm^3\ s^{-1}, \qquad (5.15)$$

$$OH + CCl_4 \rightarrow CCl_3 + HOCl, \qquad k = 1.0\times10^{-12} \exp(-2320/T) \text{ cm}^3 \text{ s}^{-1}. \qquad (5.16)$$

However, at ambient temperatures the Reactions (5.14) and (5.16) have small rate coefficients, and so the only Reaction (5.14) alone contributes significantly to the dissociation of CCl_4.

CCl_3, one of the main fragments of CCl_4 quickly reacts with O_2 to form CCl_3O_2:

$$CCl_3 + O_2 + M \rightarrow CCl_3O_2 + M \qquad k = 1.19\times10^{-32} \exp(1278/T) \text{ cm}^6 \text{ s}^{-1}. \qquad (5.17)$$

The CCl_3O_2 undergoes a chain reaction with Cl radical and produces phosgene ($COCl_2$) as one of the main end products [14, 15]:

$$CCl_3O_2 + Cl \rightarrow CCl_3O + ClO \qquad k = 1\times10^{-12} \text{ cm}^3 \text{ s}^{-1}, \qquad (5.18)$$

$$CCl_3O_2 + CCl_3O_2 \rightarrow 2\ CCl_3O + O_2 \qquad k = 8.32\times10^{-11} \text{ cm}^3 \text{ s}^{-1}, \qquad (5.19)$$

$$CCl_3O \rightarrow COCl_2 + Cl \qquad k = 4.0\times10^{13} \exp(-4600/T) \text{ s}^{-1}. \qquad (5.20)$$

Other possible pathways, which scavenge CCl_3, are reactions with O and OH,

$$CCl_3 + O \rightarrow COCl_2 + Cl \qquad k = 4.15\times10^{-11} \text{ cm}^3 \text{ s}^{-1}, \qquad (5.21)$$

$$CCl_3 + OH \rightarrow COCl_2 + HCl \qquad k = 4.15\times10^{-11} \text{ cm}^3 \text{ s}^{-1}. \qquad (5.22)$$

Another important fragment of CCl_4, CCl_2, reacts with O atoms and OH radicals to generate COCl and also slowly reacts with O_2 to form $COCl_2$.

$$CCl_2 + O \rightarrow COCl + Cl \qquad k = 1\times10^{-11}\ cm^3\ s^{-1}, \qquad (5.23)$$

$$CCl_2 + OH \rightarrow COCl + HCl \qquad k = 1\times10^{-11}\ cm^3\ s^{-1}, \qquad (5.24)$$

$$CCl_2 + O_2 \rightarrow COCl_2 + Cl \qquad k = 1\times10^{-14}\ cm^3\ s^{-1}. \qquad (5.25)$$

The COCl further reacts with O, O_2, Cl, and OH to generate CO and CO_2, the details of which are summarized in Fig. 5.1. At ambient temperatures, CO and $COCl_2$ are fairly stable molecules, though $COCl_2$ slowly reacts with O and OH.

The other end product is Cl_2, which is formed by the reaction

$$Cl + Cl + M \rightarrow Cl_2 + M \qquad k = 3.47\times10^{-33}\exp(810/T)\ cm^6\ s^{-1}. \qquad (5.26)$$

Cl is produced mainly by the ion-ion neutralization reaction of Cl^-.

5.3 Spatial Dependencies in Remediation of CCl_4

In this section, we consider the dynamics of the system, focusing on CCl_4 remediation and the temporal and spatial dependencies of important species. In the analyses that follow, a single streamer is examined using the 1-D radially dependent model as described in Section 2.2. Furthermore, we limit the discharge to the first pulse only. The standard conditions used in this chapter are the same as those used in Chapter 3 (the applied voltage is a square pulse with 40 ns duration, the initial gas pressure is 1 atm, and the initial seed electron density has a distribution 20 μm in radius and 10^9 cm^{-3}

peak value), with the exception that the temperature is 300 K. The baseline case is a gas mixture of $Ar/O_2/CCl_4$ = 79.9/20/0.1 with a pulse magnitude of 12 kV.

The production of charged species is the main process during the pulse. Figure 5.2 shows the concentration profiles of the electron, positive ions, and negative ions during and following the voltage pulse as a function of radius. During the 40-ns voltage pulse, the electron density sharply peaks at the edge of the microdischarge because electrons are rapidly consumed, primarily by the dissociative attachment to CCl_4 in the core. The Cl^-, on the other hand, shows a flat distribution in the core. Electrons also attach to oxygen to generate O^- and O_2^-, whose concentrations are 12 and 25 times less than the Cl^- concentration during the pulse. Due to the low CCl_4 concentration (0.01 mole fraction), the direct electron impact ionization of CCl_4 is negligible. The major ionization reactions involving electrons are those of Ar and O_2,

$$e + Ar \rightarrow Ar^+ + 2\,e, \qquad k = 1.18\times10^{-10}\ cm^3\ s^{-1}, \qquad (5.27)$$

$$e + O_2 \rightarrow O_2^+ + 2\,e, \qquad k = 1.77\times10^{-10}\ cm^3\ s^{-1}, \qquad (5.28)$$

$$e + O_2 \rightarrow O^+ + O + 2\,e, \qquad k = 1.45\times10^{-12}\ cm^3\ s^{-1}, \qquad (5.29)$$

where the rate coefficients are for $E/N = 2\times10^{-15}$ V cm^2. It is apparent that Ar^+ and O_2^+ are the primary ions generated by electron impact. Ar^+ is rapidly depleted due to its charge transfer reactions,

$$Ar^+ + CCl_4 \rightarrow Ar + CCl_3^+ + Cl, \qquad k = 1.0\times10^{-9}\ cm^3\ s^{-1}, \qquad (5.30)$$

$$Ar^+ + O_2 \rightarrow Ar + O_2^+, \qquad k = 4.0\times10^{-11}\ cm^3\ s^{-1}, \qquad (5.31)$$

$$Ar^+ + Ar + M \rightarrow Ar_2^+ + M, \qquad k = 2.0\times10^{-31}\ cm^6\ s^{-1}, \qquad (5.32)$$

Most of Ar^+ are consumed by the charge transfer reaction with O_2 [Reaction (5.31)]. The dime ion, Ar_2^+, also rapidly transfers its charge. Both of Ar^+ and Ar_2^+ densities have a sharp edge in their profiles [Fig. 5.2(e) and (f)]. O_2^+ depletion by charge transfer is only by the reaction with CCl_4. The O_2^+ density profile displays a much less sharp edge than Ar^+ and Ar_2^+. The CCl_3^+ density shows a steady decrease, with increasing radius during the pulse and a flatter profile within the core after the pulse.

The excited state species Ar^*, Ar^{**}, and $O(^1D)$, which can decompose CCl_4, are shown in Fig. 5.3. All of their densities have a sharp edge. Because of the larger concentration of O_2 compared to CCl_4, these species are lost preferentially to quenching by O_2 and so do not make an important contribution to CCl_4 decomposition. Compared to $O(^1D)$ in Fig. 5.3(c), the triplet state of atomic oxygen O, shown in Fig. 5.3(d), has higher concentration (by a factor of 3.6) with a flat spatial distribution. O reacts with O_2, CCl_3, and CCl_2 to generate O_3, $COCl_2$, and COCl, respectively.

The spatial dependence of the CCl_3, CCl_2, and Cl densities, the primary neutral fragments of CCl_4 are shown in Fig. 5.4. Since CCl_3 is scavenged rapidly by O_2 [as in Reaction (5.17)], the CCl_3 density shows a hollow distribution. During the pulse, the peak value of CCl_3 is more than that of CCl_2 by a factor of 5. The CCl_3 radicals are almost removed completely at around 5 μs. Unlike the CCl_3, the CCl_2 is uniformly distributed within the core. The CCl_2 concentration builds up during the leading and trailing edge of the pulse due to the reactions of excited species such as Ar^* and Ar^{**} with CCl_4 to form CCl_2 [Reaction (5.8)] and the electron-impact dissociation of CCl_4 [Reaction (5.6)]. The CCl_2 density gradually decreases after the pulse because there is a relatively slow consumption of CCl_2 by the radicals O [by Reaction (5.22)], Cl (to generate CCl_3) and O_2 [by Reaction (5.24)]. The CCl_2 radicals are not depleted until 500 μs. The Cl concentration initially created during the pulse is primarily due to the direct dissociation of CCl_4, and then continues to increase after the pulse principally from Cl^- neutralization with positive ions. The Cl density attains a peak value of 3.46×10^{14} cm^{-3} at 29 μs. The Cl density drops with time primarily due to the recombination reactions to generate Cl_2 and the reaction involving O_3 to produce ClO and O_2.

The spatial variations of the densities of oxidized species CCl_3O_2, $COCl_2$ and ClO are shown in Fig. 5.5. The concentrations of the three species have a uniform profile in the core. The CCl_3O_2 density has a peak of 2.81×10^{14} cm^{-3} at 0.9 μs, and then decreases with time primarily due to the reaction with Cl and itself [by Reactions (5.18) and (5.19)]. The $COCl_2$ and ClO concentrations continue to increase until 156 μs and 256 μs, respectively, and then decrease due to diffusing out to large radii. Finally the Cl atoms that were initially bound in CCl_4 are converted to products in the following proportions: $COCl_2$, 47.7%; ClO, 27.4; Cl_2, 21.0% with the small remainder primarily in CCl_3O_2. Approximately 99.5% of the C atoms initially bound in CCl_4 appear in $COCl_2$.

5.4 Optimization of Remediation Conditions

Approaches for optimizing remediation of CCl_4 can be expressed in term of the plasma chemical processes discussed in the prior section. We found that remediation is achieved primarily through electron attachment reactions, with excited-state atoms, radicals, and ion-assisted reactions. These species are produced during the leading and trailing edge of the pulse and consumed during remediation reactions. Therefore, in order to obtain an optimal remediation strategy, it is important to consider the effects of all the parameters that affect the formation and depletion of agents that remediate CCl_4.

To explore these dependencies we parameterized the model over the capacitance of dielectric (e_d/L, where e_d = permittivity, L = thickness of the dielectric), applied voltage, and O_2 mole fraction. Further, we will examine effects of water vapor on CCl_4 remediation in the next section. To evaluate the efficiency of remediation, the results have been summarized in the term of eV/molecule: the amount of energy (eV) required removing 1 molecule of CCl_4, typically called the *W* value. Thus, the lower the *W* value, the more efficient is the process.

Energy deposition and the *W* value for CCl_4 degradation are shown in Fig. 5.6 as a function of dielectric capacitance, where the conditions for each case are the same as that of the standard case in Section 5.3, with the exception of the dielectric capacitance being varied. As might be anticipated, the energy deposition linearly increases with increasing the dielectric capacitance. However, the *W* value increases with increasing ε_d/L due to a less efficient utilization of the reactant intermediates. Electrons, Ar^+, O_2^+, Ar^*, Ar^{**}, and $O(^1D)$, which do not quickly react with CCl_4, will be otherwise consumed.

The *W* value decreases at high applied voltages, as shown in Fig. 5.7, where the conditions for each case are the same as the standard case of Section 5.3 with the exception that the applied voltage is varied. This scaling results from the fact that the fractional power deposition producing ionization, excitation and dissociation increases with increasing E/N, especially for ionization due to the generation of more electrons, which are beneficial to CCl_4 dissociation.

Significant improvement in *W* values of CCl_4 degradation can obtained by decreasing the O_2 mole fraction in the gas mixtures, as shown in Fig. 5.8, where two initial CCl_4 concentrations (100 and 1000 ppm) are studied. The removed efficiency is higher for higher CCl_4 concentration due primarily to a more efficient utilization of the reactant intermediates. Two other *W* values have also been used for C_nCl_m. The fist is defined as the deposition energy divided by the sum of C_mCl_n destruction weighed by the number of C atoms, the second is the number of Cl atoms removed, and normalized by 1 or 4 (the number of C or Cl atoms in CCl_4),

$$W^{C}_{C_mCl_n} = \frac{E_{\text{deposition}}}{\sum_i [N_i (C_mCl_n \cdot m]_{\text{initial}} - \sum_i [N_i (C_mCl_n \cdot m]_{\text{final}}}, \tag{5.33}$$

$$W^{Cl}_{C_mCl_n} = \frac{E_{\text{deposition}}}{\sum_i [N_i (C_mCl_n \cdot n/4]_{\text{initial}} - \sum_i [N_i (C_mCl_n \cdot m/4]_{\text{final}}}. \tag{5.34}$$

These *W* values are also shown in Fig. 5.8. It is seen that W_{CCl_4}, $W^{C}_{C_mCl_n}$, and $W^{Cl}_{C_mCl_n}$ are almost the same whenever the O_2 mole fraction is greater than the CCl_4 mole fraction. This indicates that almost all the C and Cl atoms initially constrained CCl_4 and which are remediated do not go into the generation of other C_nCl_m molecules. Decreasing the O_2 mole fraction decreases the loss of electron attachment to O_2 and also increases the probability of other channels to decompose CCl_4 by Ar^+, Ar^*, and Ar** [Reactions (5.8) and (5.9)]. However, in very low O_2 concentrations, the fragments of decomposed CCl_4 can recombine to regenerate CCl_4 and also form other C_mCl_n (e.g., C_2Cl_6). We see that the three *W* values increases with decreasing O_2 when the mole fraction of O_2 is less than that of CCl_4. This trend is highlighted by $W^{C}_{C_mCl_n}$, which denotes that the C atoms initial bound in CCl_4 convert to other C_nCl_m.

5.5 Effects of H_2O on CCl_4 Remediation

In the presence of H_2O, the chemistry reactions are more complicated. The reactions to be considered in this case increase to a total of 316 from the previous set of 170. We look at systems of $Ar/O_2/H_2O/CCl_4$ = 79.9/20-X/X/0.1. Conditions otherwise are the same as the standard case.

The inclusion of H_2O influences the amounts and spatial distribution of electrons, ion and radicals. The resulting decrease in initial O_2 to accommodate the H_2O addition affects the production of electrons since there is a larger electron attachment to H_2O than to O_2 in the process of dielectric barrier discharges:

$$e + H_2O \rightarrow OH + H^-, \qquad k = 2.52\times10^{-10}\ \text{cm}^3\ \text{s}^{-1}, \qquad (5.35)$$

$$e + O_2 \rightarrow O + O^-, \qquad k = 5.31\times10^{-11}\ \text{cm}^3\ \text{s}^{-1}, \qquad (5.36)$$

where rate coefficients are shown for $E/N = 7.5 \times 10^{-16}$ V cm^2. Consequently, this could lead to the decrease in the decomposition of CCl_4 from electron attachment. Cl^- densities for H_2O mole fractions of 0.0, 10^{-2}, and 7×10^{-2} at 30 ns are shown in Fig. 5.9. The production of Cl^- decreases with increasing H_2O concentrations. This change, however, is not significant because the electron attachment to CCl_4 still dominates.

In the presence of H_2O, there is a significant change in the CCl_4 initial dissociation from charge transfers of Ar^+, O_2^+, and H_2O^+. Ar^+ is rapidly consumed by O_2

and H_2O to generate O_2^+ and H_2O^+ because O_2 and H_2O densities are higher than CCl_4. Though O_2^+ and H_2O^+ also cause the decomposition of CCl_4, they are more quickly completed by H_2O,

$$H_2O + O_2^+ + M \rightarrow O_2^+\cdot H_2O + M, \qquad k = 2.5\times10^{-28}\ \mathrm{cm^6\ s^{-1}} \tag{5.37}$$

$$H_2O + H_2O^+ + M \rightarrow H_3O^+ + OH + M, \qquad k = 2.5\times10^{-28}\ \mathrm{cm^6\ s^{-1}}. \tag{5.38}$$

$O_2^+\cdot H_2O$ rapidly reacts with H_2O to produce H_3O^+, and H_3O^+ further reacts with H_2O to generate $H_3O^+\cdot H_2O$,

$$H_3O^+ + H_2O + M \rightarrow H_3O^+\cdot H_2O + M, \qquad k = 5.0\times10^{-27}\ \mathrm{cm^6\ s^{-1}}. \tag{5.39}$$

However $H_3O^+\cdot H_2O$ is unreactive towards CCl_4. The primary charged species in the inner core of microdischarge are decomposed of Cl^- and $H_3O^+\cdot H_2O$, as shown in Fig. 5.10 for 1% mole fraction of H_2O, whereas the dominant charged species are Cl^- and CCl_3^+ in the absence of H_2O.

The CCl_3^+ density distribution in microsdischarges as a function of mole fraction of H_2O is shown in Fig. 5.11. It is seen that a small amount of H_2O considerably reduces the CCl_3^+ the density. A significant increase of the *W* value of CCl_4 (less efficient) results from increasing the water content in the gas mixture as shown in Fig. 5.12. The dominant chlorine-containing products after the discharge are similar to those in Ar/O_2 mixture, with the exception of the presence of HCl. For a 1% mole fraction of water vapor, the Cl atoms that were initially bound in CCl_4 are converted to primary products in the following proportions: $COCl_2$, 46.3%; ClO, 45.3%; Cl_2, 3.0%; HCl, 4.1%.

5.6 Concluding Remarks

The remediation of CCl_4 in dielectric barrier discharges has been theoretically investigated. We found that that in an Ar/O_2 gas mixture the dissociative charge and excited transfers from O_2^+, Ar^+, Ar^*, and Ar^{**} to CCl_4 contribute the initial decomposition of CCl_4 though the dissociative electron attachment of CCl_4 plays the primary role. Decreasing the O_2 mole fraction effectively decreases the *W* value of CCl_4 (more efficient). When the mole fraction of O_2 is approximately that of CCl_4, the best efficiency is obtained. The removal efficiency increases with higher applied voltage and smaller dielectric capacitance. The fractional conversion of CCl_4 to products by DBDs is fairly efficient for large concentrations of CCl_4. Primary products of remediation for dry mixtures are $COCl_2$, ClO, and Cl_2 with a small amount of CO and CO_2. A significant decrease in removal efficiency is found in wet mixtures largely due to the interception of O_2^+ and H_2O^+ by H_2O. In mixtures containing H_2O, HCl is also a product of the DBD operation.

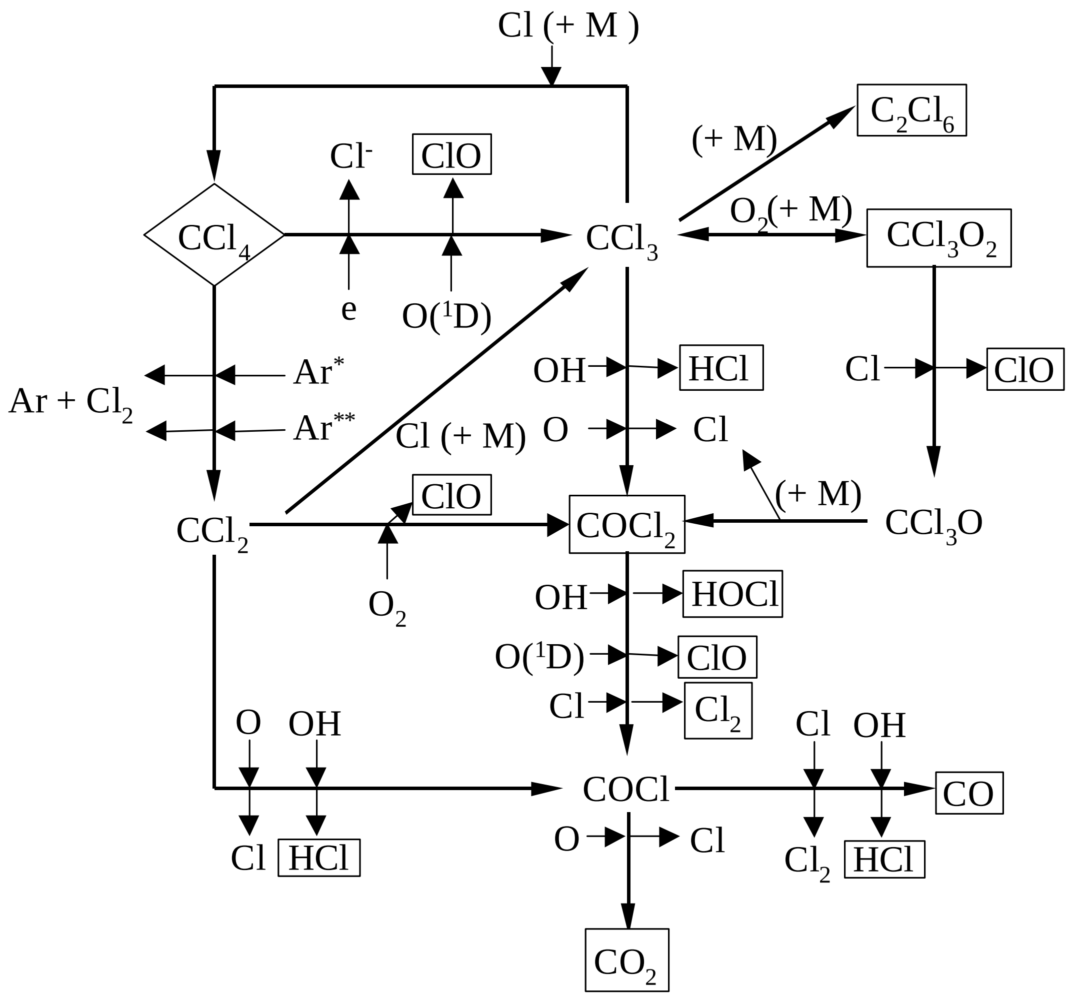

Fig. 5.1 Dominant reaction pathways in the plasma decomposition of CCl_4 in Ar/O_2 gas mixture. The initial CCl_4 is shown by a diamond. The major products are boxed.

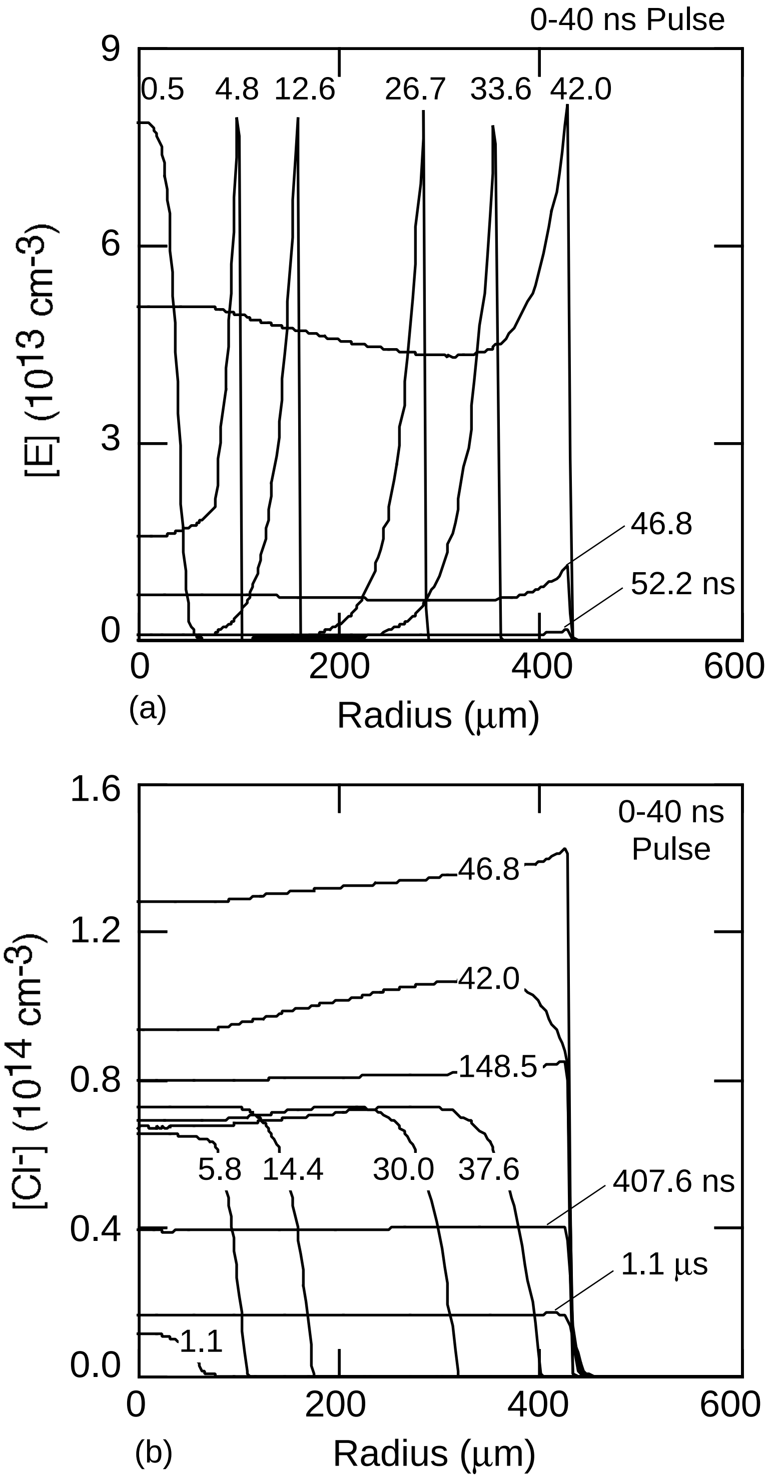

Fig. 5.2. Charged particle densities for a microdischrge in Ar/O_2/CCl_4 = 79.9/20/0.1: (a) electron density, (b) Cl^- density, (c) O^- density, (d) O_2^- density, (e) Ar^+ density, (f) Ar_2^+ density, (g) O_2^+ density, and (h) CCl_3^+ density The curves are labeled with their time after application of voltage in ns unless noted otherwise.

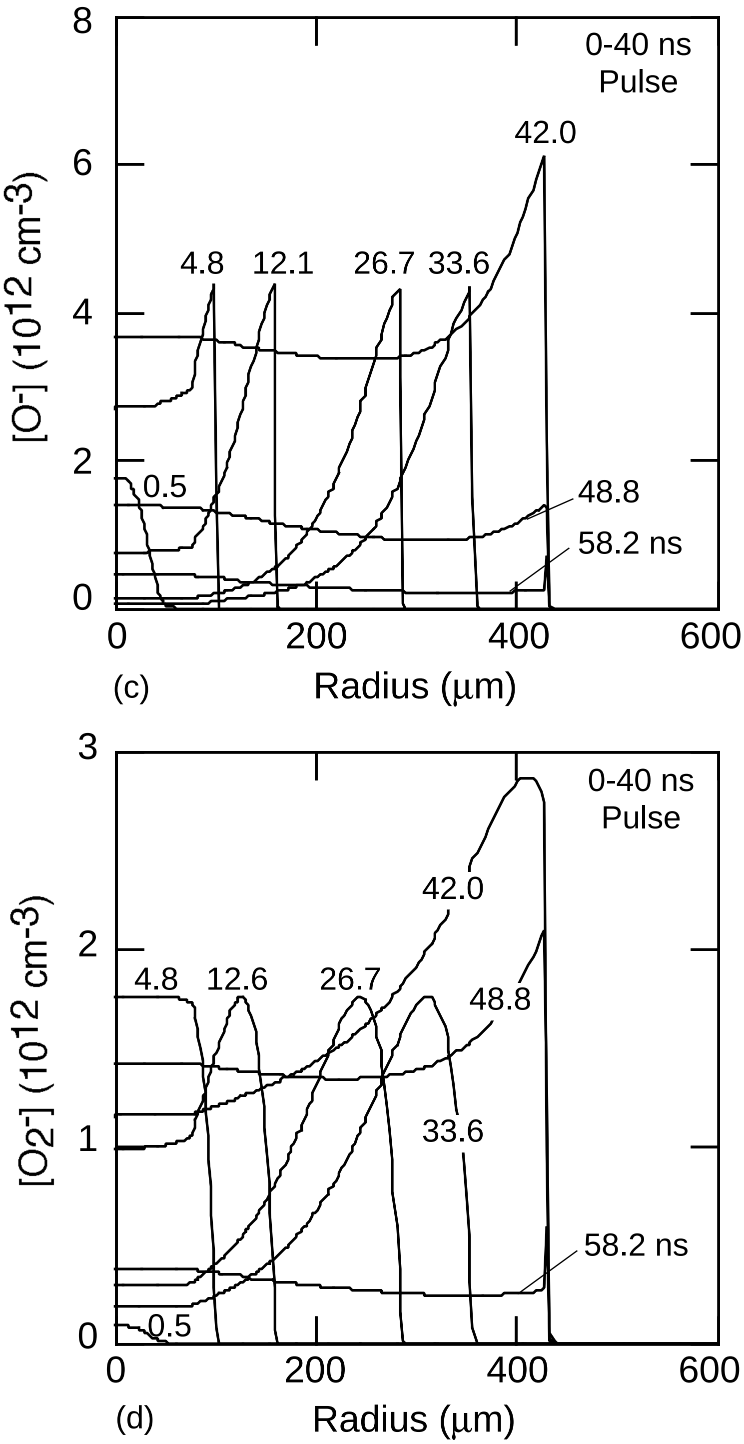

Fig. 5.2. Continued.

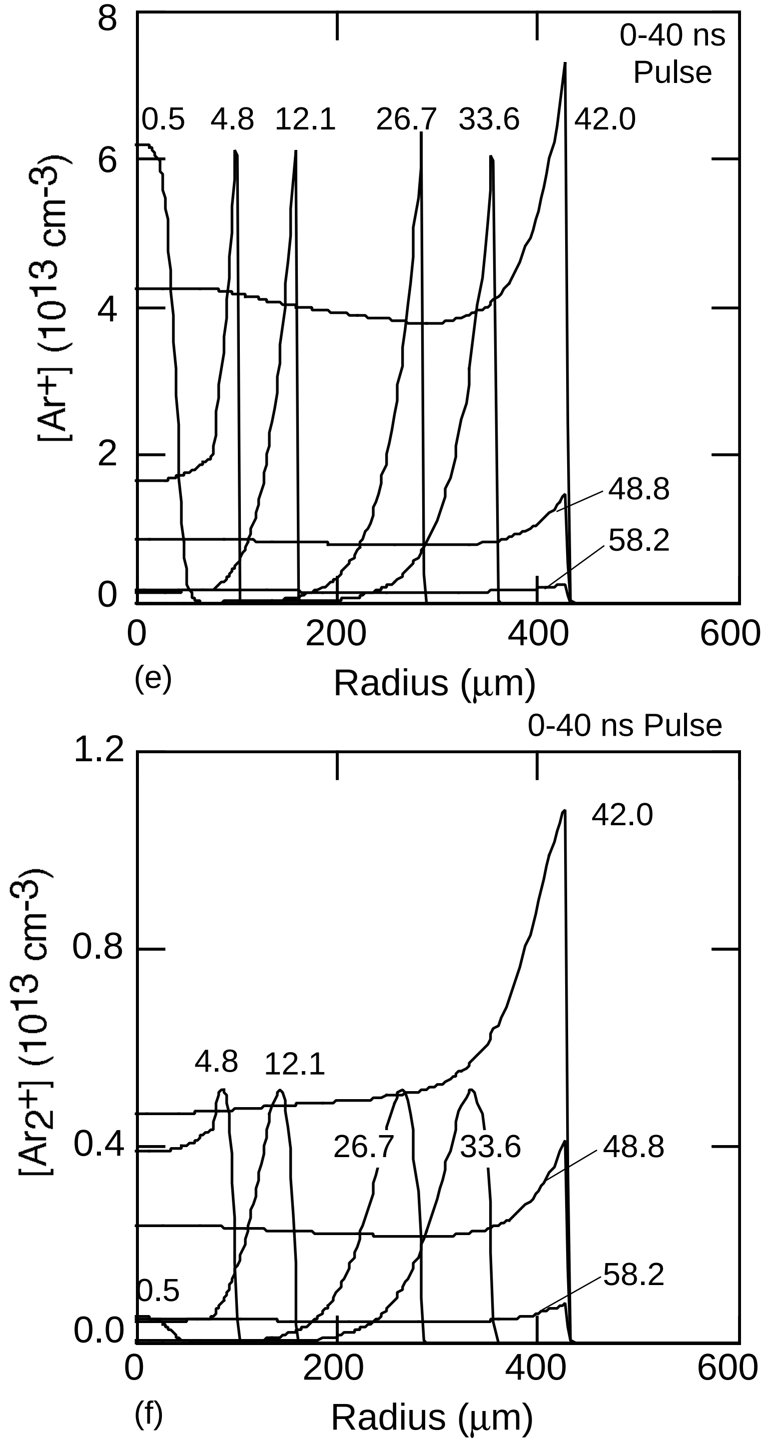

Fig. 5.2. Continued.

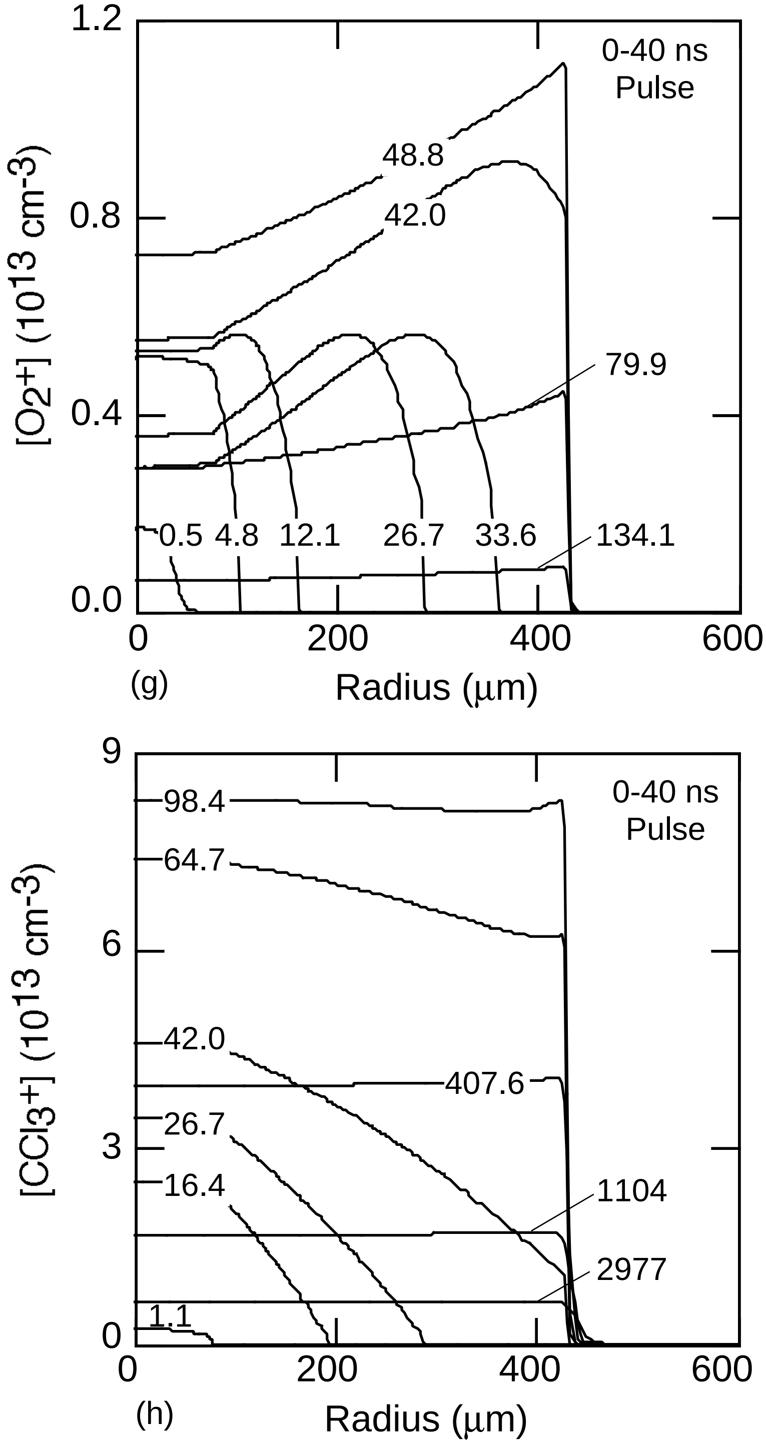

Fig. 5.2. Contined.

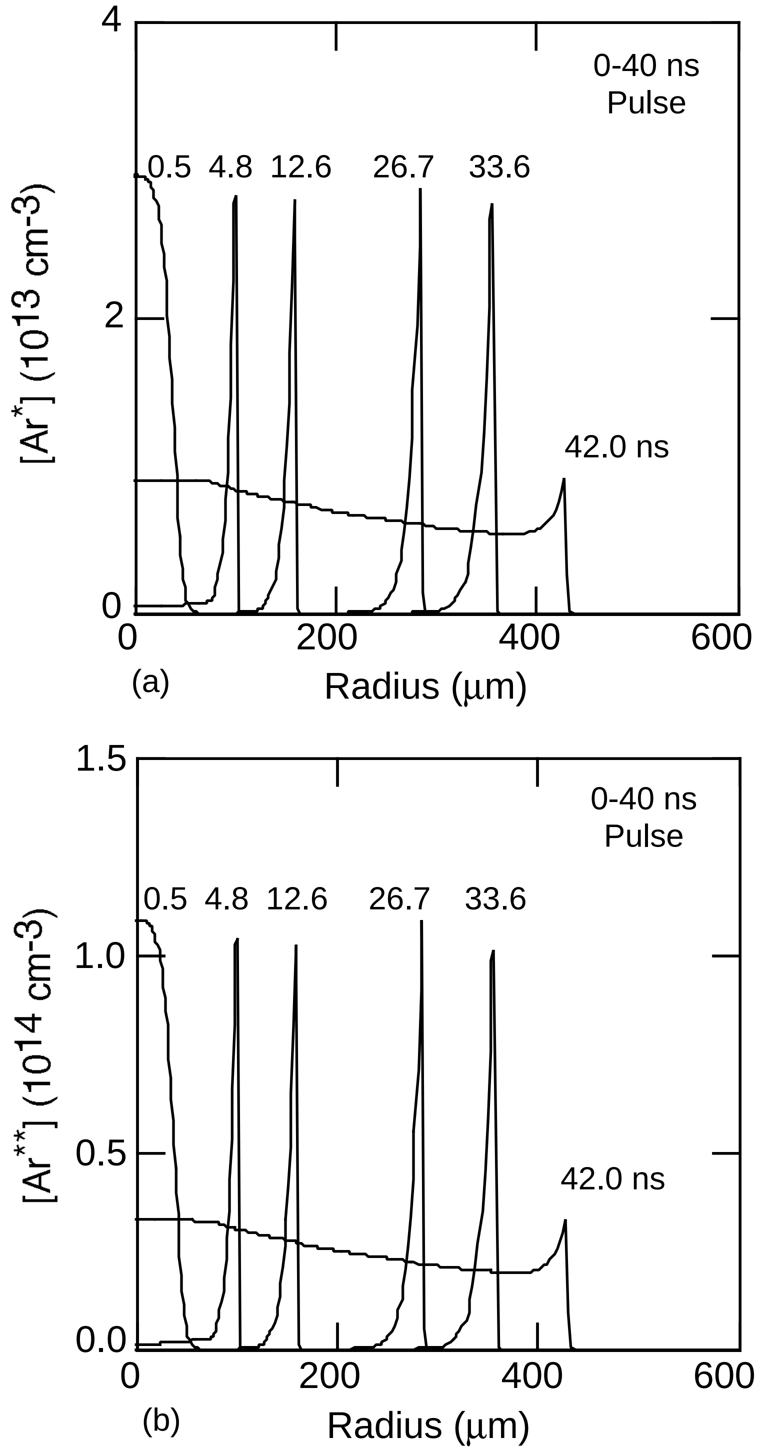

Fig. 5.3. (a) Ar* density, (b) Ar** density, (c) O(^{1}D) density and (d) O density for the conditions of Fig. 5.2. The excited state species, Ar* and Ar*, lead to the decomposition of CCl_4 by the excitation transfer. CCl_4 is almost not reacted with O but is decomposed by O(^{1}D). The curves are labeled with their time after application of voltage (ns).

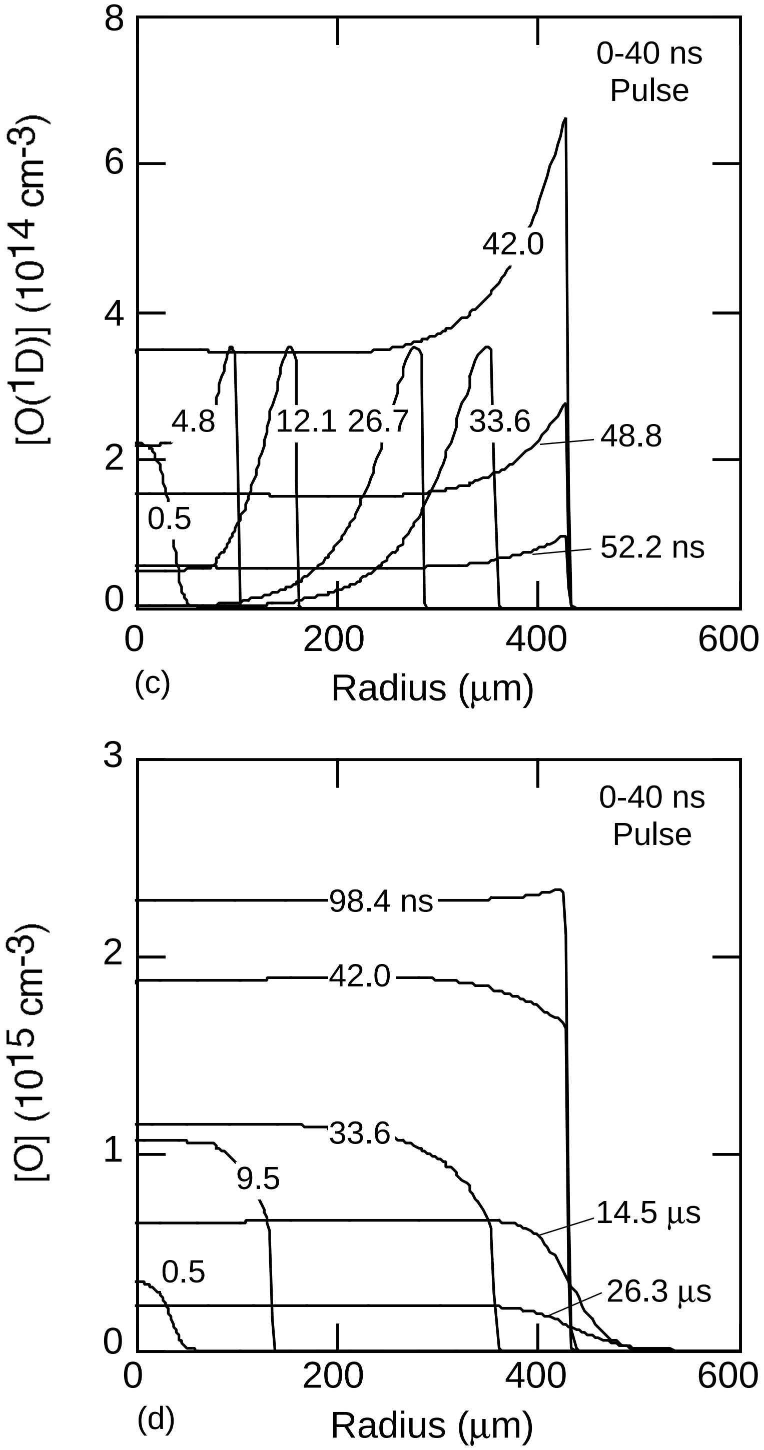

Fig. 5.3. Continued.

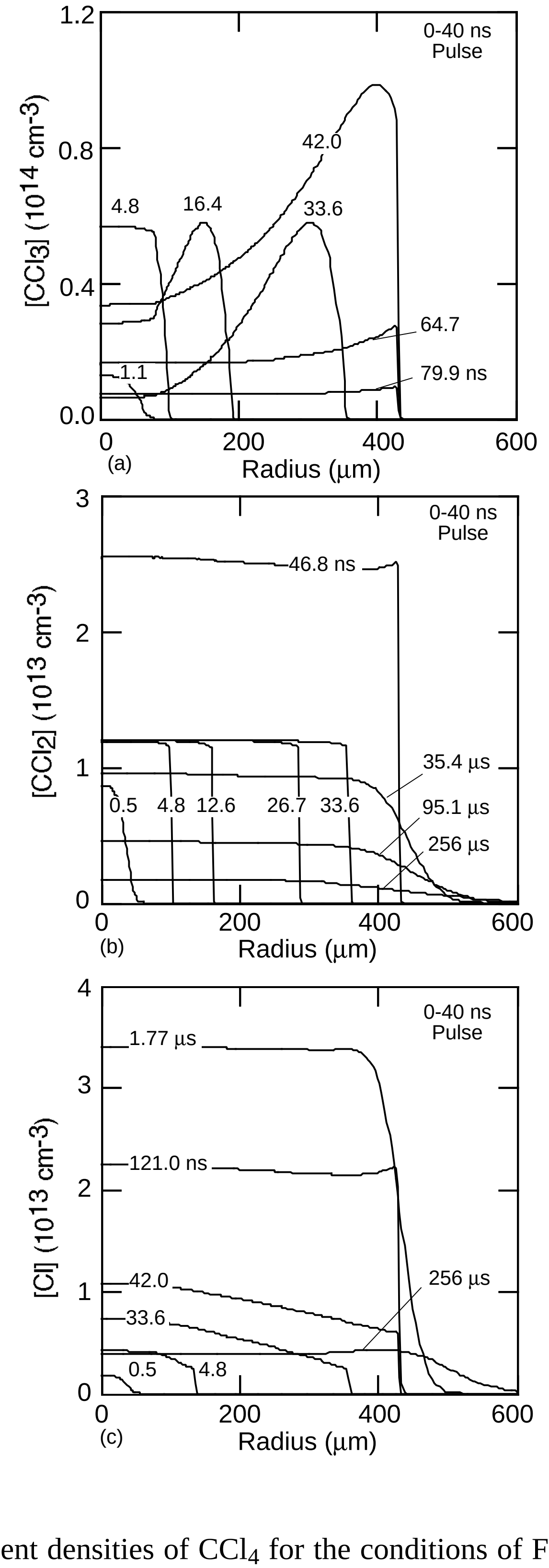

Fig. 5.4. Primary fragment densities of CCl_4 for the conditions of Fig. 5.2: (a) CCl_3 density, (b) CCl_2 density, and (c) Cl density. The CCl_3 radicals are scavenged rapidly by O_2 while the CCl_2 density slowly decreases due to a slow rates by O, Cl, and O_2. The Cl density continues to increase until the Cl^- ions are exhausted at ≈ 1.8 μs. The curves are labeled with their time after application of voltage in ns unless noted otherwise.

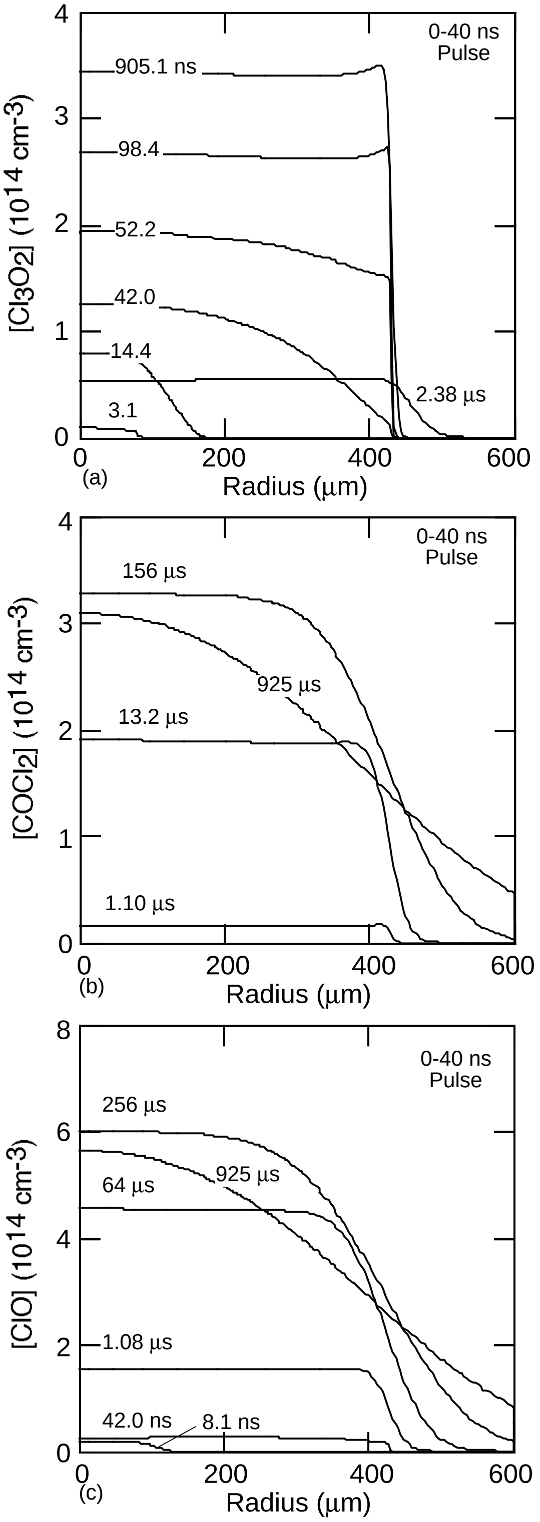

Fig. 5.5. Primary CCl_4 oxidized species densities for the conditions of Fig. 5.2: (a) CCl_3O_2 density, (b) $COCl_2$ density, and (c) ClO density. The CCl_3O_2 density has a peak at 0.9 µs, and then decreases with time primarily due to the reactions involving Cl and itself. The $COCl_2$ and ClO density continue to increase until 156 µs and 256 µs, respectively, and then decrease due to diffusing out to large radii.

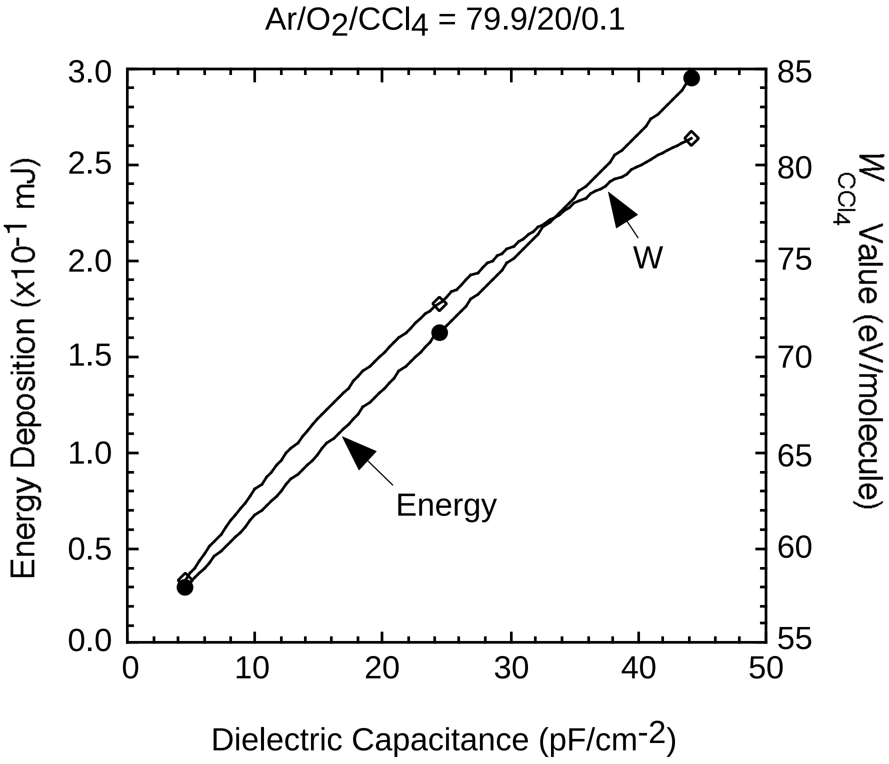

Fig. 5.6. Energy deposition and W_{CCl_4} value as a function of dielectric capacitance. The energy deposition linearly increases with increasing the dielectric capacitance. But the *W* value decreases with increasing the dielectric capacitance primarily due to a less efficient utilization the reactant intermediates.

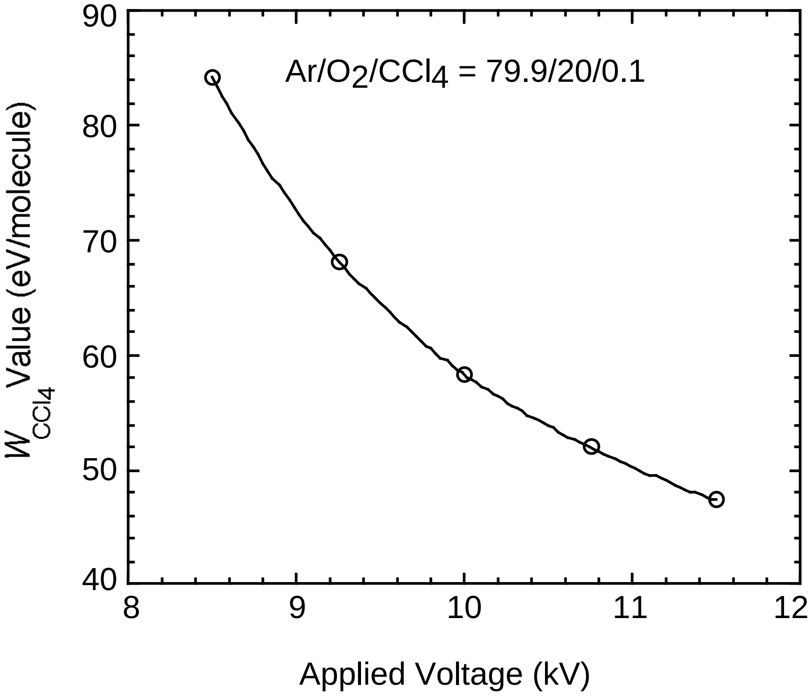

Fig. 5.7. W_{CCl_4} value as a function of applied voltage. The *W* value of CCl_4 decreases with increasing applied voltage due primarily to more efficient production of electrons and ions.

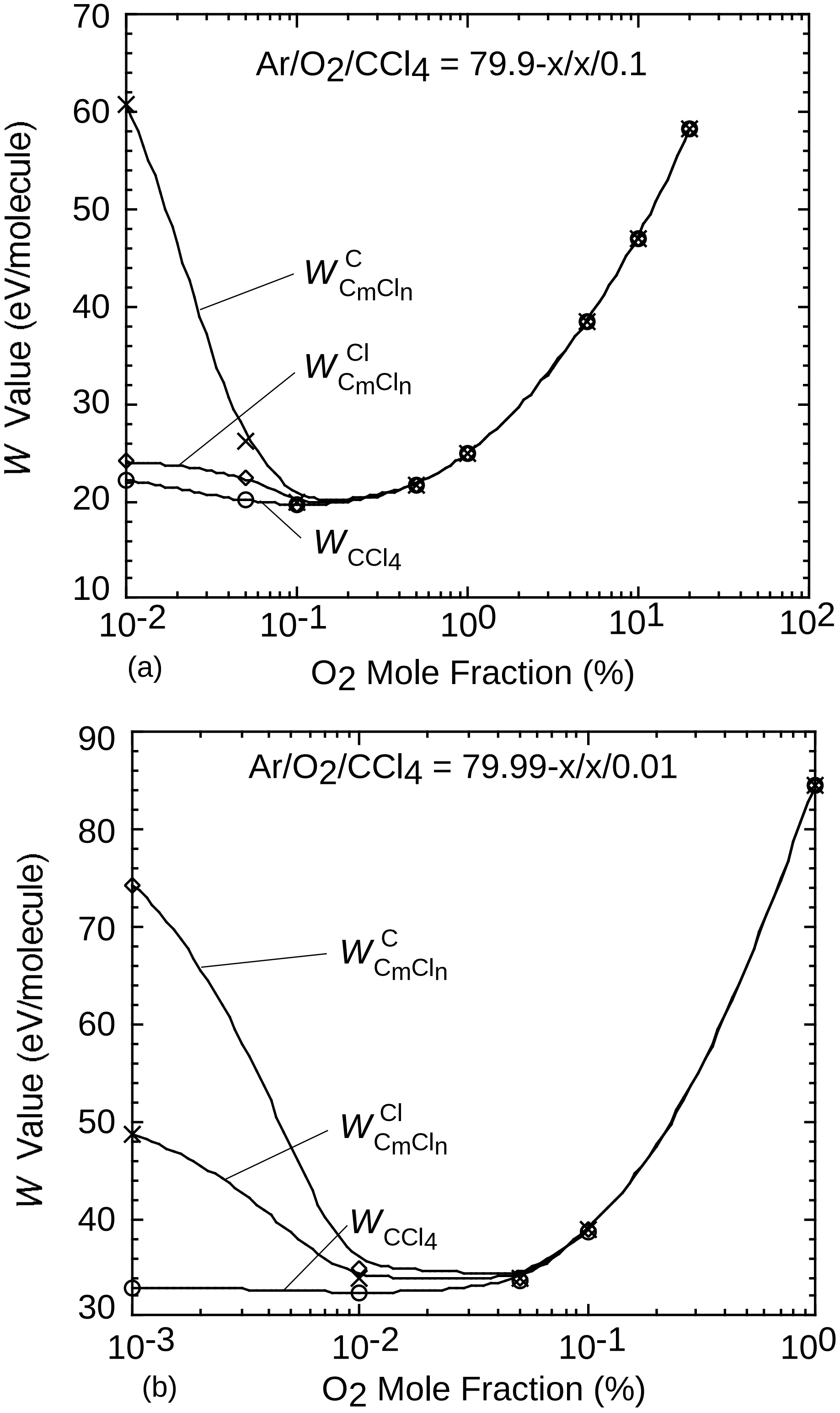

Fig. 5.8. W_{CCl_4}, $W^{C}_{C_mCl_n}$, and $W^{Cl}_{C_mCl_n}$ values as a function O_2 mole fraction. (a) CCl_4 = 0.1% (1000 ppm) and (b) CCl_4 = 0.01% (100 ppm). The removed efficiency is higher for higher CCl_4 concentration primarily due to a more efficient utilization of the reactant intermediates. The best efficiency is given when the mole fraction of $O_2 \approx (1-10)\ CCl_4$.

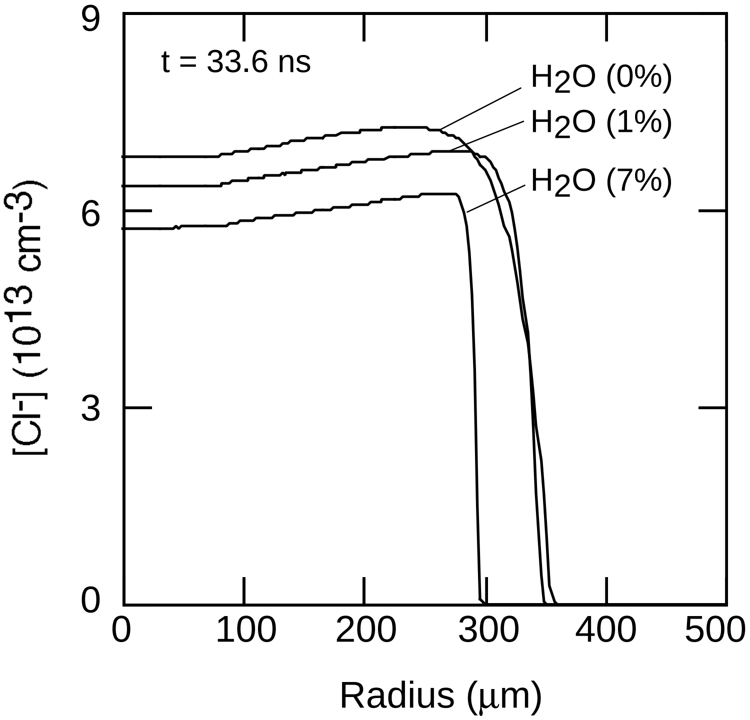

Fig. 5.9. Cl^- densities at 33.6 ns for micodischarges with varying H_2O mole fraction. The Cl^- densities decrease as increasing H_2O mole fraction. This change, however, not being really appreciable, lies with in teen percent ranges.

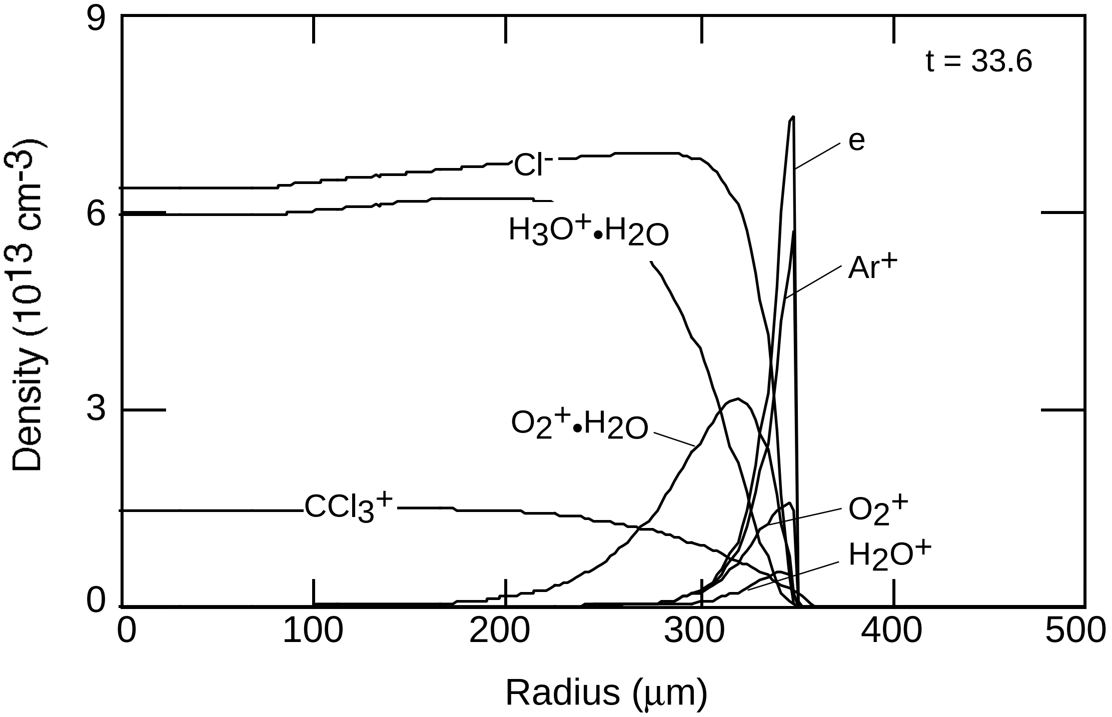

Fig. 5.10. Ion densities at 33.6 ns for micordischarge in $Ar/O_2/H_2O/CCl_4$ = 77.9/19/1/0.1. The core of the microdischarge is essentially a negative ion-positive ion plasma (mainly by Cl^- and $H_3O^+ \bullet H_2O$ plasma).

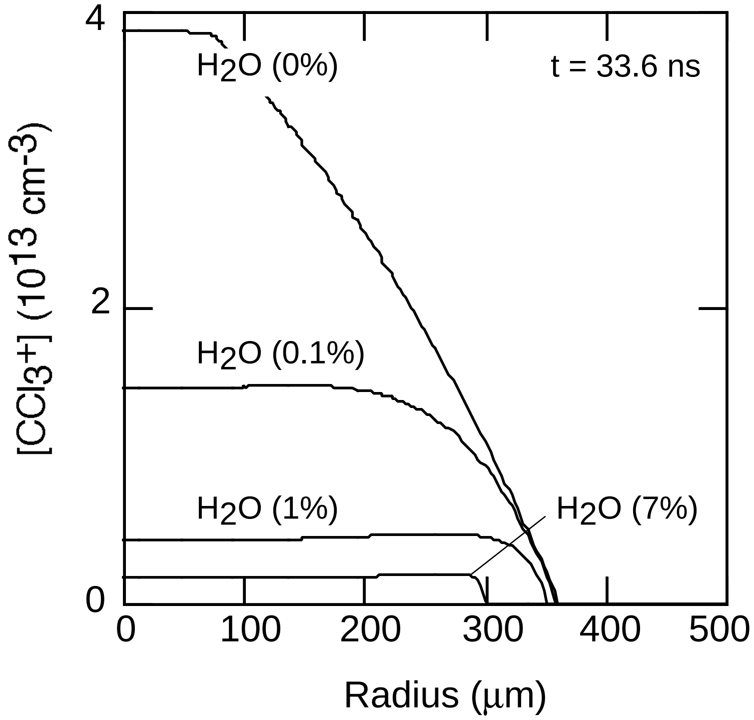

Fig. 5.11. CCl_3^+ densities at 33.6 ns for micodischarges with varying H_2O mole fraction. The CCl_3^+ densities decrease considerably with increasing H_2O mole fraction.

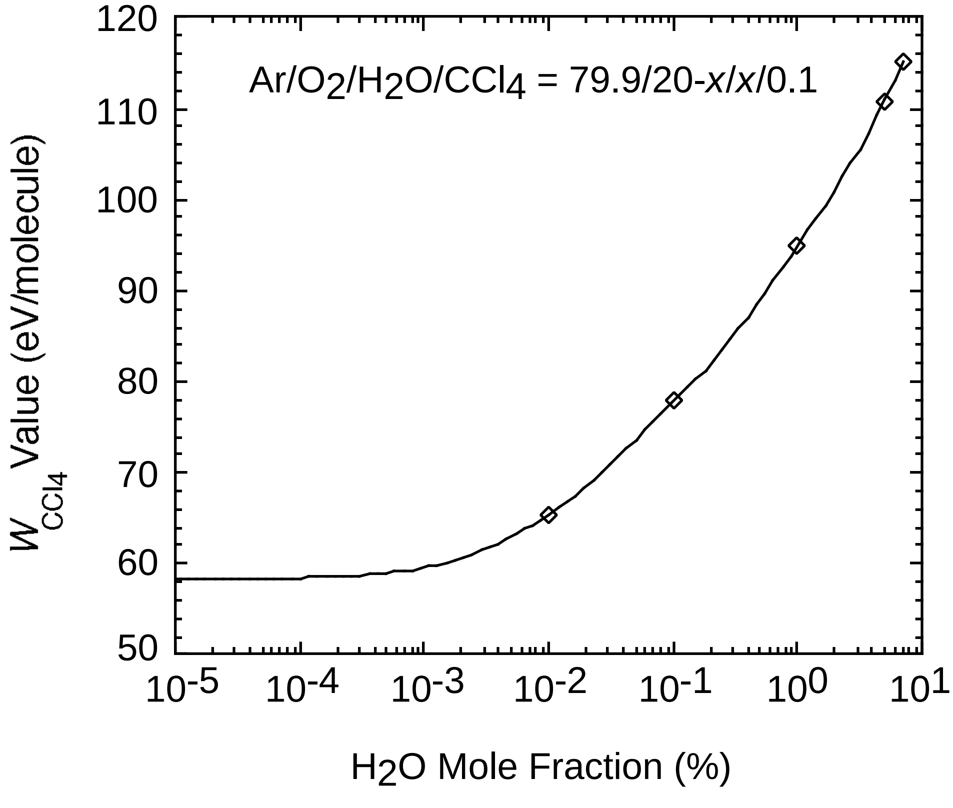

Fig. 5.12. W_{CCl_4} value as a function of water content in the gas mixture. W value of CCl_4 (less efficient) significantly increases with increasing H_2O percentage due largely to the less contribution of ion dissociative transfer from the Ar^+ and O_2^+ to CCl_4.

5.7 References

[1] W. B. DeMore, S. P. Sander, D. M. Golden, M. J. Molina, R. F. Hampson, M. J. Kurylo, C. J. Howard, and A. R. Ravishankara, JPL Publication **90-1**, 1 (1990).

[2] P. L McCarty and E. Bouwer, J. Appl. Environ. Mcrobiol. **45**, 1286 (1983).

[3] I. Barnes, V. Bastian, K. H. Becker, E. H. Fink, and F. Zabel, J. Atmos. Environ. **16**, 545 (1982).

[4] D. D. Davis, J. F. Schmidt, C. M. Neeley, and R. J. Hanranhan, J. Phys. Chem. **79**, 11 (1975).

[5] *Handbook of Environmental Fate and Exposure Data for Organic Chemicals*, edited by M. Sittig (Noyes Publishers, Park Ridge, NJ, 1991), Vol. 1.

[6] M. Tezuka, K. Momiyama, T. Edano, and S. Okada, J. Inorg. Biochem. **42**, 1 (1991).

[7] P. H. Taylor, B. Dellinger, and D. A. Tirey, Int. J. Chem. Kinet. **23**, 1051 (1993).

[8] L. J. Matheson and P. G. Tratnyek, Enviro. Sci. Technol. **28**, 2045 (1994).

[9] L. A. Rosocha, G. K. Anderson, L. A. Bechtold, J. J. Coogan, H. G. Hech, M. Kang, W. H. McCulla, R. A. Tennant, and P. J. Wantuck, in *Nonthermal Plasma Techniques for Pollution Control*, edited by B. N. Penetrante and S. E. Schultheis (Springer, Berlin, 1993), Part B, pp. 281.

[10] L. Bromberg, D. R. Cohn, R. M. Patrick, and P. Thomas, Phys. Lett. A **173**, 293 (1993).

[11] B. M. Penetrante, M. C. Hsiao, J. N. Bardsley, B. T. Merritt, G. E. Vogtlin, P. H. Wallman, A. Kuthi, C. P. Burkhart, and J. R. Bayless, Phys. Lett., **209**, 69 (1995).

[12] R. G. Tonkyn, S. E. Barlow, and T. M. Orlando, J. Appl. Phys., **79**, 3451 (1996).

[13] W. Niessen, O. Wolf, R. Schruft, and M. Neiger, J. Phys. D.: Appl. Phys., **31**, 542 (1998).

[14] J. J. Russell, J. A. Seetula, D. Gutman, F. Danis, F, Caralp, P. D. Lightfoot, R. Lesclaux, C. F. Melius, and S. M Senkan, J. Phys. Chem. **94**, 3277 (1990).

[15] R. Atkinson, D. L. Baulch, R. A. Cox, R. F. Hampson Jr., J. A. Kerr, and J. Troe, J. Phys. Chem. Ref. Data **21**, 1125 (1992).

6. MODELING EXCIMER EMISSION IN DIELECTRIC BARRIER DISCHARGES

6.1 Introduction

UV radiation, with quantum energies in the range of 3-10 eV, has a number of applications because these energetic photons are capable of splitting most chemical bonds. Examples include sterilization [1, 2], lithography [3, 4], degradation of organic compounds in flue gases and in water [5, 6], and UV-enhanced chemical vapor deposition [7-9]. All of these applications require efficient UV sources of high power that preferably radiate in a narrow selectable wavelength range. Traditional intense UV sources, such as high-pressure mercury, Xe-arc, and flash lamps, emit in a broad spectral range from 200 nm to several microns. Conventional narrow-bandwidth UV sources such as low-pressure mercury and rare-gases resonance-line lamps have small UV intensities. Though excimer lasers can be used as sources of intense narrow-bandwidth UV radiation, they are expensive in capital and operating costs, and provide only a small beam. In addition, incoherent UV sources have shown other advantages over UV lasers in photodeposition for metal, dielectric, or semiconductor layers [7, 10, 11]. For example incoherent excimer UV sources produced smooth continuous films while excimer laser deposition resulted in discontinuous grainy Pd films [7].

Excimers are bound excited states of molecules that do not have a stable molecule ground state. There are a number of methods for generating excimers, such as dielectric barrier discharges, coronas, high-energy beams, x-rays, α-particles, protons, heavy ions, synchrotron radiation, and microwave discharges [12-18]. Of these, DBDs are potentially more attractive due to their simplicity, stability, low cost, high power, and easy maintenance. Depending on the gas mixture, many different excimers could be generated in dielectric barrier discharges, which include rare gas dimers such as Ar_2^* (126 nm), Kr_2^* (146 nm), and Xe_2^* (172 nm), rare gas-halide complex such as ArF^* (193 nm), KrF^* (249 nm), XeF^* (354 nm), $ArCl^*$ (175 nm), $KrCl^*$ (222 nm), $XeCl^*$ (308 nm), $ArBr^*$ (165 nm), $KrBr^*$ (207 nm), $XeBr^*$ (283 nm), KrI^* (190 nm), and XeI^* (253 nm), and halogen dimers such as F_2^* (158 nm), Cl_2^* (259 nm), Br_2^* (289), and I_2^* (342 nm) [19-26]. Each emits radiation in a narrow wavelength band of the vacuum ultraviolet (VUV) or UV part of the spectrum.

In this chapter, the dynamics of generating radiation and excimer formation for mixtures of chlorine and xenon gases in dielectric barrier discharges will be discussed. The 1-D PCHM has been used to determine operating parameters that optimize the efficiency of generating examer radiation. Section 6.2 is an overview of the formation of excimers in Xe/Cl_2 mixtures. In Section 6.3, we present the microdischarge dynamics and the spatial dependencies of excimer and photon generation. We discuss the optimization of discharge conditions for excimer and photon generation in Section 6.4. Concluding remarks are in Section 6.5.

6.2 Formation of Excimers

The dominant reaction pathways for generating the major four excimers, $XeCl^*$ (λ = 308 nm), Xe_2^* (λ = 172 nm), Xe_2Cl^* (λ = 490 nm), and Cl_2^* (λ = 259 nm) in Xe/Cl_2 mixtures are shown in Fig. 6.1. Species and reaction rate coefficients for these and other processes are listed in Appendices A and B. Among these excited species, $XeCl^*$ is expected to be the primary excimer for Xe/Cl_2 gas mixtures. A simplified potential diagram of xenon chloride is shown in Fig. 6.2. The ground state is only weakly covalently bounded and correlates to the ground state ^{1}S xenon and ^{2}P chlorine. The three closely spaced excited states ($B_{1/2}$, $C_{3/2}$, and $D_{1/2}$) are ionically bonded and are generated by the ^{2}P xenon positive ion and ^{1}S chloride negative ion. There are different transitions from the excited states and to the ground states: $B_{1/2} \rightarrow X_{1/2}$, $B_{1/2} \rightarrow A_{1/2}$, $C_{3/2} \rightarrow A_{3/2}$, $D_{1/2} \rightarrow A_{1/2}$, and $D_{1/2} \rightarrow X_{1/2}$. Of these, the $B_{1/2} \rightarrow X_{1/2}$ transition is the strongest. Excimers in their higher-level excited states can undergo radiationless transitions to $B_{1/2}$, and the initial and final pσ orbits (B, X) that the electron occupies have the largest overlap of any of the valence orbits [27]. For simplicity, we group all these excited states into a simple species $XeCl^*$. The reaction mechanisms for the generation of $XeCl^*$ precursors involve electron impact ionization, excitation, and dissociative attachment with the feedstock gas compounds (Xe and Cl_2) as follows:

$$e + Xe \rightarrow 2\,e + Xe^+ \qquad k = 3.48\times10^{-10}\ \mathrm{cm^3\ s^{-1}} \tag{6.1}$$

$$e + Xe \rightarrow e + Xe^* \qquad k = 7.76\times10^{-10}\ \mathrm{cm^3\ s^{-1}} \tag{6.2}$$

$$e + Xe \rightarrow e + Xe^{**} \qquad k = 9.87\times10^{-10}\ \mathrm{cm^3\ s^{-1}} \tag{6.3}$$

$$e + Cl_2 \rightarrow e + Cl_2^* \qquad k = 5.61\times10^{-10}\ \mathrm{cm^3\ s^{-1}} \tag{6.4}$$

$$e + Cl_2 \rightarrow Cl + Cl^- \qquad k = 2.23\times10^{-10}\ \mathrm{cm^3\ s^{-1}} \tag{6.5}$$

where the rate coefficients listed for electron-impact processes were obtained from the solution of Boltzmann's equation at $E/N = 2\times10^{-15}$ V cm^2, Xe^* represents 6*s* states, Xe^{**} represents 6*s′* and 6*p*, and Cl_2^* represents Π_g–4*d*. Most of the $XeCl^*$ is produced by three-body recombination of Xe^+ and Cl^-, and the harpooning reaction in which the excited Xe species transfers its loosely bound outermost electron to the chorine molecule to form an electronically excited state of $XeCl^*$.

$$Xe^+ + Cl^- \ (+ M) \rightarrow XeCl^* \ (+ M) \qquad k = 2.00\times10^{-6}\ \mathrm{cm^3\ s^{-1}} \tag{6.6}$$

$$Xe^* \ (\text{or } Xe^{**}) + Cl_2 \rightarrow XeCl^* + Cl \qquad k = 7.20\times10^{-10}\ \mathrm{cm^3\ s^{-1}} \tag{6.7}$$

where the rate coefficient of Eq. (6.6) is shown for pressure = 0.6 atm. Other reactions involving Xe_2^+, Xe_2^*, and Cl_2^*, which also generate $XeCl^*$, include

$$Xe^+ + Xe + M \rightarrow Xe_2^+ + M \qquad k = 2.50\times10^{-31}\ \mathrm{cm^6\ s^{-1}} \tag{6.8}$$

$$Xe^* \ (\text{or } Xe^{**}) + Xe + M \rightarrow Xe_2^* + M \qquad k = 5.00\times10^{-32}\ \mathrm{cm^6\ s^{-1}} \tag{6.9}$$

$$Xe_2^+ + Cl^- \rightarrow XeCl^* + Xe \qquad k = 2.00\times10^{-6}\ \mathrm{cm^3\ s^{-1}} \tag{6.10}$$

$$Xe_2^* + Cl_2 \rightarrow XeCl^* + Xe \qquad k = 5.00\times10^{-10}\ \mathrm{cm^3\ s^{-1}} \tag{6.11}$$

$$Cl_2^* + Xe \rightarrow XeCl^* + Cl \qquad k = 1.50\times10^{-10}\ \mathrm{cm^3\ s^{-1}}. \tag{6.12}$$

The $XeCl^*$ excimers have a short radiation lifetime (40 ns), emitting a 308-nm UV photon and decomposing to Xe and Cl. They can also be quenched by collisions with third bodies or react with Xe to form the trimer Xe_2Cl^*.

$$XeCl^* \rightarrow Xe + Cl + h\nu \ (308\ \mathrm{nm}) \qquad k = 2.50\times10^{7}\ \mathrm{s^{-1}} \tag{6.13}$$

$$XeCl^* + Xe \rightarrow 2\ Xe + Cl \qquad k = 3.20\times10^{-12}\ \mathrm{cm^3\ s^{-1}} \tag{6.14}$$

$$XeCl^* + Cl_2 \rightarrow Xe + Cl + Cl_2 \qquad k = 8.11\times10^{-11}\ \mathrm{cm^3\ s^{-1}} \tag{6.15}$$

$$XeCl^* + 2\ Xe \rightarrow Xe_2Cl^* + Xe \qquad k = 7.30\times10^{-31}\ \mathrm{cm^6\ s^{-1}} \tag{6.16}$$

$$XeCl^* + Xe + Cl_2 \rightarrow Xe_2Cl^* + Cl_2 \qquad k = 5.30\times10^{-31}\ cm^6\ s^{-1} \qquad (6.17)$$

Other excimers, Xe_2^* (formed by Eq. 6.9), Xe_2Cl^* [formed by Eqs. (6.16) and (6.17)] and Cl_2^* [formed by Eq. (6.4)] spontaneously emit 172 nm, 490 nm, and 259 nm photons, respectively.

6.3 Spatial Dependencies in Excimer Generation

In this section, we consider the dynamics of microdischarges in Xe/Cl_2 mixtures, concentrating on the formation of UV photons, and temporal and spatial dependencies of excimers. A single streamer is examined using the 1-D radially dependent PCHM described in Section 2.2. In the results that follow, the initial seed electron density has a distribution of 20 μm in radius and a 10^9 cm^{-3} peak value, with an ambient temperature of 300 K. The applied voltage is a square pulse with 40 ns duration.

The base case is a gas mixture of Xe/Cl_2 = 99/1 at 0.6 atm gas pressure with the 10 kV pulse. Fig. 6.3 shows the electron density and gap voltage during and following the voltage pulse, whereas primary positive and negative ions are shown in Fig. 6.4. During the voltage pulse, the electron density sharply peaks at the edge of the microdischarge since electrons are rapidly consumed primarily from dissociative attachment to Cl_2. The collapsed gap voltage due to charging of the dielectric leads to lower E/N in the core where the electron attachment is enhanced. [Cl_2 has high rates of electron dissociative attachment ($1.2\times10^{-9} - 1.5\times10^{-9}$ cm^3 s^{-1}) at small electron temperatures (0.1 – 0.2 eV).] Xe^+ also displays a peak at the edge of microdischarge because these ion are quickly consumed by generating the dimer ions Xe_2^+ [Eq. (6.8)], by charge transfer to Cl_2:

$$Xe^+ + Cl_2 \rightarrow Xe + Cl_2^+ \qquad k = 6.0\times10^{-11}\ cm^3\ s^{-1} \qquad (6.18)$$

and by the three-body recombination with Cl^-. The Xe_2^+ and Cl^- density profiles display a less sharp edge than those of Xe^+ and electrons, while the Cl_2^+ density shows a steady decrease with increasing radius.

The neutral excited species Xe^* and Xe^{**}, which are precursors to the generation of $XeCl^*$, also have sharp edges (as does the Xe^+) and have approximately the same densities, as shown in Fig. 6.5. These species are lost primarily by radiative relaxation ($Xe^* \rightarrow Xe$, $k = 3.93\times10^6\ s^{-1}$; $Xe^{**} \rightarrow Xe$, $k = 3.0\times10^7\ s^{-1}$), harpooning reactions [Eq. (6.7)], dimerzation (Eq. 6.9) and Penning ionization:

$$Xe^* \text{ (or } Xe^{**}) + Cl_2 \rightarrow Xe + Cl_2^+ \qquad k = 5.0\times10^{-10}\ cm^3\ s^{-1}. \qquad (6.19)$$

The behavior of $XeCl^*$ and its corresponding photon generation at 308 nm are shown in Fig. 6.6. The formation of the $XeCl^*$ excimer is delayed compared to electron generation due to there being two or three steps required for its formation. The total generation of 308-nm photons is ultimately uniform across the microdischarge. The emissions of other photons (172 nm, 490 nm, and 259 nm emitted by Xe_2^*, Xe_2Cl^*, and Cl_2^* respectively) are shown in Fig. 6.7. The distribution of the total number of these photons appears fairly uniform across the entire microdischarge. The ratios of the total number of 308-nm photons to those at 172 nm, 490 nm, and 259 nm photons are 2.63, 0.99, and 6075.4 respectively. In addition, Xe_2Cl^* displays a long lifetime since its quenching rate is nearly independent of the Xe pressure and only dependent on the Cl_2 density [28]. Cl_2^* has a short lifetime due to a quick consumption by conversion to $XeCl^*$, and Xe_2^* has a lifetime similar to $XeCl^*$.

Electron attachment significantly increases with increasing Cl_2 mole fraction. As a result, the dynamics of the microdischarge can be changed. The results for Xe/Cl_2 = 95/5 with otherwise the same conditions as the base case are shown in Figs. 6.8-6.10. The electron density and gap voltage for different times are shown in Fig. 6.8. The electron density in the core is driven to such a low value during the pulse that there is not an immediate second avalanche in the core at the end of pulse. Instead, after the pulse, the electron density shell propagates towards the center of the microdischarge due to there being high gap voltages in the core. $XeCl^*$ and 308-nm photons are regenerated in the core as the second avalanche moves towards the center, as shown in Fig. 6.9. The total number of 308 nm photons is slightly lower than the base case. However, the generation of 172 nm (Xe_2^*) and 490 nm (Xe_2Cl^*) photons dramatically decreases and the generation of 259 nm photons increases compared to the Xe/Cl_2 =99/1 case, as shown in Fig. 6.10. This trend is due to the fact that Cl_2 is very efficient at quenching Xe_2^* and Xe_2Cl^*, and the higher Cl_2 mole fraction is beneficial to generating Cl_2^*.

6.4 Optimization of Discharge Conditions for Excimer and Photon Generation

The efficiency of UV photon generation in DBDs depends on the dielectric properties, gas composition, gas pressure, and applied voltage. In this section, we describe the consequences of varying these factors for Xe/Cl_2 gas mixtures. In the following discussion, the base case from the last section is used as a starting point. The photon generation efficiency (h_λ) and the time-averaged photon flux (G_λ) for photon wavelength λ are defined as

$$h_l = \frac{E_l \int_0^T dt \int_0^R N_l(t,r) \cdot 2prdr}{\int_0^T dt \int_0^R \mathbf{j}(t,r) \cdot \mathbf{E}(t,r) \cdot 2prdr} \tag{6.20}$$

$$G_l = L_{gap} \cdot f_{appl.} \cdot D_{micro} \cdot \int_0^T dt \int_0^R N_l(t,r) \cdot 2prdr \tag{6.21}$$

where E_l and $N_l(t, r)$ are the photon energy and spontaneous emission density, L_{gap} is the gap spacing between the two electrodes, R is the microdischarge radius and T is the longest decay time of all excimers (5 μs is generally used). The terms $\mathbf{j}$ and $\mathbf{E}$ are the current density and electric field. The terms $f_{appl.}$ and $D_{micro.}$ are the frequency of applied voltage and the microdischarge density. In the following results, $f_{appl.}$ = 1 KHz and $D_{micro.}$ = 100 cm^{-2}, which are typical values for DBDs, are used. Since the 259-ns emission from Cl_2^* is much lower, we only calculate the results of 308 nm, 172 nm, and 490 nm emissions.

We first investigate the outcome of varying the applied voltage amplitude V_0 on photon emission in DBDs. It is known that increasing V_0 increases light emission due largely to increasing energy deposition. The time-averaged fluxes and efficiencies of generation are shown in Fig. 6.11 as a function of the applied voltage. The photon fluxes approximately quadratically increase, with applied voltage reflecting the increase in stored energy. The flux of 308 nm emission is almost equal to that of 490 nm which is coincidental and not “physics.” When the applied voltage magnitude is increased, a higher fraction of power deposition goes into producing excitation and ionization. As a result, the efficiencies of 308 nm and 490 nm generations improve at higher applied voltage. However the efficiency of 172 nm generation has a weaker dependence on the applied voltage since increasing it is rapidly quenched by reactions such as with Cl_2.

The consequences of dielectric capacitance (e_d/L, where e_d = permittivity and L = thickness of the dielectric) on the photon emission fluxes and photon generation efficiencies are shown in Fig. 6.12. With a larger dielectric capacitance, more current is required to charge the dielectric. Therefore, more energy is deposited in the plasma and the corresponding photon fluxes are larger [Fig. 6.12(a)].

The effect of Cl_2 mole fraction on the photon fluxes and generation efficiency are shown in Fig. 6.13. When the Cl_2 mole fraction is larger than 1%, the generation of 308 nm photons is dominant. There is an optimum efficiency for 308 nm generation at $Cl_2 \approx$ 1%. Increasing Cl_2 concetration enhances the ion transfer reaction from Xe^+ to Cl_2 [Eq. (6.18)], which results in consuming more Xe^+, but leads to an increase of Cl^- generation. Both Xe^+ and Cl^- are important precursors forming $XeCl^*$ [via Eq. (6.6)]. However, the fluxes and generation efficiency for 172 nm and 490 nm photons strongly decrease with increasing Cl_2, since Cl_2 can efficiently quench Xe_2^* and Xe_2Cl^*.

We also investigated the consequences of gas pressure on the photon fluxes and efficiencies at the same initial $(E/N)_0 = 3.4\times10^{-15}$ V cm^2 as shown in Fig. 6.14. The emissions of three photons increase with increasing gas pressure due to higher gas density resulting in more UV emission. The efficiencies of 308 nm and 490 nm photon generation are improved at low pressures due to decreased quenching. However the efficiency of 172 nm photon generation is high at high-pressures because three body collisions are more efficient to generate Xe_2^* [Eq. (6.9)].

6.5 Concluding Remarks

Dielectric barrier discharges are a promising technology for high-intensity sources of specific UV and VUV radiation. In this chapter, the microdischarge dynamics in DBDs for Xe/Cl_2 mixtures has been investigated. The emissions from $XeCl^*$, Xe_2^*, and Xe_2Cl^* excimers have been discussed for a variety of operating conditions. The electron density shows a shell expansion during pulse due to dielectric charging and attachment of Cl_2 at small radii at lower *E/N*. The strong attachment for high Cl_2 concentration (e.g., 5%) leads to shell propagation to smaller radii after the pulse. Energy deposition, photon generation, and efficiency are higher when using larger applied voltage. Increasing capacitance of the dielectric increases the energy deposition and total light generation, but decrease the efficiency of photon generation. The Cl_2 has an optimum value for the efficiency of 308 nm photon generation. Lower gas pressure with a fixed applied voltage can lead to an intense discharge due to higher *E/N*, resulting in an improvement in the efficiencies of 308 nm and 490 nm photon generation. However, 172 nm photon generation favors a higher-pressure condition since Xe_2^* is formed via a three body reaction.

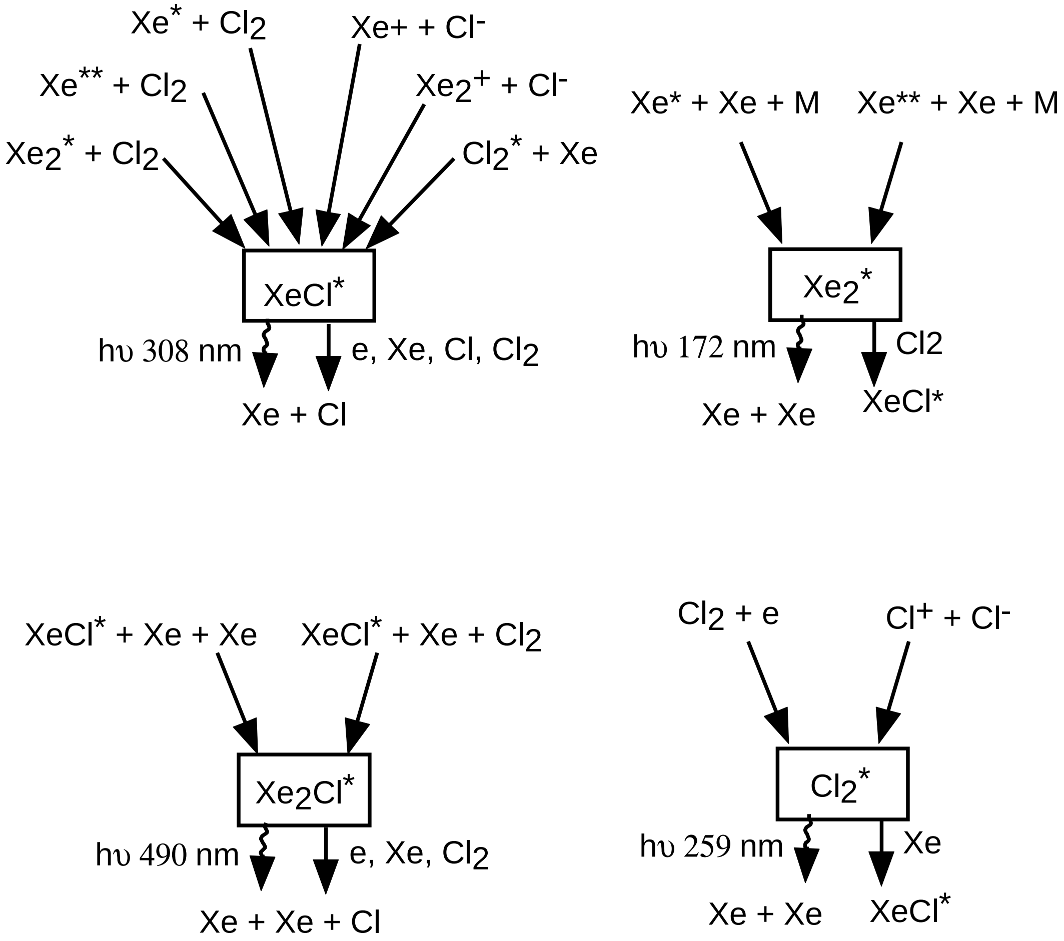

Fig. 6.1. Dominant reaction pathways for generating main excimers in Xe/Cl_2 gas mixture. The major excimers are boxed.

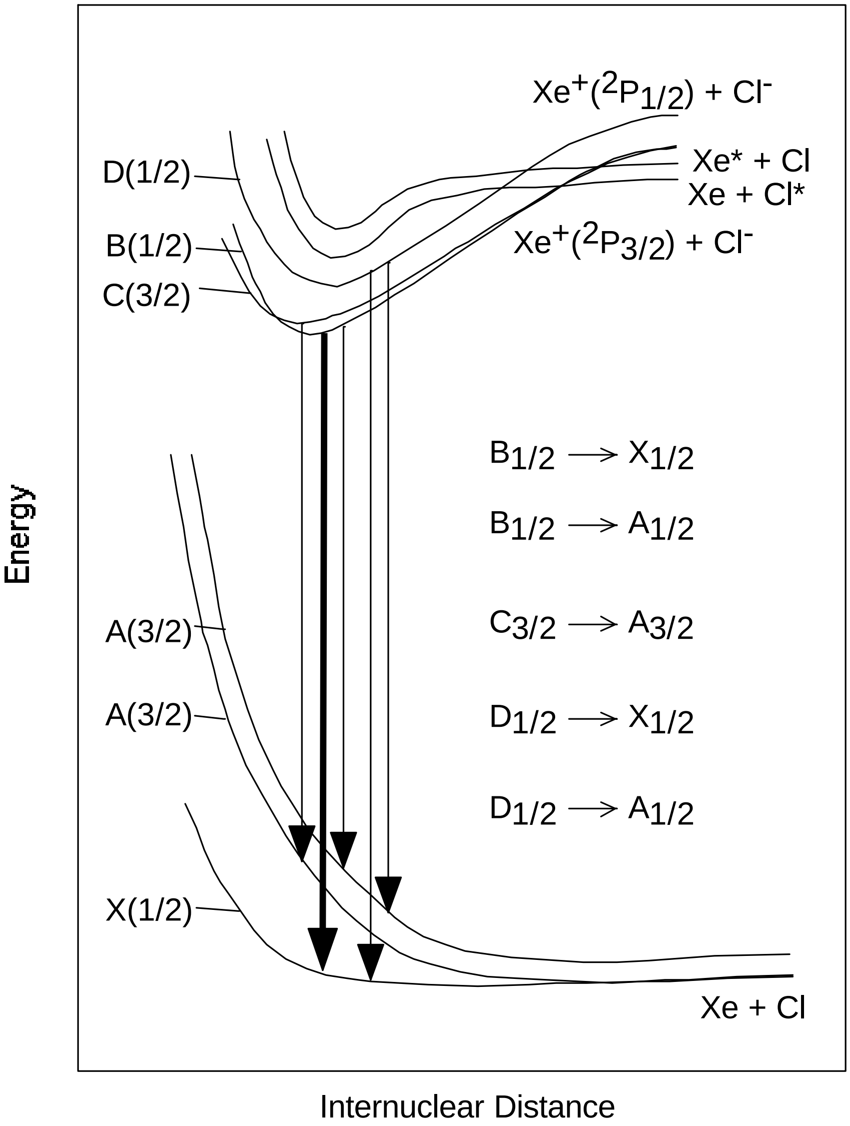

Fig. 6.2. Potential energy diagram of xenon chloride and corresponding excimer transitions.

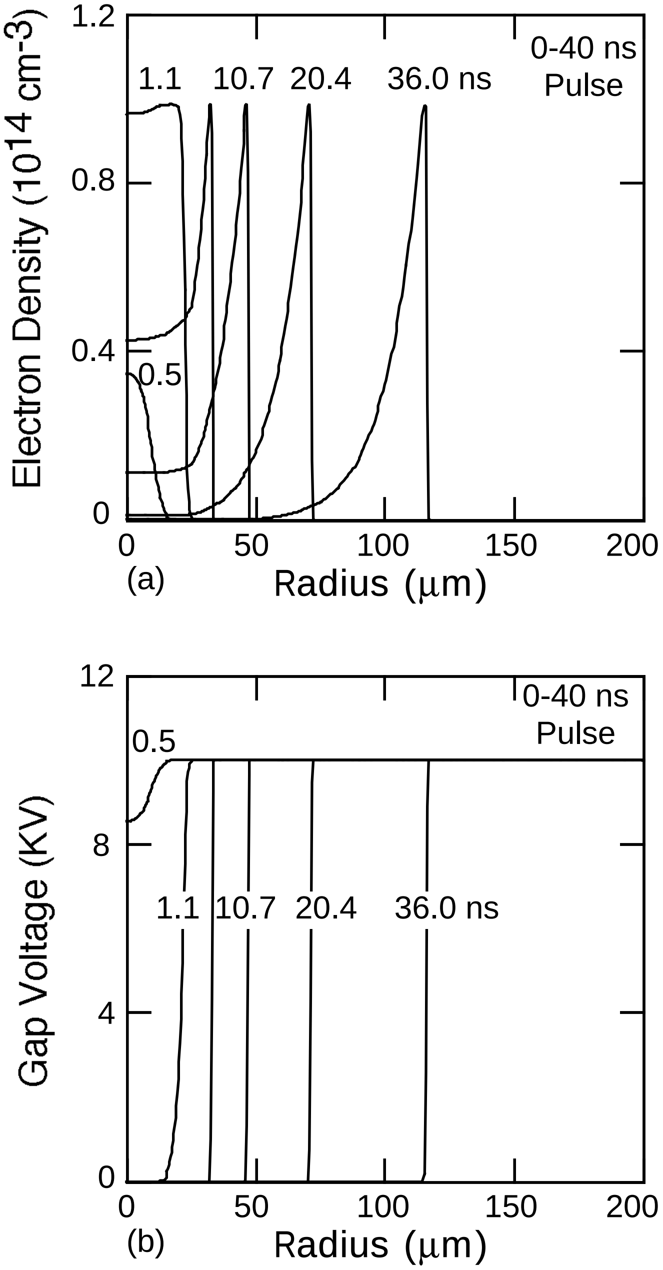

Fig. 6.3. Microdischarge parameters for a Xe/Cl_2 = 99/1 mixture at 0.6 atm gas pressure: (a) electron density during the pulse, (b) gap voltage during the pulse, (c) electron density after the pulse, and (d) gap voltage after the pulse. The larger rate of attachment to Cl_2 at low E/N depletes the electron density in the core of the microdischarge as the dielectric charges. A secondary avalanche is produced when the line voltage is pulled to zero due to the fact that the dielectric in the core of microdischarge fully charges. The curves are labeled with their time after application of voltage (ns).

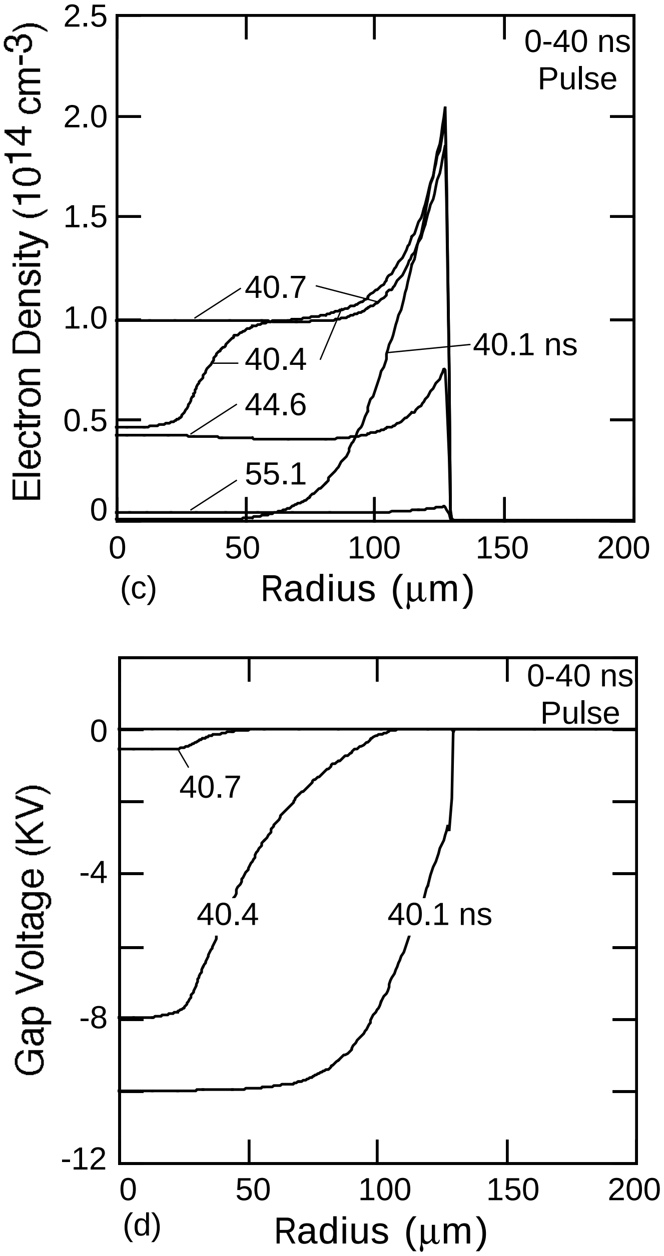

Fig. 6.3. Continued.

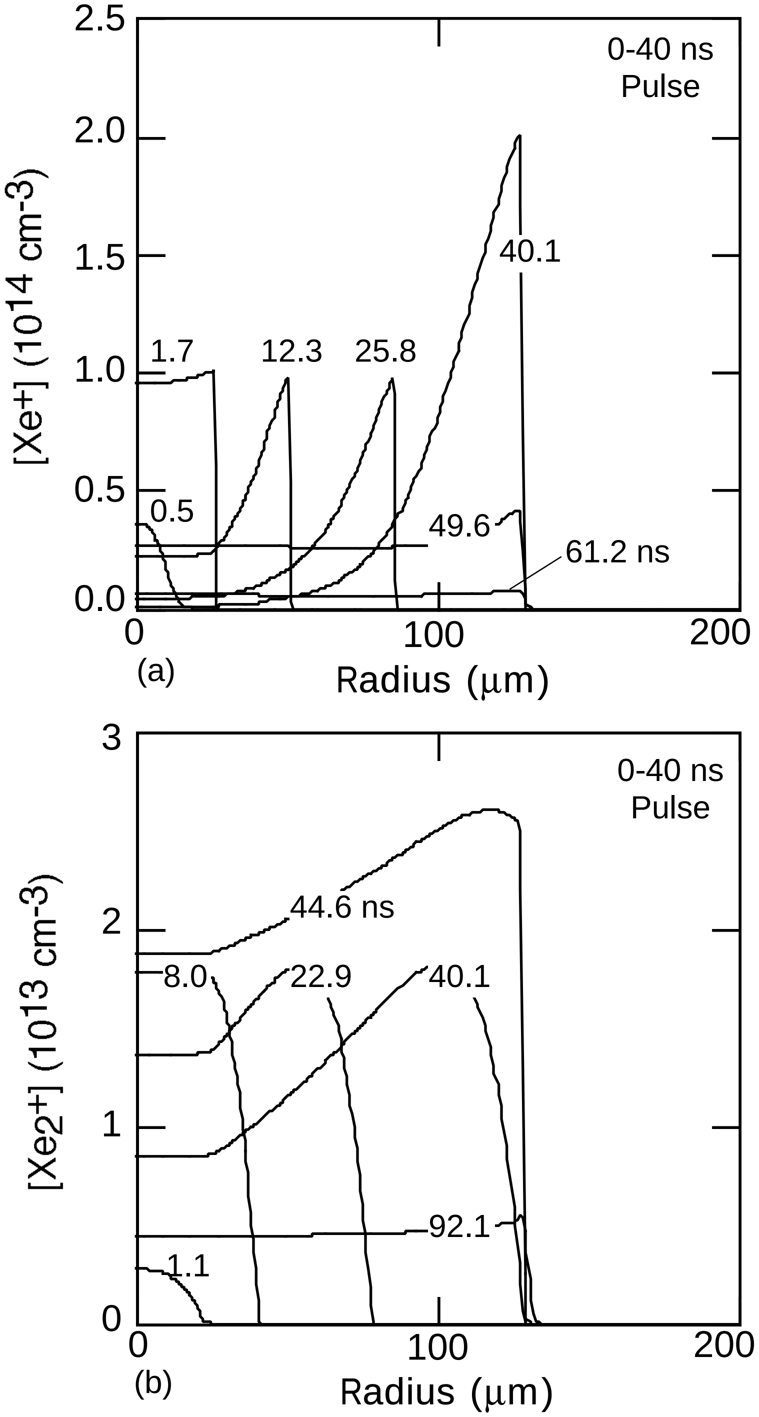

Fig. 6.4. Charged particle densities for the conditions of Fig. 6.3: (a) Xe^+ density, (b) Xe_2^+ density, (c) Cl_2^+ density, and (d) Cl^- density. Xe^+ density has a sharp peak at the edge of microdischarge since it is quickly consumed by generation the Xe_2^+ and charge transferring to Cl_2.

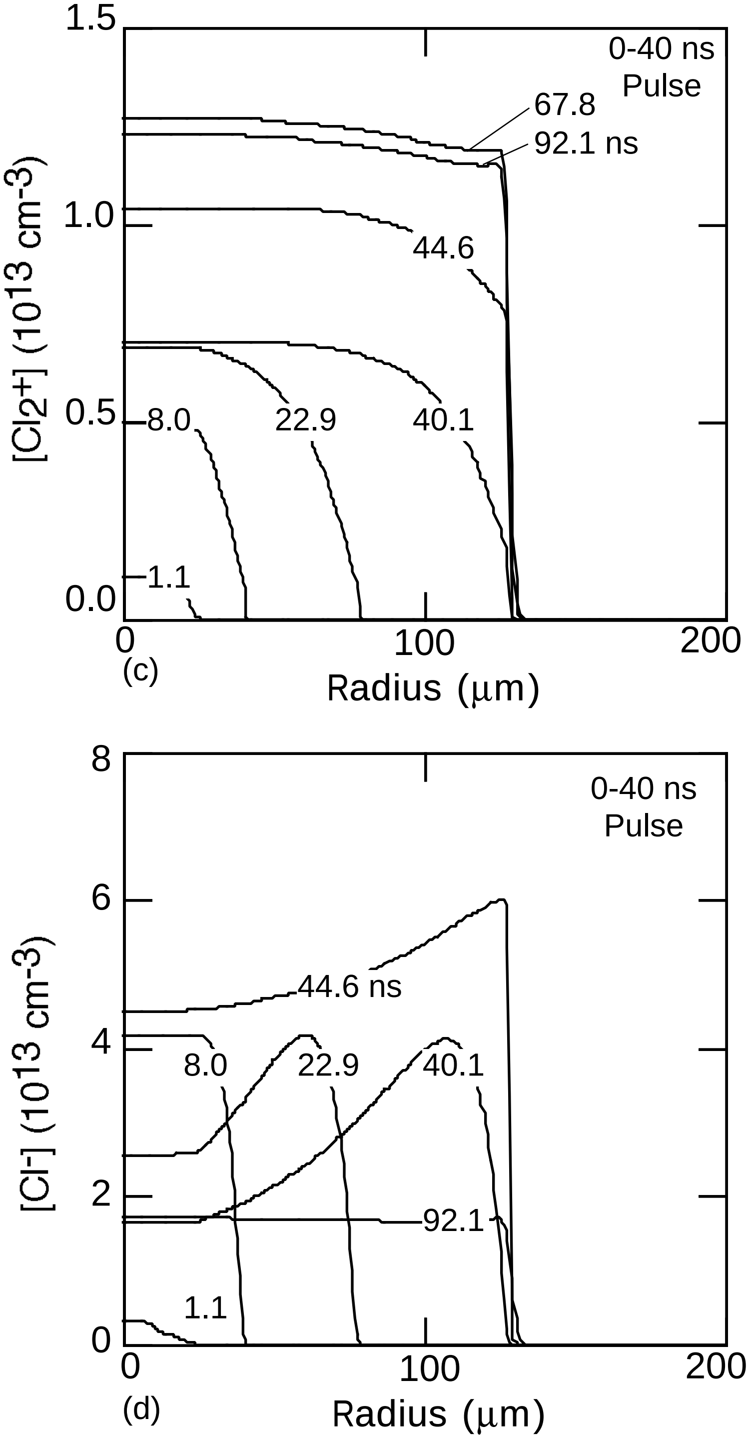

Fig. 6.4. Continued.

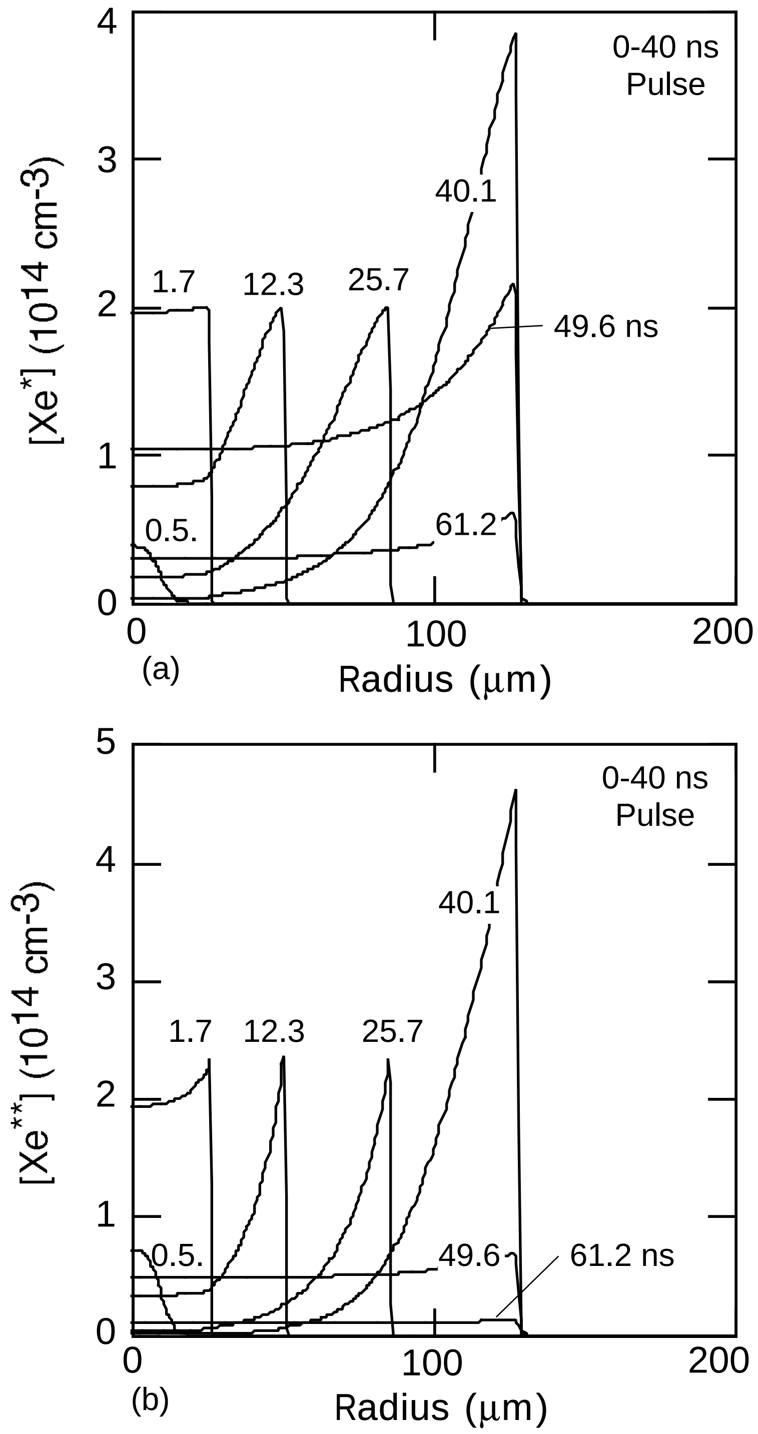

Fig. 6.5. Excited state xenon densities for the conditions of Fig. 6.3: (a) Xe* density and (b) Xe** density. Both of Xe* and Xe** have a sharp edge due to the quick consumption from direct decay, Harpoonging reactions, penning ionization, and the reaction for generatin Xe_2*.

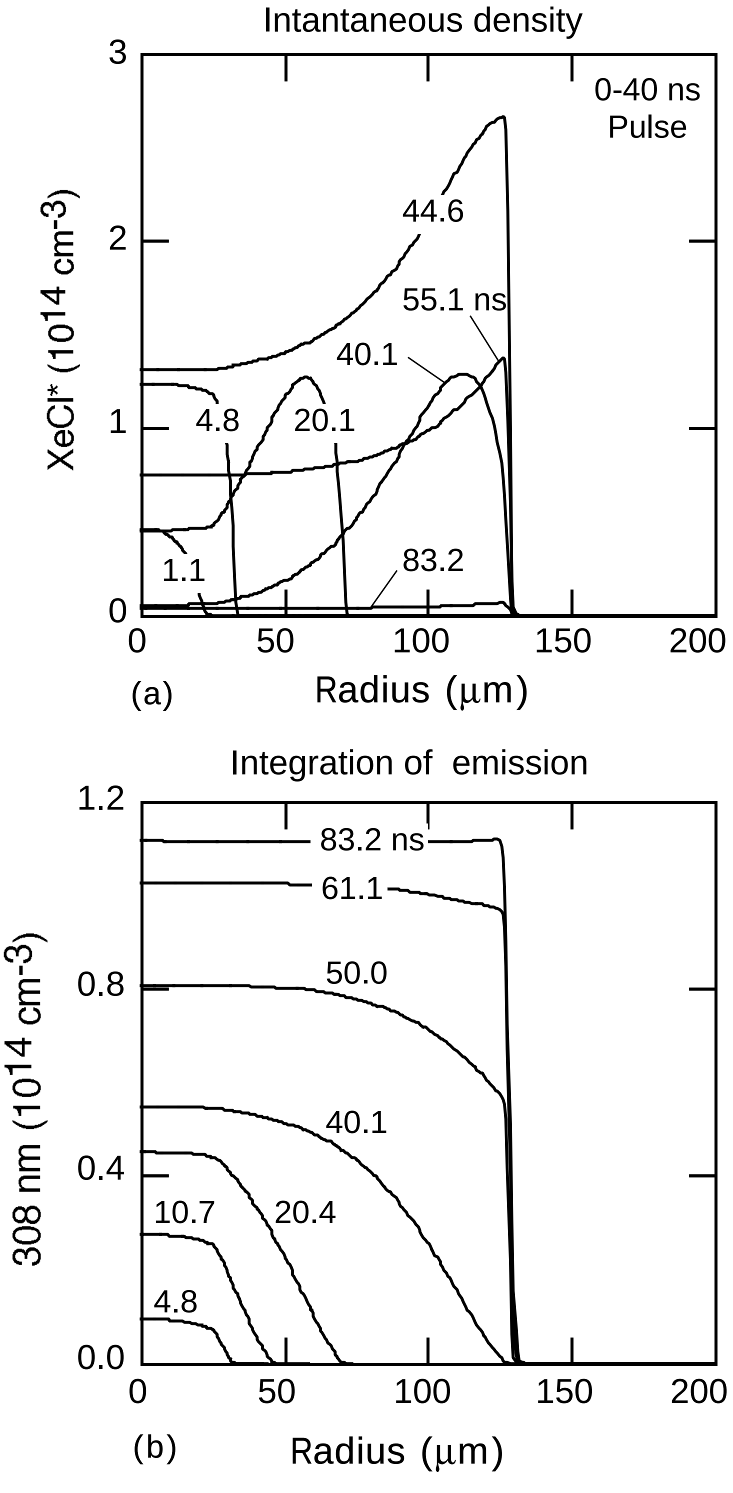

Fig. 6.6. (a) XeCl* density at various time and (b) integration of the corresponding emission for the conditions of Fig. 6.3. The total generation 308-nm photon is ultimately uniform across the microdischarge.

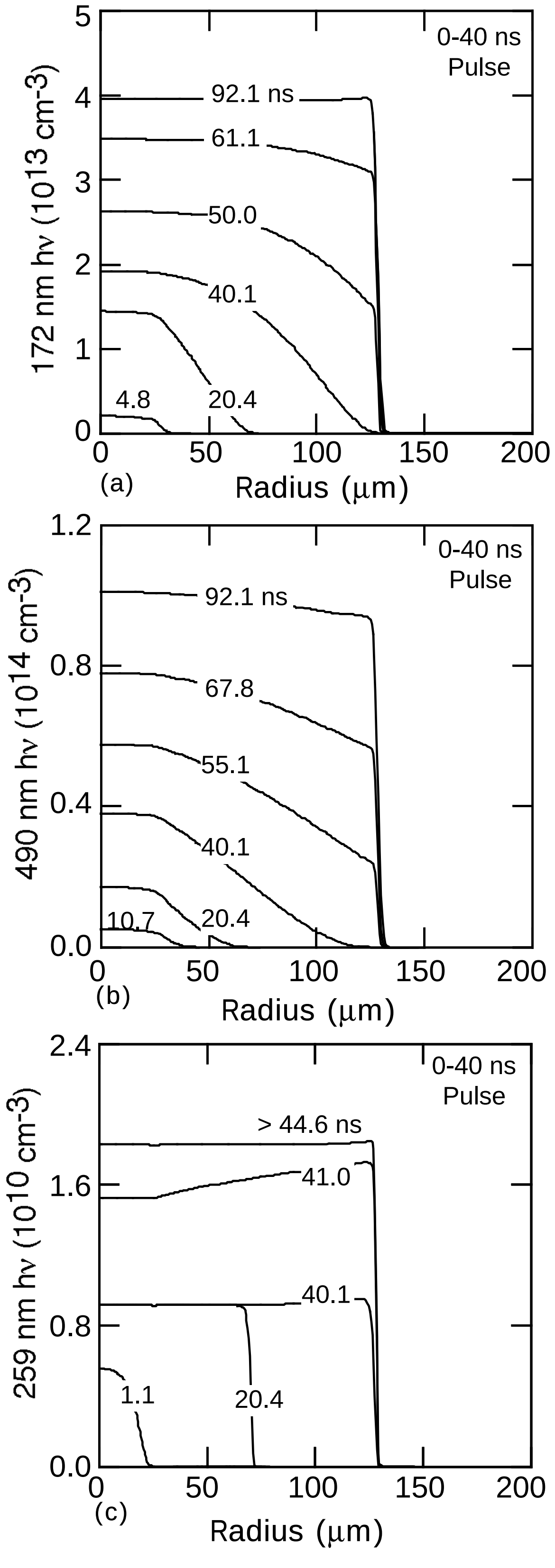

Fig. 6.7. Integration of emission from (a) 172 nm photon (resulting from Xe_2^*), (b) 490 nm photon (resulting from Xe_2Cl^*), and (c) 259 nm photon (resulting from Cl_2^*) for the conditions of Fig. 6.3.

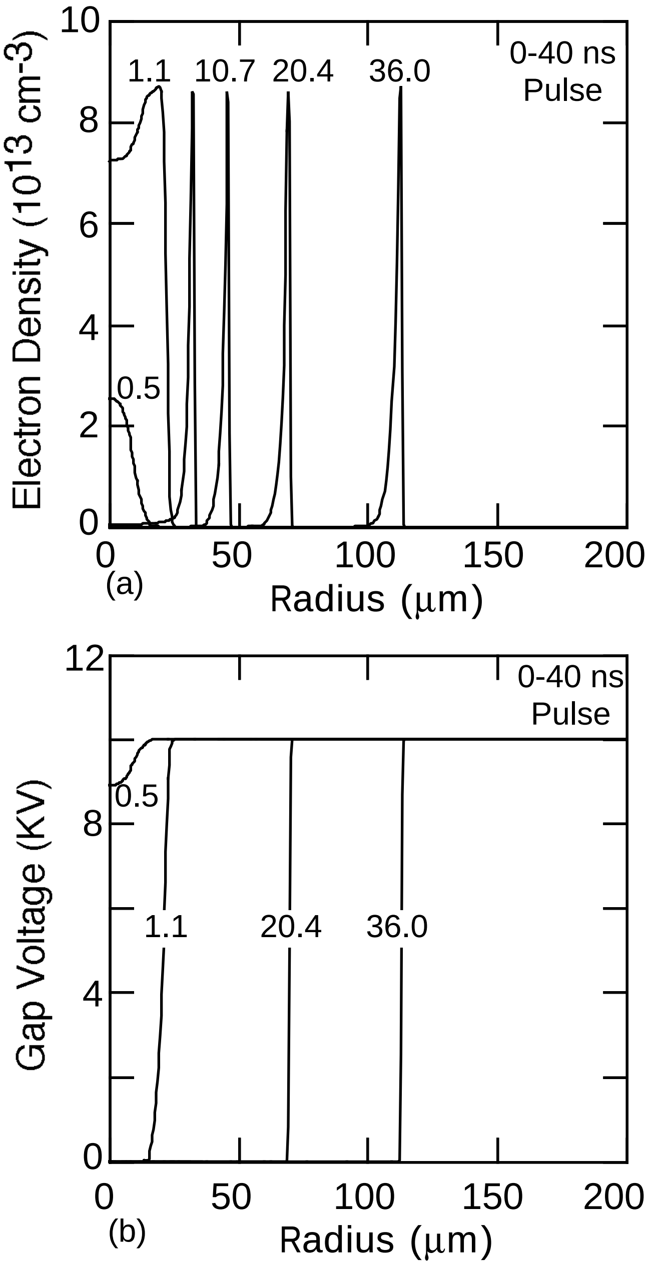

Fig. 6.8. Microdischarge parameters for a Xe/Cl_2 = 99/5 mixture at 0.6 atm gas pressure: (a) electron density during the pulse, (b) gap voltage during the pulse, (c) electron density after the pulse, and (d) gap voltage after the pulse. As the Cl2 denstiy increases, the "shell" of expanding electron density becomes thinner, and the electron density in the core is driven to such low value during the pulse that there is not an immediate second avalanche in the core at the end of pulse. After the pulse, the electron density shell propagates towards the center of the microdischarge due to high gap voltages in the core. The curves are labeled with their time after application of voltage (ns).

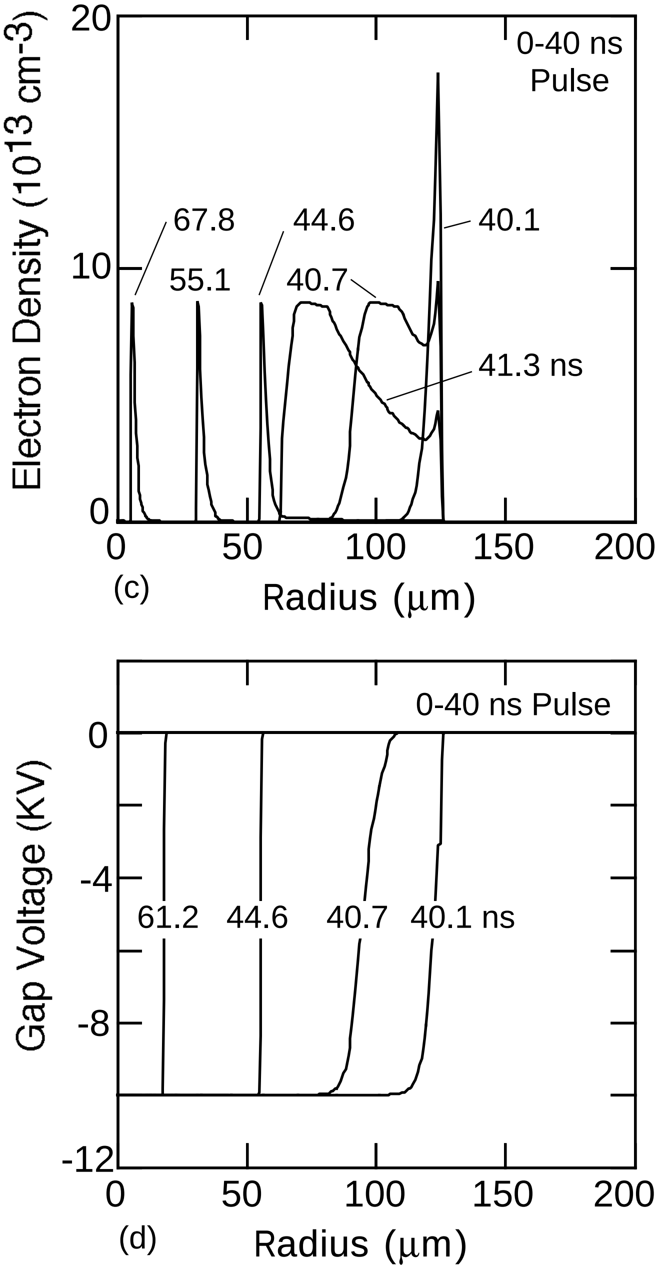

Fig. 6.8. Continued.

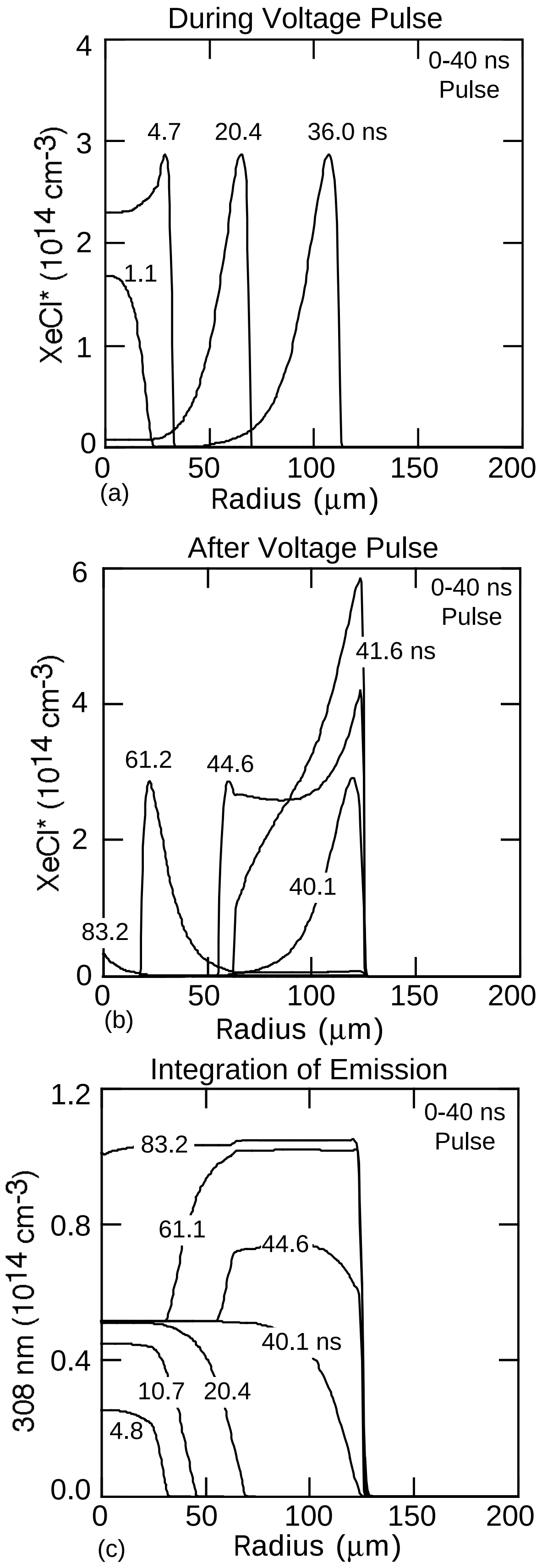

Fig. 6.9. (a) XeCl* density during the pulse, (b) XeCl* density after the pulse, and (c) integration of the corresponding emission. The conditions are the same as in Fig. 6.8. XeCl* and 308-nm photon in the core is regenerated as the second avalanche moves towards the center after the pulse.

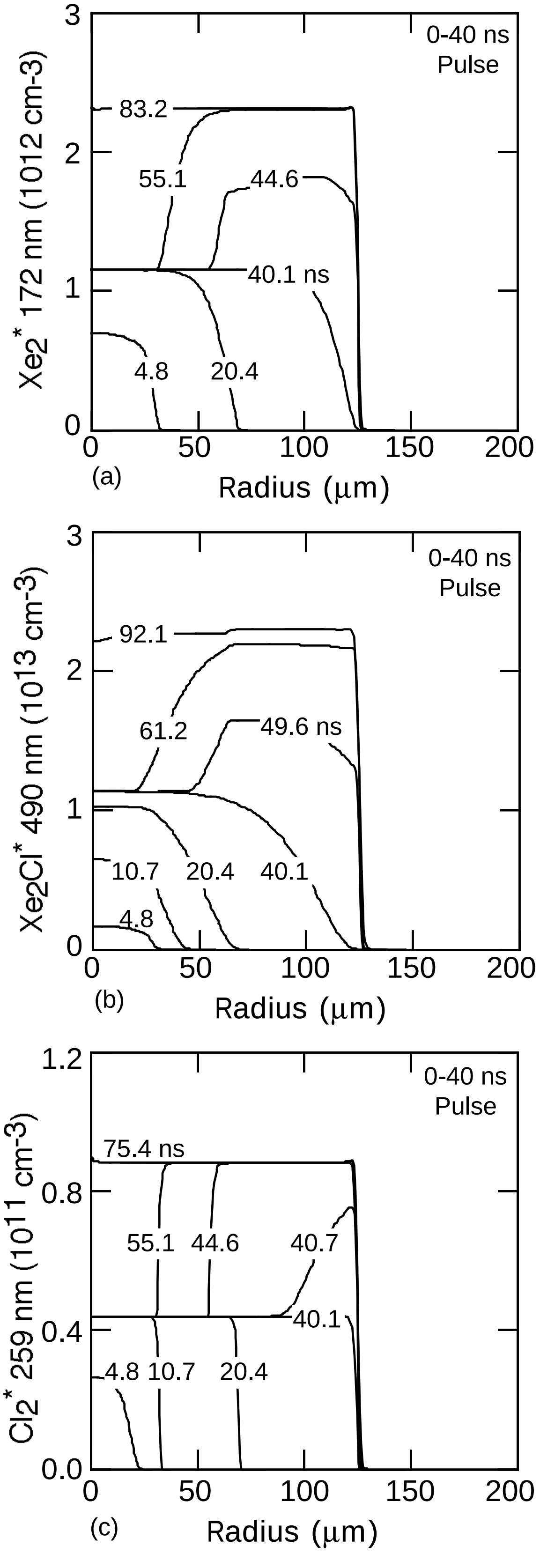

Fig. 6.10. Integration of emission from (a) 172 nm photon (resulting from Xe_2*), (b) 490 nm photon (resulting from Xe_2Cl*), and (c) 259 nm photon (resulting from Cl_2*) for the conditions of Fig. 6.8.

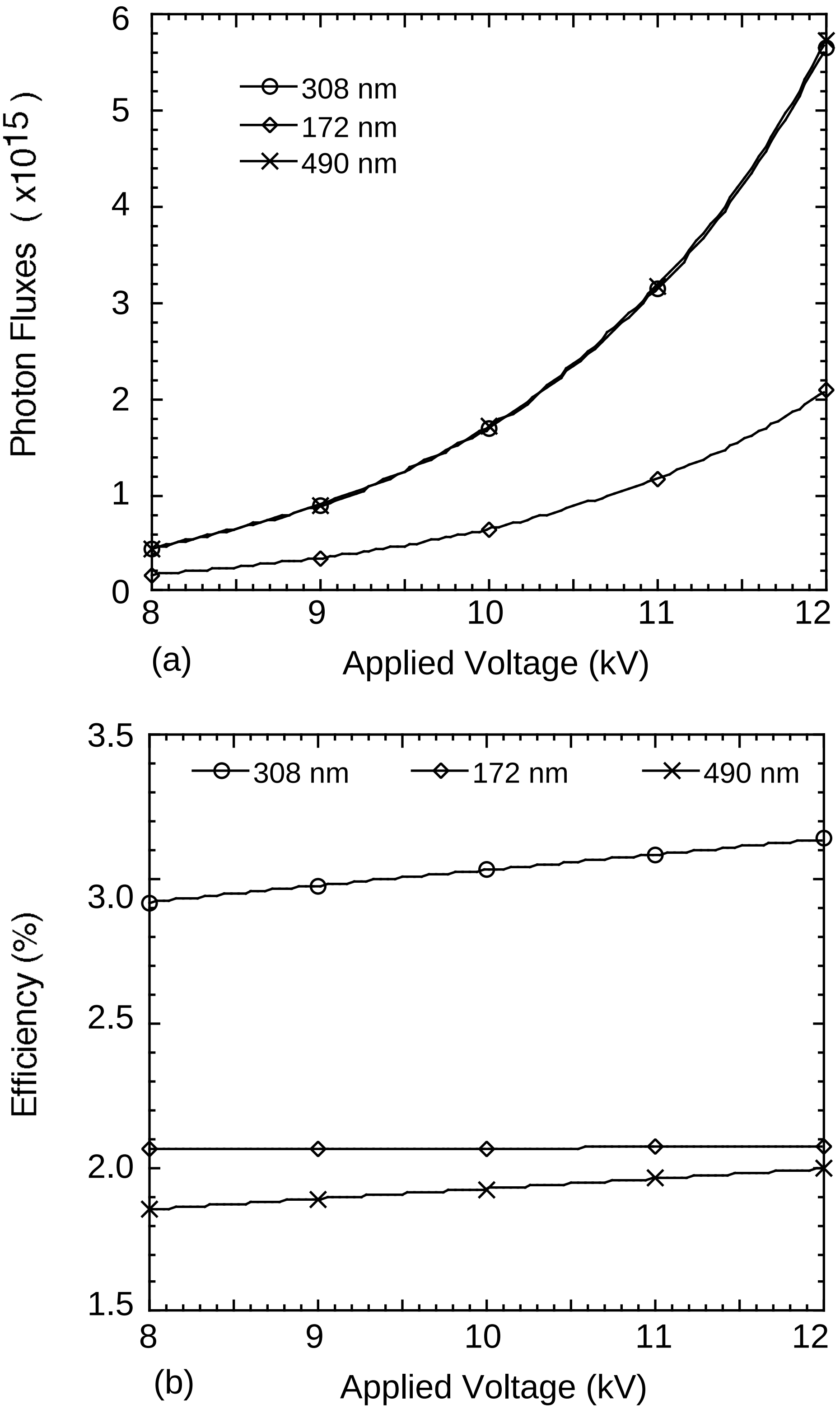

Fig. 6.11. Effect of varying the applied voltage amplitude on (a) time-average photon fluxes and (b) photon generation efficiency for 308, 172, and 490 nm.

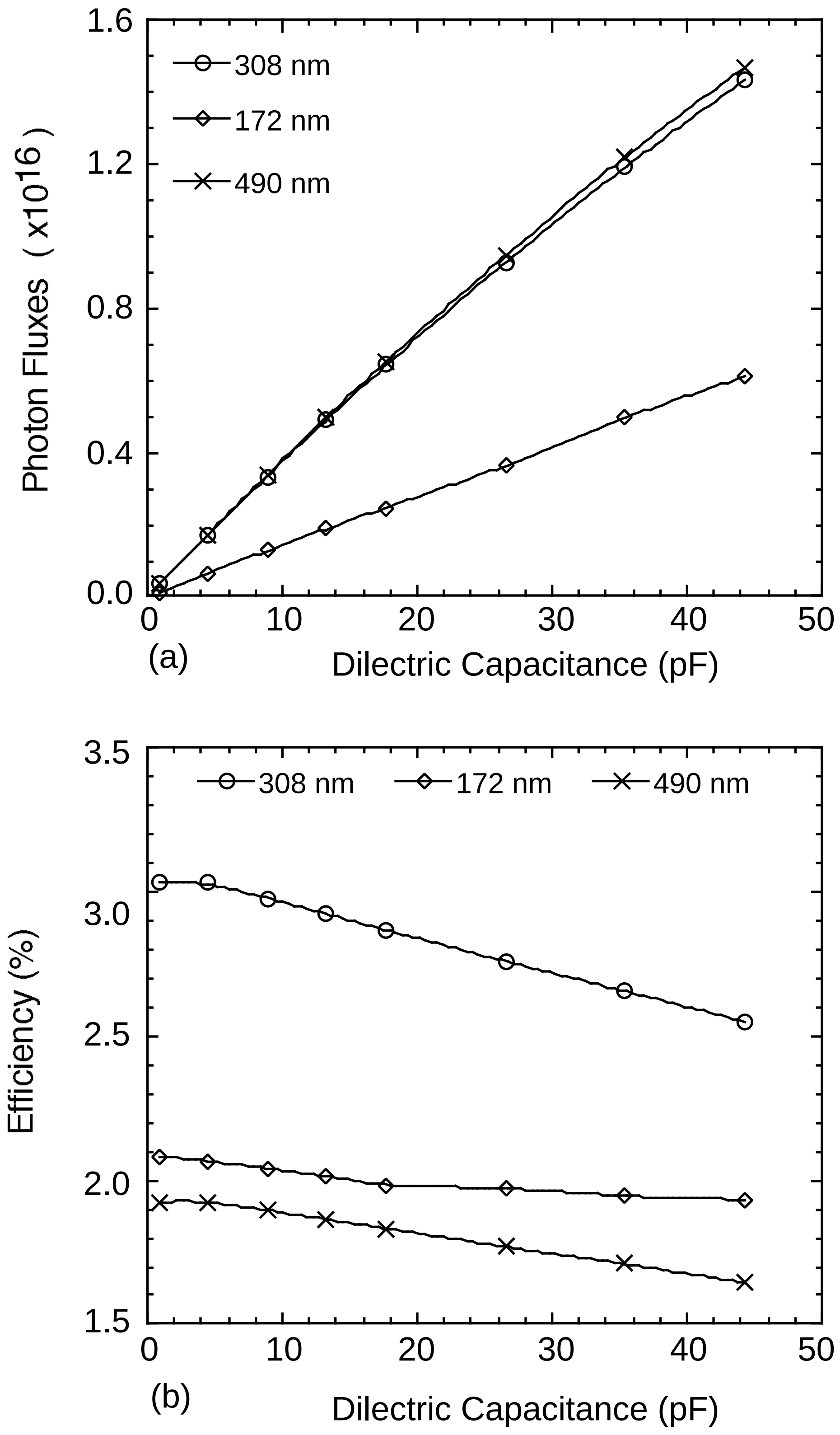

Fig. 6.12. Effect of dielectric capacitance on (a) time-average photon fluxes and (b) photon generation efficiency for 308, 172, and 490 nm.

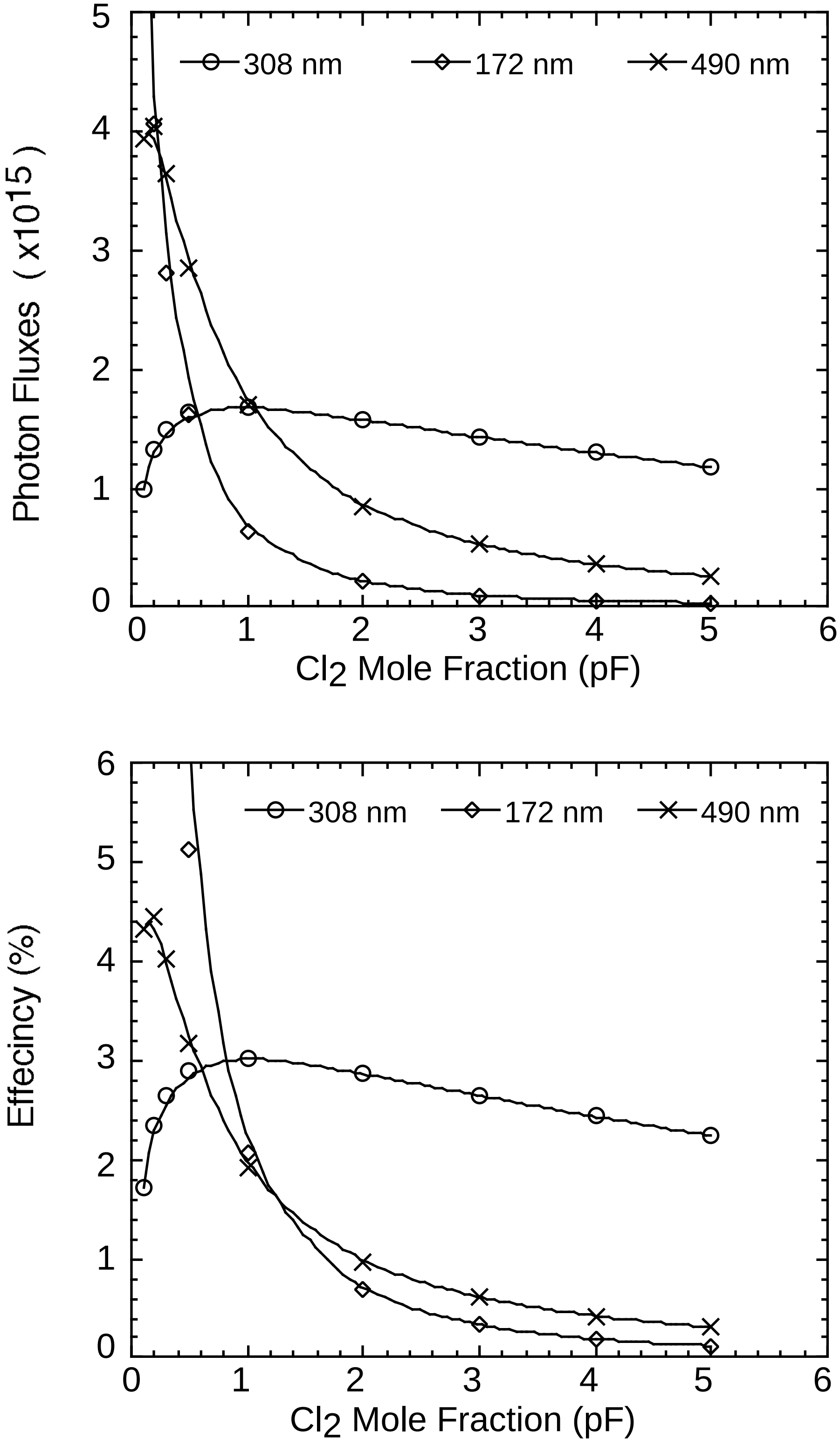

Fig. 6.13. Effect of Cl_2 mole fraction on (a) time-average photon fluxes and (b) photon generation efficiency for 308, 172, and 490 nm.

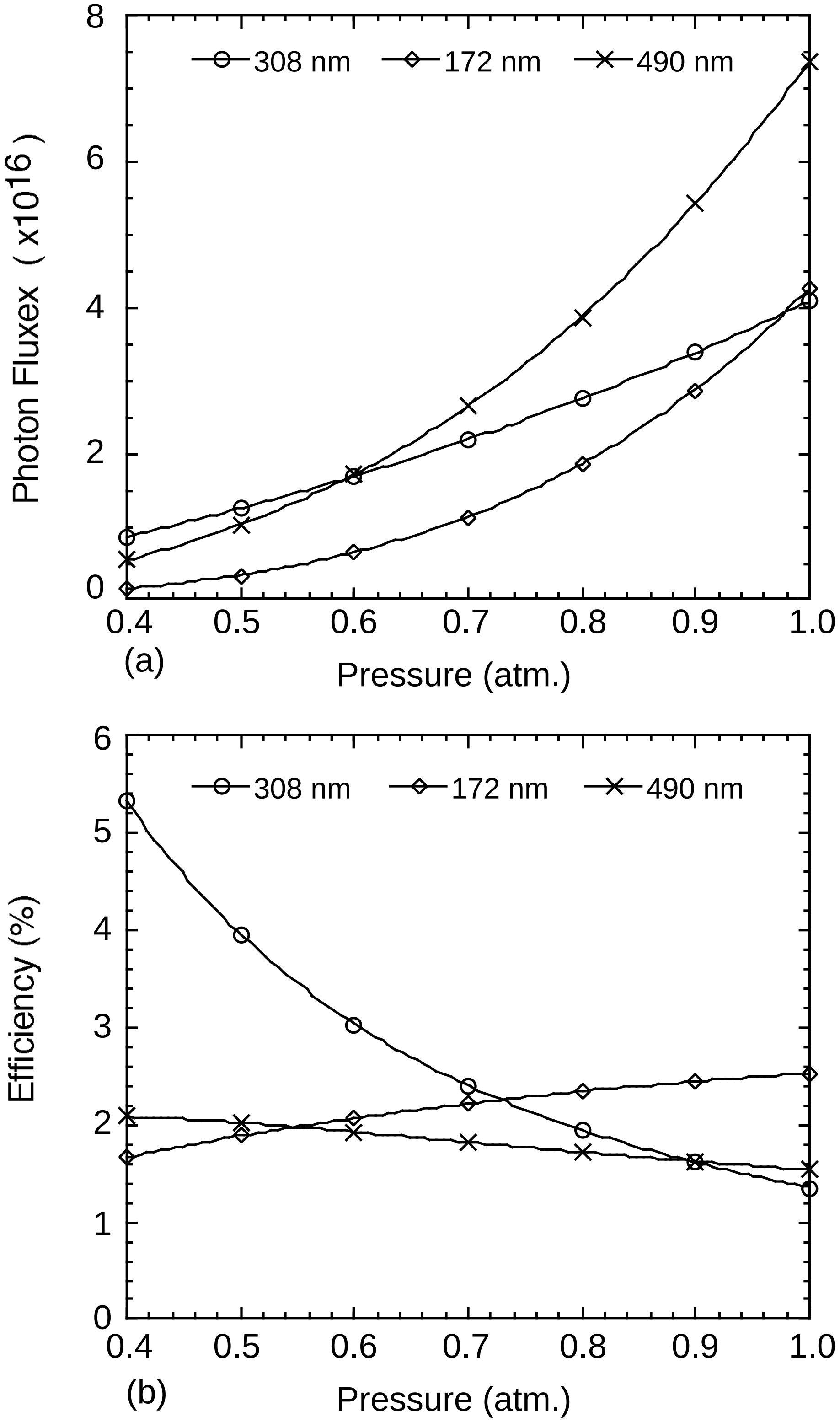

Fig. 6.14. Effect of gas pressure on (a) time-average photon fluxes and (b) photon generation efficiency for 308, 172, and 490 nm.

6.6 References

[1] A. M. Braun, M. T. Maurette, E. Oliveros, *Photochemical Technology* (John Wiley, New York, 1991).

[2] R. F. Scheir and B. F. Fencl, Heat. Pip. Air Cond. J. **68**, 109 (1996).

[3] D. J. Elliott, *Microlithography: Process Technology for IC Fabrication* (New York : McGraw-Hill, 1986).

[4] D. Collier and W. Pantley, Laser Focus World **34**, 63 (1998).

[5] H. Scheytt, H. Esron, L. Prager, R. Mehnert, and C. von Sonntag, in *Proceedings of the NATO Advanced Research Workshop on Non-Thermal Plasma Techniques for Pollution Control, Part B*, edited by P. Penetrante and S. Schulthesis (Springer-Verlag, Berlin, 1993) pp. 91-101.

[6] O. Legrini, E. Oliveros, and A. M. Braun, Chem. Rev. **93**, 671 (1993).

[7] U. Kogelschatz, Appl. Surf. Sci. **54**, 410 (1992).

[8] M. E. Gross, A. Appelbaum, and P. K. Gallagher, J. Appl. Phys. **61**, 1628 (1987).

[9] H. Esrom and U. Kogelschatz, Mater. Res. Soc. Symp. Proc. **158**, 189 (1990).

[10] H. Esrom, J. Demny, and U. Kogelschatz, Chemtronics, **4**, 202 (1989).

[11] T. H. Baum, J. Electrochem. Soc. **137**, 252 (1990).

[12] B. Eliasson and U. Kogelschatz, IEEE Trans. Plasma Sci. **19**, 309 (1991).

[13] H. A. Koehler, L. J Ferderber, D. L. Redhead, and P. J. Ebert, Phy. Rev. A **9**, 768 (1974)

[14] O. Dutuit, R. A. Gutchek, and J. Lecalve, Chem. Phys. Lett. **58**, 66 (1978).

[15] M. Kitamura, K. Mitsuka, and H. Sato, Appl. Surf. Sci. **79/80**, 507 (1994).

[16] T. Gerber, W. Luethy, and P. Burkhard, Opt. Commun. **35**, 242 (1980).

[17] W. Wieme, J. Lenaerts, J. Chem . Phys. **74**, 483 (1981).

[18] D. J. Eckstrom, H. H. Nakano, D. C. Lorents, T. Rothem, J. A. Betts, M. Lainhart, K. J. Triebes, and D. A. Dakin, J. Appl. Phys. **64**, 1691 (1988).

[19] B. Gellert and U. Kogelschaz, Appl. Phys. B: Photophys. Laser Chem. **52**, 14 (1991).

[20] B. Eliasson and U. Kogelschaz, Appl. Phys. B: Photophys. Laser Chem. **46**, 299 (1991).

[21] U. Kogelschaz, Pure Appl. Chem. **62**, 1667 (1990).

[22] J.-Y. Zhang and Ian W. Boyd, J. Appl. Phys. **80**, 633 (1996).

[23] J.-Y. Zhang and Ian W. Boyd, J. Appl. Phys. **84**, 1174 (1998).

[24] Z. Falkenstein and J. J. Coogan, J. Phys. D: Appl. Phys. **30** 2704 (1997).

[25] B. Eliasson and B. Gellert, J. Appl. Phys. **68**, 2026 (1990).

[26] B. Eliasson, M. Hirth, and U. Kogelschaz, J. Phys. D: Appl. Phys. **20** 1412 (1987).

[27] C. K. Rhodes, *Excimer Lasers*, Vol. 30 of Topics in Applied Physics (Springer, Berlin, 1984).

[28] D. C. Lorents, Gaseous Electronics Conference, Boulder, CO, October 1984.

7. PLASMA REMEDIATION OF PERFLUOROCOMPOUNDS IN INDUCTIVELY COUPLED PLASMA REACTORS

7.1 Introduction

Perfluorinated compounds (PFCs), gases which have large global warming potentials [1], are widely used in plasma processing for etching and chamber cleaning [2-5]. Due to under utilization of the feedstock gases or by-product generation, the effluents from plasma tools using these gases typically have large mole fractions of PFCs. The use of plasma burn-boxes located downstream of the plasma chamber has been proposed as a remediation method for abating PFC emissions with the goals of reducing the cost of PFC abatement and avoiding the NO_x formation usually found with thermal treatment methods.

In this chapter, results from the two-dimensional Hybrid Plasma Equipment Model (HPEM) have been used to investigate the scaling of plasma abatement of PFCs using plasma burn-boxes. An inductively coupled plasma (ICP)-etching chamber is modeled to determine the utilization of the feedstock gases and the generation of by-products. The effluent from the etching chamber is then passed through a plasma burn-box excited by a second inductively coupled source.

In Section 7.2, we investigate RF discharges sustained in Ar/C_2F_6 and Ar/CF_4 mixtures in a low-pressure plasma (10 mTorr)-etching reactor. In Section 7.3, after a validation for comparison of predicted C_2F_6 abatement with experimental results, we present discharges in the etching effluent mixed with O_2, H_2, or H_2O in a relatively high-pressure (150 mTorr) plasma burn-box. Our concluding remarks are in Section 7.4.

7.2 Plasma Characteristics, Consumption and Generation of PFCs in an ICP Etching Reactor

Schematics of the plasma etching chamber and burn-box used in this study are shown in Fig. 7.1. The species and reactions included for the low and high-pressure reactors are listed in Appendixes A and B. The plasma etching chamber is a 13.56 MHz ICP reactor with four coils on top of a dielectric window using Ar/C_2F_6 (or Ar/CF_4) as the process gas mixture at 10 mTorr. A 20-cm diameter wafer with a conductivity of 0.05 $(\Omega\text{-cm})^{-1}$ sits on the substrate. The feedstock gas is flowed into the chamber through a showerhead nozzle, and the exhaust gases are pumped out at the bottom of the chamber. The burn-box, which is located downstream of a turbopump, is also an ICP reactor operating at a higher pressure of 150 mTorr. O_2, H_2 or H_2O are injected into the burn-box as additive gases through a ring nozzle at the top of the reactor. The input fluxes to the burn-box are obtained from the output fluxes of the etching chamber. We assumed there was no compositional changes of the effluent in the turbopump.

The baseline case for the plasma etching reactor uses an Ar/C_2F_6 = 60/40 mixture at 10 mTorr with 650 W ICP power. Reactive sticking coefficients and returning products are shown in Table 7.1. The power deposition, electron density and the electron source for this case are shown in Fig. 7.2. The power deposition has a maximum of ≈1.7 W/cm^3 located off axis, 0.5 cm below the quartz window, and under the two middle coils. Since diffusion is the dominant mechanism for electron transport, the electron density (peak value of 2.2×10^{11} cm^{-3}), and the electron source have peak values near the reactor axis. (No attempt was made to make reactive fluxes to the substrate uniform as a function of position.) Positive ions (Ar^+ and CF_3^+) are first generated by electron impact ionization of Ar and C_2F_6, and secondarily by dissociative charge transfer of Ar^+ to C_2F_6

and its fragments. Negative ions (F^- and CF_3^-) are generated by electron impact dissociative attachment, first of the feedstock C_2F_6 and secondarily from the dissociation fragments. Ion densities, shown in Fig. 7.3, have the same general shape as the electron density with the exception that the dominant negative ion F^- is less extended due to its trapping at the peak of the plasma potential. Because there is charge exchange to C_2F_6 and because Ar has the higher ionization threshold (16 eV for Ar and 14.2 eV C_2F_6), the peak density of Ar^+ (1.96×10^{11} cm^{-3}) is about 0.7 times that of CF_3^+ (2.75×10^{11} cm^{-3}), even though there is a larger Ar input gas mole fraction. The negative ions are dominated by F^- with an on-axis maximum density of 2.24×10^{11} cm^{-3} (about 0.9 times the electron density) which is two orders of magnitude larger than that of CF_3^-. F^- generation by electron impact dissociative attachment occurs by at least four dissociative attachment processes and by charge transfer from CF_3^-,

$$e + C_2F_6 \rightarrow C_2F_5 + F^- \tag{7.1a}$$

$$e + C_2F_5 \rightarrow C_2F_4 + F^- \tag{7.1b}$$

$$e + CF_3 \rightarrow CF_2 + F^- \tag{7.1c}$$

$$e + CF_2 \rightarrow CF + F^- \tag{7.1d}$$

$$CF_3^- + F \rightarrow CF_3 + F^- \tag{7.1e}$$

CF_3^- is dominantly generated only by electron impact dissociative attachment from C_2F_6 and CF_4.

The densities of C_2F_6, CF_3 and CF_2 are shown in Fig. 7.4. The C_2F_6 is quickly dissociated upon injection into the plasma. There is some reformation of C_2F_6 in the plasma and on walls. CF_3 is a primary fragment of dissociative electronic excitation of C_2F_6 and dissociative excitation transfer from Ar* to C_2F_6, while CF_2 is produced by dissociation of CF_3 and CF_4. Due to subsequent reassociation, the density of CF_3 increases near the pump port, while the density of CF_2 has a maximum at the reactor axis due to its continuous loss (recombination of CF_2 with F, F_2, CF_3 and itself) after being produced. Other C_xF_y species (C_2F_4, C_2F_5 and CF_4), shown in Fig. 7.5, are slowly generated by radical recombination through gas phase and wall reactions. The mole fractions of neutral species in the effluent from our baseline etching reactor consist of:

Ar	0.415	CF_3	0.141	CF_2	0.111
C_2F_6	0.093	SiF_2	0.074	F	0.071
CF_4	0.047	C_2F_3	0.018	C_2F_5	0.018
F_2	0.009	C_2F_4	0.003.		

The total output flowrate is 242.8 sccm, larger than the input flow rate due to dissociation.

Since CF_4 is also frequently used as a process gas, we also examined Ar/CF_4 ICP etching discharges. The baseline case is the same as that for Ar/C_2F_6 with the exception that CF_4 replaces C_2F_6. For the CF_4 case, the shapes of the profiles of electron, ions and neutrons do not appreciably change. The mole fractions in the effluent for the Ar/CF_4 base case are:

Ar	0.477	CF_3	0.066	CF_2	0.077
C_2F_6	0.008	SiF_2	0.090	F	0.117
CF_4	0.132	C_2F_3	0.012	C_2F_5	0.004
F_2	0.014	C_2F_4	0.002.		

The total output flowrate of 212.7 sccm is smaller than that for the Ar/C_2F_6 case corresponding to a lower total amount of dissociation.

A design of experiments (DOE) was performed to characterize the consumption of C_2F_6 in the etching chamber. The fractional consumption of C_2F_6 in the etching chamber as a function of mole fraction of C_2F_6 (40 – 60%), gas flow rate (100-300 sccm), and power deposition (350-650W) is shown in Fig. 7.6. The consumption is based on the outflow (sccm) compared to the inflow (sccm). The consumption scales almost linearly with power deposition, and decreases with increasing gas flow rate (equivalently, having shorter gas residence time) and input C_2F_6 mole fraction. Using higher power and lower flowrate, one expects to increase the C_2F_6 consumption since more energy is deposited per input C_2F_6 molecule. These results can be summarized in terms of energy per molecule (eV/molecule) required for consumption of C_2F_6. The energy, typically called the *W*-value, is shown in Fig. 7.7. A small *W*-value corresponds to higher efficiency. Low *W*-values were obtained at high C_2F_6 mole fraction and high flowrate. For higher C_2F_6 mole fractions there is a more energy deposition to C_2F_6, and for a higher flowrate there is less power expended in the dissociation products. The total generation of radicals (CF_2, CF_3, C_2F_3, C_2F_5, and F) and other PFCs is almost linearly proportional to the C_2F_6 consumption.

A similar DOE was carried out for Ar/CF_4 gas mixtures. CF_4 shows similar systematic trends in consumption and in *W*-values. However for given conditions, the consumption is generally lower and *W*-values higher than Ar/C_2F_6 due to the lower rate of dissociation of CF_4. To compare the baseline cases using Ar/C_2F_6 or Ar/CF_4 = 60/40 with 650 W power deposition, the consumption and *W*-values are 72% and 158 eV/molecule for C_2F_6, and 65% and 175 eV/molecule for CF_4. The total generation of C_xF_y in the effluent for the CF_4 cases is approximately half that of the corresponding C_2F_6

cases. The output amounts of CF_2 and CF_3 for the C_2F_6 case are larger by factors of 2.44 and 1.65, respectively, compared to the CF_4 case, largely a consequence of the branching ratios for fragmentation of the feedstocks which favor CF_x production from C_2F_6. There are, however, slightly more F radicals in the effluent for Ar/CF_4 mixtures.

7.3 Plasma Abatement of PFCs in a Burn-Box

In order to abate the PFCs emitted by the etching chamber, the effluent is passed through the plasma burn-box. The effluents for Ar/C_2F_6 discharges consist mainly of Ar, undissociated C_2F_6, CF_x radicals, newly generated PFCs (CF_4, C_2F_4, and C_2F_5), fluorine (F and F_2), and the etch product (SiF_2). In this section we first present a comparison between our computed results and those measured experimentally for abatement of C_2F_6 for validation purposes, and then discuss the remediation of simulated effluent from the plasma etching chamber using O_2, H_2, or H_2O as additives.

7.3.1 Validation

The plasma remediation model was validated by comparing our results to experiments by Sawin and Vitale [6] for abatement of C_2F_6 in an ICP reactor. Their reactor is a 10-cm diameter stainless steel tube with an internal coil. The feedstock gas was C_2F_6/O_2 = 50/50. They found that C_2F_6 is decomposed in the plasma reactor, but CF_4 is generated as a product, which coincides with the observations of Hartz et al. [7].

The formation of CF_4 largely depends on the availability of F atoms to recombine with CF_3. Through our parameterizations, we found that the branching ratio for $e + C_2F_6 \rightarrow C_2F_5 + F^-$ or $CF_3 + CF_3^-$ significantly affects the net destruction of C_2F_6 and the formation of CF_4 for Sawin and Vitale's conditions. For example, the mole fractions of C_2F_6 remaining and CF_4 formation in the exhaust of the burn-box are shown in Fig. 7.8(a) as a function of the branching ratio of $e + C_2F_6 \rightarrow CF_3 + CF_3^-$. The total flowrate is 400 sccm, the pressure is 500 mTorr, and the power deposition is 500 W. An increase in this branching (and decrease in branching for $C_2F_5 + F^-$) produces more CF_3, which can recombine more rapidly with F to form CF_4 and with another CF_3 radicals to reform C_2F_6. Any C_2F_5 generated can rapidly react with F to generate additional CF_3. A branching ratio of 58% best matches experimental data. Using this branching, comparisons between experiments and simulations as a function of power deposition are shown in Fig. 7.8(b). Over the range of power investigated, the model agrees well with the experiments. The C_2F_6 destruction increases with increasing power while the CF_4 production increases. At the highest power (1000 W) there is 40% C_2F_6 decomposition and 25% CF_4 generation.

At 500 mTorr, the plasma is generated dominantly near the coils due to the finite electromagnetic skin depth and rapid electron thermalization. For example, the electron density and the rate of electron impact dissociation of C_2F_6 are shown in Fig. 7.9, along with the advective gas velocity field, for the 500 W case. The maximum electron density (5.3×10^{11} cm^{-3}) is near the middle coil and decreases by a factor of 30 at the center of the burn-box. The dissociation rate of C_2F_6 is correspondingly smaller in the center where the advective gas velocity is highest. This pass through of gases in the center of reactor contributes to the lower level of C_2F_6 degradation under the experimental condition [6].

As will be discussed later, CF_4 generation is via radical recombination between F and CF_3. At 500 mTorr, the rate constant of $CF_3 + F \rightarrow CF_4$ is given by [8]

$$k_2 = 3.5\times10^{-8}\left(\frac{T_{gas}}{298}\right)^{-7.73}\exp\left(-\frac{2210}{T_{gas}}\right)\ \mathrm{cm^3/s} \tag{7.2}$$

where T_{gas} is the gas temperature. At 500 W, the mean gas temperature in the reactor is ≈400 K, at which $k_9 = 1.1 \times 10^{-11}$ $\mathrm{cm^3/s}$. As a result CF_4 production is favored. Higher mean gas temperatures result in lower rates of CF_4 production, as will be discussed below.

W-values for C_2F_6 and for all C_xF_y as a function of power for the experimental conditions are shown in Fig. 7.10. To quantify the destruction efficiency of all C_xF_y species, we define its *W*-value as the input energy divided by the sum of C_xF_y destruction weighted by the number of F atoms and normalized by 6 (the number of F atoms in C_2F_6),

$$W\left(\mathrm{C}_x\mathrm{F}_y\right) = \frac{P}{\sum_i [F_i(\mathrm{C}_x\mathrm{F}_y)\cdot y/6]_{input} - \sum_i [F_i(\mathrm{C}_x\mathrm{F}_y)\cdot y/6]_{output}} \tag{7.3}$$

where *P* is the power deposition, F_i is the flow rate (input or output) of *i*th C_xF_y. The *W*-value would equal that for C_2F_6 if it was completely oxidized with there being no C_xF_y fragments. The weighting of the *W*-value with the number of F atoms in the molecule is a qualitative judgment that larger dissociation products are "less good." $W(C_xF_y)$-value is 5-10 times larger than $W(C_2F_6)$-value since more energy is required to abate the products of the dissociation of C_2F_6 than to simply destroy C_2F_6. Both *W*-values increase with increasing power, indicating lower efficiency. Although higher power deposition produces higher densities of radicals, the higher radical densities result in more rapid radical-radical recombination reactions. As the power deposition increases and more dissociation is produced, the incremental dissociation is less efficient because more power goes into the dissociation products.

7.3.2 O_2 as an additive for PFC abatement

We first consider O_2 as an additive gas for PFC abatement of effluent from the etching chamber in the plasma burn-box. The desired reaction pathway is to oxidize C_xF_y to CO_2. Electron impact of O_2 generates O, $O(^1D)$ and O^+, which in turn react with the PFCs and CF_x radicals mainly as follows:

$$O\ [\text{or } O(^1D)] + CF_3 \rightarrow COF_2 + F \qquad k_{4a} = 3.1\times10^{-11}\ \text{cm}^3\ \text{s}^{-1} \qquad (7.4a)$$

$$O\ [\text{or } O(^1D)] + CF_2 \rightarrow COF + F \qquad k_{4b} = 1.4\times10^{-11}\ \text{cm}^3\ \text{s}^{-1} \qquad (7.4b)$$

$$O\ [\text{or } O(^1D)] + CF \rightarrow CO + F \qquad k_{4c} = 2.4\times10^{-11}\ \text{cm}^3\ \text{s}^{-1} \qquad (7.4c)$$

$$O^+ + C_2F_6 \rightarrow C_2F_5^+ + FO \qquad k_{4d} = 3.0\times10^{-11}\ \text{cm}^3\ \text{s}^{-1} \qquad (7.4d)$$

$$\rightarrow CF_3^+ + CF_3 + O \qquad k_{4e} = 1.5\times10^{-9}\ \text{cm}^3\ \text{s}^{-1} \qquad (7.4e)$$

$$O^+ + CF_4 \rightarrow CF_3^+ + FO \qquad k_{4f} = 1.4\times10^{-9}\ \text{cm}^3\ \text{s}^{-1} \qquad (7.4f)$$

where rate coefficients are shown for T_g = 500 K. The dominant reaction products of O atoms with CF_x are COF, COF_2, and CO. It is important to note that at low gas temperatures O and $O(^1D)$ do not directly react with CF_4 or C_2F_6, and O_2 is generally unreactive with C_xF_y fragments. Remediation dominantly occurs by radical-radical reactions. The desired end product CO_2 can be formed via further reactions of COF with O or $O(^1D)$, and COF_2 with $O(^1D)$.

$$\text{O [or O}(^1\text{D})] + \text{COF} \rightarrow \text{CO}_2 + \text{F} \qquad k_{5a} = 9.3\times10^{-11}\ \text{cm}^3\ \text{s}^{-1} \qquad (7.5\text{a})$$

$$\text{O}(^1\text{D}) + \text{COF}_2 \rightarrow \text{CO}_2 + \text{F}_2 \qquad k_{5b} = 5.3\times10^{-11}\ \text{cm}^3\ \text{s}^{-1} \qquad (7.5\text{b})$$

Although PFC dissociation primarily takes place through electron impact, there are several other pathways (e.g. dissociative charge transfer with O^+, Ar^+, F^+, and F_2^+) for dissociaiton. For example, approximately 62% of CF_3 production is by direct electron impact of C_2F_6 and 10% results from charge transfer reactions.

In our baseline case, the effluent comes into the burn-box through the top of the reactor while O_2 is injected through a ring nozzle pointing radially inward. The plasma burn-box is cylindrical with an inner radius of 2.5 cm and a length of 26.5 cm. Two coils are placed near the middle of the tube with a power deposition of 500 W. The effluent from the plasma-etching reactor operating at $Ar/C_2F_6 = 40/60$, 200 sccm flowrate and 350 W power is used as input. This case was selected because its effluent contains a relatively high mole fraction of C_2F_6 (0.289) with a variety of other C_xF_y species (0.173 CF_3, 0.057 CF_4, 0.055 CF_2, 0.011 C_2F_4, and 0.02 C_2F_5). In addition, 150 sccm O_2 is injected from the nozzle on the side wall. The power deposition, electron density, electron temperature, and plasma potential for this case are shown in Fig. 7.11. The peak electron density is $\approx 1.2 \times 10^{12}$ cm^{-3} with an off-axis maximum located 7.3 mm from the side wall. The inductively coupled power deposition has a maximum of 15 W/cm^3 and is located approximately 3.3 mm inside the quartz tube. These peak values are larger than the plasma etching chamber due to the higher power density (W/cm^3) and the shorter electron energy relaxation length at the higher pressure. The distance of the peak power deposition from the wall is smaller than that in the plasma etching reactor due to the shorter skin depth resulting from a higher electron density. The electron temperature, peak value 3.1 eV, varies moderately near the coils in the radial direction and extends as a "hot zone" about 5 cm above and below the coils.

As the gas passes through the volume rear the coils, the O_2 density rapidly decreases due to electron impact dissociation and ionization while the O density increases, as shown in Fig. 7.12. For our baseline case, CF_2 CF_3, C_2F_3, C_2F_4, and C_2F_5 are nearly totally eliminated (~100%), and C_2F_6 is decreased by 53% in passing through the burn-box. As shown in Figs. 7.12 and 7.13, their concentrations significantly decrease as the gas flow passes through the region near the coils where the oxygen radicals and electron densities are large. ($O(^1D)$ and O^+ have high densities only in plasma region since they react with other species or quench quickly after being generated.) The concentrations of major oxidation products (CO, CO_2, COF_2) increase downstream of the coil region as does CF_4, as shown in Fig. 7.14. These oxidation products can be remediated by conventional means. For example, COF_2 is easily removed by processing the gas stream through a water bubbler or water spray. This method is also effective at removing the other major byproducts, such as F and F_2. CO can be converted to CO_2 using a platinum catalyst. However CF_4 is an undesirable by-product since it is also a PFC with high global warming potential. A summary of the abatement efficiencies and end-products for the base case appears in Table 7.2.

Note that a significant amount of CF_4 is produced above the inlet value due to back diffusion of F atoms produced lower in the reactor, which recombine with CF_3. The total amount of CF_4 in the gas stream actually increases by a factor of 2.4 for the base case. CF_4 is primarily generated by recombination,

$$CF_3 + F \xrightarrow{M} CF_4. \tag{7.6}$$

The rate coefficient for this process is strongly dependent on gas temperature and pressure. At 150 mTorr the rate coefficient is [8]

$$k_7 = 4.9\times10^{-9}\left(\frac{T_g}{300}\right)^{-7.84}\exp\left(-\frac{1876.4}{T_g}\right)\text{cm}^{-3}\text{ s}^{-1}. \tag{7.7}$$

The rates coefficient decreases by a factor of 4.5 by increasing the temperature from 300 K (k = 9.42 × 10^{-12} cm^3s^{-1}) to 500 K (k = 2.09 × 10^{-12} cm^3s^{-1}) and a factor of 158 with a temperature increase to 1000 K (k = 5.97 × 10^{-14} cm^3s^{-1}). Therefore, generating CF_4 could be reduced if the gas temperature is increased. For the base case, the wall temperature is fixed at 400 K, resulting in a mean gas temperature in the burn-box of ≈500 K, at which the rate coefficient for CF_4 formation is still large. By increasing the wall temperature, the bulk gas temperature also increases, and the CF_4 in the exhaust decreases. This trend is shown in Fig. 7.15. The remaining C_2F_6 also decreases as the wall and gas temperatures increase (and gas densities decrease) due to more favorable overlap of the region of high-power deposition with the flow field of the C_2F_6. The electron density shifts toward the center of the reactor due to the lower gas density.

The abatement of C_2F_6 and the generation of CF_4 are shown in Fig. 7.16 as a function of power and injected O_2 for the output effluent from the plasma etching reactor for the base case. [These results were obtained by performing a design-of-experiments and using a quadratic model (with cross terms) to fit the results to a response surface. A portion of the curvature of the surfaces results from the fit.] C_2F_6 abatement increases with increasing power and O_2 injection since there is more dissociation of O_2 and more subsequent reactions of O [and $O(^1D)$] with CF_x radicals. At low injected O_2, CF_4 generation increases with increasing power since much of the CF_3 produced by the dissociation of C_2F_6 is converted to CF_4 instead of reacting with oxygen radicals. At higher amounts of injected O_2, CF_4 generation decreases with increasing power since the CF_3 from the dissociation of C_2F_6 and other C_xF_y is converted rapidly to COF_2 in the oxygen-radical-rich environment. The transition is at about 90 sccm of injected O_2 for these conditions. These trends generally agree with Hartz et al. [7].

The abatement efficiency h is defined as the sum of the output flow rate of C_xF_y species weighted by the number of F atoms divided by the input flow rate,

$$h = 1 - \frac{\sum_i [f_i(\mathrm{C}_x\mathrm{F}_y)\cdot y]_{output}}{\sum_i [f_i(\mathrm{C}_x\mathrm{F}_y)\cdot y]_{input}} \tag{7.8}$$

where f_i is the flow of the ith C_xF_y species in sccm. We again prejudice the calculation of efficiency by assuming that larger C_xF_y are "less good." Both h and the W-value for destruction are shown in Fig. 7.17 for the conditions of Fig. 7.16. The efficiency h increases with increasing power deposition and the amount of injected O_2 due to there being more CF_x radical and O atom generation. However the W-value increases (lower power efficiency) with increasing power deposition (and particularly so at lower O_2

injection) since at higher power deposition more power is expended to further dissociate the products (e.g., COF_2 and CO_2).

7.3.3 H_2 as an additive for PFC abatement

In this subsection, we investigate H_2 as an additive gas for PFC abatement. Electron impact dissociation of H_2 generates H, which in turn becomes the primary species for abating CF_x radicals. The dominant abatement reactions are [9,10]

$$CF_3 + H \rightarrow CF_2 + HF, \qquad k_{9a} = 9.0\times10^{-11}\ \mathrm{cm^3\ s^{-1}} \qquad (7.9a)$$

$$CF_2 + H \rightarrow CF + HF, \qquad k_{9b} = 3.9\times10^{-11}\ \mathrm{cm^3\ s^{-1}} \qquad (7.9b)$$

$$CF + H \rightarrow C + HF, \qquad k_{9c} = 1.9\times10^{-11}\ \mathrm{cm^3\ s^{-1}} \qquad (7.9c)$$

In mixtures containing H_2, another significant process is the reaction between H_2 and F [9],

$$H_2 + F \rightarrow H + HF \qquad k_{10} = 1.43\times10^{-10}\exp(-528/T_g)\ \mathrm{cm^3\ s^{-1}} \qquad (7.10)$$

which can substantially reduce the F atom density. The decrease in higher-order CF_x radicals and the reduction in the availability of free fluorine further reduce the production of PFCs by reassociation, particularly so for CF_4.

The standard case is the same as that for using O_2 as an additive except that H_2 is injected at 150 sccm instead of oxygen. Selections of the results for the standard case are in Figs. 7.18 and 7.19, where the electron density and densities of C_2F_6, CF_4, CF_3, CF_2, CF, HF, and C are shown. Compared to the case using O_2 as the additive, the profile of the electron density is more extended due to the lower rate of attachment to H_2, and the maximum electron density is increased by a factor of 2.1. The concentrations of C_2F_6, CF_4, and CF_3 decrease, and the concentrations of CF, HF, and C increase as the gas passes through the region of high plasma density. HF is the major product (0.49) leaving the burn-box with there being lesser amounts of CF (0.094), C (0.074) and CF_2 (0.041). The higher mole fractions of CF and CF_2 in the exhaust gas compared to using O_2 as the additive are due in part to there being insufficient H to reduce them to C. C_2F_6 and CF_3, the two primary C_xF_y species in the etching reactor effluent, are abated by 54.7% and 95.5%, respectively. (See Table 7.2 for other C_xF_y species.) The CF_4 mole fraction, which is increased by 240% when using O_2 as an abatement addictive gas, is reduced by 23.5%. However, there is a significant increase in the amount of C_2F_4 (by a factor 2.4) due to the relatively high concentration of CF_2. C_2F_4 is still, however, a small mole fraction (<1%) in the exhaust.

The abatement efficiency η and *W*-value for C_xF_y species as a function of power deposition and the amount of injected H_2 are shown in Fig. 7.20. Note that we chose a larger input of H_2 compared to the DOE using O_2 since three H_2 molecules are needed to remove all the F atoms in a C_2F_6 molecule. Only a single O_2 molecule is needed to oxidize a C_2F_6 if the oxidation product is CO or COF_2, and two O_2 molecules are required if the oxidation product is CO_2. At high power and high H_2 feed, almost all of the C and F atoms, which are initially bound in C_xF_y species, are converted to C and HF. As a consequence, η approaches 100%. As with using O_2 as an additive, increasing power deposition also increases the *W*-value of C_xF_y (less efficient).

7.3.4 H_2O as an additive for PFC abatement

H_2O is another promising additive for abating PFCs [11]. When using H_2O as an additive, electron impact dissociation produces O, H, and OH radicals. As discussed above, H and O are precursors for PFC remediation; however, OH can also remediate PFCs by both oxidizing CF_x and preventing its reassociation to make CF_4 [9]:

$$OH + CF_3 \rightarrow COF_2 + HF, \qquad k_{11a} = 3.32\times10^{-11}\ cm^3\ s^{-1} \qquad (7.11a)$$

$$OH + CF_2 \rightarrow COF + HF, \qquad k_{11b} = 6.64\times10^{-12}\exp(-1762.5/T_g)\ cm^3\ s^{-1} \qquad (7.11b)$$

$$k_{11b}(500\ K) = 2.0\times10^{-13}\ cm^3\ s^{-1}$$

$$OH + CF \rightarrow CO + HF, \qquad k_{11c} = 6.64\times10^{-11}\exp(-503/T_g)\ cm^3\ s^{-1} \qquad (7.11c)$$

$$k_{11c}(500\ K) = 2.4\times10^{-11}\ cm^3\ s^{-1}$$

$$OH + CO \rightarrow CO_2 + HF, \qquad k_{11d} = 1.18\times10^{-9}\left(\frac{T_g}{300}\right)^{0.98}\exp\left(\frac{94.03}{T_g}\right)cm^3\ s^{-1} \qquad (7.11d)$$

$$k_{11d}(500\ K) = 2.3\times10^{-9}\ cm^3\ s^{-1}$$

H_2O can also directly react with F, which acts as a sink to remove free fluorine atoms that might otherwise recombine to form CF_4.

$$F + H_2O \rightarrow OH + HF \qquad k_{12} = 1.11\times10^{-11}(T_g/300)^{1.5}\ cm^3\ s^{-1}. \qquad (7.12)$$

$$k_{12}(500\ K) = 2.4\times10^{-9}\ cm^3\ s^{-1}$$

This reaction generates OH, which is then available for further remediation, thereby forming a chain reaction.

To examine the utility of H_2O as an additive gas for the abatement of PFCs, the standard burn-box case was modeled using 150 sccm of water vapor as an additive gas at 500 W power deposition. The results show that H_2O is more effective for PFC abatement than either O_2 or H_2 in agreement with experiments by Tonnis et al. [11]. For example, the two major C_xF_y species in the etching effluent, C_2F_6 and CF_3, are abated by 73% and 98% without there being additional CF_4 generation. CF_4 (a minority C_xF_y species in the etching effluent) is reduced by 9.7%. Other C_xF_y species are also decreased to different extents as shown in Table 7.2. The exception is that there is a slight increase of C_2F_4. Selections of results for electron, C_2F_6, CF_3, and CF_4 densities are shown in Fig. 7.21. The electron density is higher than the base case with O_2 as an additive, but lower than for H_2, due largely to the rate of attachment of H_2O being between O_2 and H_2. The major products are HF, COF_2, CO, and C, as shown in Fig. 7.22. For the base case, the F atoms that were initially bound in all C_xF_y were converted to products in the following proportions: HF, 59.8%, and COF_2, 40%. Only traces of F are in other species (COF, F_2, FO, F, and CF_3O_2). The carbon atoms initially bound in C_xF_y were converted to products in the following proportions: COF_2, 63.3%; CO, 31.4%; C, 3.9%; and CO_2, 1.4%. At higher power and higher water vapor input, all C_xF_y can be decreased to low concentrations. For example, h and W-values for C_xF_y species as a function of power and injected water vapor are shown in Fig. 7.23. High h is obtained at high powers with a rich input feed of H_2O. Low W-value (high efficiency) is obtained at high input H_2O

flowrates with low power. These trends are similar to the cases using H_2 additive except for there being a higher efficiency and lower *W*-value.

7.4 Concluding Remarks

Results from a computational investigation of the consumption and generation of PFCs in an ICP etching reactor for Ar/C_2F_6 and Ar/CF_4 gas mixtures and the abatement of the effluent in an ICP burn-box have been discussed. The model was validated by comparison to experiments by Sawin and Vitale [6] using C_2F_6/O_2 mixtures. C_2F_6 (or CF_4) consumption in the etching reactor is proportional to ICP power deposition, and inversely proportional to C_2F_6 mole fraction and total gas flow rate. We found a ceiling of 158 eV/molecule for consumption of C_2F_6 and 175 eV/molecule for CF_4 for our baseline cases, Ar/C_2F_6 (or Ar/CF_4) = 60/40 at 500 W power deposition. The generation of C_xF_y in the effluents for Ar/C_2F_6 gas mixtures is approximately twice that for Ar/CF_4 gas mixture under the same conditions. There is slightly more generation of F and F_2 for the CF_4 feedstock gas.

In general, CF_4 generation occurs during abatement of C_2F_6 using O_2 as an additive, especially for high power with low O_2 input due to low concentrations of O and $O(^1D)$ atoms while there are large densities of F and CF_3. At high gas temperatures, there is a significant reduction of CF_4 generation since the rate coefficient for recombination of CF_3 and F is strongly dependent on temperature. The major oxidation products are COF_2, CO and CO_2. H_2 can be used as an alternative to O_2 for an abatement additive without producing CF_4 since hydrogen reacts rapidly with free fluorine which would otherwise reassociate with CF_x to form CF_4. F and C atoms initially contained in C_xF_y were converted to HF and C. Generation of C atoms could be problematic due to their deposition on surfaces. It was also shown that H_2O is a promising and efficient abatement additive gas since it is a source of oxygen, hydrogen and hydroxyl radicals, produced in beneficial mole fractions. The primary products of abatement using water vapor are HF, CO, COF_2 with small amounts of C and CO_2.

Table 7.1 Reactive sticking coefficients for species on walls and wafer.

Species	Boundary	Reaction Probability	Species Returning to Plasma
Ar	Walls or Wafer	1.0	Ar
Ar^+	Walls or Wafer	1.0	Ar
Ar^*	Walls or Wafer	1.0	Ar
CF_4	Walls or Wafer	1.0	CF_4
CF_3	Walls or Wafer	0.995	CF_3
	Walls or Wafer	0.005	0.5 C_2F_6
CF_3^+	Walls or Wafer	1.0	CF_3
CF_3^-	Walls or Wafer	1.0	CF_3
CF_2	Walls	0.990	CF_2
	Walls	0.010	0.5 C_2F_4
	Wafer	0.940	CF_2
	Wafer	0.060	0.5 (C_2F_3 + SiF_2)
F	Walls	0.995	F
	Walls	0.005	0.5 F_2
	Wafer	0.900	F
	Wafer	0.100	0.5 SiF_2
F^-	Walls or Wafer	1.0	F
F_2	Walls or Wafer	1.0	F_2
C_2F_3	Walls or Wafer	1.0	C_2F_3
C_2F_4	Walls or Wafer	1.0	C_2F_4
C_2F_5	Walls or Wafer	1.0	C_2F_5
C_2F_6	Walls or Wafer	1.0	C_2F_6
SiF_2	Walls or Wafer	1.0	SiF_2

Table 7.2 Abatement of species, primary products, and W-value of C_xF_y for the standard cases using O_2, H_2 or H_2O as additives.

Species	Fractional abatement[a] for additives $\frac{\text{Initial} - \text{Final}}{\text{Initial}}$		
	O_2	H_2	H_2O
C_2F_6	0.53	0.54	0.73
C_2F_5	>0.99	-0.47	0.37
C_2F_4	>0.99	-2.71	-0.31
C_2F_3	>0.99	0.22	0.35
CF_4	-1.4	0.23	0.04
CF_3	>0.99	0.96	0.98
CF_2	>0.99	-0.42	0.05
Products	COF_2, CO, CO_2, F, F_2	HF ,CF,C	HF, COF_2, CO, CF, C, CO_2
η of all C_xF_y	0.54	0.42	0.65
W value of C_xF_y (eV)	124.9	159.8	119.3

[a] Total abatement has value 1.0. Negative values of abatement denotes net production of that species.

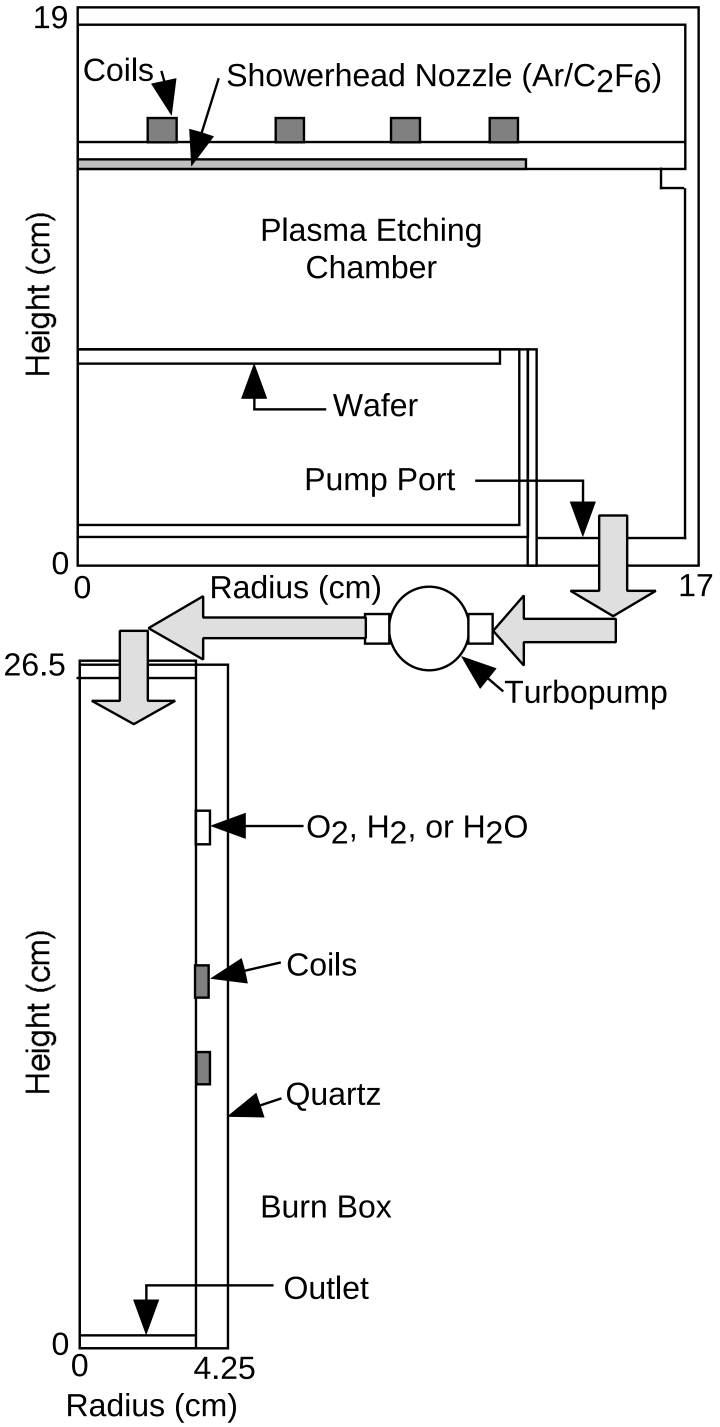

Fig. 7.1. Schematics of the inductively coupled plasma etching reactor and plasma burn-box. The rectangular cross section coils for both of the devices are driven at 13.56 MH. A turbopump is between the etching reactor and burn-box.

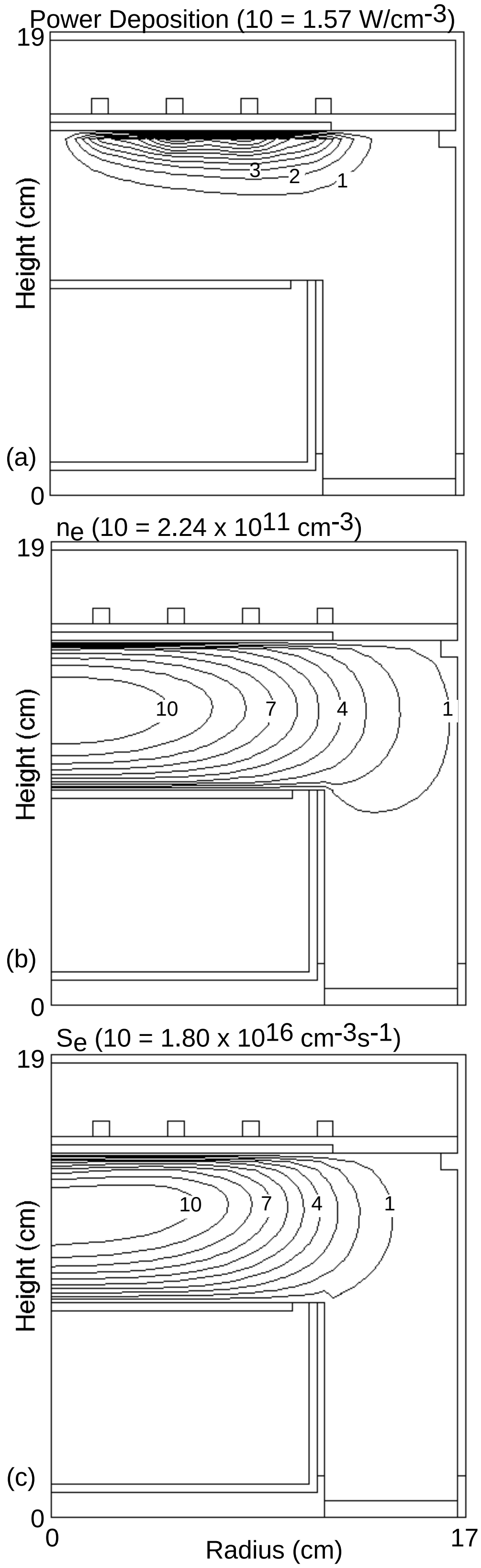

Fig. 7.2. Plasma parameters for the standard case for the plasma etching reactor (Ar/C_2F_6 = 60/40, 10 mTorr, and 650 W inductively coupled power): (a) power deposition, (b) electron density, and (c) electron source by electron impact.

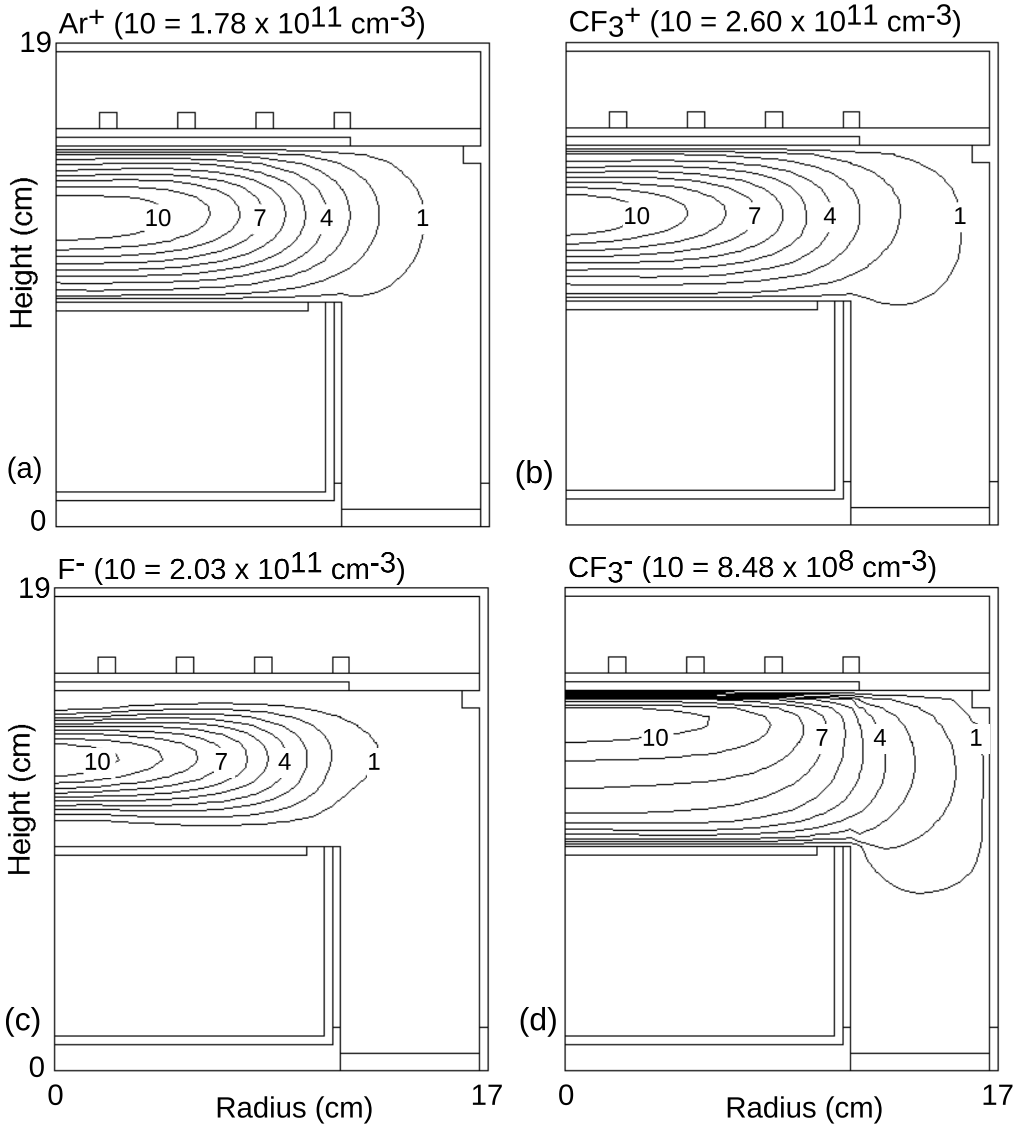

Fig. 7.3. Ion densities for the standard case for the plasma etching reactor: (a) Ar$^+$, (b) CF$_3^+$, (c) F$^-$, and (d) CF$_3^+$. The peak density of CF$_3^+$ is larger than that of Ar$^+$, though there is larger Ar input gas mole fraction. The negative ions are dominated by F$^-$. The contours are labeled by their relative magnitudes with the maximum values noted at the top of each figure.

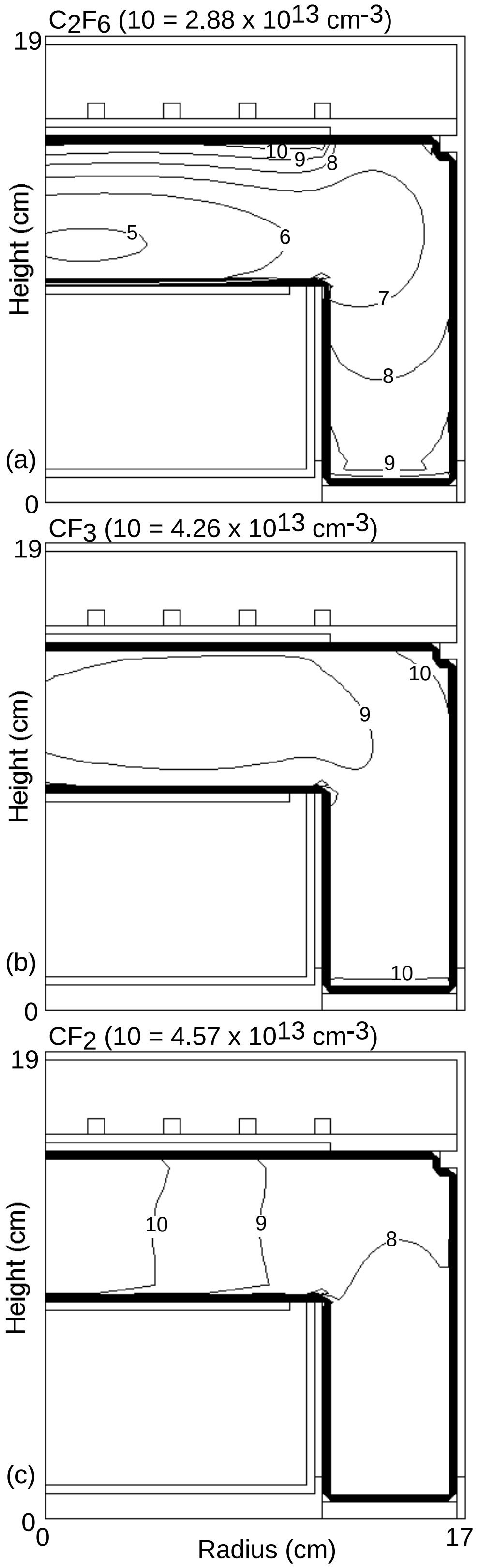

Fig. 7.4. Densities of input PFC and primary CF_x fragment densities for the standard case of a plasma etching reactor: (a) C_2F_6, (b) CF_3, and (c) CF_2. C_2F_6 is quickly dissociated upon injection into plasma. The density of CF_3 increases near surfaces due to recombination of plentiful CF_3^+. The contours are labeled by their relative magnitudes with the maximum values noted at the top of each figure.

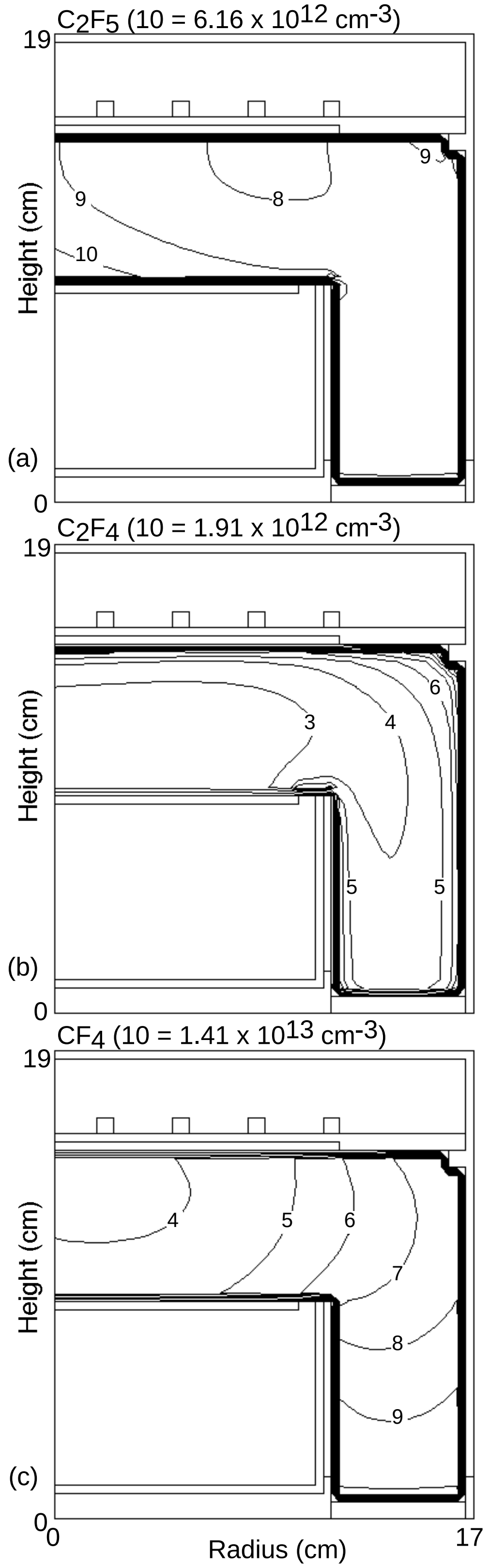

Fig. 7.5. Densities of PFCs generated by the process for the standard case of a plasma etching reactor: (a) C_2F_5, (b) C_2F_4, and (c) CF_4. These species are generated by radical recombination through gas phase and wall reactions.

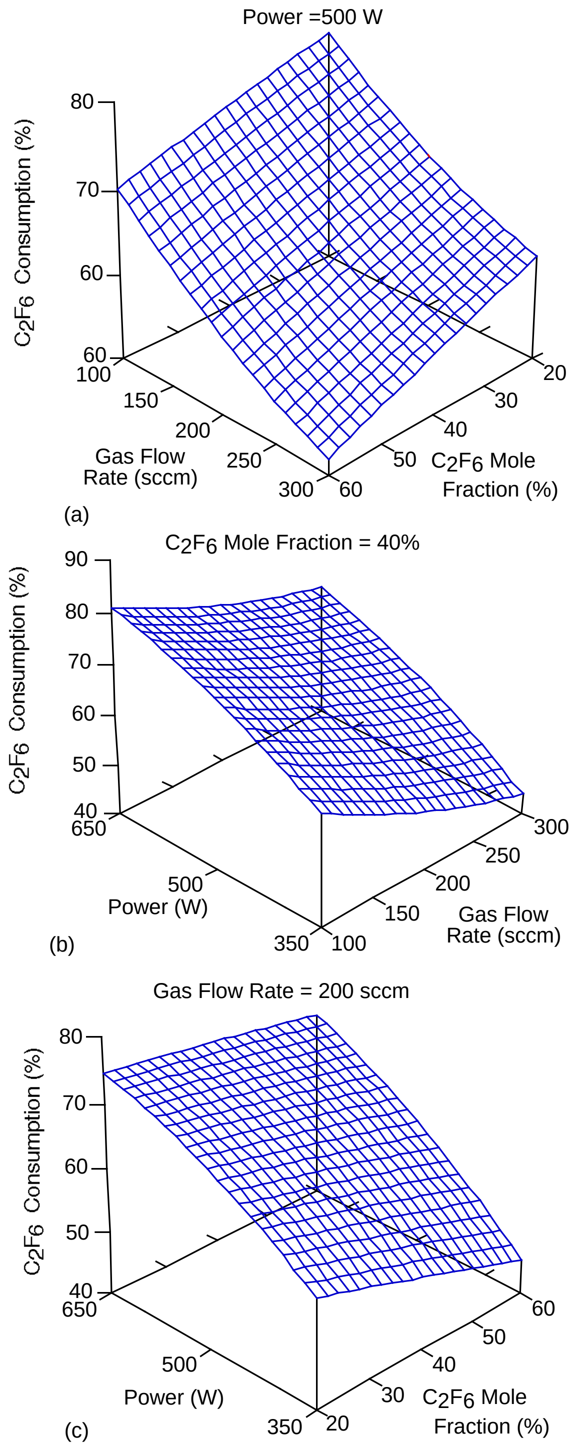

Fig. 7.6. Consumption of C_2F_6 for plasma etching reactor as a function of power, gas flowrate, and C_2F_6 mole fraction. (These figures are the the output of a design-of-experiments whose response surface was fitted with a quadratic with cross terms. Some curvature of the surface results from the numerical fitting. Note that the independent variables have different orientations to obtain a better view angle.) The conditions held constant are: (a) power at 500 W, (b) C_2F_6 mole fraction at 40%, and (c) gas flowrate at 200 sccm. Consumption of C_2F_6 increases with increasing power, decreasing flowrate, and decreasing C_2F_6 mole fraction.

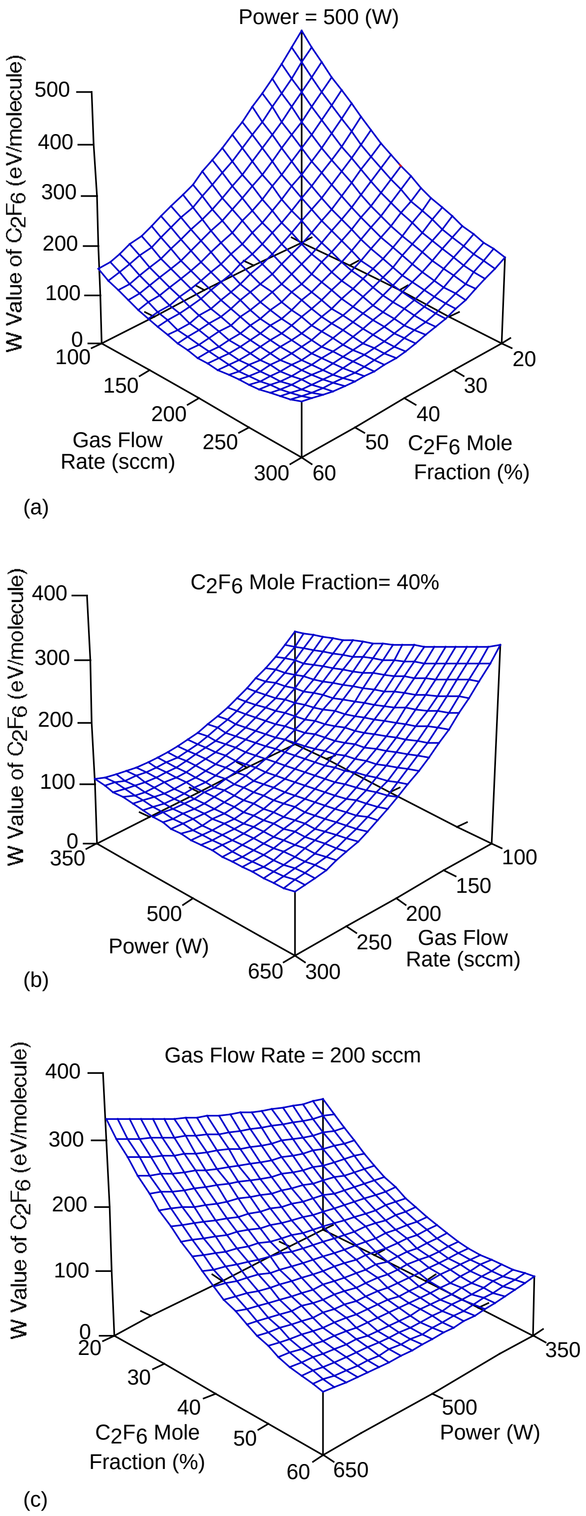

Fig. 7.7. *W*-values (eV/molecule) for consumption of C_2F_6 for the plasma etching reactor as a function of power, gas flowrate, and C_2F_6 mole fraction. The conditions held constant are: (a) power at 500 W, (b) C_2F_6 mole fraction of 40%, and (c) gas flowrate at 200 sccm. Low *W*-values (high efficiency) are obtained at high C_2F_6 mole fraction and high flowrates. There is a weak dependence on power, with lower power being more efficient.

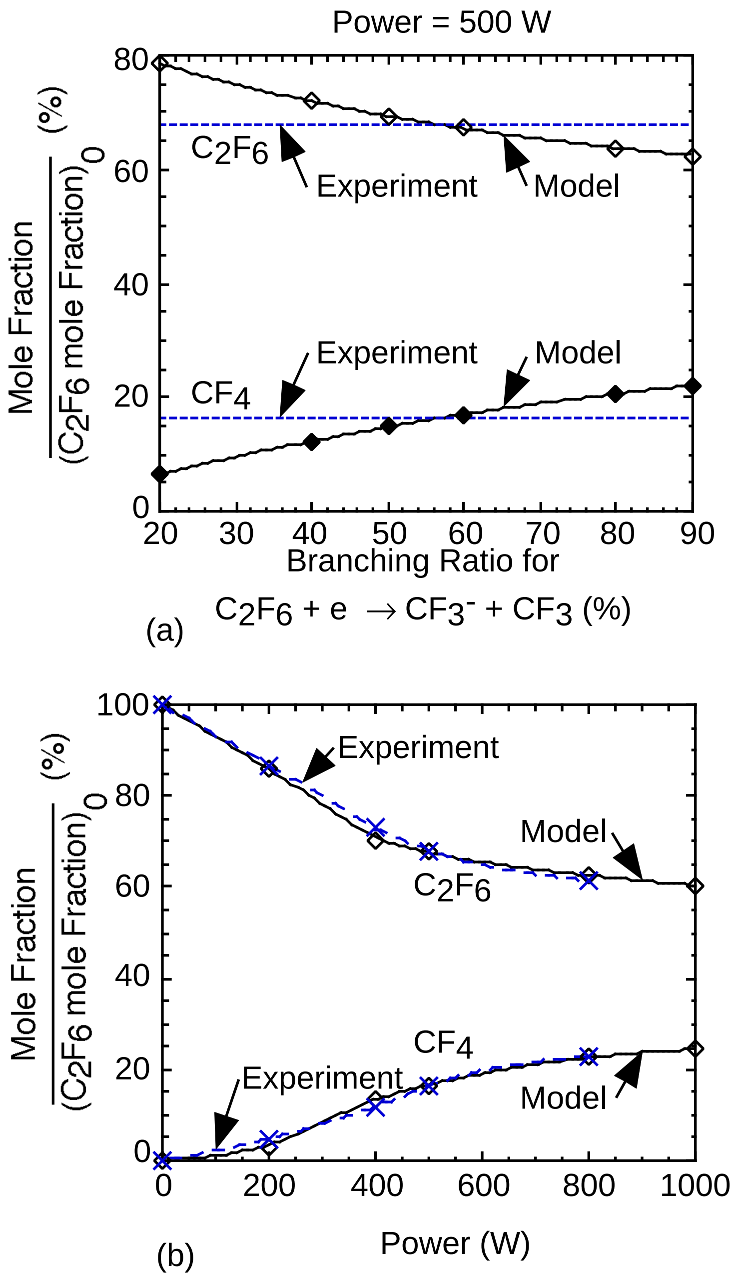

Fig. 7.8. Comparison of the mole fractions of C_2F_6 remaining and the formation of CF_4 obtained from the model and the experiments of Sawin and Vitale for a burn-box with an internal coil (C_2F_6/O_2 = 50/50, 500 mTorr, 400 sccm flowrate): (a) mole fractions as a function of the branching ratio of $e + C_2F_6 \rightarrow CF_3^- + CF_3$ at a power deposition of 500 W and (b) mole fractions as a function of power with a branching ratio of 58%.

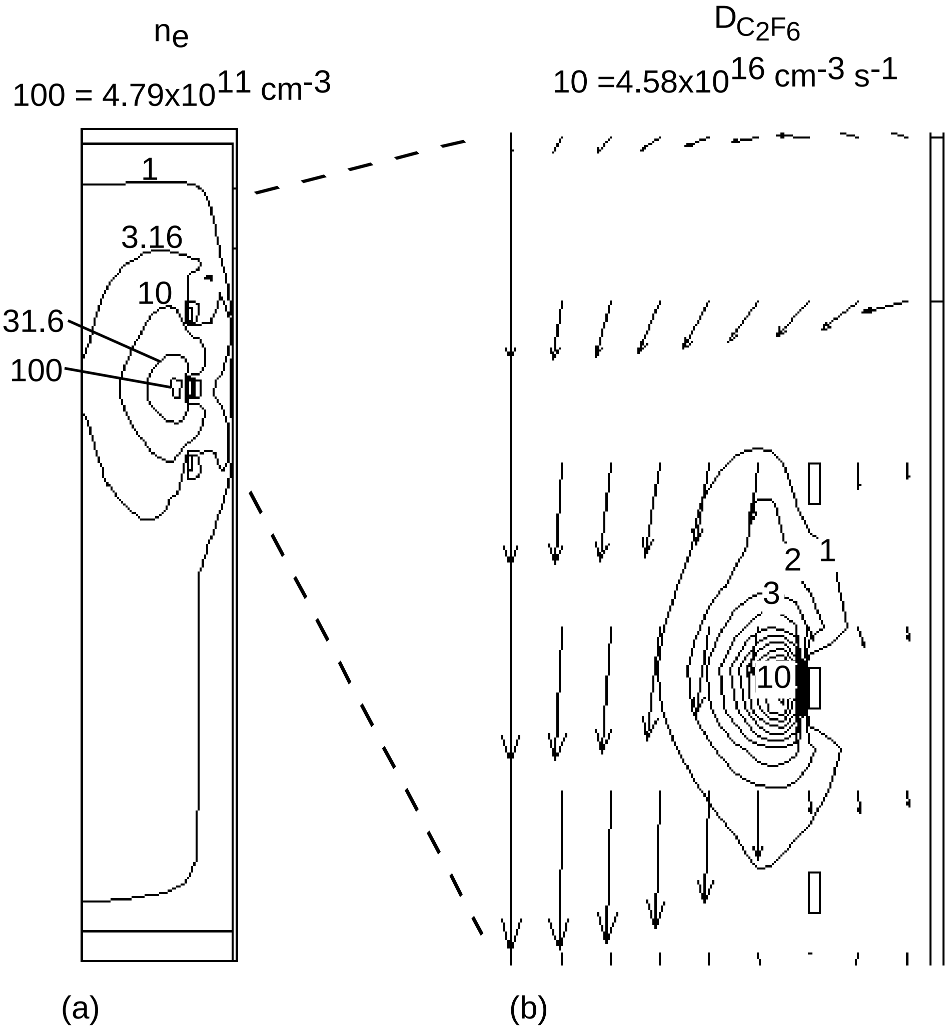

Fig. 7.9. Computed plasma parameters for the 500 W experimental case: (a) electron density (with a logarithm scale) and (b) rate of electron impact dissociation of C_2F_6 with the advective field shown with vectors. The low abatement obtained with this case is partly a consequence of flow through low plasma density regions.

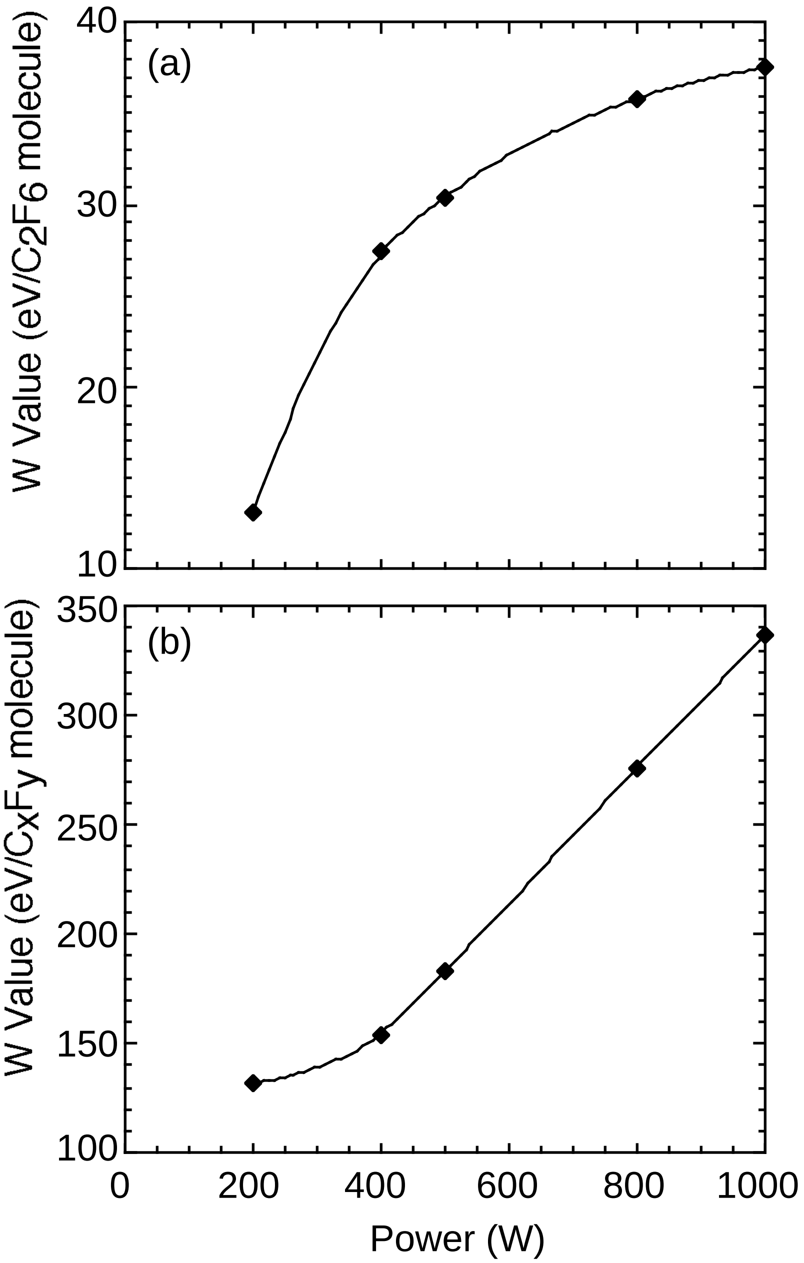

Fig. 7.10. *W*-values as a function of power for the experimental conditions: (a) *W*-values for C_2F_6 destruction and (b) *W*-values for destruction of all C_xF_y. The *W*-value of C_xF_y is higer than that of C_2F_6 primarily since dissociation products of C_2F_6 form other C_xF_y species (as opposed to being oxidized).

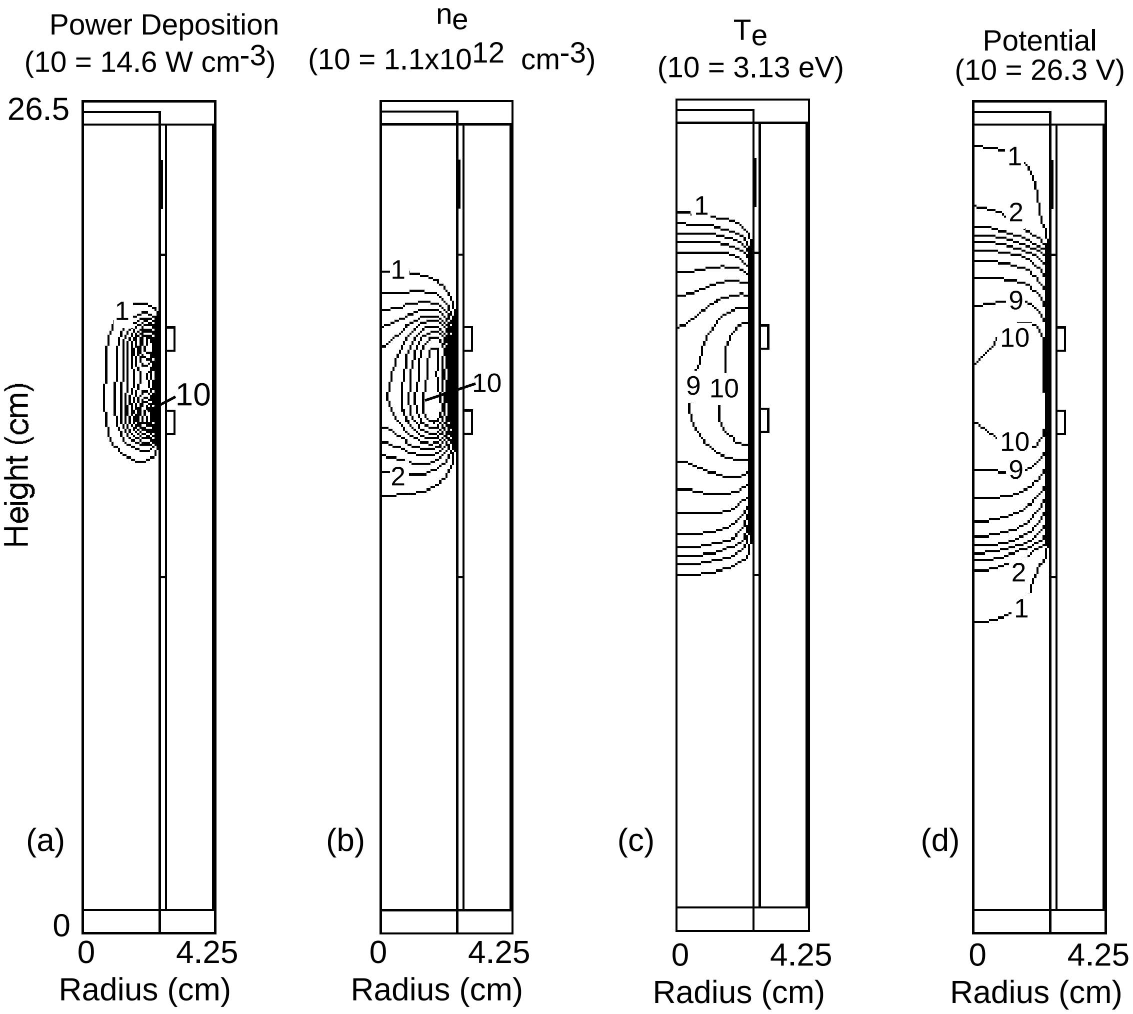

Fig. 7.11. Plasma parameters for the baseline case of plasma burn-box using O_2 as an abatement additive gas. The base-case conditions are using effluent from the plasma etching chamber operating at Ar/C_2F_6 = 40/60, 10 mTorr, 200 sccm, 350 W, and the burn-box operating at 150 mTorr, 500 W with 150 sccm of injected O_2: (a) power deposition, (b) electron density, (c) electron temperature, and (d) plasma potential. The effluent comes in the burn-box through the top of the reactor and O_2 is injected through a ring nozzle pointing radially inward. The contours are labeled by their relative magnitudes with the maximum values noted at the top of each figure.

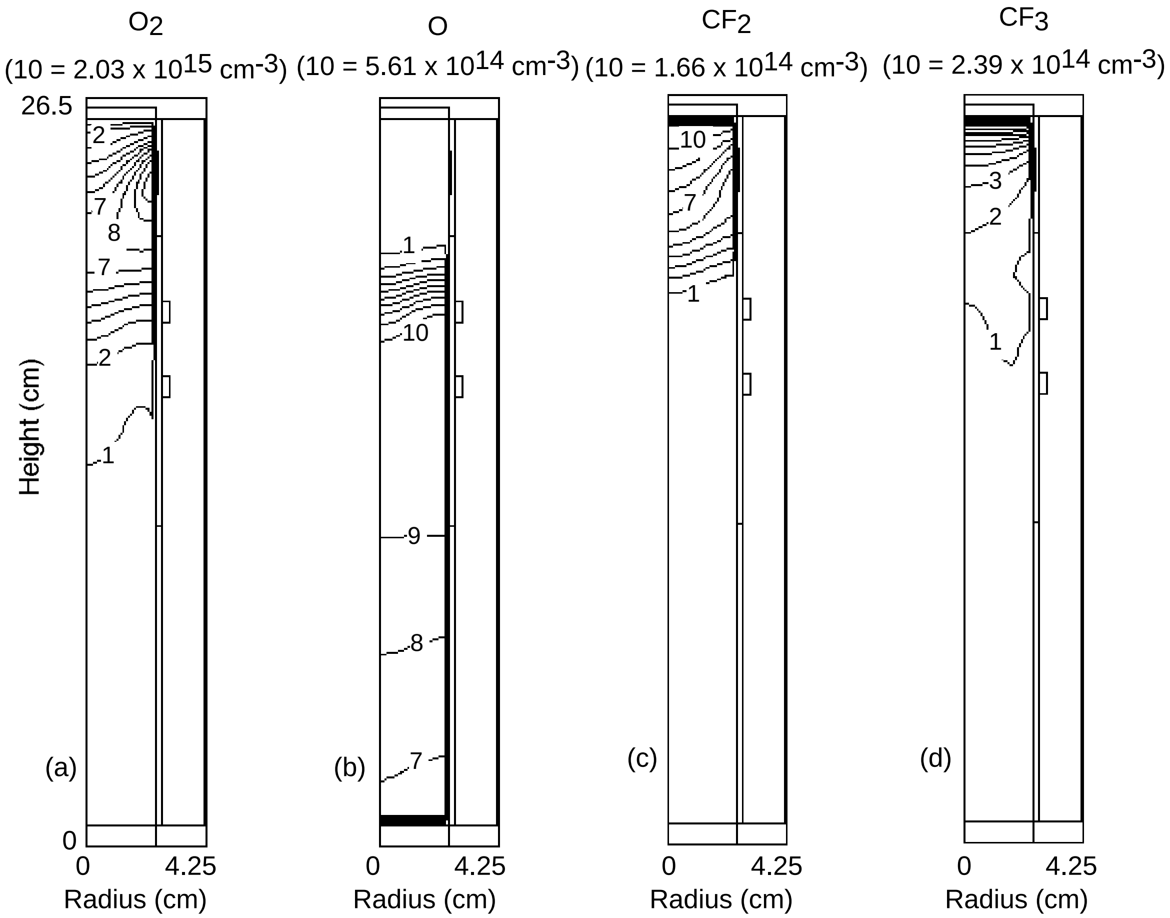

Fig. 7.12. Species densities for the baseline case of the plasma burn-box using O_2 as an additive: (a) O_2, (b) O, (c) CF_2, and (d) CF_3. O_2 is largely consumed in the plasma zone generating O radicals. CF_n is largely oxidized as it passes through the plasma zone. The contours are labeled by their relative magnitudes with the maximum values noted at the top of each figure.

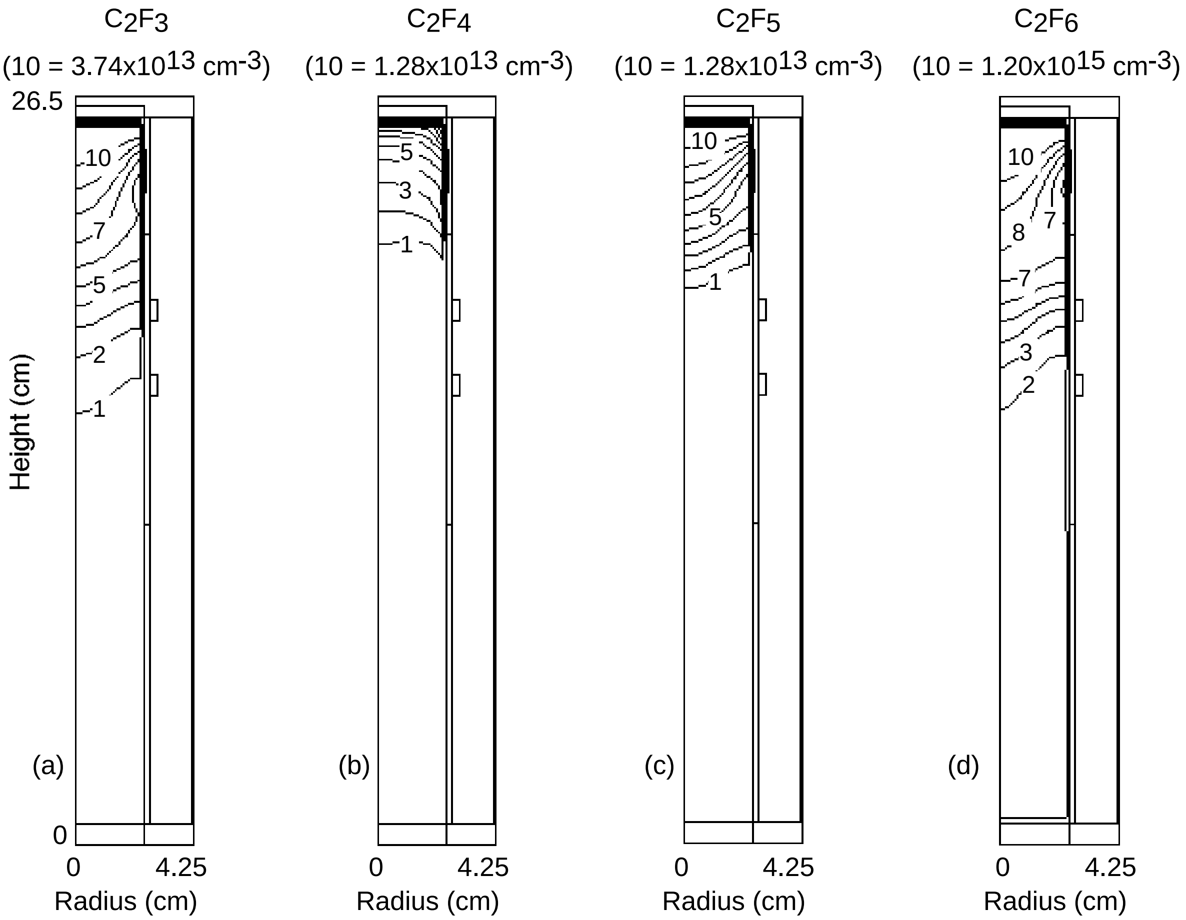

Fig. 7.13. Species densities for the baseline case of the plasma burn-box using O_2 as an additive: (a) C_2F_3, (b) C_2F_4, (c) C_2F_5, and (d) C_2F_6. Injected PFCs are largely abated by electron impact dissociation followed by oxidation. The contours are labeled by their relative magnitudes with the maximum values noted at the top of each figure.

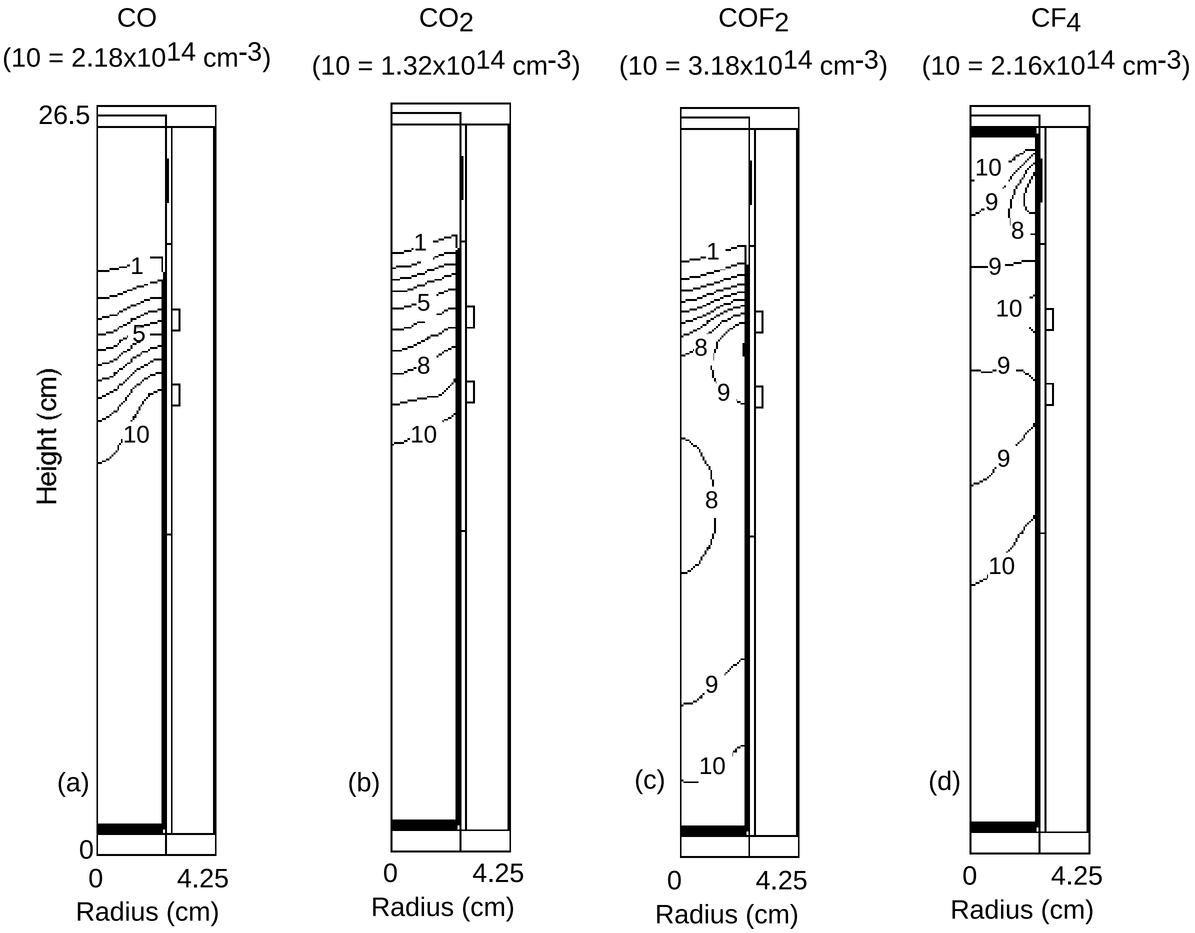

Fig. 7.14. Species densities for the baseline case of the plasma burn-box using O_2 as an additive: (a) CO, (b) CO_2, (c) COF_2, and (d) CF_4. Oxidation products are geneated as the effluent passes through the plasma zone. Production of CF_4 occurs throughout the reactor. The contours are labeled by their relative magnitudes with the maximum values noted at the top of each figure.

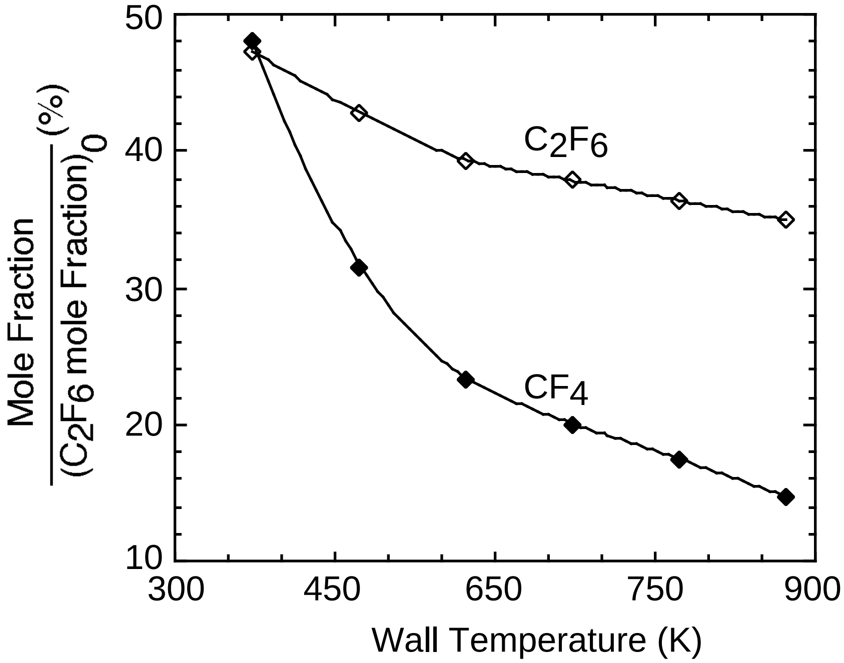

Fig. 7.15. C_2F_6 and CF_4 in the output stream (normalized by their input values) as a function of wall temperature for the baseline case of the plasma burn-box using O_2 as an additive. Increasing wall and therefore gas temperature reduces the rate of CF_4 recombination.

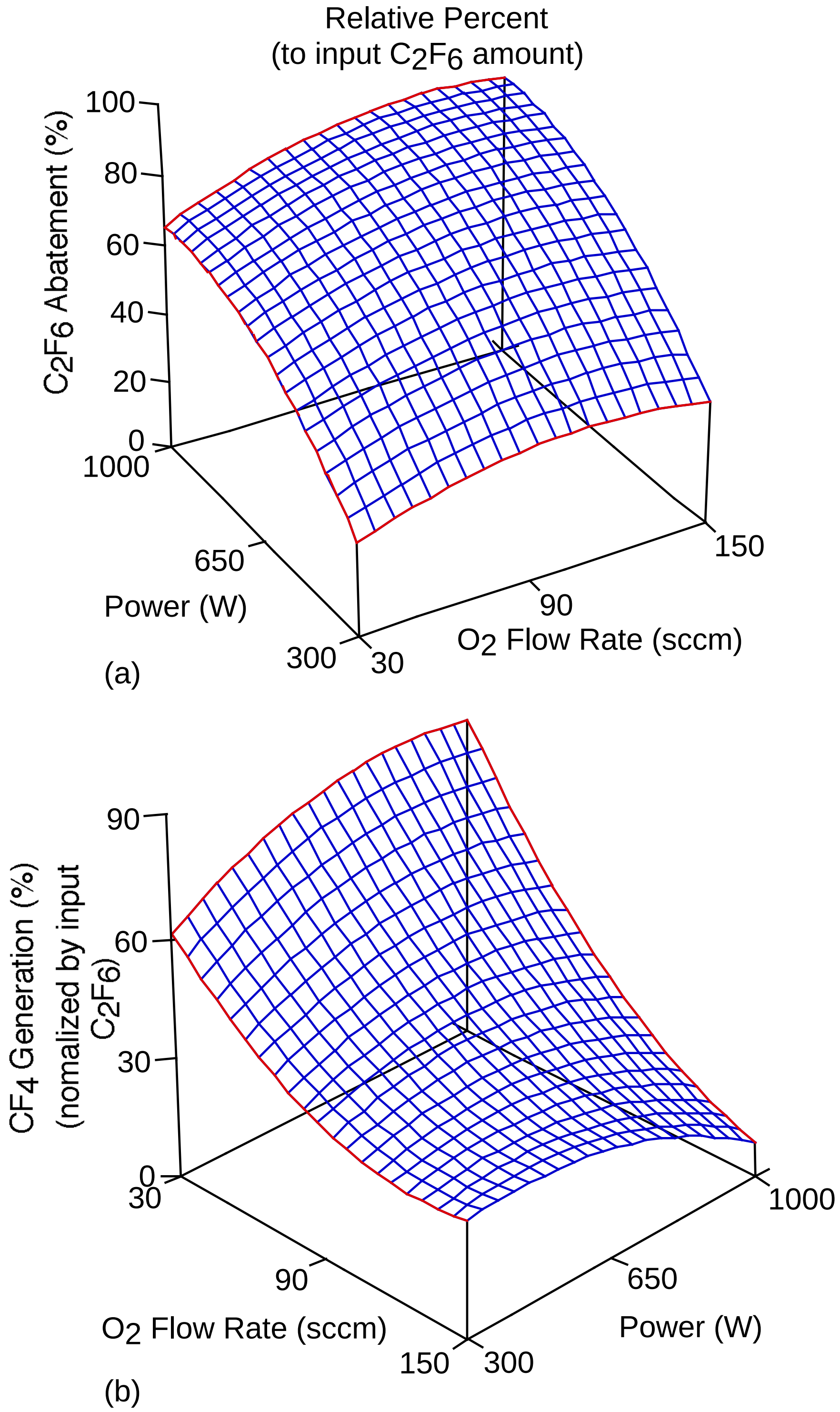

Fig. 7.16. Consumption of C_2F_6 and formation of CF_4 as a function of power and injected O_2 in the plasma burn-box: (a) abatement of C_2F_6 and (b) generation of CF_4 normalized by the input C_2F_6 flow rate. (These figures are the the output of a design of experiments whose response surface was fitted with a quadratic with cross terms. Some curvature of the surface results from the numerical fitting. Note that the independent variables have different orientations to obtain a better view angle.) CF_4 generation is most problematic at high powers and low oxygen flow rates.

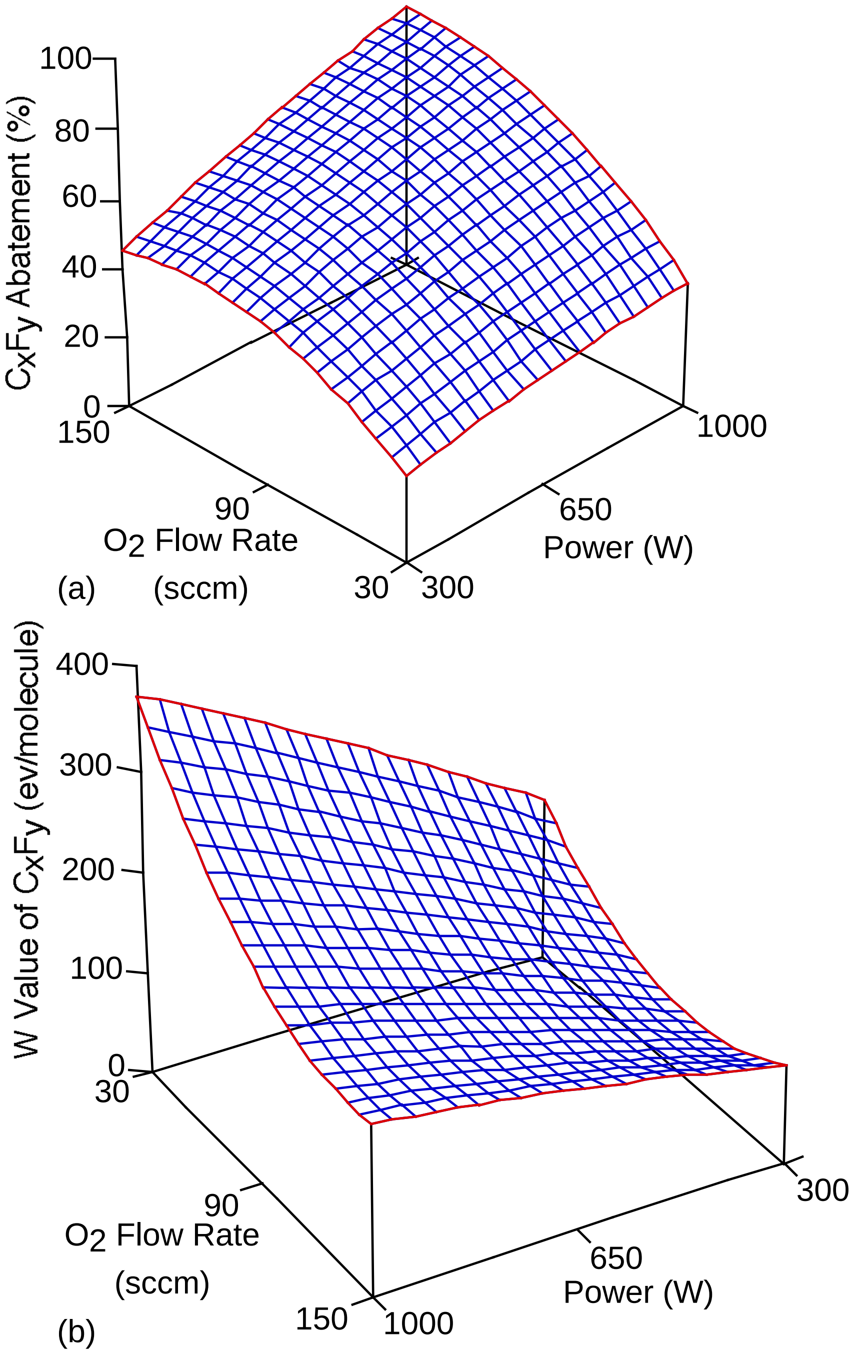

Fig. 7.17. Efficiencies for removal or conversion of all C_xF_y as a function of power and injected O_2 in the plasma burn-box: (a) fractional C_xF_y abatement and (b) W-value for C_xF_y abatement (Note that the independent variables have different orientations to obtain a better view angle.) Although abatement maximizes at high power and high oxygen flow rate, the efficiency is low (high W-value).

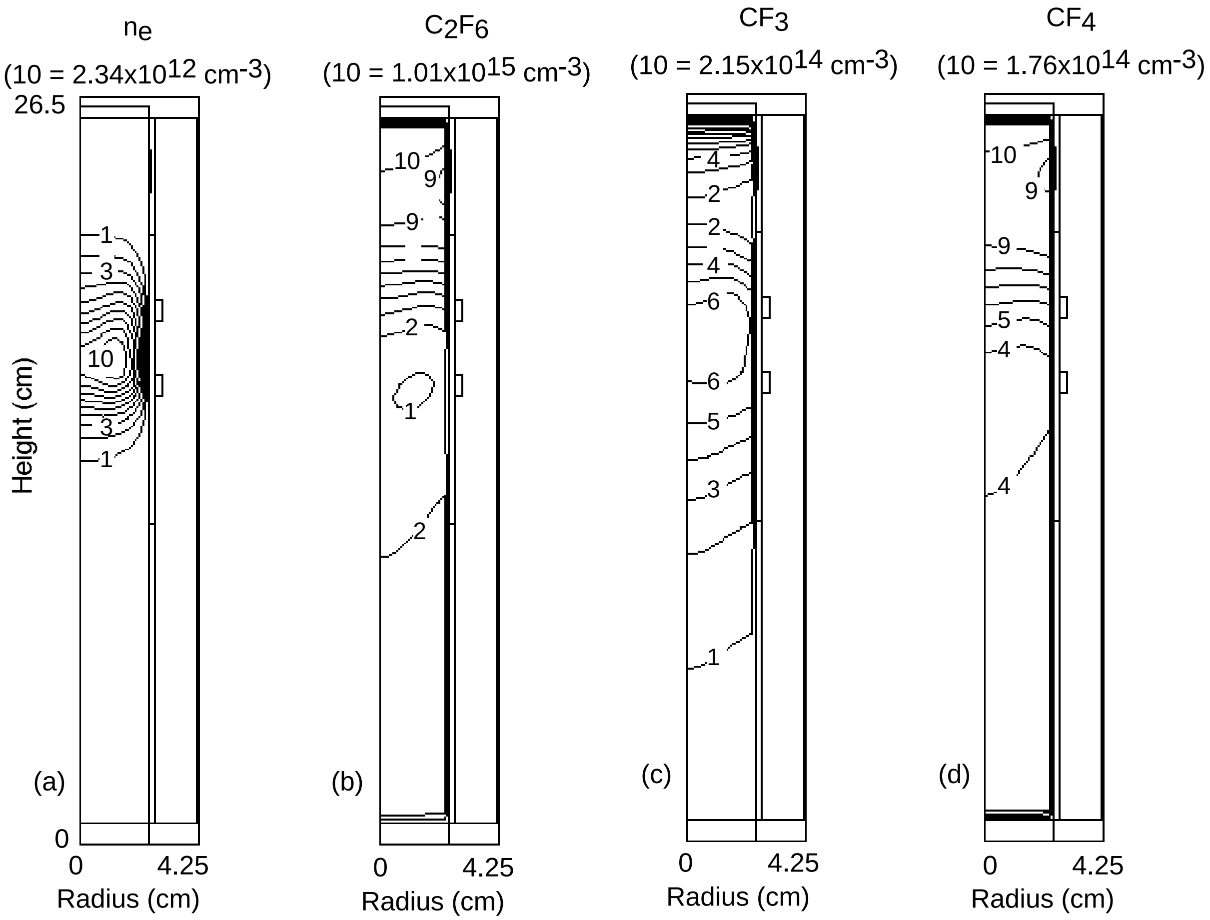

Fig. 7.18. Species densities for the baseline case of the plasma burn-box using H_2 as an abatement additive gas: (a) electron density, (b) C_2F_6, (c) CF_3, and (d) CF_4. The plasma is more diffuse compared to using O_2 as an additive due to the lower rate of attachment to H_2. The contours are labeled by their relative magnitudes with the maximum values noted at the top of each figure.

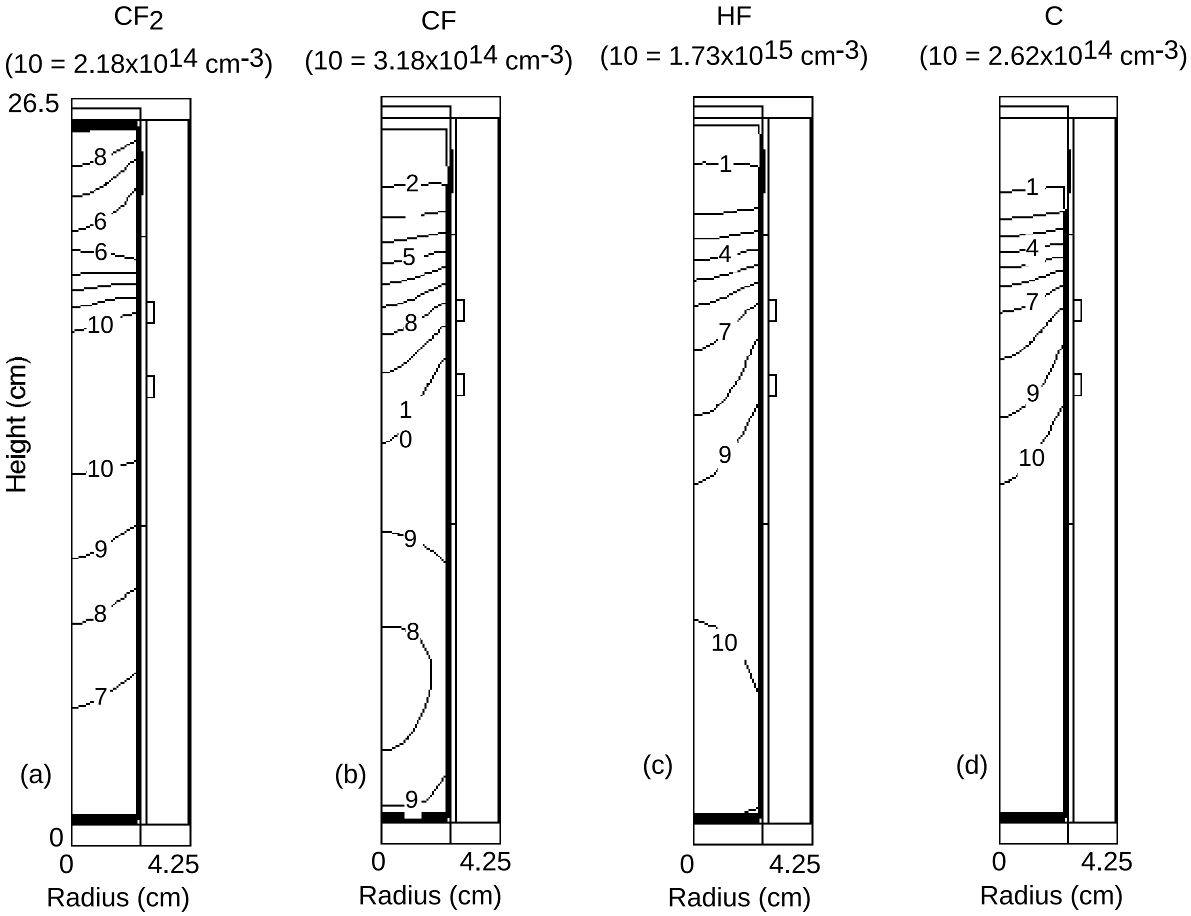

Fig. 7.19. Dissociation products and final product densities for the baseline case of the plasma burn-box using H_2 as an additive: (a) CF_2, (b) CF, (c) HF, and (d) C. The contours are labeled by their relative magnitudes with the maximum values noted at the top of each figure.

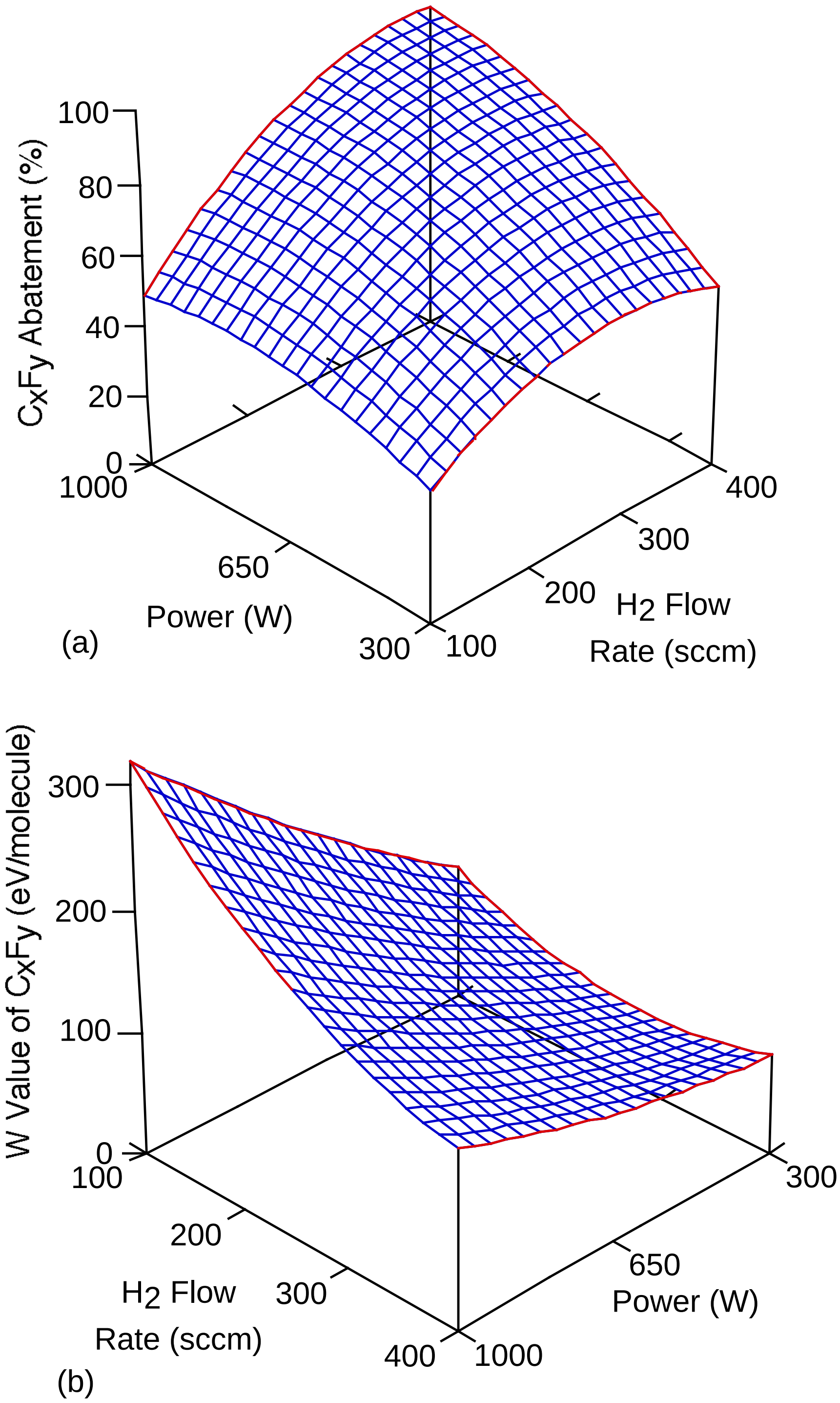

Fig. 7.20. Efficiencies for abatement of all C_xF_y as a function of power and injected H_2 in the plasma burn-box: (a) fractional C_xF_y abatement and (b) *W*-value for C_xF_y. (Note that the independent variables have different orientations in order to obtain a better view angle.).

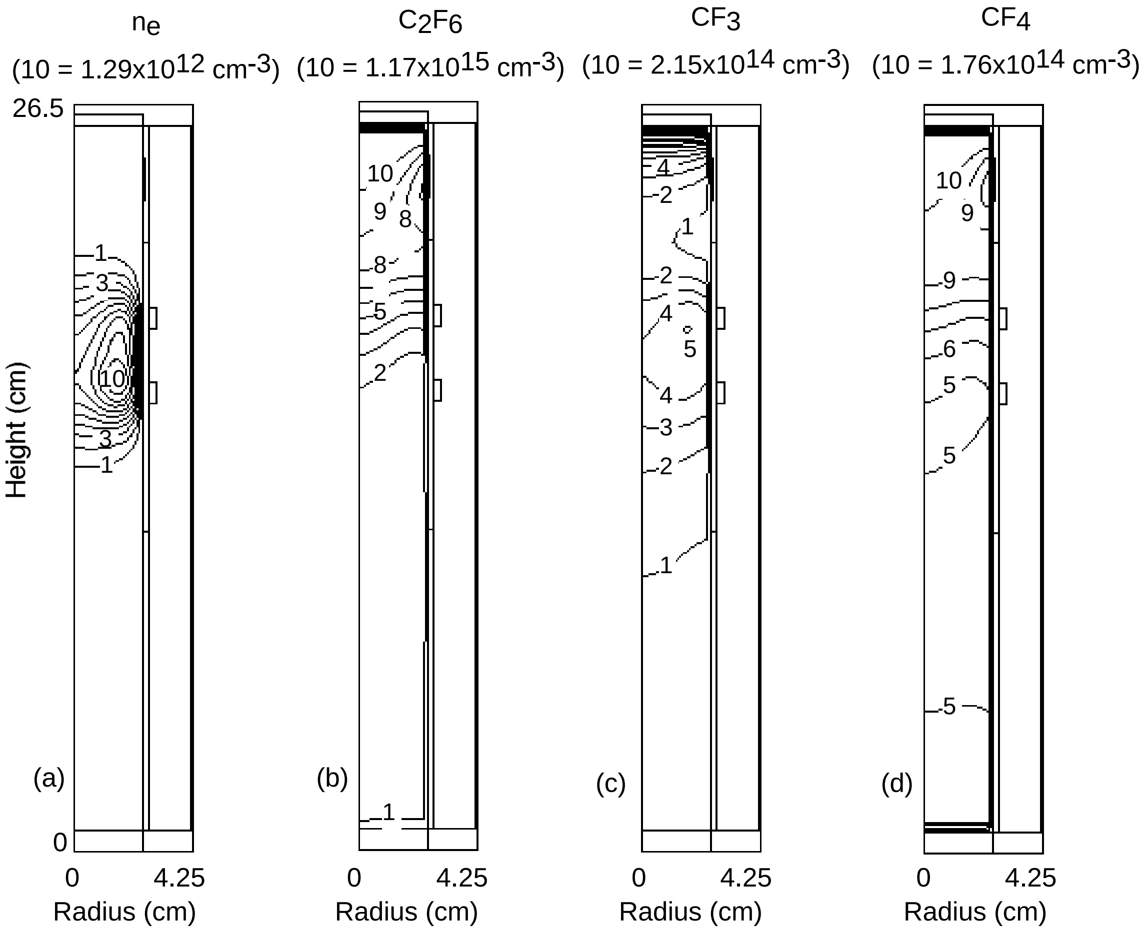

Fig. 7.21. Species densities for the baseline case of the plasma burn-box using H_2O as an abatement additive gas: (a) electron density, (b) C_2F_6, (c) CF_3, and (d) CF_4. The contours are labeled by their relative magnitudes with the maximum values noted at the top of each figure.

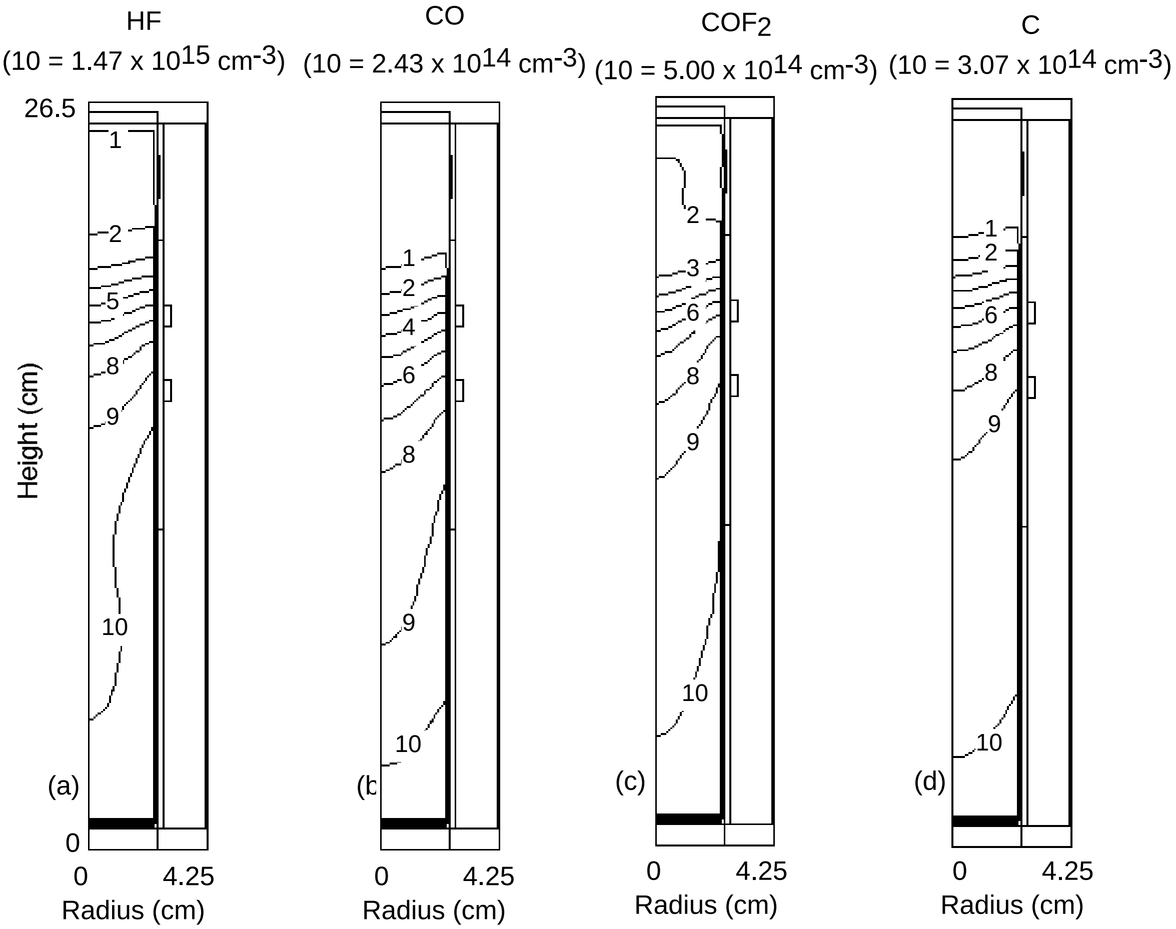

Fig. 7.22. Primary product densities for the baseline case of the plasma burn-box using H_2O as an additive: (a) HF, (b) CO, (c) COF_2, and (d) C. The contours are labeled by their relative magnitudes with the maximum values noted at the top of each figure.

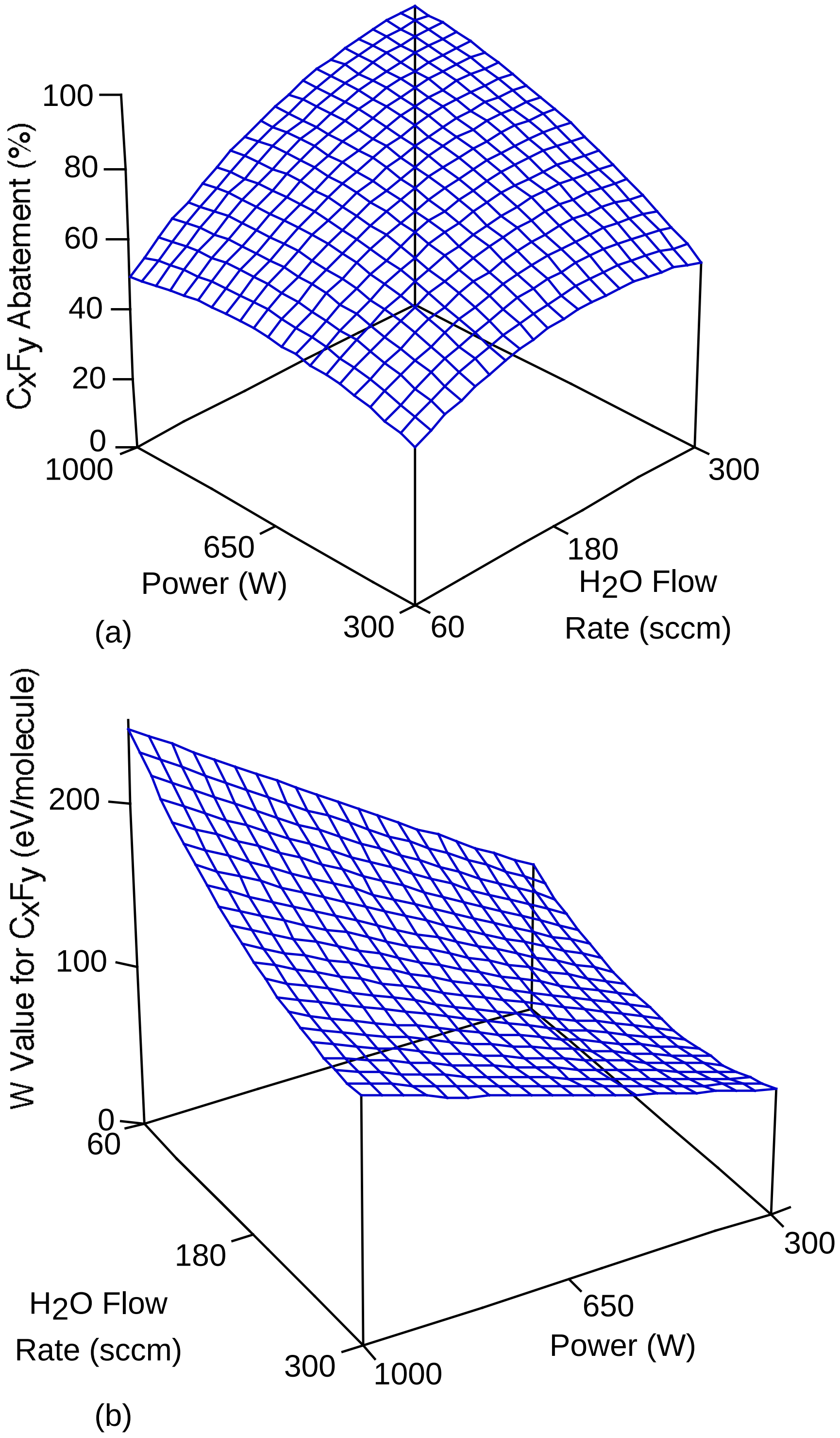

Fig. 7.23. Efficiencies for abatement of all C_xF_y as a function of power and injected H_2O in the plasma burn-box: (a) fractional C_xF_y abatement and (b) *W*-value for C_xF_y. (Note that the independent variables have different orientations to obtain a better view angle.)

7.5 References

[1] J. V. Gompel and T. Walling, Semicond. Int., 95, (1997).

[2] K. Takahashi, M. Hori, and T. Goto, J. Vac. Sci. Technol. A**14**, 2004 (1996).

[3] M. A. Sobolewski, J. G. Langan, and B. S. Felker, J. Vac. Sci. Technol. **B 16**, 173 (1998).

[4] T. E. F. M. Standaert, M. Schaepkens, N. R. Rueger, P. G. M., Sebel, G. S. Oehrlein, and J. M. Cook, J. Vac. Sci. Technol. A**16**, 239 (1998).

[5] B. E. E. Kastenmeier, P. J. Matsui, G. S. Oehrlein, and J. G. Langan, J. Vac. Sci. Technol. A**16**, 2047 (1998).

[6] H. H. Sawin and S. A. Vitale, 51th Gaseous Electronics Conference, Maui, Hawaii, Oct., 1998.

[7] C. L. Hartz, J, W. Bevaan, M. W. Jackson, and B. A. Wofford, Environ. Sci. Technol. **32**, 682 (1998).

[8] D. R. F. Burgess, Jr., National Institute of Standards and Technology (private communication).

[9] D. R. F. Burgess, Jr., M. R. Zachariah, W. Tsang, and P. R. Westmoreland, Prog. Energy Combust. Sci., **21**, 453,1996.

[10] C. Tsai and D. L. McFadden, J. Phys. Chem. **93**, 2471 (1989).

[11] E. J. Tonnis, V. Vartanian, L. Beu, T. Lii, R. Jewett, and D. Graves, *Evaluation of a Litmas "Blue" Point-of-Use (POU) Plasma Abatement Device for Perfluorocompound (PFC) Destruction*., SEMATECH Technology Transfer 98123605A-TR, 1998.

8. CONCLUDING REMARKS

One and two-dimensional plasma chemistry and hydrodynamics models have been developed to study dielectric barrier discharge processing of high pressure gas streams to be applied to micodischarge dynamics, toxic gas remediation, and UV and VUV sources. The 2-D hybrid plasma equipment model has also been used to examine low gas pressure plasma consumption and generation of PFCs in an ICP etching reactor and abatement of PFCs in a plasma burn box. These models allow for a detailed study of plasma induced chemical reactions and provide important insight into process trade-offs, resulting in our ability to optimize the operation conditions.

The properties of the filamentary microdischarges found in dielectric barrier discharges depend on the manner of charging of the dielectric. The charging of the dielectric removes voltage from the gap thereby reducing E/N and producing a transition from an avalanching discharge to a recombination or attachment dominated discharge. Microdischarge dynamics have been investigated for gas mixtures with varying degrees of electronegativity using the 1-D DBD model. In electropositive mixtures, the expanding microdischarge maintains a fairly uniform electron density as a function of radius, except for a small reduction in the core of the microdischarge due to electron-ion recombination. In electronegative gas mixtures, the electron density has a maximum value near the streamer edge due to dielectric charging and attachment at small radii at lower E/N, especially for thermal attaching gas mixtures such as those containing CCl_4. We found that the expansion and ultimate stalling of the microdischarge is largely determined by charging of dielectric at larger radii than the core of the microdischarge.

A 2-D DBD model has also been developed to investigate multiple-microdischarge dynamics in dielectric barrier discharges. The closely spaced expanding microdischarges retain their initial circular shapes until they collide and physically contact. The avalanche stalls at the interface, but continues to expand on other sides. The dynamics of adjacent microdischarges are similar to a single microdischarge, with the exception that the electron density peaks at the interface by at most a few tens of percent. The residual charge on the dielectric in DBDs from a preceding microdischarge can significantly change the dynamics of microdischarges produced by the next voltage pulse. The residual charge produces an additional voltage across the gap for the subsequent microdischarge, thereby leading to more intense avalanche and providing a mechanism for microdischarges to expand beyond their individual domains.

Remediation of carbon tetrachloride (CCl_4) proceeds by a serial of chemical reactions in DBDs. Though dissociative electron attachment is primarily responsible for initial dissociation of CCl_4, dissociative excitation and charge exchange from Ar^*, Ar^{**}, Ar^+, and O_2^+ to CCl_4 also play significant roles. Decreasing the O_2 mole fraction can considerably increase the remediation efficiency of CCl_4 due largely to enhancing the dissociative excitation transfer. The optimum amount of O_2 is 1–3 times that of Cl_2 for $Ar/O_2/CCl_2$ gas mixtures. The decrease in removal efficiency in the presence of small amounts of water vapor results from the interception of Ar^+ and O_2^+ by H_2O. The products of remediation are primarily $COCl_2$ and ClO.

The excimer radiation from $XeCl^*$ at 308 nm, Xe_2Cl^* at 490 nm, and Xe_2^* at 172 nm was examined in DBDs in Xe/Cl_2 gas mixtures. When the Cl_2 mole fraction < 1%, decreasing Cl_2 decreases the $XeCl^*$ formation, but significantly improves the generation of Xe_2^* and Xe_2Cl^* since the presence of Cl_2 efficiently quenches Xe_2^* and Xe_2Cl^*. At approximately 1% Cl_2 there is an optimum efficiency for producing $XeCl^*$ due to a trade-off between several reactions. When the Cl_2 mole fraction exceeds the optimum, the generation of $XeCl^*$ dominates, however its corresponding generation efficiency slowly decreases with increasing Cl_2. The strong attachment at high Cl_2 concentration ($\geq$ 5%) leads to the electron density shell propagating to smaller radii after the pulse. Though increasing dielectric capacitance increases all rates of excimer formation resulting due to the higher energy deposition, the efficiencies of photon generation decreases. Higher applied voltage improves both intensities and efficiencies of photon generation. At higher gas pressures, Xe_2^* is produced more efficiently due to three-body collisions.

The characteristics of Ar/C_2F_6 (or Ar/CF_4) gas mixtures in an ICP etching reactor have been investigated using the HPEM. The consumption of C_2F_6 (or CF_4) and the generation of other PFCs in the etching reactor are proportional to the ICP power deposition and inversely proportional to the C_2F_6 (or CF_4) mole fraction and total gas flow rate. The efficiency of removal of C_2F_6 (eV/molecule), though, is only strongly dependent on the C_2F_6 mole fraction and total gas flow rate. The effluents from the plasma etching reactor were be fed into an ICP burn box, where the remaining PFCs were destroyed using O_2, H_2, and H_2O as additive gases. In general, CF_4 generation occurs during abatement of C_2F_6 using O_2 as an additive. CF_4 is not, however, substantially produced when H_2 or H_2O is used as additives. The efficiency of PFC abatement (as measured by eV/molecule abated) decreases with increasing power and decreasing additive mole fraction.

APPENDIX A. LIST OF SPECIES FOR $N_2/O_2/H_2O$, $Ar/O_2/H_2O/CCl_4$, Xe/Cl_2, AND $Ar/CF_4/C_2F_6/H_2/O_2/H_2O$ PLASMAS

Ar	Ar^+	Ar^*	Ar^{**}	Ar_2^+
Ar_2^*	C	C^+	CCl_4	CCl_3
CCl_2	CCl_3^+	CCl_2^+	CCl_2^+	CCl^+
CCl_3O	CCl_3O_2	CHCl	$CHCl_2$	$CHCl_3$
CHOCl	COCl	$COCl_2$	CO	CO_2
CO_2^+	C_2O	C_2Cl	C_2Cl_2	C_2Cl_3
C_2Cl_4	C_2Cl_5	C_2Cl_6	Cl	Cl^+
Cl^*	Cl^-	ClO	ClOO	Cl_2
Cl_2^*	Cl_2^+	Cl_2O	CF_4	CF_3
CF_2	CF	CF_3^+	CF_3^-	CF_2^+
C_2F_6	C_2F_5	$C_2F_5^+$	C_2F_4	$C_2F_4^+$
C_2F_3	COF	COF_2	CF_3O_2	F
F^+	F^-	F_2	F_2^+	FO
H	H^+	H^-	HCl	HCO
HOCl	HO_2	H_2	H_2^+	H_3O^+
$H_3O^+\cdot H_2O$	H_2O_2	N	N_2	$N_2(A)$
$N_2(v)$	$N2^+$	O	O^-	O^+
$O(^1D)$	O_2	O_2^+	$O_2(v)$	$O_2^+\cdot H_2O$
O_3	OH	Xe	Xe^*	Xe^{**}
Xe^+	$XeCl^*$	Xe_2^*	Xe_2^+	

APPENDIX B. LIST OF REACTIONS FOR $N_2/O_2/H_2O$, $Ar/O_2/H_2O/CCl_4$, Xe/Cl_2 AND $Ar/CF_4/C_2F_6/H_2/O_2/H_2O$ PLASMAS

Electron Impact and Recombination [a]

Reaction	Rate Coefficient [b]	Ref.
$e + N_2 \rightarrow N_2^+ + e + e$	c	[1]
$e + N_2 \rightarrow N_2(v) + e$	c	[1]
$e + N_2(v) \rightarrow N_2 + e$	c	[1]
$e + N_2 \rightarrow N_2(A) + e$	c	[1]
$e + N_2 \rightarrow N + N + e$	7.05×10^{-10}	[1]
$e + N_2(A) \rightarrow N_2(v) + e$	c	[1]
$e + N_2(A) \rightarrow N_2 + e$	c	[1]
$e + N_2(A) \rightarrow N_2^+ + e + e$	c	[1]
$e + N_2^+ \rightarrow N + N$	2.00×10^{-7}	[2]
$e + O \rightarrow O(^1D) + e$	c	[3]
$e + O \rightarrow O^+ + e + e$	c	[3]
$e + O(^1D) \rightarrow O + e$	c	[3]
$e + O(^1D) \rightarrow O^+ + e + e$	c	[3]
$e + O_2 \rightarrow O^- + O$	c	[4]
$e + O_2 \rightarrow O(^1D) + O + e$	c	[4]
$e + O_2 \rightarrow O + O + e$	c	[4]
$e + O_2 \rightarrow O_2^+ + e + e$	c	[4]
$e + O_2 \rightarrow O^+ + O + e + e$	c	[5]
$e + O_2 \rightarrow O_2(v) + e$	c	[4]
$e + O_2 + M \rightarrow O_2^- + M$	1.00×10^{-31} cm^6 s^{-1}	[6]
$e + O_2^+ \rightarrow O(^1D) + O$	$2.00\times10^{-7}T_e^{-0.5}$	d
$e + O_2^+ \rightarrow O(^1D) + O$	2.0×10^{-8}	e, [7]
$e + O_3 \rightarrow e + O_2 + O(^1D)$	5.0×10^{-10}	d
$e + H_2 \rightarrow H + H + e$	c	[8]
$e + H_2 \rightarrow H_2^+ + e + e$	c	[8]

$e + H_2 \rightarrow H + H + e$	c	[8]
$e + H_2 \rightarrow H + H + e$	c	[8]
$e + H_2^+ \rightarrow H + H$	c	[8]
$e + H_2O \rightarrow OH + H^-$	c	[9]
$e + H_2O \rightarrow OH + H + e$	c	[9]
$e + H_2O \rightarrow O(^1D) + H_2 + e$	c	[9]
$e + H_2O \rightarrow H_2O^+ + e + e$	c	[9]
$e + H_2O \rightarrow H_2O^+ + e + e$	c	[10]
$e + H_2O \rightarrow H^- + OH$	c	[10]
$e + H_2O^+ \rightarrow O + H_2$	1.0×10^{-7}	[11]
$e + H_3O^+ \rightarrow H_2O + H$	2.0×10^{-7}	e, [11]
$e + H_2O^+ \rightarrow OH + H$	$6.60\times10^{-6}T_e^{-0.5}$	[11]
$e + H_2O^+ \rightarrow O + H + H$	$2.88\times10^{-6}T_e^{-0.5}$	[11]
$e + H_2O^+ \rightarrow O + H_2$	$2.52\times10^{-6}T_e^{-0.5}$	[11]
$e + CO \rightarrow O^- + C$	c	[12]
$e + CO_2 \rightarrow CO + O + e$	c	[12]
$e + CO_2 \rightarrow CO + O^-$	c	[12]
$e + CO_2 \rightarrow CO_2^+ + e + e$	c	[12]
$e + CO_2 \rightarrow O^- + CO$	c	[12]
$e + CO_2^+ \rightarrow CO + O$	$2.00\times10^{-7}T_e^{-0.5}$	d
$e + Cl \rightarrow Cl^* + e$	c	[13]
$e + Cl \rightarrow Cl^+ + e + e$	c	[13]
$e + Cl_2 \rightarrow Cl + Cl^-$	c	[14]
$e + Cl_2 \rightarrow Cl + Cl + e$	c	[14]
$e + Cl_2 \rightarrow Cl_2^* + e$	c	[14]
$e + Cl_2 \rightarrow Cl_2+ + e + e$	c	[14]
$e + Cl^* \rightarrow Cl^+ + e + e$	c	[13]
$e + Cl^- \rightarrow Cl + e + e$	c	[13]
$e + Cl_2^+ \rightarrow Cl + Cl$	1.00×10^{-8}	d

$e + CCl_4 \rightarrow CCl_3^+ + Cl + e + e$	2.053×10^{-9}	[15]
$e + CCl_4 \rightarrow CCl_2^+ + Cl_2 + e + e$	4.611×10^{-11}	[15]
$e + CCl_4 \rightarrow CCl^+ + Cl_2 + Cl + e + e$	1.259×10^{-11}	[15]
$e + CCl_4 \rightarrow Cl_2^+ + CCl_2 + e + e$	1.029×10^{-14}	[15]
$e + CCl_4 \rightarrow Cl^+ + CCl_3 + e + e$	4.631×10^{-13}	[15]
$e + CCl_4 \rightarrow CCl_3 + Cl^-$	1.622×10^{-9}	[15]
$e + CCl_4 \rightarrow CCl_2 + Cl + Cl + e$	3.393×10^{-8}	[15]
$e + CCl_3^+ \rightarrow CCl_2 + Cl$	$2.00\times10^{-7}T_e^{-0.5}$	[16]
$e + CCl_2^+ \rightarrow CCl + Cl$	$2.00\times10^{-7}T_e^{-0.5}$	[16]
$e + CCl^+ \rightarrow C + Cl$	$2.00\times10^{-7}T_e^{-0.5}$	[16]
$e + Cl_2^+ \rightarrow Cl + Cl$	$2.00\times10^{-7}T_e^{-0.5}$	[16]
$e + Cl^+ \rightarrow Cl$	$2.00\times10^{-7}T_e^{-0.5}$	[16]
$e + C^+ \rightarrow C$	$2.00\times10^{-7}T_e^{-0.5}$	[16]
$e + H_3O^+{\cdot}H_2O \rightarrow H + H_2O + H_2O$	$2.00\times10^{-7}T_e^{-0.5}$	d
$e + O_2^+{\cdot}H_2O \rightarrow O_2 + H_2O$	$2.00\times10^{-7}T_e^{-0.5}$	d
$e + CF_2 \rightarrow CF + F + e$	c	e, [17]
$e + CF_2 \rightarrow CF + F^-$	c	e, [17]
$e + CF_3O_2 \rightarrow CF_3 + O_2 + e$	c	e, [17]
$e + COF_2 \rightarrow COF + F + e$	c	e, [17]
$e + C_2F_3 \rightarrow CF + CF_2 + e$	c	e, [18]
$e + F \rightarrow F^+ + e + e$	c	[19]
$e + F_2 \rightarrow F^- + F$	c	[20]
$e + F_2 \rightarrow F + F + e$	c	[20]
$e + F_2 \rightarrow F_2^+ + e + e$	c	[20]
$e + F_2^+ \rightarrow F + F$	2.0×10^{-8}	e, [7]
$e + Ar \rightarrow Ar^* + e$	c	[21]
$e + Ar \rightarrow Ar^{**} + e$	c	[21]
$e + Ar \rightarrow Ar^+ + e + e$	c	[22]
$e + Ar^* \rightarrow Ar^+ + e + e$	c	[23]

$e + Ar^{*} \rightarrow Ar^{**} + e$	c	[24]
$e + Ar^{*} \rightarrow Ar + e$	c	[24]
$e + Ar^{**} \rightarrow Ar^{+} + e + e$	c	[24]
$e + Ar^{**} \rightarrow Ar + e$	c	[24]
$e + Ar_2^{+} \rightarrow Ar^{*} + Ar$	1.00×10^{-7}	d
$e + Ar_2^{*} \rightarrow Ar + Ar + e$	1.00×10^{-7}	d
$e + Xe \rightarrow Xe^{*} + e$	c	[25]
$e + Xe \rightarrow Xe^{**} + e$	c	[26]
$e + Xe \rightarrow Xe^{+} + e + e$	c	[27]
$e + Xe^{*} \rightarrow Xe + e$	c	[28]
$e + Xe^{*} \rightarrow Xe^{+} + e + e$	c	[28]
$e + Xe^{*} \rightarrow Xe^{**} + e$	c	[28]
$e + Xe^{**} \rightarrow Xe^{*} + e$	c	e, [28]
$e + Xe^{**} \rightarrow Xe + e$	c	e,[26]
$e + Xe^{**} \rightarrow Xe^{+} + e + e$	c	[29]
$e + Xe_2^{*} \rightarrow Xe_2^{+} + e + e$	c	[29]
$e + Xe_2^{+} \rightarrow Xe^{*} + Xe$	c	[30]
$e + CF_4 \rightarrow CF_3 + F^{-}$	c	[31]
$e + CF_4 \rightarrow CF_3^{-} + F$	c	[31]
$e + CF_4 \rightarrow CF_3 + F + e$	c	[31]
$e + CF_4 \rightarrow CF_3^{+} + F + e + e$	c	[31]
$e + CF_4 \rightarrow CF_2 + F + F + e$	c	[31]
$e + CF_3 \rightarrow CF_2 + F + e$	c	e, [31]
$e + CF_3 \rightarrow CF_2 + F^{-}$	c	e, [31]
$e + C_2F_6 \rightarrow CF_3^{+} + CF_3 + e + e$	c	[32]
$e + C_2F_6 \rightarrow CF_3 + CF_3^{-}$	c	[32]
$e + C_2F_6 \rightarrow C_2F_5 + F^{-}$	c	[32]
$e + C_2F_6 \rightarrow CF_3 + CF_3 + e$	c	[32]
$e + C_2F_6 \rightarrow CF_2 + CF_3 + e$	c	[32]

$e + C_2F_4 \rightarrow CF_2 + CF_2 + e$	c	e, [32]
$e + C_2F_4 \rightarrow C_2F_4^+ + e + e$	c	e, [32]
$e + C_2F_4 \rightarrow F^- + C_2F_3$	c	[32]
$e + CF_3^+ \rightarrow CF_2 + F$	2.0×10^{-8}	e, [33]
$e + C_2F_5^+ \rightarrow CF_3 + CF_2$	2.0×10^{-8}	e, [33]
$e + C_2F_4^+ \rightarrow CF_2 + CF_2$	2.0×10^{-8}	e, [27]

Reactions of $N_2/O_2/H_2O$

Reaction	Rate Coefficient [b]	Ref.
$N + N + M \rightarrow N_2 + M$	3.90×10^{-33}	[34]
$N_2(A) + N_2 \rightarrow N_2 + N_2$	2.40×10^{-14}	[34]
$N_2(v) + N_2 \rightarrow N_2 + N_2$	1.0010^{-16}	[35]
$N_2(v) + N \rightarrow N_2 + N$	1.00×10^{-14}	[35]
$N_2(v) + N_2(v) \rightarrow N_2 + N_2(v)$	1.00×10^{-15}	[35]
$N_2(A) + O_2 \rightarrow O + O + N_2$	1.50×10^{-12}	[36]
$N_2(A) + O_2 \rightarrow O_2 + N_2$	2.80×10^{-11}	[36]
$N_2(A) + H_2 \rightarrow N_2 + H_2$	2.60×10^{-11}	[36]
$O + O_2 + M \rightarrow O_3 + M$	$6.9\times10^{-34}(T/300)^{-1.25}$ cm^6 s^{-1}	[37]
$O + O_2 + H_2O \rightarrow O_3 + H_2O$	2.90×10^{-34} cm^6 s^{-1}	[38]
$O + O_3 \rightarrow O_2 + O_2$	$8.0\times10^{-12}\exp(-2060/T)$	[37]
$O + OH \rightarrow H + O_2$	$4.34\times10^{-11}(T/300)^{-0.5}\exp(-30/T)$	[39]
$O + OH + M \rightarrow HO_2 + M$	2.76×10^{-31} cm^6 s^{-1}	[40]
$O + O + M \rightarrow O_2 + M$	$5.21\times10^{-35}\exp(9000/T)$ cm^6 s^{-1}	[41]
$O + H + M \rightarrow OH + M$	1.62×10^{-32} cm^6 s^{-1}	[42]
$O + H_2 \rightarrow OH + H$	$1.33\times10^{-15}(T/298)^{6.52}\exp(-1457/T)$	[43]
$O + HO_2 \rightarrow OH + O_2$	$2.9\times10^{-11}\exp(200/T)$	[37]
$O + H_2O_2 \rightarrow OH + HO_2$	$1.1\times10^{-12}\exp(-2000/T)$	[44]
$O(^1D) + O_3 \rightarrow O_2 + O + O$	1.20×10^{-10}	[41]
$O(^1D) + N_2 \rightarrow O + N_2$	$1.8\times10^{-11}\exp(107/T)$	[37]

$O(^1D) + O_2 \rightarrow O + O_2$	3.80×10^{-11}	[34]
$O(^1D) + H_2O \rightarrow O + H_2O$	1.20×10^{-11}	[34]
$O(^1D) + H_2O \rightarrow OH + OH$	2.20×10^{-10}	[34]
$O(^1D) + H_2O \rightarrow H_2 + O_2$	2.30×10^{-12}	[45]
$O(^1D) + H_2 \rightarrow OH + H$	1.10×10^{-10}	[45]
$O_2(v) + O_2 \rightarrow O_2 + O_2$	1.10×10^{-16}	[46]
$O_2(v) + O_2(v) \rightarrow O_2 + O_2$	1.10×10^{-14}	[46]
$H + O_2 \rightarrow OH + O$	$2.8\times10^{-7}T^{-0.9}\exp(-8750/T)$	[47]
$H + OH + M \rightarrow H_2O + M$	4.30×10^{-31} cm^6 s^{-1}	[34]
$H + O_2 + M \rightarrow HO_2 + M$	$5.64\times10^{-28}T^{-1.6}$ cm^6 s^{-1}	[48]
$H + H + M \rightarrow H_2 + M$	4.80×10^{-33} cm^6 s^{-1}	[37]
$H + HO_2 \rightarrow OH + OH$	$2.8\times10^{-10}\exp(-480/T)$	[47]
$H + HO_2 \rightarrow H_2 + O_2$	$1.1\times10^{-10}\exp(-1070/T)$	[47]
$H + HO_2 \rightarrow H_2O + O$	9.40×10^{-13}	[45]
$H + O_3 \rightarrow OH + O_2$	$1.4\times10^{-10}\exp(-480/T)$	[37]
$OH + OH \rightarrow O + H_2O$	$3.5\times10^{-16}T^{1.4}\exp(200/T)$	[47]
$OH + HO_2 \rightarrow H_2O + O_2$	8.00×10^{-11}	d
$OH + O_3 \rightarrow HO_2 + O_2$	$1.9\times10^{-12}\exp(-1000/T)$	[45]
$OH + OH + O_2 \rightarrow H_2O_2 + O_2$	$4.02\times10^{-31}(T/298)^{-2}$ cm^6 s^{-1}	[44]
$OH + H_2O_2 \rightarrow H_2O + HO_2$	$2.9\times10^{-12}\exp(-160/T)$	[45]
$OH + M \rightarrow O + H + M$	$4\times10^{-9}\exp(-5000/T)$	[47]
$OH + O_2 \rightarrow O + HO_2$	$3.7\times10^{-11}\exp(-26500/T)$	[47]
$OH + H \rightarrow O + H_2$	$1.14\times10^{-12}T^{0.67}\exp(-518/T)$	[11]
$OH + H_2 \rightarrow H_2O + H$	$7.7\times10^{-12}\exp(-2100/T)$	[47]
$O^+ + O_2 \rightarrow O_2^+ + O$	1.90×10^{-11}	[6]
$O^+ + O_2^- \rightarrow O + O_2$	$2.0010^{-6}(T/300)^{-0.5}$	[49]
$O_2^+ + O_2^- \rightarrow O_2 + O_2$	2.00×10^{-6}	[6]
$O^- + N_2^+ \rightarrow O + N_2$	$3.00\times10^{-6}(T/300)^{-0.5}$	d
$O^- + H_2O^+ \rightarrow O + H_2O$	$3.00\times10^{-6}(T/300)^{-0.5}$	[49]

$O^- + O_2^+ \rightarrow O + O_2$	$3.00\times10^{-6}(T/300)^{-0.5}$	[49]
$O^- + O^+ + M \rightarrow O_2 + M$	1.20×10^{-25} cm^6 s^{-1}	d
$O_2^- + N_2^+ \rightarrow N_2 + O_2$	2.00×10^{-6} $(T/300)^{-0.5}$	[34]
$H_2O^+ + O_2^- \rightarrow H_2O + O_2$	2.00×10^{-6}	d
$H^- + N_2^+ \rightarrow H + N_2$	3.00×10^{-6}	d
$H^- + H_2O^+ \rightarrow H + H_2O$	3.00×10^{-6}	[49]
$H^- + O_2^+ + M \rightarrow H_2O + M$	1.20×10^{-25} cm^6 s^{-1}	d
$H^- + O^+ + M \rightarrow OH + M$	1.20×10^{-25} cm^6 s^{-1}	d
$HO_2 + H_2 \rightarrow H_2O_2 + H$	$5.0\times10^{-11}\exp(-13100/T)$	[47]
$HO_2 + O_3 \rightarrow OH + O_2 + O_2$	$1.4\times10^{-14}\exp(-600/T)$	[37]
$HO_2 + HO_2 + M \rightarrow H_2O_2 + O_2 + M$	$1.9\times10^{-33}\exp(980/T)$ cm^6 s^{-1}	[37]
$H_2O + H \rightarrow H_2 + OH$	$1.03\times10^{-16}T^{1.9}\exp(-9265/T)$	[47]
$H_2O + O \rightarrow OH + OH$	$7.6\times10^{-15}T^{1.3}\exp(-8605/T)$	[47]

Additional reactions of $Ar/O_2/H_2O/CCl_4$

Reaction	Rate Coefficient [b]	Ref.
$OH + CO \rightarrow CO_2 + H$	$5.13\times10^{-13}\exp(-370/T)$	[50]
$OH + Cl \rightarrow O + HCl$	$9.8\times10^{-12}\exp(-2860/T)$	[37]
$OH + HCl \rightarrow H_2O + Cl$	$2.999\times10^{-12}\exp(-414.5/T)$	[37]
$H + HCl \rightarrow H_2 + Cl$	$1.32\times10^{-11}\exp(-1710/T)$	[37]
$H + ClOO \rightarrow OH + ClO$	5.64×10^{-11}	[37]
$H + Cl_2 \rightarrow HCl + Cl$	$1.41\times10^{-10}\exp(-606.1/T)$	[51]
$H + HOCl \rightarrow HCl + OH$	$1.66\times10^{-11}\exp(-505.1/T)$	[51]
$H + H_2O_2 \rightarrow H_2O + OH$	$1.7\times10^{-11}\exp(-1800/T)$	[44]
$H + H_2O_2 \rightarrow HO_2 + H_2$	$8\times10^{-11}\exp(-4000/T)$	[47]
$H_2 + O_2 \rightarrow H + HO_2$	$2.4\times10^{-10}\exp(-28500/T)$	[47]
$H_2O_2 + O_2 \rightarrow HO_2 + HO_2$	$9\times10^{-11}\exp(-20000/T)$	[47]
$O + ClOO \rightarrow ClO + O_2$	$5.25\times10^{-11}\exp(-252.2/T)$	[51]
$O + Cl_2 \rightarrow ClO + Cl$	$2.09\times10^{-11}\exp(-1414/T)$	[52]

$O + HCl \rightarrow OH + Cl$	$9.784\times10^{-12}\exp(-3308/T)$	[37]
$O_2^+ \cdot H_2O + H_2O \rightarrow H_3O^+ + OH + O_2$	1.20×10^{-9}	[34]
$O_2^+ \cdot H_2O + Cl^- \rightarrow O_2 + H_2O + Cl$	5.00×10^{-8}	[34]
$H_2O_2 + Cl \rightarrow HO_2 + HCl$	$1.1\times10^{-11}\exp(-980/T)$	[53]
$HCO + H \rightarrow H_2 + CO$	2.00×10^{-10}	[47]
$HCO + O \rightarrow H + CO_2$	5.00×10^{-11}	[37]
$HCO + O \rightarrow OH + CO$	5.00×10^{-11}	[47]
$HCO + OH \rightarrow H_2O + CO$	5.00×10^{-11}	[47]
$HCO + HO_2 \rightarrow OH + H + CO_2$	5.00×10^{-11}	[47]
$HCO + HCO \rightarrow H_2 + CO + CO$	5.00×10^{-12}	[47]
$HCO + M \rightarrow H + CO + M$	$8.5\times10^{-3}T^{-2.14}\exp(-10278/T)$	[47]
$HCO + O_2 \rightarrow HO_2 + CO$	$8.5\times10^{-11}\exp(-850/T)$	[47]
$HOCl + O \rightarrow OH + ClO$	$1.00\times10^{-11}\exp(-2200/T)$	[37]
$HOCl + OH \rightarrow H_2O + ClO$	$3\times10^{-12}\exp(-500.2/T)$	[37]
$C + CO + M \rightarrow C_2O + M$	6.30×10^{-32} cm^6 s^{-1}	[54]
$C + O_2 \rightarrow CO + O$	2.60×10^{-11}	[41]
$CCl + O \rightarrow COCl$	1.00×10^{-12}	d
$CCl + O_2 \rightarrow COCl + O$	2.90×10^{-12}	[37]
$CCl + OH \rightarrow HCl + CO$	4.00×10^{-11}	d
$CCl + O \rightarrow ClO + C$	$1.38\times10^{-10}\exp(-16048/T)$	[41]
$CCl_4 + O(^1D) \rightarrow CCl_3 + ClO$	3.54×10^{-10}	[55]
$CCl_3 + OH \rightarrow HCl + COCl_2$	1.00×10^{-11}	d
$CCl_2 + O \rightarrow COCl + Cl$	1.00×10^{-11}	d
$CCl_2 + O_2 \rightarrow COCl_2 + O$	1.00×10^{-13}	[56]
$CCl_2 + OH \rightarrow HCl + COCl$	1.00×10^{-11}	d
$CCl_2 + Cl_2 \rightarrow CCl_3 + Cl$	$8.33\times10^{-12}\exp(-1515/T)$	[56]
$CCl_3 + H_2 \rightarrow CHCl_3 + H$	$8.32\times10^{-12}\exp(-7196/T)$	[41]
$CCl_3 + O \rightarrow Cl + COCl_2$	4.15×10^{-11}	[37]
$CCl_3 + O_2 + M \rightarrow CCl_3O_2 + M$	$3.244\times10^{-23}T^{-3}\exp(2.922\times10^{-8}/T)$ cm^6 s^{-1}	[57]

$CCl_3 + Cl_2 \rightarrow CCl_4 + Cl$	$4.17\times10^{-12}\exp(-3019/T)$	[58]
$CCl_3 + CCl_3 \rightarrow C_2Cl_6$	$8.4\times10^{-12}\exp(52/T)$	[59]
$CCl_3 + CCl_3 \rightarrow C_2Cl_4 + Cl_2$	$3.72\times10^{12}T^{-4.43}\exp(-4545T)$	[51]
$CCl_3 + CHCl_2 \rightarrow C_2Cl_4 + HCl$	$3.89\times10^{-4}T^{-2.45}\exp(3232/T)$	[51]
$CCl_3 + O_3 \rightarrow CCl_3O + O_2$	5.00×10^{-13}	d
$CCl_4 + O \rightarrow ClO + CCl_3$	$1.98\times10^{-13}\exp(-2200/T)$	[60]
$CCl_4 + OH \rightarrow HOCl + CCl_3$	$1.0\times10^{-12}\exp(-2320/T)$	[37]
$CCl_3O \rightarrow COCl_2 + Cl$	1.00×10^{5}	[37]
$CCl_3O_2 \rightarrow CCl_3 + O_2$	$4.485\times10^{-20}T^{-1.0}\exp(-11070/T)$	[37]
$CCl_3O_2 + CCl_3 \rightarrow CCl_3O + CCl_3O$	1.00×10^{-12}	[37]
$CCl_3O_2 + Cl \rightarrow COCl_2 + ClO + Cl$	2.00×10^{-10}	[61]
$CCl_3O_2 + CCl_3O_2 \rightarrow CCl_3O + CCl_3O + O_2$	8.32×10^{-11}	[51]
$C_2Cl + O_2 \rightarrow COCl + CO$	$1.66\times10^{-11}\exp(-2525/T)$	[51]
$C_2Cl_2 + O \rightarrow CCl_2 + CO$	1.18×10^{-10}	[51]
$C_2Cl_2 + O_2 \rightarrow COCl + COCl$	$1.66\times10^{-13}\exp(-2525/T)$	[51]
$C_2Cl_2 + ClO \rightarrow CO + CCl_3$	1.66×10^{-13}	[51]
$C_2Cl_2 + OH \rightarrow CO + CHCl_2$	1.66×10^{-12}	[51]
$C_2Cl_2 + Cl \rightarrow C_2Cl + Cl_2$	$3.32\times10^{-10}\exp(-7576/T)$	[51]
$C_2Cl_2 + ClO \rightarrow C_2Cl + Cl_2O$	$1.66\times10^{-10}\exp(-20200/T)$	[51]
$C_2Cl_2 + OH \rightarrow C_2Cl + HOCl$	$1.66\times10^{-10}\exp(-5051/T)$	[51]
$C_2Cl_3 + Cl_2 \rightarrow C_2Cl_4 + Cl$	$4.17\times10^{-12}\exp(-1515/T)$	[51]
$C_2Cl_3 + Cl \rightarrow C_2Cl_4$	$7.42\times10^{9}T^{-7.21}\exp(-2879/T)$	[51]
$C_2Cl_3 + Cl \rightarrow C_2Cl_2 + Cl_2$	$8.72\times10^{-7}T^{-1.66}\exp(-2576/T)$	[51]
$C_2Cl_3 + O_2 \rightarrow COCl_2 + COCl$	$1.66\times10^{-13}\exp(-2525/T)$	[51]
$C_2Cl_3 + O \rightarrow CO + CCl_3$	1.66×10^{-11}	[51]
$C_2Cl_3 + ClO \rightarrow CO + CCl_4$	1.66×10^{-11}	[51]
$C_2Cl_3 + M \rightarrow C_2Cl_2 + Cl + M$	$8.31\times10^{-9}\exp(-14140/T)$	[51]
$C_2Cl_3 + M \rightarrow C_2Cl_2 + Cl + M$	$1.32\times10^{-9}\exp(-14140/T)$	[51]
$C_2Cl_3 + O_2 \rightarrow COCl_2 + COCl$	$1.66\times10^{-13}\exp(-2525/T)$	[51]

$C_2Cl_4 + O \rightarrow COCl_2 + CCl_2$	$1.66\times10^{-13}\exp(-2525/T)$	[51]
$C_2Cl_4 + Cl \rightarrow C_2Cl_5$	$4.37\times10^{11}T^{-7.71}\exp(-2.677\times10^{3}/T)$	[51]
$C_2Cl_4 + OH \rightarrow C_2Cl_3 + HOCl$	$1.66\times10^{-11}\exp(-6061/T)$	[51]
$C_2Cl_4 + OH \rightarrow CHCl_2 + COCl_2$	$1.66\times10^{-11}\exp(-1010/T)$	[51]
$C_2Cl_4 + ClO \rightarrow CCl_3 + COCl_2$	$1.66\times10^{-11}\exp(-1010/T)$	[51]
$C_2Cl_4 + Cl \rightarrow C_2Cl_3 + Cl_2$	$1.66\times10^{-11}\exp(-9091/T)$	[51]
$C_2Cl_5 + Cl \rightarrow CCl_3 + CCl_3$	$2.82\times10^{3}T^{-4.01}\exp(-6111/T)$	[51]
$C_2Cl_5 \rightarrow C_2Cl_4 + Cl$	$2.51\times10^{13}\exp(-7800/T)$	[41]
$C_2Cl_5 + Cl \rightarrow Cl_2 + C_2Cl_4$	$6.61\times10^{-9}\exp(-603/T)$	[41]
$C_2Cl_6 + Cl \rightarrow Cl_2 + C_2Cl_5$	$6.61\times10^{-9}\exp(-603/T)$	[41]
$CHCl + Cl_2 \rightarrow CHCl_2 + Cl$	$1.66\times10^{-11}\exp(-505.1/T)$	[51]
$CHCl + O_2 \rightarrow COCl + OH$	$1.66\times10^{-11}\exp(-505.1/T)$	[51]
$CHCl_3 + O \rightarrow OH + CCl_3$	$4.79\times10^{-12}\exp(-2525/T)$	[51]
$CHCl_3 + OH \rightarrow H_2O + CCl_3$	$1.15\times10^{-11}\exp(-1667/T)$	[51]
$CHCl_3 + Cl \rightarrow HCl + CCl_3$	5.69×10^{-12}	[37]
$CHCl_3 + O \rightarrow COCl_2 + HCl$	$1.66\times10^{-13}\exp(-2020/T)$	[51]
$CHCl_3 + O \rightarrow CCl_3 + OH$	$4.79\times10^{-12}\exp(-2525/T)$	[51]
$CHCl_3 + Cl \rightarrow CHCl_2 + Cl_2$	$1.66\times10^{-10}\exp(-10610/T)$	[51]
$CHCl_3 + Cl \rightarrow CCl_3 + HCl$	$1.15\times10^{-11}\exp(-1667/T)$	[51]
$CHCl_2 + O_2 \rightarrow CHOCl + ClO$	$1.66\times10^{-11}\exp(-14140/T)$	[51]
$CHCl_2 + O \rightarrow CHOCl + Cl$	1.66×10^{-10}	[51]
$CHOCl + M \rightarrow CO + HCl + M$	$1.66\times10^{-7}\exp(-20200/T)$	[51]
$CHOCl + Cl \rightarrow COCl + HCl$	$3.31\times10^{-11}\exp(-1515/T)$	[51]
$CHOCl + O \rightarrow OH + COCl$	5.00×10^{-13}	d
$CHOCl + O(^1D) \rightarrow OH + COCl$	1.00×10^{-10}	d
$Cl + H_2O \rightarrow OH + HCl$	$2.79\times10^{-11}\exp(-8670/T)$	[41]
$Cl + HO_2 \rightarrow HCl + O_2$	3.00×10^{-11}	[37]
$Cl + H_2 \rightarrow HCl + H$	$3.7\times10^{-11}\exp(-2300/T)$	[37]
$Cl + O_2 + M \rightarrow ClOO + M$	$8.996\times10^{-30}T^{-1.45}\exp(2.911\times10^{-8}/T)$ cm^6 s^{-1}	[37]

$Cl + O_3 \rightarrow ClO + O_2$	$2.069\times10^{-11}\exp(-236.9/T)$	[37]
$Cl + CCl_3 \rightarrow CCl_4$	5.00×10^{-11}	[37]
$Cl + HOCl \rightarrow Cl_2 + OH$	$3.00\times10^{-12}\exp(-129.8/T)$	[37]
$Cl + HOCl \rightarrow HCl + ClO$	$3.00\times10^{-12}\exp(-129.8/T)$	[37]
$Cl + ClO \rightarrow O + Cl_2$	$1.74\times10^{-12}\exp(-4590/T)$	d
$Cl + ClOO \rightarrow Cl_2 + O_2$	1.40×10^{-10}	[37]
$Cl + ClOO \rightarrow ClO + ClO$	8.00×10^{-12}	[37]
$Cl + CCl_2 \rightarrow CCl_3$	5.00×10^{-11}	d
$Cl + HO_2 \rightarrow OH + ClO$	$1.05\times10^{-10}\exp(-858.6/T)$	[51]
$ClO + H_2 \rightarrow HCl + OH$	4.98×10^{-16}	[37]
$ClO + H_2 \rightarrow HOCl + H$	1.10×10^{-20}	[44]
$ClO + O \rightarrow Cl + O_2$	$3.00\times10^{-11}\exp(-6.995/T)$	[37]
$ClO + ClO \rightarrow Cl_2 + O_2$	4.90×10^{-15}	[37]
$ClO + ClO \rightarrow Cl + ClOO$	3.40×10^{-15}	[37]
$ClO + CO \rightarrow CO_2 + Cl$	$1.00\times10^{-12}\exp(-3737/T)$	[51]
$ClO + O_3 \rightarrow ClOO + O_2$	$1.00\times10^{-12}\exp(-4000/T)$	[37]
$Cl_2O + O \rightarrow ClO + ClO$	$2.90\times10^{-11}\exp(-630/T)$	[53]
$Cl_2O + OH \rightarrow HOCl + ClO$	$1.70\times10^{-12}\exp(420/T)$	[62]
$ClOO + CO \rightarrow CO_2 + CIO$	$1.66\times10^{-10}\exp(-10100/T)$	[51]
$ClOO + M \rightarrow Cl + O_2 + M$	$2.8\times10^{-10}\exp(-1820/T)$	[53]
$Cl_2 + O \rightarrow ClO + Cl$	4.20×10^{-13}	[63]
$Cl_2 + OH \rightarrow HOCl + Cl$	$1.7\times10^{-12}\exp(-911/T)$	[64]
$CO + H + M \rightarrow HCO + M$	$1.99\times10^{-33}\exp(-842/T)$ $cm^6\ s^{-1}$	[41]
$CO + O_3 \rightarrow O_2 + CO_2$	4.00×10^{-25}	[41]
$CO + O_2 \rightarrow CO_2 + O$	$4.2\times10^{-12}\exp(-24000/T)$	[47]
$CO + O + M \rightarrow CO_2 + M$	$1.7\times10^{-33}\exp(-1510/T)$ $cm^6\ s^{-1}$	[47]
$CO + HO_2 \rightarrow OH + CO_2$	$2.5\times10^{-10}\exp(-11900/T)$	[47]
$CO_2 + H \rightarrow CO + OH$	$2.5\times10^{-10}\exp(-13300/T)$	[47]
$CO_2 + O \rightarrow CO + O_2$	$2.8\times10^{-11}\exp(-26500/T)$	[47]

$C_2O + O \rightarrow CO + CO$	9.51×10^{-11}	[41]
$C_2O + O_2 \rightarrow CO_2 + CO$	3.30×10^{-13}	[41]
$CO_2 + O(^1D) \rightarrow O + CO_2$	1.05×10^{-10}	[65]
$COCl + M \rightarrow CO + Cl + M$	$4.1\times10^{-10}\exp(-2960/T)$	[66]
$COCl + Cl \rightarrow CO + Cl_2$	$2.16\times10^{-9}\exp(-1.67\times10^{3}/T)$	[37]
$COCl + O_2 \rightarrow CO_2 + ClO$	1.00×10^{-11}	e, [51]
$COCl + O \rightarrow CO + ClO$	1.00×10^{-11}	d
$COCl + H \rightarrow CO + HCl$	1.66×10^{-10}	[51]
$COCl + OH \rightarrow CO + HOCl$	1.66×10^{-10}	[51]
$COCl + O \rightarrow CO_2 + Cl$	1.66×10^{-11}	[51]
$COCl + ClO \rightarrow CO + Cl_2O$	1.66×10^{-10}	[51]
$COCl + ClO \rightarrow CO_2 + Cl_2$	1.66×10^{-10}	[51]
$COCl_2 + O_3 \rightarrow COCl + ClO + O_2$	1.00×10^{-15}	d
$COCl_2 + Cl \rightarrow COCl + Cl_2$	$5.25\times10^{-11}T^{0.5}\exp(-10100/T)$	[51]
$COCl_2 + OH \rightarrow COCl + HOCl$	$1.66\times10^{-12}\exp(-5051/T)$	[51]
$COCl_2 + H \rightarrow COCl + HCl$	$1.66\times10^{-11}\exp(-1010/T)$	[51]
$COCl_2 + O \rightarrow ClO + COCl$	9.96×10^{-15}	[67]
$COCl_2 + O(^1D) \rightarrow ClO + COCl$	1.00×10^{-10}	[53]
$O^+ + Cl^- \rightarrow O + Cl$	5.00×10^{-8}	[49]
$O^+ + CCl_4 \rightarrow CCl_3^+ + Cl + O$	1.00×10^{-9}	d
$O_2^+ + Cl^- \rightarrow O_2 + Cl$	1.00×10^{-8}	[49]
$O_2^+ + CCl_4 \rightarrow CCl_3+ + Cl + O_2$	1.00×10^{-9}	d
$O_2^+ + H_2O + M \rightarrow O_2^+{\cdot}H_2O + M$	2.50×10^{-28} cm^6 s^{-1}	[34]
$O_2^+{\cdot}H_2O + O_2^- \rightarrow O_2 + O_2 + H_2O$	$2.00\times10^{-6}(T/300)^{-0.5}$	d
$O^- + H_3O^+ \rightarrow OH + H_2O$	$3.00\times10^{-6}(T/300)^{-0.5}$	d
$O^- + O_2^+{\cdot}H_2O \rightarrow O + O_2 + H_2O$	$3.00\times10^{-6}(T/300)^{-0.5}$	d
$O^- + H_3O^+{\cdot}H_2O \rightarrow OH + H_2O + H_2O$	$3.00\times10^{-6}(T/300)^{-0.5}$	d
$O^- + CO_2^+ \rightarrow O + CO_2$	$3.00\times10^{-6}(T/300)^{-0.5}$	d
$H_2O^+ + H_2O \rightarrow H_3O^+ + OH$	1.70×10^{-9}	[34]

$H_2O^+ + O_2 \rightarrow O_2$+ + H_2O	4.30×10^{-10}	[34]
$H_2O^+ + Cl^- \rightarrow H_2O + Cl$	$5.00\times10^{-8}(T/300)^{-0.5}$	[49]
$H_2O^+ + CCl_4 \rightarrow CCl_3$+ + Cl + H_2O	1.00×10^{-9}	d
$H_3O^+ + Cl^- \rightarrow H_2O + HCl$	$5.00\times10^{-8}(T/300)^{-0.5}$	[49]
$H_3O^+{\cdot}H_2O + Cl^- \rightarrow H_2O + H_2O + HCl$	$5.00\times10^{-8}(T/300)^{-0.5}$	[49]
$H_3O^+ + H_2O + M \rightarrow H_3O^+{\cdot}H_2O + M$	5.00×10^{-27} cm^6 s^{-1}	[34]
$H_3O^+{\cdot}H_2O + O_2^- \rightarrow H_2O + H_2O + HO_2$	$2.00\times10^{-6}\ (T/300)^{-0.5}$	d
$H_3O^+ + O_2^- \rightarrow H_2O + HO_2$	2.00×10^{-6}	d
$H^- + H_3O^+ \rightarrow H_2 + H_2O$	$3.00\times10^{-6}\ (T/300)^{-0.5}$	d
$H^- + O_2^+{\cdot}H_2O \rightarrow HO_2 + H_2O$	$3.00\times10^{-6}\ (T/300)^{-0.5}$	d
$H^- + H_3O^+{\cdot}H_2O \rightarrow H_2 + H_2O + H_2O$	$3.00\times10^{-6}\ (T/300)^{-0.5}$	d
$H^- + CO_2^+ \rightarrow H + CO_2$	$3.00\times10^{-6}\ (T/300)^{-0.5}$	d
$C^+ + H^- \rightarrow C + H$	$5.00\times10^{-8}\ (T/300)^{-0.5}$	[49]
$C^+ + O^- \rightarrow C + O$	5.00×10^{-8}	[49]
$C^+ + O_2^- \rightarrow C + O_2$	5.00×10^{-8}	[49]
$C^+ + Cl^- \rightarrow C + Cl$	5.00×10^{-8}	[49]
$CCl^+ + H^- \rightarrow CCl + H$	5.00×10^{-8}	[49]
$CCl^+ + O^- \rightarrow CCl + O$	5.00×10^{-8}	[49]
$CCl^+ + O_2^- \rightarrow CCl + O_2$	5.00×10^{-8}	[49]
$CCl^+ + Cl^- \rightarrow CCl + Cl$	5.00×10^{-8}	[49]
$CCl_2^+ + O_2^- \rightarrow CCl_2 + O_2$	5.00×10^{-8}	[49]
$CCl_2^+ + Cl^- \rightarrow CCl_2 + Cl$	5.00×10^{-8}	[49]
$CCl_2^+ + H^- \rightarrow Cl_2 + H$	5.00×10^{-8}	[49]
$CCl_2^+ + O^- \rightarrow Cl_2 + O$	5.00×10^{-8}	[49]
$CCl_2^+ + O_2^- \rightarrow Cl_2 + O_2$	5.00×10^{-8}	[49]
$CCl_2^+ + Cl^- \rightarrow Cl_2 + Cl$	5.00×10^{-8}	[49]
$CCl_2^+ + O^- \rightarrow CCl_2 + O$	5.00×10^{-8}	[49]
$CCl_3^+ + H^- \rightarrow CCl_3 + H$	5.00×10^{-8}	[49]
$CCl_3^+ + O^- \rightarrow CCl_3 + O$	5.00×10^{-8}	[49]

$CCl_3^+ + O_2^- \rightarrow CCl_3 + O_2$	5.00×10^{-8}	[49]
$CCl_3^+ + Cl^- \rightarrow CCl_3 + Cl$	5.00×10^{-8}	[49]
$CCl_2^+ + H^- \rightarrow CCl_2 + H$	5.00×10^{-8}	[49]
$Cl^+ + H^- \rightarrow Cl + H$	5.00×10^{-8}	[49]
$Cl^+ + O^- \rightarrow Cl + O$	5.00×10^{-8}	[49]
$Cl^+ + O_2^- \rightarrow Cl + O_2$	5.00×10^{-8}	[49]
$Cl^+ + Cl^- \rightarrow Cl + Cl$	5.00×10^{-8}	[49]
$CO_2^+ + Cl^- \rightarrow CO_2 + Cl$	5.00×10^{-8}	[49]
$CO_2^+ + O_2^- \rightarrow CO_2 + O_2$	$2.00\times10^{-6}\ (T/300)^{-0.5}$	d
$CO_2^+ + O_2 \rightarrow O_2^+ + CO_2$	5.60×10^{-11}	[34]
$Ar^+ + O_2 \rightarrow O_2^+ + Ar$	4.00×10^{-11}	d
$Ar^+ + O_3 \rightarrow O_2+ + Ar + O$	4.00×10^{-11}	d
$Ar^+ + CCl_4 \rightarrow CCl_3+ + Cl + Ar$	1.00×10^{-9}	d
$Ar^+ + Ar + M \rightarrow Ar_2^+ + M$	$2.00\times10^{-31}\ cm^6\ s^{-1}$	[68]
$Ar^* + CCl_4 \rightarrow CCl_2 + Cl_2 + Ar$	1.00×10^{-10}	d
$Ar^{**} \rightarrow Ar^*$	$1.00\times10^{6}\ s^{-1}$	d
$Ar^{**} + CCl_4 \rightarrow CCl_2 + Cl_2 + Ar$	1.00×10^{-10}	d
$Ar^{**} + Ar + M \rightarrow Ar_2^* + M$	$3.00\times10^{-33}\ cm^6\ s^{-1}$	d
$Ar_2^* \rightarrow Ar + Ar$	6.00×10^{7}	d
$Ar_2^+ + O_2 \rightarrow O_2^+ + Ar + Ar$	1.20×10^{-10}	[68]
$Ar^+ + H_2O \rightarrow H_2O^+ + Ar$	1.60×10^{-9}	[68]
$Ar_2^+ + H_2O \rightarrow H_2O^+ + Ar + Ar$	2.00×10^{-9}	[68]
$Ar_2^+ + CCl_4 \rightarrow CCl_3+ + Ar + Ar$	1.00×10^{-9}	d
$Ar^+ + Cl^- \rightarrow Ar + Cl$	1.00×10^{-7}	e, [49]
$Ar_2^+ + Cl^- \rightarrow Ar + Ar + Cl$	1.00×10^{-7}	e, [49]
$Ar^+ + O^- \rightarrow Ar + O$	1.00×10^{-7}	e, [49]
$Ar_2^+ + O^- \rightarrow Ar + Ar + O$	1.00×10^{-7}	d
$Ar_2^* + Ar_2^* \rightarrow Ar_2^+ + e + Ar + Ar$	3.00×10^{-10}	d
$Ar^* + O_2 \rightarrow O(^1D) + O + Ar$	2.10×10^{-10}	[69]

$Ar^{**} + O_2 \rightarrow O(^1D) + O + Ar$	2.10×10^{-10}	[69]
$Ar^{*} + O_3 \rightarrow O(^1D) + O_2 + Ar$	2.10×10^{-10}	d
$Ar^{**} + O_3 \rightarrow O(^1D) + O_2 + Ar$	2.10×10^{-10}	d
$Ar^{*} + H_2O \rightarrow H + OH + Ar$	2.10×10^{-10}	[69]
$Ar^{**} + H_2O \rightarrow H + OH + Ar$	2.10×10^{-10}	[69]

Additional reactions of Xe/Cl_2

Reaction	Rate Coefficient [b]	Ref.
$Cl + Cl + Cl_2 \rightarrow Cl_2 + Cl_2$	5.40×10^{-32} cm^6 s^{-1}	[70]
$Cl + Cl + Xe \rightarrow Cl_2 + Xe$	5.40×10^{-32} cm^6 s^{-1}	e, [70]
$Cl^- + Cl^+ \rightarrow Cl + Cl$	1.00×10^{-7}	e, [49]
$Cl^- + Cl_2^+ \rightarrow Cl_2 + Cl$	1.00×10^{-7}	e, [49]
$Cl^+ + Cl_2 \rightarrow Cl_2^+ + Cl$	5.40×10^{-10}	[71]
$Cl^* \rightarrow Cl$	1.00×10^{7} s^{-1}	[72]
$Cl^- + Cl^+ \rightarrow Cl_2^*$	2.00×10^{6} s^{-1}	[73]
$Cl_2^* \rightarrow Cl_2 + h\nu$ (259 nm)	7.22×10^{7} s^{-1}	[73]
$Xe^* + Xe^* \rightarrow Xe^+ + Xe + e$	5.00×10^{-10}	[74]
$Xe^* + Xe + Xe \rightarrow Xe_2^* + Xe$	5.00×10^{-32} cm^6 s^{-1}	[73]
$Xe^* + Xe + Cl_2 \rightarrow Xe_2^* + Cl_2$	5.00×10^{-32} cm^6 s^{-1}	e, [73]
$Xe^* + Cl_2 \rightarrow XeCl^* + Cl$	7.20×10^{-10}	[75, 76]
$Xe^{**} + Cl_2 \rightarrow XeCl^* + Cl$	7.20×10^{-10}	[75, 76]
$Xe^{**} + Xe + Xe \rightarrow Xe_2^* + Xe$	5.00×10^{-32} cm^6 s^{-1}	[73]
$Xe^{**} + Xe + Cl_2 \rightarrow Xe_2^* + Cl_2$	5.00×10^{-32} cm^6 s^{-1}	e, [73]
$Xe^{**} + Xe^{**} \rightarrow Xe^+ + Xe + e$	5.00×10^{-10}	e, [74]
$Xe^{**} \rightarrow Xe^*$	3.00×10^{7} s^{-1}	[72]
$Xe^+ + Cl^- \rightarrow XeCl^*$	2.00×10^{-6} (at $p = 0.6$ atm, pressure-dependent)	[77]
$Xe^+ + Xe + Xe \rightarrow Xe_2^+ + Xe$	2.50×10^{-31} cm^6 s^{-1}	[78]
$Xe^+ + Xe + Cl_2 \rightarrow Xe_2^+ + Cl_2$	2.50×10^{-31} cm^6 s^{-1}	e, [78]
$Xe_2^* + Xe_2^* \rightarrow Xe_2^+ + Xe + Xe + e$	3.30×10^{-10}	[73]

$Xe_2^* \rightarrow Xe + Xe + h\nu$ (172 nm)	7.22×10^{7}	[73]
$Xe_2^* + Cl_2 \rightarrow XeCl^* + Xe + Cl$	5.00×10^{-10}	[76]
$Xe_2^+ + Cl^- \rightarrow XeCl^* + Xe$	1.70×10^{-6} (at p = 0.6 atm, pressure-dependent)	[77]
$XeCl^* \rightarrow Xe + Cl + h\nu$ (308 nm)	2.50×10^{-7}	[73]
$XeCl^* + Xe \rightarrow Xe + Xe + Cl$	7.30×10^{-12}	[79]
$XeCl^* + Cl_2 \rightarrow Cl_2 + Xe + Cl$	8.8×10^{-11}	[79]
$XeCl^* + Xe + Xe \rightarrow Xe_2Cl^* + Xe$	7.30×10^{-31}	[80]
$XeCl^* + Xe + Cl_2 \rightarrow Xe_2Cl^* + Cl_2$	7.30×10^{-31} cm^{6} s^{-1}	[73]
$Xe_2Cl^* + Cl_2 \rightarrow Xe + Xe + Cl + Cl_2$	2.60×10^{-10}	[73]
$Xe_2Cl^* + Xe \rightarrow Xe + Xe + Xe + Cl$	6.0×10^{-15}	[73]
$Xe_2Cl^* \rightarrow Xe + Xe + h\nu$ (490 nm)	7.40×10^{6} s^{-1}	[81]

Additional reactions of $Ar/CF_4/C_2F_6$

Reaction	Rate Coefficient [b]	Ref.
$Ar^+ + Ar \rightarrow Ar + Ar^+$	1.0×10^{-9}	[82]
$Ar^+ + CF_4 \rightarrow CF_3^+ + F + Ar$	7.0×10^{-10}	[82]
$Ar^+ + CF_3 \rightarrow CF_3^+ + Ar$	7.0×10^{-10}	[82]
$Ar^+ + C_2F_6 \rightarrow CF_3^+ + CF_3 + Ar$	9.58×10^{-10}	[82]
$Ar^+ + C_2F_5 \rightarrow C_2F_5^+ + Ar$	1.0×10^{-10}	e, [83]
$Ar^+ + C_2F_4 \rightarrow C_2F_4^+ + Ar$	1.0×10^{-10}	e, [83]
$Ar^* + Ar^* \rightarrow Ar^+ + Ar + e$	5.0×10^{-10}	[84]
$Ar^* + CF_4 \rightarrow CF_2 + F_2 + Ar$	4.0×10^{-11}	[85]
$Ar^* + CF_3 \rightarrow CF_2 + F + Ar$	4.0×10^{-11}	[85]
$Ar^* + CF_2 \rightarrow CF + F + Ar$	4.0×10^{-11}	[85]
$Ar^* + C_2F_5 \rightarrow CF_2 + CF_3 + Ar$	4.0×10^{-11}	[85]
$Ar^* + C_2F_3 \rightarrow CF_2 + CF + Ar$	4.0×10^{-11}	[85]
$Ar^* + C_2F_6 \rightarrow CF_3 + CF_3 + Ar$	4.0×10^{-11}	[85]
$Ar^* + C_2F_4 \rightarrow CF_2 + CF_2 + Ar$	4.0×10^{-11}	[85]
$CF_3^+ + CF_3 \rightarrow CF_3^+ + CF_3$	1.0×10^{-9}	[82]

$CF_3^+ + C_2F_6 \rightarrow C_2F_5^+ + CF_4$	3.50×10^{-11}	[82]
$C_2F_5^+ + C_2F_5 \rightarrow C_2F_5^+ + C_2F_5$	1.0×10^{-9}	[82]
$C_2F_4^+ + C_2F_4 \rightarrow C_2F_4^+ + C_2F_4$	1.0×10^{-9}	[82]
$F^- + Ar^+ \rightarrow F + Ar$	1.0×10^{-7}	[86]
$F^- + CF_3^+ \rightarrow F + CF_3$	1.0×10^{-7}	[86]
$F^- + C_2F_4^+ \rightarrow F + C_2F_4$	1.0×10^{-7}	[86]
$F^- + C_2F_5^+ \rightarrow F + C_2F_5$	1.0×10^{-7}	[86]
$CF_3^- + Ar^+ \rightarrow CF_3 + Ar$	1.0×10^{-7}	[86]
$CF_3^- + CF_3^+ \rightarrow CF_3 + CF_3$	1.0×10^{-7}	[86]
$CF_3^- + C_2F_4^+ \rightarrow CF_3 + C_2F_4$	1.0×10^{-7}	[86]
$CF_3^- + C_2F_5^+ \rightarrow CF_3 + C_2F_5$	1.0×10^{-7}	[86]
$CF_3^- + F \rightarrow CF_3 + F^-$	5.0×10^{-8}	[86]
$F + F + M \rightarrow F_2 + M$	$2.4\times10^{-33}(T/298)^{0.033}\ \mathrm{cm^6\ s^{-1}}$	[87]
$F + C_2F_4 \rightarrow CF_3 + CF_2$	4.0×10^{-11}	[88]
$F + C_2F_5 \rightarrow CF_3 + CF_3$	1.0×10^{-11}	[88]
$F + C_2F_3 \rightarrow C_2F_4$	1.0×10^{-12}	[89]
$F + CF_3 \rightarrow CF_4$	$1.99\times10^{-10}(T/300)^{-7.71}\exp(-1183.4/T)$	[90]
$F + CF_2 \rightarrow CF_3$	8.40×10^{-15}	[88]
$F_2 + CF_2 \rightarrow CF_3 + F$	4.56×10^{-13}	[89]
$F_2 + CF_3 \rightarrow CF_4 + F$	1.88×10^{-14}	[89]
$CF_3 + CF_3 \rightarrow C_2F_6$	7.67×10^{-12}	[89]
$CF_2 + CF_2 \rightarrow C_2F_4$	5.0×10^{-14}	[89]
$CF_2 + CF_3 \rightarrow C_2F_5$	8.26×10^{-13}	[89]

Additional reactions of $Ar/CF_4/C_2F_6/H_2/O_2/H_2O$

Reaction	Rate Coefficient [b]	Ref.
$Ar^+ + O_2 \rightarrow O_2^+ + Ar$	5.1×10^{-11}	[91]
$Ar^+ + O \rightarrow O^+ + Ar$	1.0×10^{-11}	[92]
$Ar^* + O_2 \rightarrow O + O + Ar$	2.1×10^{-10}	[93]
$Ar^* + O \rightarrow O(^1D) + Ar$	4.1×10^{-11}	[94]

$Ar^* + H_2 \rightarrow Ar + H + H$	2.1×10^{-10}	[93]
$Ar^* + H_2O \rightarrow Ar + OH + H$	2.1×10^{-10}	[93]
$Ar^+ + H_2 \rightarrow Ar + H_2^+$	1.0×10^{-9}	[94]
$Ar^+ + H_2O \rightarrow Ar + H_2O^+$	1.4×10^{-9}	[94]
$F^+ + H_2 \rightarrow H_2^+ + F$	1.2×10^{-9}	[94]
$F^+ + H_2O \rightarrow H_2O^+ + F$	7.97×10^{-11}	[94]
$F^- + H \rightarrow e + HF$	1.6×10^{-9}	[94]
$H^- + H \rightarrow e + H_2$	1.8×10^{-9}	[94]
$H^- + H_2O \rightarrow OH^- + H_2$	3.7×10^{-9}	[94]
$H^- + Ar^+ \rightarrow H + Ar$	1.0×10^{-7}	e, [86]
$H^- + CF_3^+ \rightarrow H + CF_3$	1.0×10^{-7}	e, [86]
$H^- + O_2^+ + M \rightarrow HO_2 + M$	1.2×10^{-25} cm^6 s^{-1}	e, [86]
$H^- + O^+ + M \rightarrow OH + M$	1.2×10^{-25} cm^6 s^{-1}	e, [86]
$H^- + F^+ + M \rightarrow HF + M$	1.2×10^{-25} cm^6 s^{-1}	e, [86]
$H^- + F_2^+ \rightarrow H + F_2$	5.0×10^{-8}	e, [86]
$H^- + C_2F_4^+ \rightarrow H + C_2F_4$	1.0×10^{-7}	e, [86]
$H^- + C_2F_5^+ \rightarrow H + C_2F_5$	1.0×10^{-7}	e, [86]
$OH^- + H \rightarrow e + H_2O$	1.4×10^{-9}	[94]
$OH^- + O \rightarrow e + HO_2$	2.0×10^{-10}	[94]
$OH^- + Ar^+ \rightarrow OH + Ar$	1.0×10^{-7}	e, [86]
$OH^- + CF_3^+ \rightarrow OH + CF_3$	1.0×10^{-7}	e, [86]
$OH^- + O_2^+ \rightarrow OH + O_2$	1.0×10^{-7}	e, [86]
$OH^- + O^+ \rightarrow OH + O$	1.0×10^{-7}	e, [86]
$OH^- + F^+ \rightarrow OH + F$	1.0×10^{-7}	e, [86]
$OH^- + F_2^+ \rightarrow OH + F_2$	1.0×10^{-7}	e, [86]
$OH^- + C_2F_4^+ \rightarrow OH + C_2F_4$	1.0×10^{-7}	e, [86]
$OH^- + C_2F_5^+ \rightarrow OH + C_2F_5$	1.0×10^{-7}	e, [86]
$H_2^+ + O_2 \rightarrow O_2^+ + H_2$	7.56×10^{-9}	[94]
$H_2^+ + C_2F_6 \rightarrow CF_3^+ + CF_3 + H_2$	5.0×10^{-10}	[94]

$H_2^+ + H_2O \rightarrow H_2 + H_2O^+$	3.6×10^{-9}	[94]
$H_2^+ + CF_3^- \rightarrow H_2 + CF_3$	1.0×10^{-7}	e, [86]
$H_2^+ + F^- \rightarrow H_2 + F$	1.0×10^{-7}	e, [86]
$H_2^+ + O^- \rightarrow H_2 + O$	1.0×10^{-7}	e, [86]
$H_2^+ + H^- \rightarrow H_2 + H$	1.0×10^{-7}	e, [86]
$H_2^+ + OH^- \rightarrow H_2 + OH$	1.0×10^{-7}	e, [86]
$H_2O^+ + CF_3^- \rightarrow H_2O + CF_3$	1.0×10^{-7}	e, [86]
$H_2O^+ + F^- \rightarrow H_2O + F$	1.0×10^{-7}	e, [86]
$H_2O^+ + O^- \rightarrow H_2O + O$	1.0×10^{-7}	e, [86]
$H_2O^+ + H^- \rightarrow H_2O + H$	1.0×10^{-7}	e, [86]
$H_2O^+ + OH^- \rightarrow H_2O + OH$	1.0×10^{-7}	e, [86]
$H_2O^+ + H_2O \rightarrow H_3O^+ + OH$	1.7×10^{-9}	[94]
$H_3O^+ + H^- \rightarrow H_2 + H_2O$	1.0×10^{-7}	e, [86]
$H_3O^+ + O^- \rightarrow OH + H_2O$	1.0×10^{-7}	e, [86]
$H_3O^+ + F^- \rightarrow H_2O + HF$	1.0×10^{-7}	e, [86]
$H_3O^+ + CF_3^- \rightarrow H_2O + HF + CF_2$	1.0×10^{-7}	e, [86]
$H_3O^+ + OH^- \rightarrow H_2O + H_2O$	1.0×10^{-7}	e, [86]
$H + H + M \rightarrow H_2 + M$	8.1×10^{-33} cm^6 s^{-1}	[95]
$H + OH + M \rightarrow H_2O + M$	$1.56\times10^{-31}(T/300)^{-1.21}\times\exp(295.3/T)$ cm^{-6}s^{-1}	[44]
$H + O + M \rightarrow OH + M$	4.33×10^{-32} cm^6 s^{-1}	[96]
$H + O_2 + M \rightarrow HO_2 + M$	$1.94\times10^{-32}(T/300)^{-0.7}\times\exp(144.3/T)$ cm^6 s^{-1}	[44]
$H + HO_2 \rightarrow O + H_2O$	$3.84\times10^{-11}(T/300)^{-0.46}\exp(-677.9/T)$	[96]
$H + HO_2 \rightarrow H_2 + O_2$	$2.34\times10^{-11}(T/300)^{-0.59}\exp(-320.8/T)$	[96]
$H + HO_2 \rightarrow OH + OH$	$1.58\times10^{-10}\exp(-365.2/T)$	[96]
$H + CF_3 \rightarrow CF_2 + HF$	9.0×10^{-11}	[97]
$H + CF_2 \rightarrow CF + HF$	$3.32\times10^{-10}\exp(-629/T)$	[89]
$H + CF \rightarrow C + HF$	1.9×10^{-11}	[89]
$H + C_2F_5 \rightarrow C_2F_4 + HF$	2.0×10^{-11}	[89]
$H + F_2 \rightarrow F + HF$	1.53×10^{-11}	[89]

$H + COF \rightarrow CO + HF$	1.93×10^{-10}	[89]
$C + O_2 \rightarrow CO + O$	3.3×10^{-11}	[54]
$H_2 + F \rightarrow HF + H$	$1.43\times10^{-10}\exp(-528.0/T)$	[89]
$H_2 + O(^1D) \rightarrow OH + H$	1.1×10^{-10}	[53]
$OH + F \rightarrow O + HF$	3.32×10^{-11}	[89]
$OH + CF_3 \rightarrow COF_2 + HF$	3.32×10^{-11}	[89]
$OH + CF_2 \rightarrow COF + HF$	$6.64\times10^{-12}\exp(-1762.5/T)$	[89]
$OH + CF \rightarrow HF + CO$	$6.64\times10^{-11} \exp(-503/T)$	[89]
$OH + CO \rightarrow H + CO_2$	$1.18\times10^{-13}(T/300)^{-0.98}\exp(-94.3/T)$	[89]
$HO_2 + F \rightarrow O_2 + HF$	8.28×10^{-11}	[98]
$HO_2 + CF_3 \rightarrow COF_2 + HF + O$	1.66×10^{-11}	[89]
$HO_2 + CF_2 \rightarrow COF_2 + OH$	$1.66\times10^{-11} \exp(-1762.5/T)$	[89]
$HO_2 + O \rightarrow OH + O_2$	$3.0\times10^{-11} \exp(200/T)$	[99]
$HO_2 + OH \rightarrow H_2O + O_2$	5.1×10^{-11}	[100]
$H_2O + F \rightarrow OH + HF$	$1.11\times10^{-11}(T/300)^{1.5}$	[89]
$H_2O + O(^1D) \rightarrow OH + OH$	2.5×10^{-10}	[101]
$O^+ + CF_4 \rightarrow CF_3^+ + FO$	1.4×10^{-9}	[102]
$O^+ + CF_3 \rightarrow CF_3^+ + O$	1.0×10^{-10}	[94]
$O^+ + C_2F_6 \rightarrow CF_3^+ + CF_3 + O$	1.47×10^{-9}	[102]
$O^+ + C_2F_6 \rightarrow C_2F_5^+ + FO$	3.0×10^{-11}	[102]
$O^+ + C_2F_4 \rightarrow C_2F_4^+ + O$	1.3×10^{-9}	[84]
$F^+ + CF_4 \rightarrow CF_3^+ + F_2$	1.0×10^{-9}	[84]
$F^+ + CF_3 \rightarrow CF_3^+ + F$	1.0×10^{-9}	[84]
$F^+ + C_2F_6 \rightarrow C_2F_5^+ + F_2$	1.0×10^{-9}	[84]
$F^+ + C_2F_5 \rightarrow C_2F_4^+ + F_2$	1.0×10^{-9}	[84]
$F^+ + C_2F_4 \rightarrow C_2F_4^+ + F$	1.0×10^{-9}	[84]
$F^+ + O \rightarrow O^+ + F$	1.0×10^{-10}	[84]
$F^+ + O_2 \rightarrow O_2^+ + F$	6.4×10^{-10}	[84]
$F^+ + O_2 \rightarrow O^+ + FO$	1.6×10^{-10}	[84]

$F^+ + F \rightarrow F + F^+$	1.0×10^{-9}	e, [84]
$F_2^+ + CF_4 \rightarrow CF_3^+ + F + F_2$	1.0×10^{-10}	e, [84]
$F_2^+ + CF_3 \rightarrow CF_3^+ + F_2$	1.0×10^{-10}	e, [84]
$F_2^+ + C_2F_4 \rightarrow C_2F_4^+ + F_2$	1.0×10^{-10}	e, [84]
$F_2^+ + C_2F_5 \rightarrow C_2F_5^+ + F_2$	1.0×10^{-10}	e, [84]
$F_2^+ + F_2 \rightarrow F_2^+ + F_2$	1.0×10^{-9}	e, [84]
$O_2^+ + C_2F_4 \rightarrow C_2F_4^+ + O_2$	9.8×10^{-10}	[83]
$O_2^+ + C_2F_5 \rightarrow C_2F_5^+ + O_2$	1.0×10^{-10}	e, [83]
$O_2^+ + O_2 \rightarrow O_2^+ + O_2$	1.0×10^{-9}	[84]
$F^- + O_2^+ \rightarrow F + O_2$	1.0×10^{-7}	e, [86]
$F^- + O^+ \rightarrow F + O$	1.0×10^{-7}	e, [86]
$F^- + F_2^+ \rightarrow F + F_2$	1.0×10^{-7}	e, [86]
$F^- + F^+ \rightarrow F + F$	1.0×10^{-7}	e, [86]
$F + CF_3 \rightarrow CF_4$	$4.9\times10^{-9}(T/300)^{-7.84}\exp(-1876.4/T)$ (at p = 150 mTor, pressure-dependent)	[90]
$F + CF_2 \rightarrow CF_3$	4.14×10^{-14} (at p = 150 mTor, pressure-dependent)	[88]
$F + COF \rightarrow COF_2$	2.76×10^{-13}	[88]
$F + CO \rightarrow COF$	3.87×10^{-16}	[88]
$O^- + Ar^+ \rightarrow O + Ar$	1.0×10^{-7}	e, [86]
$O^- + O_2^+ \rightarrow O + O_2$	1.0×10^{-7}	e, [86]
$O^- + O^+ \rightarrow O + O$	1.0×10^{-7}	e, [86]
$O^- + F_2^+ \rightarrow O + F_2$	1.0×10^{-7}	e, [86]
$O^- + F^+ \rightarrow O + O$	1.0×10^{-7}	e, [86]
$O^- + CF_3^+ \rightarrow O + CF_3$	1.0×10^{-7}	e, [86]
$O^- + C_2F_4^+ \rightarrow O + C_2F_4$	1.0×10^{-7}	e, [86]
$O^- + C_2F_5^+ \rightarrow O + C_2F_5$	1.0×10^{-7}	e, [86]
$CF_3^- + O_2^+ \rightarrow CF_3 + O_2$	1.0×10^{-7}	e, [86]
$CF_3^- + O^+ \rightarrow CF_3 + O$	1.0×10^{-7}	e, [86]
$CF_3^- + F_2^+ \rightarrow CF_3 + F_2$	1.0×10^{-7}	e, [86]
$CF_3^- + F^+ \rightarrow CF_3 + CF_3$	1.0×10^{-7}	e, [86]

$O^- + O \rightarrow O_2 + e$	3.0×10^{-10}	[94]
$O + O + M \rightarrow O_2 + M$	1.0×10^{-33} cm^6 s^{-1}	[95]
$O(^1D) + CF_4 \rightarrow O + CF_4$	1.8×10^{-13}	[88]
$O(^1D) + COF_2 \rightarrow O + COF_2$	5.3×10^{-11}	[88]
$O(^1D) + COF_2 \rightarrow F_2 + CO_2$	2.1×10^{-11}	[88]
$O(^1D) + O_2 \rightarrow O + O_2$	$3.2\times10^{-11}\exp(67/T)$	[53]
$O(^1D) + CF_3 \rightarrow COF_2 + F$	3.1×10^{-11}	[88]
$O(^1D) + CF_2 \rightarrow COF + F$	1.4×10^{-11}	[88]
$O(^1D) + CF_2 \rightarrow CO + F + F$	4.0×10^{-12}	[88]
$O(^1D) + CF \rightarrow CO + F$	$6.64\times10^{-11}\exp(-503/T)$	[88]
$O(^1D) + COF \rightarrow CO_2 + F$	9.3×10^{-11}	[88]
$O(^1D) + CF_3O_2 \rightarrow COF_2 + F + O_2$	1.0×10^{-11}	[88]
$O(^1D) + FO \rightarrow O_2 + F$	5.0×10^{-11}	[88]
$O + CF_3 \rightarrow COF_2 + F$	3.1×10^{-11}	[88]
$O + CF_2 \rightarrow COF + F$	1.4×10^{-11}	[88]
$O + CF_2 \rightarrow CO + F + F$	4.0×10^{-12}	[88]
$O + CF \rightarrow CO + F$	$6.64\times10^{-11}\exp(-503/T)$	[89]
$O + COF \rightarrow CO_2 + F$	9.3×10^{-11}	[88]
$O + CF_3O_2 \rightarrow COF_2 + F + O_2$	1.0×10^{-11}	[88]
$O + FO \rightarrow O_2 + F$	5.0×10^{-11}	[88]
$O + F + M \rightarrow FO + M$	1.0×10^{-33} cm^6 s^{-1}	[89]
$O + C_2F_5 \rightarrow COF_2 + CF_3$	3.65×10^{-11}	[89]
$O_2 + CF_3 \rightarrow CF_3O_2$	4.44×10^{-14}	[89]
$COF + CF_2 \rightarrow CF_3 + CO$	3.0×10^{-13}	[89]
$COF + CF_2 \rightarrow COF_2 + CF$	3.0×10^{-13}	[89]
$COF + CF_3 \rightarrow CF_4 + CO$	1.0×10^{-11}	[89]
$COF + CF_3 \rightarrow COF_2 + CF_2$	1.0×10^{-11}	[89]
$COF + COF \rightarrow COF_2 + CO$	1.0×10^{-11}	[89]
$COF + OH \rightarrow CO_2 + CO_2$	1.0×10^{-11}	[89]

$CF_2 + CF_3 \rightarrow C_2F_5$	5.36×10^{-12}	[89]
$CF_3 + CF_3 \rightarrow C_2F_6$	7.26×10^{-12}	[89]

[a] Only reactions directly affecting specises densities are shown here. Additional electron impact collisions (e.g., momentum transfer, vibrational excitation) are included in the EETM.

[b] Rate coefficients have units $cm^3\ s^{-1}$ unless noted otherwise.

[c] Computed using the electron energy distribution and electron impact cross section from cited reference.

[d] Estimated.

[e] Estimated. See cited reference for similar reaction.

B.1 References

[1] Y. Itikawa, M. Hayashi, A. Ichimura, K. Onda, K. Sakimoto, K. Takayanagi, M. Nakamura, H. Nishimura, and T. Takayanagi, J. Phys. Chem. Ref. Data Reprint Number 299, **15** (3), 985 (1986).

[2] J. M. A. Mitchell, Phys. Rep. **186**, 215 (1990).

[3] R. R. Laher and F. R. Gilmore, J. Phys. Chem. Ref. Data **19**, 277 (1990).

[4] A. V. Phelps, JILA Information Center Report No. 28, University of Colorado (1985).

[5] E. Krishnakumar and S. K. Srivastava, Int. J. Mass Spect. Ion Proc. **113**, 1 (1992).

[6] J. J. Lowke, and R. Morrow, IEEE Trans. Plasma Sci. **23**, 661 (1995).

[7] J. B. A. Mitchell, Phys. Rep. **186**, 215 (1990).

[8] M. Hayashi, J. De Physique, Colloque C7, Supplement **40**, C7/45 (1979).

[9] M. Hayashi, *Electron Collision Cross-Sections for Molecules Determined from Beam and Swarm Data*, edited by L.C. Pitchford, B.V. Mckoy, A. Chutjian, S. Trajmar (Springer-Verlag, New York, 1989), pp. 234.

[10] M. Hayashi, in Proceedings of the Meeting of the 4th International Swarm Seminar and the Inelastic Electron-Molecular Collision Symposium, July 19-23, (1985), pp. 345.

[11] B. R. Rowe, F. Vallee, J. L. Queffelec, J. C. Gomet, and M. Morlais, J. Phys. Chem. **88**, 845 (1988).

[12] J.J. Lowke, A.V. Phelps and B.W. Irwin, J. Appl. Phys. **44**, 4664 (1973).

[13] D. C. Griffin, M. S. Pindzola, T. W. Gorczyca, and N. R. Badnell, Phys. Rev. A **51**, 2265 (1995).

[14] G. L. Rogoff, J. M. Kramer, and R. B. Piejek, Trans. Plasma Sci. **14**, 103 (1986).

[15] K. Leiter, K. Stephan, E. Märk, and T. D. Märk, Plasma Chem. Plasma Proc. **4** (4), 235 (1984).

[16] J. B. A. Mitchell, Phys. Rpts. **186**, 215 (1990)

[17] R. A. Bonham, Jpn. J. Appl. Phys., Part 1 **33**, 4157 (1994)

[18] M. Hayashi, in *Gaseous Dielectrics V*, edited by L. G. Christophorou and D. W. Bouldin (Pergamon, New York, 1987), p. 456.

[19] W. L. Morgan, KINEMA: The Plasma Chemistry Code, Version 1.51, (Monument, CO, 1994).

[20] M. Hayashi and T. Nimura, J. Appl. Phys. **54**, 4879 (1983).

[21] K. Tachibana, Phys. Rev. A**34**, 1007 (1986).

[22] D. Rapp and P. Englander-Golden, J. Chem. Phys. **43**, 1464 (1965).

[23] M. Hayashi, Nagoya Institute of Technology Report No. IPPJ-AM-19, 1991.

[24] F. Kannari, M. Obara, T. Fujioka, J. Appl. Phys. **57**, 4390 (1985)

[25] N. J. Mason and W. R. Newell, J. Phys. B **20**, 1357 (1987)

[26] T. Y. Suzuki, Y. Sakai, B. S. Min, T. Takayanagi, K. Wakiya, H. Suzuki, T. Inaba, and H. Takuma, Phys. Rev. A **43**, 5867 (1991).

[27] D. Rapp and P. Englander-Golden, J. Chem. Phys. **43**, 1464 (1965).

[28] D. J. Eckstrom, H. H. Nakano, D. C. Lorents, T. Rothem, J. A. Betts, M. E. Lainhart, D. A. Dakin, and J. A. Maenchen, J. Appl. Phys. **64**, 1679 (1988).

[29] J. W. Shon, Ph.D. dissertation, University of Illinois, 1993.

[30] J. Bretagne, J. Godart, and V. Puech, J. Phys. D **15**, 2205 (1982).

[31] R. A. Bonham, Jpn. J. Appl. Phys., Part 1 **33**, 4157 (1994)

[32] M. Hayashi, in *Gaseous Dielectrics V*, edited by L. G. Christophorou and D. W. Bouldin (Pergamon, New York, 1987), p. 456.

[33] M. Hayashi and T. Nimura, J. Appl. Phys. **54**, 4879 (1983).

[34] J. C. Person and D. O. Ham, Radiat. Phys. Chem. **31**, 1 (1988).

[35] J. P. Boeuf and E. E. Kunhardt, J. Appl. Phys. **60**, 915, (1986).

[36] L. G. Piper, J. Chem. Phys. **87**, 1625 (1987).

[37] F. Westley, J. T. Herron, R. J. Cvetanovic, R. F. Hampson, and W. G. Mallard, NIST Chemical Kinetics Database, NIST Standard Reference Database 17, National Institute of Standards and Technology, Standard Reference Data Program, Gaithersburg, MD 20899.

[38] L. Elias, E. A. Ogryzlo, and H. I. Schiff, Can. J. Chem. **37**, 1680 (1959).

[39] W. Tsang and R. F. Hampson, J. Phys. Chem. Ref. Data, **15**, 1087 (1986).

[40] R. Atkinson, D. L. Baulch R. A. Cox, R. F. Hampson, Jr., J. A. Kerr, and J. Troe, J. Phys. Chem. Ref. Data, **18**, 881 (1989).

[41] W. G. Mallard, F. Westley, J. T. Herron, and R. F. Hampson, NIST Chemical Kinetics Database-Version 6.0, NIST Standard Reference Database 17. National Institute of Standards and Technology, NIST Standard Reference Data, Gaithersburg, MD (1994).

[42] R. K. Bera and R. J. Hanrahan, J. Appl. Phys. **62**, 2523 (1987).

[43] D. C. Robie, S. Arepalli, N. Presser, T. Kitsopoulos, and R. J. Gordon, J. Chem. Phys. **92**, 7382 (1990).

[44] D. L. Baulch, C. J. Cobos, R. A. Cox, C. Esser, P. Frank, T. Just, J. A. Kerr, M. J. Pilling, J. Troe, R. W. Walker and J. Warnatz, J. Phys. Chem. Ref. Data **21**, 411 (1992).

[45] S. Mukkavilli, C. K. Lee, K. Varghese, and L. L. Tavlarides, IEEE Trans. Plasma Sci. **16**, 652 (1988).

[46] K. V. Baiadze, V. M. Vetsko, S. A. Zdhanok, A. P. Napartovich, and A. N. Starotin, Sov. J. Plasma Phys. **5**, 515 (1979).

[47] W. Tsang and R. F. Hampson, J. Phys. Chem. Ref. Data **15**, 1087 (1986).

[48] R. Atkinson, D. L. Baulch R. A. Cox, R. F. Hampson, Jr., J. A. Kerr, and J. Troe, J. Phys. Chem, Ref. Data, **18**, 881 (1989).

[49] R. E. Olson, J. R. Peterson, and J. Moseley, J. Chem. Phys. **53**, 3391 (1970).

[50] G. Dixon-Lewis, Proc. Roy. Soc. London A **330**, 219 (1972).

[51] W. D. Chang and S. M. Senkan, Environ. Sci. Technol. **23**, 442 (1989).

[52] W. D. Chang, S. B. Karra, and S. M. Senkan, Combust. Sci. Technol. **49**, 107 (1986).

[53] R. Atkinson, D. L. Baulch, R. A. Cox, R. F. Hampson, J. A. Kerr, and J. Troe, J. Phys. Chem. Ref. Data **21**,1125 (1992).

[54] D. Husain, and L. J. Kirsch, Trans. Faraday Soc. **67**, 2025 (1971).

[55] R. T. Watson, J. Phys. Chem. Ref. Data **6**, 871 (1977).

[56] Z. Falkenstein, J. Adv. Oxid. Technol. **1**, 223 (1997).

[57] W. Forst and F. Caralp, J. Chem. Soc. Faraday Trans. **87**, 2307 (1991).

[58] M. Weissman, and S. W. Benson, Int. J. Chem. Kinet. **12**, 403 (1980).

[59] C. J. Cobos and J Troe, Chem. Phys. Lett. **113**, 419 (1985).

[60] J. T. Herron, J. Phys. Chem. Ref. Data **17**, 967 (1988).

[61] J. J. Russell, J. A. Seetula, D. Gutman, F. Danis, F. Caralp, P. D. Lightfoot, R. Lesclaux, C. F. Melius and S. M. Senkan, J. Phys. Chem. **94**, 3277 (1990).

[62] P. S. Stevens; J. G. Anderson, J. Phys. Chem. **96**, 1708 (1992).

[63] P. H. Wine, J. M. Nicovich, and A. R. Ravishankara, J. Phys. Chem. **89**, 3914 (1985).

[64] R. B. Boodaghians, I. W. Hall, and R. P. Wayne, J. Chem. Soc. Faraday Trans. **83**, 529 (1987).

[65] J. Shi and J. R. Barker, Int. J. Chem. Kinet. **22**, 1283 (1990).

[66] J. M. Nicovich, K. D. Kreutter, and P. H. Wine, J. Chem. Phys. **92**, 3539 (1990).

[67] J. T. Herron and R. E. Huie, J. Phys. Chem. Ref. Data **2**, 467 (1973).

[68] D. Albritton, At. Data. Nucl. Data Tables 22, **8** (1978).

[69] L. G. Piper, J. E. Velazco, and D. W. Setser, J. Chem. Phys. **59**, 3323 (1973).

[70] D. L. Baulch, J. Duxbury, S. J. Grant, and D. C. Montague, J. Phys. Chem. Ref. Data **10**, Suppl. 1, 1 (1981).

[71] F. Kannari, D. Kimura and J. J. Ewing, J. Appl. Phys. **68**, 2615 (1990).

[72] T. H. Johnson, H. E. Cartland, T. C. Genoni, and A. M. Hunter, J. Appl. Phys. **66**, 5707 (1988).

[73] H. Hokazono, K. Midoridawa, M. Obara, and T. Fujioda, J. Appl. Phys. **56**, 680 (1984).

[74] M. Ohwa, T. J. Moratz, and M. J. Kushner, J. Appl. Phys. **66**, 5131 (1989).

[75] N. Nishida, T. Takashima, F. K. Tittel, F. Kannari and M. Obara, J. Appl. Phys. **67**, 3932 (1990).

[76] D. C. Lorents, 37th Gaseous Electronics Conference, Boulder, CO, 1984 (Bull. Amer. Phy. Soc. **30**, 148 (1985).

[77] J. M. Hoffman and H. B. Moreno, SAND80-1486, UC-34a (1980).

[78] L. A. Levin, S. E. Moody, E. L. Klosterman, R. E. Center, and J. J. Ewing, IEEE J. Quantum Electron. **17**, 2282 (1981).

[79] D. L. Huestis, R. M. Hill, H. H. Nakano, and D. C. Lorents, J. Chem. Phys. **69**, 5133 (1978).

[80] M. M. Turner and W. Smith, IEEE Trans. Plasma Sci. **19**, 350 (1990).

[81] O. Lamrous, A. Gaouar, and M. Yousfi, J. Appl. Phys., **79**, 6775 (1996).

[82] E. Fisher, M. E. Weber, and P. B. Armentrout, J. Chem. Phys. **76**, 4932 (1982).

[83] G. K. Jarvis, C. A. Mayhew, and R. P. Tuckett, J. Phys. Chem. **100**, 17166 (1996).

[84] P. K. Leichner and R. J. Ericson, Phys. Rev. A **9**, 251 (1974).

[85] J. E. Velazco, J. H. Koltz, and D. W. Sester, J. Chem. Phys. **65**, 3468 (1976).

[86] R. E. Olson, J. R. Peterson, and J. Moseley, J. Chem. Phys. **53**, 3391 (1971).

[87] E. L. Duman, N. P. Tishchenko, and I. P. Shmatov, Dokl. Phys. Chem. **295**, 5 (1987).

[88] I. C. Plumb, K. R. Ryan, Plasma Chem. Plasma Proc. **6**, 205 (1986).

[89] D. R. F. Burgess, Jr., M. R. Zachariah, W. Tsang, and P. R. Westmoreland, Prog. Energy Combust. Sci. **21**, 453,1996.

[90] D. R. F. Burgess, Jr., National Institute of Standards and Technology (private communication).

[91] D. L. Parent, R. Derai, G. Mauclaire, M. Heninger, R. Marx, M. E. Rincon, A. O'Keefe, and M. T. Bowers, Chem. Phys. Lett. **117**, 127 (1985).

[92] P. Gaucherel, Int. J. Mol. Spec. **25**, 211 (1977).

[93] L. G. Piper, J. E. Velazco, and D. W. Setser, J. Chem. Phys. **59**, 4932 (1973).

[94] Y. Ikezoe, S. Matsuoka, M. Takebe, and A. Viggiano, *Gas-phase Ion-Molecule Reaction Rate Constants Through 1986* (Maruzen, Tokyo, 1987).

[95] J. C. Person and D. O. Ham, Radiat. Phys. Chem. **31**, 1 (1988).

[96] W. Tsang and R. F Hampson, J. Phys. Chem. Ref. Data **15**, 1087 (1986).

[97] C. Tsai and D. L. McFadden, J. Phys. Chem. **93**, 2471 (1989).

[98] C. D. Walther and H. G. Wagner, Ber. Bunsenges. Phys. Chem. **87**, 403 (1983).

[99] W. B DeMore, D. M. Golden, R. F. Hampson, C. J. Howard, M. J. Kurylo, M. J. Molina, A. R. Ravishankara, and S. P. Sander, JPL Publication **1**, 87 (1987).

[100] J. P. Burrows, D. I. Cliff, G. W. Harris, B. A. Thrush, and J. P. T. Wilkinson, Proc. Roy. Soc. London A **368**, 463 (1980).

[101] L. C. Lee, and T. G. Slanger, Geophys. Res. Lett. **6**,165 (1979).

[102] E. R. Fisher and P. R. Armentrout, J. Phys. Chem. **95**, 6118 (1991).